



**The Impact of Polymeric Flocculants on the Sedimentation,
Flotation and Dewatering of Radwaste Suspensions**

Alexander Peter Geoffrey Lockwood

Submitted in accordance with the requirements for the degree of
Doctor of Philosophy

The University of Leeds

School of Chemical and Process Engineering

18th April 2021

I, the candidate, confirms that the work submitted is my own, except where work which has formed part of jointly-authored publications has been included. The contribution of myself and the other authors to this work has been explicitly indicated below. I confirm that appropriate credit has been given within the thesis where reference has been made to the work of others.

The work in chapter 3 of this thesis has been published as follows:

1. Lockwood, A.P.G., Peakall, J., Warren, N. J., Barnes, M., Randell, G., Harbottle, D., Hunter, T. N. 2021. Structure and sedimentation characterisation of sheared Mg(OH)₂ with anionic polymers. *Chemical Engineering Science*. **231**, 116274.

The work in chapter 4 of this thesis has been published as follows:

2. Lockwood, A.P.G., Kok Shun, P., Basharat, N., Barber, T., Peakall, J., Warren, N. J., Barnes, M., Randell, G., Harbottle, D., Hunter, T. N. 2020. Flotation using anionic surfactants for rapid dewatering of Mg(OH)₂ radwaste suspensions. *RSC Advances [In peer review]*.

The preliminary work in chapter 5 of this thesis has been published as follows:

3. Lockwood, A.P.G., Wadsley, G., Peakall, J., Warren, N. J., Barnes, M., Randell, G., Harbottle, D., Hunter, T. N. 2020. Amphiphilic block copolymers for flocculation and hydrophobization of legacy waste suspensions in flotation driven dewatering operations. *Waste Management Symposium 2020*. Phoenix, Arizona, USA.

The preliminary work in chapter 6 of this thesis has been published as follows:

4. Lockwood, A.P.G., Hussain, S., Peakall, J., Warren, N. J., Barnes, M., Randell, G., Harbottle, D., Hunter, T. N. 2021. A comparison of the sedimentation dynamics of statistical and diblock copolymer flocculation aids in radwaste dewatering. *Waste Management Symposium 2021*. Phoenix, Arizona, USA.

Within this thesis Chapter 1, 2 and 3 contain some relevant introductory based material from papers 1, 2 and 4. For all the publications and conference proceedings, I was responsible for designing and performing the experiments, analysing the data and writing the publications. The contribution of co-authors to publications has predominately been advisory, consistent with their role as academic supervisors and industrial supervisors of this PhD.

The exception to this is that in Chapter 3, Stuart Micklethwait aided in performing cryogenic-scanning electron microscopy used to qualitatively determine $Mg(OH)_2$ -polymer floc structure and properties. In Chapter 4, Phillip Kok Shun and Nabil Basharat, aided in data collection for the Bikerman column foam stability tests. Additionally, author Thomas barber, synthesised the sodium lauroyl isethionate material used as a collector in flotation operation. In Chapter 5, Georgina Wadsley performed the data collection for the UV-visibility spectroscopy tests, though the isotherms were computed and data analysed by myself. In Chapter 5, Casey Thomas, aided in and training of equipment use and collection of oscillatory surface tension and elasticity measurements. In Chapter 6, Serish Hussain, completed bed consolidation tests for the PAA-*co*-PAM flocculated system due to local lab COVID-19 restrictions.

This copy has been supplied on the understanding that it is copyright material and that no quotation from the thesis may be published without proper acknowledgement. The right of Alexander Peter Geoffrey Lockwood to be identified as Author of this work has been asserted by him in accordance with the Copyright, Designs and Patents Act 1988.

© 2021 The University of Leeds and Alexander Peter Geoffrey Lockwood

Signed



Alexander Peter Geoffrey Lockwood

Acknowledgements

I would like to extend my deepest gratitude to the final year Masters of Engineering students I supervised, Philip Kok Shun, Nabil Basharat and Georgina Wadsley, for their help in data collection. Especially during the vast amount of flotation campaigns that were completed for this thesis. I would like to thank Stuart Micklethwait for his guidance and advice in the completion of both scanning electron microscopy and cryogenic scanning electron microscopy. I extend my appreciation to Dr Nicholas Warren, Dr Stephen Knox and Dr Sam Parkinson for their guidance and training in reversible addition-fragmentation chain-transfer polymerisation and benchtop nuclear magnetic resonance analysis of polymer samples. I would like to thank Martyn Barnes and Prof Geoff Randall of Sellafield Ltd. for their guidance in the industrial relevance and application of this research. I would also like to thank and acknowledge Casey Thomas, Prof Grant Webber and Prof Erica Wanless of the University of Newcastle (Australia) for their training and guidance on oscillatory tensiometry for investigation of amphiphilic block copolymer aqueous solution interfacial surface and elasticity. I would also like to thank the Engineering and Physical Sciences Research Council (EPSRC) and Sellafield Ltd. for funding this research.

I would like to thank all the members of the Next Generation Nuclear Centre for Doctoral Training cohort 3 and the entirety of the University of Leeds nuclear engineering research group (with a shout out to Dr Alastair Baker, Dr Lee Mortimer and Dr Andrea De Santis for organising group meetings, seminars and most importantly the socials!). I would like to thank everyone for continuing to meet for both research and social gathering during the COVID-19 pandemic, the continued contact really helped me to maintain a positive mental attitude and remember that I was not alone during this difficult time. By extension I believe we all need to thank Eric Yuan for the development of Zoom video conferencing. I would like to thank my parents Geoffrey and Sharon Lockwood, my sister Rachael and my partner Ria for their unwavering support. Finally I would like thank particularly Flump, who sadly passed away during my time as a doctoral candidate.

Abstract

The use of polymeric flocculants is receiving greater interest as a cheap, easily deployable and effective reagent to aggregate fine radwaste particulates, thus enhancing contaminant recovery in nuclear decommissioning. Particularly in the UK, where a significant volume of $\text{Mg}(\text{OH})_2$ based sludge has developed as part of the UK waste inventory in *in situ* environments. Removal and treatment of this radionuclide impregnated sludge is crucial for current decommissioning strategies. This sludge is a polydisperse distribution of particle sizes, from fuel fragments to colloidal $\text{Mg}(\text{OH})_2$. Current strategies are dominated by the use of gravity driven operations such as sedimentation and thickening, technologies which have low reliance on mechanical parts being impervious to failure, which are difficult and expensive to address in radioactive environments. Whilst coarser particle sizes settle with ease, the colloidal and fine material is more problematic to remove through sedimentation. Whilst it is known, and was shown in this work that polymeric flocculants can improve suspension residence times, the role of floc structure is not fully understood and was probed in depth in this thesis, where due to the lack of inter-aggregate spacing, larger flocs made from poly(acrylic acid)-*co*-polyacrylamide settling aids were most influential on sedimentation rates when scrutinised with fractal modified hindered settling models.

As the decommissioning of facilities which hold the $\text{Mg}(\text{OH})_2$ sludge inventory is time critical due to degradation of the building structures, an alternative to the use of gravity driven sedimentation is dispersed air flotation. Flotation was investigated as a rapid alternative to remove suspended $\text{Mg}(\text{OH})_2$ material using traditional anionic surfactant collectors, sodium dodecyl sulphate and sodium lauroyl isethionate. In order to optimise the process, the optimum dose of hydrophobic surface modifier, known as a collector, was found to be determined to be a function of collector surface coverage. A common observation of surfactant collector driven flotation is that there is a hydrodynamically limited operational envelope for recoverable particle size distributions. Where fines lack the inertia to overcome the slip streams generated by rising bubbles and coarse particles have high bubble detachment energies. There was also significant water entrainment during flotation using surfactants. Polymeric flocculants were synthesised as block copolymers, poly(acrylic acid)-*b*-poly(n-butyl

acrylate), to display amphiphilic properties. These amphiphilic block copolymers were deployed as dual flocculation-flotation aids to aggregate fines to possess the inertia for bubble attachment, whilst lacking the interfacial surface energy reduction to result in excess water entrainment. It was found that the relative hydrophobic chain length of these macrosurfactants was highly influential on flotation and flocculation performance, with greater collector efficiencies than traditional surfactants due to their superior water retention.

The different approaches were compared by hypothesising five deployment strategies, including sedimentation without polymers, sedimentation with the optimum dosages for flocculation and sedimentation using both poly(acrylic acid)-*co*-polyacrylamide and poly(acrylic acid)-*b*-poly(n-butyl acrylate). Finally, sedimentation rates were compared pre and post-flotation using poly(acrylic acid)-*b*-poly(n-butyl acrylate). The consolidated bed post flotation was also compared for the 5 scenarios and additional considerations for selecting an optimum strategy were also discussed to inform on possible future work.

Table of Contents

Acknowledgements	iv
Abstract	v
Table of Contents	vii
Chapter 1: Introduction	2
1.1) Sellafield and dewatering legacy spent nuclear fuel ponds	2
1.2) Solution requirements	6
1.3) Technology selection	7
1.3.1) Polymeric settling aids.....	7
1.3.2) Flotation using traditional collector agents.....	10
1.3.3) Flotation using novel polymeric collector agents	11
1.4) Thesis Delivery	13
Chapter 2: Literature Review	15
2.1) Magnox sludge and radwaste analogues.....	15
2.2) Polymers and particle interactions.....	20
2.2.1) Types of polymers and their interactions with particles	20
2.2.2) Polymer adsorption and the role of molecular weight and charge density.....	22
2.2.3) Flocculation mechanisms and non-equilibrium effects	25
2.2.4) Floc growth and breakage.....	32
2.3) Quantifying floc structure.....	35
2.3.1) Visualising floc structure	35
2.3.2) Mandelbrot's Fractal dimension for aggregates	36
2.3.3) Determining fractal dimension	38
2.4) Sedimentation analysis and modelling	45
2.4.1) The role of polymers in improving settling rates.....	45
2.4.2) Stokes Law and multiple fractal particle modifications	46
2.5) Surface active molecules and macromolecules (SAMs).....	51
2.5.1) Amphiphilic surfactants and block copolymer properties	51
2.5.2) Surface tension and dilational viscoelasticity.....	52
2.6) Flotation.....	60
2.6.1) Flotation in nuclear and bubble attachment factors	60
2.6.2) Surface coverage and hydrophobisation	62
2.6.3) Role of particles in foam stabilisation	66
2.6.4) Quantifying foam stability: dynamic foam stability index.....	68

2.6.5) Dewatering efficiencies.....	71
2.7) Polymers as collectors for flotation	72
2.7.1) Hydrodynamic considerations and aggregation advantages	72
2.7.2) Minerals vs nuclear	75
Chapter 3: Structure and sedimentation characterisation of sheared Mg(OH)₂ with anionic polymers	78
3.1) Introduction.....	78
3.2) Theory	81
3.2.1) Fractal dimension	81
3.2.2) Modified Stokes law	82
3.3) Materials and methodology.....	84
3.3.1) Materials	84
3.3.2) Production of flocculated particle suspensions.....	85
3.3.3) Size and structural characterization	86
3.3.4) Gravimetric sedimentation performance.....	89
3.4) Results and discussion	89
3.4.1) Size and structure characterization of flocculated Mg(OH) ₂	89
3.4.2) Measurement and prediction of floc sedimentation rates	100
3.5) Conclusions.....	110
3.6) Nomenclature for Chapter 3.....	111
Chapter 4: Flotation using anionic surfactants for rapid dewatering of Mg(OH)₂ radwaste suspensions	114
4.1) Introduction.....	114
4.2) Experimental	116
4.2.1) Materials	116
4.2.2) Particle size analysis	117
4.2.3) FBRM measurement	117
4.2.4) Collector adsorption onto Mg(OH) ₂	118
4.2.5) Foamability tests	119
4.2.6) Flotation experiments.....	120
4.3) Results and discussion	122
4.3.1) Natural aggregation characterisation	122
4.3.2) Collector adsorption and effect on particle aggregation	125
4.3.3) Foamability	131
4.3.4) Flotation performance	134
4.4) Conclusions.....	140

4.5) Nomenclature for Chapter 4	141
Chapter 5: Utilising amphiphilic block copolymer self-assembly for dual flocculation-flotation dewatering optimisation.....	143
5.1) Introduction.....	143
5.2) Materials and experimental methodology.....	147
5.2.1) Materials	147
5.2.2) Synthesis and Characterisation of Poly(acrylic acid)-b-poly(n-butyl acrylate).....	147
5.2.3) Interfacial tension and viscoelasticity characterisation	149
5.2.4) Polymer-particle adsorption.....	150
5.2.5) Flocc structure characterisation	151
5.2.6) Sedimentation and flotation performance and analysis	152
5.3) Results and discussion	153
5.3.1) Interfacial tension and dilational viscoelasticity.....	153
5.3.2) Polymer-particle adsorption.....	158
5.3.3) Flocc structure characterisation	162
5.3.4) Sedimentation and flotation performance.....	165
5.4) Conclusions.....	178
5.5) Nomenclature for Chapter 5	180
Chapter 6: A comparison of the sedimentation dynamics of statistical and block copolymer flocculation aids in radwaste dewatering	182
6.1) Introduction.....	182
6.2) Deployment scenarios.....	183
6.3) Materials and methodology	185
6.3.1) Materials	185
6.3.2) Flocc structure characterisation	186
6.3.3) Sedimentation analysis and settled bed concentration.....	187
6.4) Results, discussion and implementation considerations	188
6.4.1) Scenario 4 and 5 flocc size characterisation.....	188
6.4.2) Scenario 5 sedimentation model selection and validation	189
6.4.3) Scenario 5 post-flotation sedimentation modelling	192
6.5) Conclusions.....	197
Chapter 7: Conclusions and future work	199
7.1) Conclusions.....	199
7.2) Future work.....	203

Bibliography	205
Appendix A: Supplementary data for Chapter 3	226
A.1) Detailed description of Mg(OH) ₂ characterisation	226
A.2) Supplementary figures	227
Appendix B: Supplementary data for Chapter 4.	234
Appendix C: Supplementary data for Chapter 5.....	236
C.1) Detailed description of amphiphilic block copolymer synthesis	236
C.2) Supplementary Figures.....	240

Part I

**Introduction and review of literature associated with the scope of the
established investigation parameters**

Chapter 1: Introduction

1.1) Sellafield and dewatering legacy spent nuclear fuel ponds

Sellafield was constructed in the late 1940s to be the site of a rapid atomic weapon development programme in response to the ceasing of Anglo-American atomic weaponry collaboration post World War II. The initial efforts to transmute U^{238} to weapons grade Pu^{239} were completed using the historic Windscale Pile reactors, which had a sole use of plutonium generation¹. The following iteration of UK nuclear reactors were the Magnox fleet. Named after the alloy which their fuel cladding is composed of, Magnox reactors were primarily utilised for energy production. However, Calder Hall and Chapelcross (earlier facilities) allocated most of their fuel towards plutonium production for the weapons effort². Due to the low burn-up required for weapons-grade isotopic purity, high throughputs of Magnox fuel resulted in the requirement for large water cooling facilities to be commissioned². There are two major legacy ponds at the Sellafield site, the Pile Fuel Storage Pond (PFSP) and the First-Generation Magnox Storage Pond (FGMSP) shown in Fig. 1.1. These facilities were constructed in 1949 and 1962 respectively as open-air structures designed to receive and store irradiated fuel from Windscale Pile and Magnox reactors, and to de-clad fuel rods prior to the fuel being processed. PFSP ceased operating in 1962 though waste was still imported into the mid-70s and FGMSP accepted fuel until 1992^{3,4}.



Figure 1.1: Legacy spent nuclear fuel pond at Sellafield⁵.

After a long storage period and being placed into a passive care and maintenance regime, the fuel rods, primarily their cladding (mainly Magnox), started corroding in the pond with the mechanisms described in Eqn. 1.1 to produce $Mg(OH)_2$. This has given rise to increased radiation levels from mobile soluble and particulate fission products (from 6 mm uranium fuel material to nanometre scale brucite colloids), which in turn have increased pond water turbidity⁵⁻⁷. These ponds have accumulated significant quantities of waste materials amongst the skips of fuel, including but not limited to large inventories of corroded Magnox sludge, fuel rod fragments, metal fragments (from fuel skips), concrete degradation products (from the pond infrastructure), wind-blown sand, and other materials such as bird guano and animal remains (see Fig. 1.2)⁴.

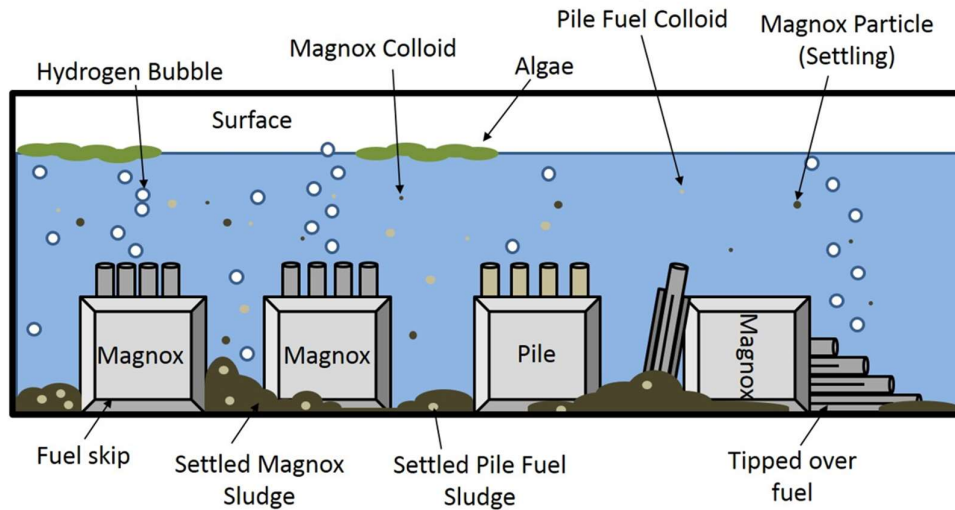


Figure 1.2: Diorama of the challenges to legacy nuclear fuel storage ponds, illustrating Magnox fuel corrosion products, hydrogen generation and algal blooms.

Due to the open-air nature of the facility, the spent Magnox clad fuel has been subject to external contaminants, resulting in a restricted ability to control pond water chemistry which has resulted in organic contamination from algal blooms^{8,9}. FGMSP Magnox fuel cladding corrosion has resulted in a large inventory of sludge and suspended particulates estimated to be $\sim 1300 \text{ m}^3$, allowing soluble radionuclides to leach out of the fuel rods causing activity levels to rise to the order of $1000 \times 10^6 \text{ MBq.m}^{-3}$ ^{6,10,11}.

Maher *et al.*⁷ linked an activity increase in Sellafield site discharges to the Irish sea to the fact that site ion exchange plant (SIXEP) effluent streams contain suspended particles and colloids that could firstly interfere with the ion exchange process in SIXEP. Mg(OH)₂ based colloids will dissolve in the carbonation stage of SIXEP so that the feed pH is compatible with the ion exchange stage. Dissolved Mg²⁺ ions may compete with target radionuclides to occupy sorption sites on the clinoptilolite ion exchange (IX) media, increasing waste volumes due to an increased frequency of spent IX bed changes^{12,13}. Secondly, Mg(OH)₂ colloids act as a vector for the transport of radionuclides to the Irish sea¹⁴. Colloids are known as potential controllers of radionuclide speciation and transport due to their small size and high surface area to mass ratio⁷. They are capable of incorporating radionuclides into their structure, particularly the actinides. Mg(OH)₂ particles have been reported to retain various radionuclides efficiently.

A study by Maher *et al.*⁷ showed that Pu(V) and Am(III) had strong sorption to larger brucite colloid particulates. Any radionuclides associated with larger particles should be most easily removed by the initial sand filtration column in SIXEP (see process flow diagram in Fig. 1.3), and this is probably responsible for most of the removal of actinide activity from the feed solution. However, the sand bed filter will not remove all colloids. It would be expected that a simple ion exchange column would be relatively ineffective at removing any radionuclides that were incorporated within colloidal material⁷. This colloid incorporation likely accounts for the rise in total alpha activity being discharged to the sea with the increasingly intensive retrieval operations occurring on site, particularly FGMSR. Thus FGMSR retrieval programme has become subject to an effort to reduce the transport of colloidal material to SIXEP during its aggressive decommissioning programme^{7,14,15}.

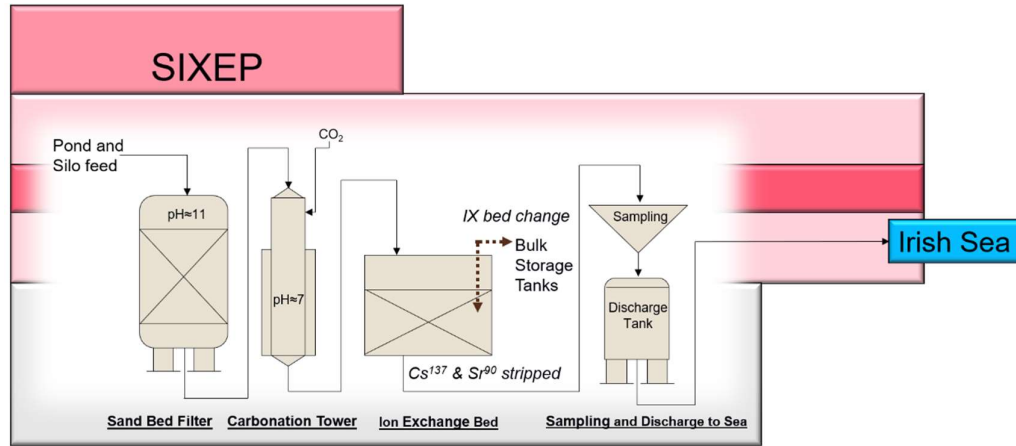


Figure 1.3: Site ion exchange effluent plant (SIXEP) process flow diagram. Showing the initial filtration stage of the FGMSP and silo feed through sand bed filters at pH 11. The feed is then carbonated to acidify the feed to pH 7 before stripped of Cs¹³⁷ and Sr⁹⁰ in an ion exchange column. The ion exchange media bed is changed and spent bed is sent to bulk storage tanks. The feed is then sampled and held in a discharge tank before being committed to the Irish sea.

To remove the large inventory of sludge in FGMSP, the sludge packaging plant (SPP1) was commissioned. In this process, Mg(OH)₂ sludge material is pumped at a maximum solids concentration of 2.5 vol.% using a floating platform⁶. This material is transferred at a rate of 30 m³.h⁻¹ to an adjacent dewatering facility known as the sludge packaging plant (SPP1). In this facility, 80 m³ batches of sludge are transferred into the three 450 m³ tanks (see Fig. 1.4), where the solid sludge material sediments under gravity. The lower turbidity supernatant liquor is transferred to SIXEP via an effluent decanting tank (opportunity for settling aid deployment) and the sludge can then be encapsulated for final disposal when a geological disposal facility becomes available⁶. SPP1 has in-built pulse jet mixers, which when a downstream disposal facility becomes available, will be able to resuspend the settled sludge and transport the slurry to downstream processing.

However, there are implicit performance limitations, due to the wide range of particle sizes, therefore sedimentation of sludge material from FGMSP may not target the smaller diameter particulates which could lead to downstream abatement issues as previously discussed^{6,7}. Additionally, sludge dewatering is a notoriously slow process with long residence times. Research into Mg(OH)₂ sedimentation of similar concentrations by Johnson et al.¹⁶ has found sedimentation rates less than 0.5 cm.min⁻¹. Assuming that slurry batches are consistently 2.5 vol.% solids concentration in 80m³ batches, it will take at least 650 sludge transfers to completely empty FGMSP of sludge⁶. Therefore, as the

decommissioning rate determining step to reduce risk on site, technologies that decrease SPP1 dewatering time are of particular interest to Sellafield.

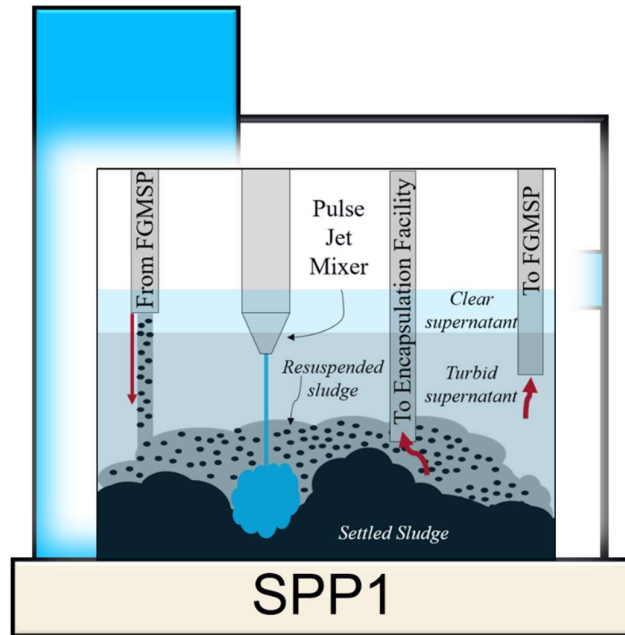


Figure 1.4: Diorama of sludge packaging plant 1 (SPP1).

1.2) Solution requirements

Nuclear is different. There is substantially stricter regulation on engineering design compared to most other industry barring aviation. The nuclear industry processes volumes that are generally much smaller and often in batches than industries such as minerals processing or water treatment. Consequently, the economics of the process have different priorities; in the nuclear industry these are primarily driven by safety. As the activity concentration of the FGMSF water is likely primarily from the Magnox sludge, the pipework and retrieval processes have to be shielded. This may impact upon an operator's ability to monitor slurry properties. Monitoring and sampling in general is difficult in the nuclear industry due to the challenge imposed by the high radioactivity. *In situ* characterisation is required to be robust both mechanically and analytically in radiation fields. Conversely, *ex situ* sampling not only may not be representative of the entire sludge population being processed, but carries a risk of increased worker dose, thus volumes should be kept as low as reasonably practical (ALARP). Therefore, nuclear waste management processes, particularly those processing sludge, require robustness to handle broad feed envelopes due to uncertainty in material characterisation and must be a tried and

tested technology. Due to the radioactivity, technologies must meet the requirement for minimal intervention, thus should be simple, robust and have a minimal number of moving parts⁵.

Sellafield in particular has some additional constraints such as geographic space making deploying engineering solutions more complex, as it is very difficult to retrofit new technology into existing facilities. Thus any retrofitted technology must have a small geographic footprint, bespoke design and be modular for components to break down for easier instalment in a legacy waste management facility. Processes that require additives to enable or to enhance the process are not favoured by the nuclear industry, therefore if they must be used, there must be confidence that they will not generate further secondary waste and/or be compatible with the long-term stability of the final waste product which is yet to be determined⁵. These process requirements are summarised in Fig. 1.5.

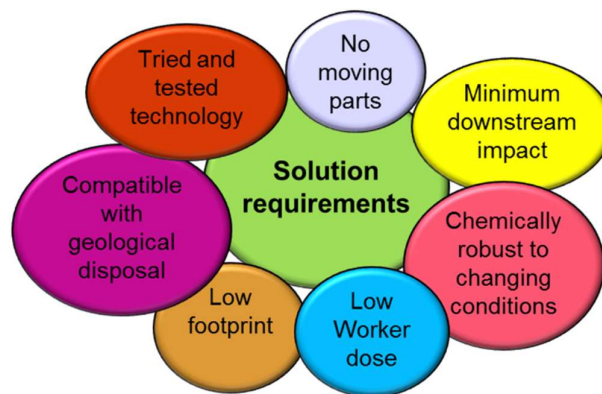


Figure 1.5: Summary of decommissioning technology requirements.

1.3) Technology selection

1.3.1) Polymeric settling aids

In order to improve long residence times in these dewatering facilities, it is common practice to utilise polyelectrolyte macromolecules known as polymeric flocculants¹⁷⁻²⁰. These reagents adsorb to the surface of particles and allow aggregation of smaller particulates into more settleable flocs, improving their overall sedimentation rates, which by Stokesian reasoning is a function of floc size and density^{17,21-23}. As $Mg(OH)_2$ based colloids have been reported to have a slight cationic surface charge^{7,16,24}, and anionic polymer flocculation agents have previously been deployed to aid sedimentation of cationic

particles, it is likely that anionic reagents will have a strong affinity for $\text{Mg}(\text{OH})_2$ corrosion products. Polymeric flocculants can be applied as low concentration organic additives, potentially below the concentration of organic material such as algal blooms⁹. Additionally, waste treatment methods such as thermal treatment, a vitrification process where waste is conditioned by calcining and immobilisation in a borosilicate glass²⁵⁻²⁷, would combust the organic material removing them from the final stored waste composition.

Typically water treatment industries opt for low charge density (30%-40% anionic strength) statistical copolymers, which have a random configuration of anionic to non-ionic monomers to achieve the required charge density and are usually in the order of 10^5 - 10^7 $\text{g}\cdot\text{mol}^{-1}$ molecular weight^{20,28}. It should be noted that non-ionic polymers can also be used which bond to particle surfaces via hydrogen bonding and hydrophobic interactions rather than electrostatic forces²⁹. These polymers adsorb to cationic particle surfaces, but due to their slow surface conformation kinetics, possess a residual polymer chain length in the form of 'loops' and 'tails', which expand out into solution past the electrical double layer stability region (Debye length) of the particulates, allowing them to bind to adjacent particles in suspension^{17,30-34}(see Fig. 1.6). This 'bridging' flocculation mechanism creates large open and porous structures which have superior sedimentation dynamics to the initial suspension^{17,35,36}. Other flocculation mechanisms have been investigated, such as "charge patch" flocculation, which uses smaller (10^4 - 10^5 $\text{g}\cdot\text{mol}^{-1}$) polymers of 80-100% charge densities to adsorb denser and flatter onto a particle's surface, resulting in localised charge reversal allowing particles to electrostatically bind. This mechanism conversely produces smaller but denser flocs than bridging flocculation^{17,19,33,37,38}.

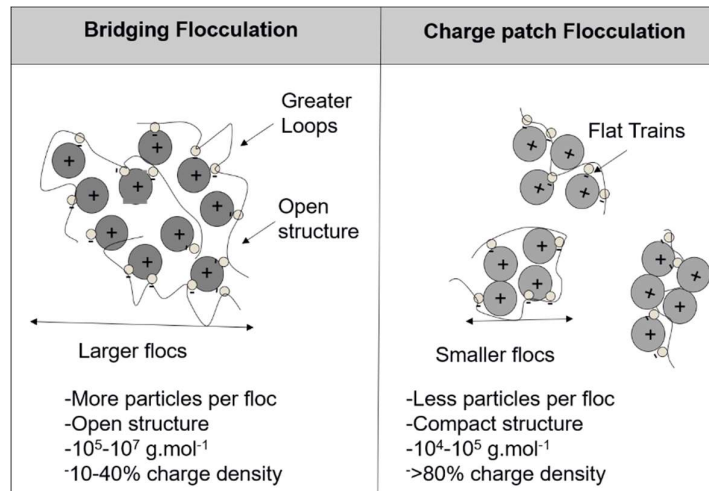


Figure 1.6: Diagram showing the difference in floc characteristics as a function of flocculation mechanism.

As the SPP1 tanks are heavily shielded to prevent exposing workers to radiation dosages, monitoring the sedimentation rate and clear supernatant-suspension interfacial height (or mudline) is problematic⁵. Visual observations cannot be made as workers would be exposed to the radiation ‘shine-path’ and current *in situ* monitoring such as cameras are not adequate to determine the position of the mudline. Whilst some progress has been made on *in situ* acoustic backscatter monitoring, there is still additional work required for deployment, especially regarding determination of floc structure²². Research into sedimentation models has developed quite substantially since the original Stokes sedimentation model in 1851 for an individual floc was conceived³⁹. There have been notable developments on this model, including the Richardson-Zaki equation in 1954⁴⁰. The Richardson-Zaki model incorporated a function to account for the permeability of a consolidating bed as a function of solids concentration and an exponent, which is a function of the turbulence of particle displaced fluid, accounting for hindered settling effects in multiple particle sedimentation systems²¹. As it is known from microscopic investigation^{35,41-43} and floc formation models^{38,44,45} that flocs are more open, less dense and larger structures than in their unflocculated state, a term must be introduced to represent these properties. Mandelbrot introduced the world to fractal mathematics in 1975⁴⁶. Which allowed aggregates to be modelled and described using a fractal dimension, a power law which could describe the decreasing density as a floc diameter increases which has been exploited to mathematically describe floc structure since its inception^{36,38,47-53}. This could then be incorporated into the Stokes sedimentation model to account for the decreasing density as a floc grows and

incorporated with drag and shape effects. Most recently, fractal modifications have been applied to batch sedimentation scenarios and have been shown to achieve first approximations of individual and zonal settling rates^{16,18,44,49,50,54}.

Fractal modified sedimentation models do require determination of certain inputs such as structural properties i.e. floc size distributions and solid contents in addition to structural characteristics such as the fractal dimension. To keep radiation dose to workers ALARP, online *in situ* monitoring is preferred to determine suspension properties. A well utilised technique that can be deployed to monitor dynamic floc sizes online is a focused beam reflectance meter (FBRM), which has been deployed in the minerals industry to measure the effect of shear on flocculation kinetics⁵⁵⁻⁶⁰. Understanding the particle size distribution of the radwaste suspensions is important as the current sedimentation models require a single representative diameter to model the sedimentation of a polydisperse particulate suspension. However, there are currently no *in situ* methodologies to analyse fractal dimension, therefore selected methodologies must be safety driven to keep radiation doses to workers ALARP and by extension sample volumes must also be ALARP. Static light scattering (SLS) has been shown to be an effective, cheap and rapid low volume *ex situ* method to determine fractal dimension of flocs which could be used by SPP1 operators^{19,44,48,53,61-64}. Combining *in situ* FBRM and low volume *ex situ* SLS will provide inputs for fractal modified suspension sedimentation models which can be used to predict zonal settling rates and by extension optimum SPP1 residence times.

1.3.2) Flotation using traditional collector agents

Flotation has been deployed in various industries including mineral engineering⁶⁵⁻⁶⁹ and water treatment⁷⁰⁻⁷³. Flotation cells such as the 'Jameson cell' have been deployed in industry. Jameson cells have been shown to achieve a high throughput in a small area, are easy to operate and tune for feed variations, conduct stable operation with minimal operator involvement, require minimal maintenance due to few moving parts, are easy to install and commission and have flexible cell designs⁷⁴. In particular, the Jameson cell downcomer provides high mixing and particle bubble contact profiles without the need for moving parts, as moving parts may be susceptible to breakage and as a result difficult to repair in a radioactive environment. Flotation cells have varying geographical footprints depending on the cell model with as low as 0.19 m² occupation footprint⁶⁶. Designs have even adapted

to be modular and mobile for deployment at nuclear accident sites such as the meltdown site of Fukushima Daichi⁷⁵. So due to the previously discussed characteristics of the flotation cell and how well they align with the solution requirements shown in Fig. 1.5, flotation has received recent interest from the nuclear industry^{71,75-77}. However, $Mg(OH)_2$ based wastes have received little to no attention in regards to flotation. Surfactants utilised as ‘collectors’ have been successfully deployed to hydrophobise particulates so that they have high surface energy and can attach to air-water interfaces such as rising bubbles⁷⁸⁻⁸¹. However, understanding the role of collector adsorption onto particle surfaces still requires additional research, in particular the relationship between collector surface adsorption density and the effect that this adsorption has on flotation performance and particle aggregation⁷¹. Understanding the role of collector adsorption onto $Mg(OH)_2$ surfaces, and the point of monolayer to bilayer adsorption transition, will allow the design of a flotation process with rapid dewatering kinetics. With high dewatering ratios and facilitate an alternative technology to sedimentation which can be subject to process intensification^{80,82}.

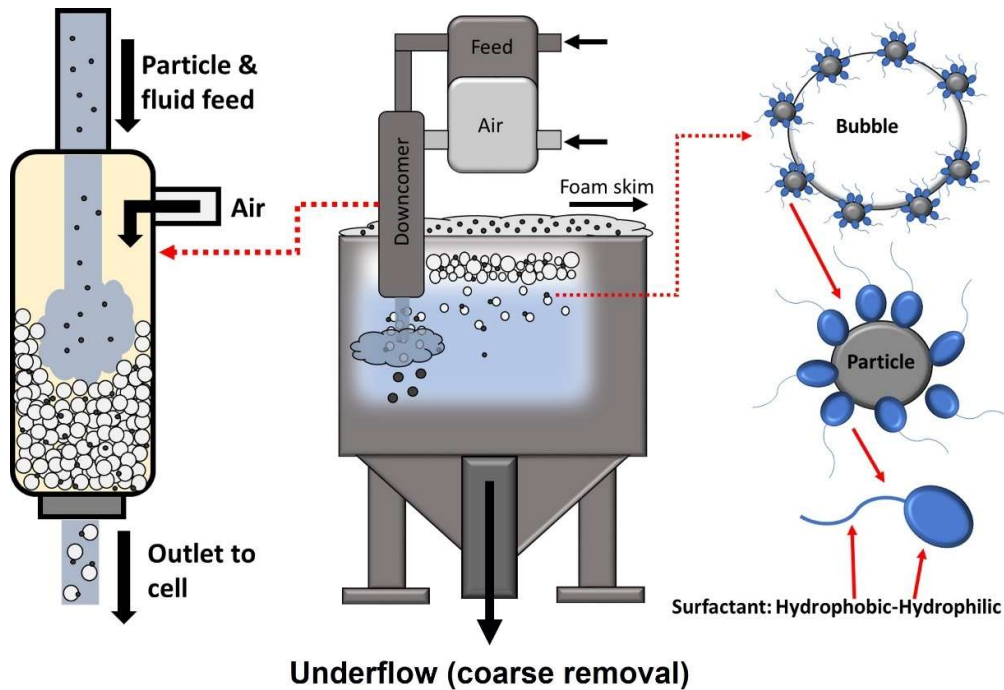


Figure 1.7: Diagram of Jameson Cell and surfactant-particle monolayer adsorption.

1.3.3) Flotation using novel polymeric collector agents

Drawbacks with surfactants as collectors are that foaming agents are not preferable for downstream processing, particularly regarding foaming in the SIXEP carbonation tower. Additionally, surfactants can be uneconomic with regards to retaining water. This has

become problematic not just for the nuclear industry, where wasted water is considered to be secondary waste generation, but also in minerals operations being performed in countries where water is a scarce commodity such as Australia. Additionally, flotation is a hydrodynamically dependent process, where particle size is a major factor in particle-bubble attachment interactions^{78,83}. Particles that are too large (coarse) have greater bubble detachment energies due to the balance of buoyant and gravitational forces. Conversely, particles which are too fine lack the inertia to overcome the slipstreams created by rising bubbles preventing particle bubble attachment⁸⁴.

This has driven research into dual flocculation-collector reagents which can aggregate fine particles so that they are compatible with the flotation cell hydrodynamic operating envelope. Particularly, the development of stimuli-responsive copolymers. Whilst these reagents have been shown to be effective at dually flocculating and floating fine particles, there are restraints on their deployability due to the nature of the stimuli changes which are often temperature switches⁸⁵⁻⁸⁸ or pH triggered⁸⁹. This has both economic and regulatory concerns in regards to changing the conditions of the waste streams to be compatible with these reagents^{5,84}. The use of amphiphilic block copolymers has received attention in recent years for their analogous behaviour to surfactants, however they have displayed an ability to have tuneable properties in regard to their surface activity⁹⁰⁻⁹³ and flocculation capacity^{85,94}. Whilst to the author's knowledge they have not been deployed in flotation operations previously, the selection of the hydrophilic and hydrophobic comonomer and their relative chain lengths has been shown to provide highly hydrophobising environments resulting in polymeric self-assembly at great enough relative hydrophobicity^{93,95-98}. Even completely liberating water from the adsorbed block copolymer layers on the surface of particles⁹⁴. It is suspected that from these characteristics that amphiphilic block copolymers may provide the same mechanistic advantages as stimuli responsive polymers without trigger requirements. Whilst amphiphilic block copolymers are likely to have poor selectivity properties which are important to the minerals industry⁸⁸, they could be deployable as effective solid-liquid separation operations where flotation can target fines and improve the sedimentation dynamics of coarse particles in sequential flotation-thickening operations^{76,99}.

1.4) Thesis Delivery

Chapter 2 of this thesis will focus on the literature and previous research around $\text{Mg}(\text{OH})_2$ based radwaste suspension, the use of various polymers to flocculate similar materials with focus on the resultant structure and sedimentation behaviour as a function of polymer ionic charge density and shear conditions. The use of predictive sedimentation models will also be discussed. Dispersed air flotation to dewater similar suspensions will also be investigated, looking at the role of surfactant collector adsorption onto particle surfaces and their influence on particle aggregation and foam stability. Finally the role of novel copolymers as collector agents will be discussed in previous literature.

Chapters 3-6 will consist of original research conducted by the author. Chapter 3 investigates the utilisation of common commercial polymer agents of varying ionic charge density to flocculate and settle a suspended $\text{Mg}(\text{OH})_2$ radwaste analogue looking at the differences in floc size, structure and sedimentation behaviour. Chapter 4 investigates the use of a common surfactant based collector sodium dodecyl sulphate. This was compared to a surfactant not previously used as a collector, but is ubiquitous in the personal goods industry, sodium lauroyl isethionate. The adsorption behaviour of the two collectors was compared and related to the aggregation behaviour of a $\text{Mg}(\text{OH})_2$ radwaste analogue and the dispersion-surfactant foam stability was investigated. The adsorption behaviour was then linked to the flotation of the radwaste analogue using four metrics: mass recovery, water retention, residual suspension concentration and dewatering efficiency. Chapter 5 investigates the use of novel amphiphilic block copolymers of varying hydrophobic chain length to flocculate and float the same $\text{Mg}(\text{OH})_2$ radwaste suspensions. The interfacial properties of the block copolymers were investigated by analysing the changes in interfacial surface tension and dilational viscoelasticity as a function of copolymer concentration. Similarly to Chapter 3, the floc size and structural characteristics were analysed and the sedimentation rates of the polymers were analysed as function of block copolymer concentration. The flotation performance of the block copolymers were analysed using the same metrics as Chapter 4. Finally, the hydrodynamic limitation of flotation were probed by taking floc samples in the flotation cell before flotation and from those in the recovered foam phase.

Chapter 6 compares the floc structure and sedimentation behaviour of the commercial statistic copolymer and novel block copolymer systems. Five hypothetical deployment scenarios were proposed and the behaviour of the two polymers was compared in terms of sedimentation rates and consolidated bed concentrations. These scenarios included firstly sedimentation without any polymers, then two scenarios comparing the optimum sedimentation dosages for the commercial statistical and novel block copolymers using sedimentation only. Finally, two scenarios comparing the novel block copolymers' optimum flotation concentration, including the sedimentation performance only and sedimentation post-flotation. Chapter 7 discusses the conclusions of the author's research and compares it to the previous literature, and finally discusses the possible avenues for future investigation. It should be noted that all error bars in this work are standard error.

Chapter 2:

Literature Review

2.1) Magnox sludge and radwaste analogues

In order to investigate the deployment of polymeric flocculants and surfactants to dewater the Magnox era nuclear wastes, the first stage of this research is to identify a viable radwaste analogue to perform experiments on. The radionuclide loading in real Magnox sludge and resultant cost of sampling from the first generation Magnox storage pond (FGMSP) is not possible from both a safety and economic stand point¹¹. Magnox fuel rods (see Fig. 2.1A) consist of a $Mg(OH)_2$ based alloy cladding (0.7% aluminium and 500 ppm Beryllium)⁸. After being left to corrode for decades, the Magnox alloy corrodes as per Eqn. 1.1 in Section 1.1 and produces either partially or fully corroded $Mg(OH)_2$ based sludge material pictured in Fig. 2.1B and Fig. 2.1C respectively.



Figure 2.1: A) a Magnox fuel canister. B) Partially corroded Magnox alloy. C) Corroded Magnox sludge⁵.

This corrosion of the fuel cladding has liberated $Mg(OH)_2$ particulates into the supernatant FGMSP water⁶. Particulates from FGMSP (and various downstream facilities such as the SIXEP bulk storage tanks and holding tanks) have been sampled and characterised by Gregson et al.¹⁰⁰ using a combination environmental scanning electron microscopy (ESEM) with Energy Dispersive X-Ray analysis (ESEM/EDX), micro-Raman spectroscopy and Fourier transform infra-red spectroscopy (FT-IR). The ESEM analysis identified the morphology to primarily consist of interlock platelets which is typical of brucite phase of $Mg(OH)_2$ and is shown in the ESEMs and EDX spectra in Fig. 2.2A-2.2C. Elevated levels of Al (greater than the 0.7% in the initial alloy⁸) were found to have converted some of the material to $(Mg_6Al_2(CO_2)(OH)_{16} \cdot 4H_2O)$ hydrotalcite and was found to incorporate uranium species in its structure as indicated in Fig. 2.2C¹⁰⁰.

This uranium bearing hydrotalcite phase was also identified by Maher et al.⁷ (see Fig. 2.2D-E) in an investigation to actinide incorporation onto the FGMSP particulate structures,

which have been previously reported to utilise Pu's high redox sensitivity (as it exhibits multiple oxidation states) to escape the Sellafield ion exchange effluent plant (SIXEP) unabated by incorporating itself onto $Mg(OH)_2$ colloidal material¹⁰¹. Maher et al.⁷ found that this hydroxalcite as well as brucite phases were present, where due to the high surface to volume ratio, americium and plutonium were also present on the $Mg(OH)_2$ colloidal structure in addition to uranium species. It was also observed that the particles and colloids in the SIXEP bulk storage tank liquor are magnesium-rich. The exception being the larger, hydroxalcite-like particles which Gregson et al.¹⁰⁰ also identified in Al-rich structures, the particle morphology in the samples was indistinct, although previous characterisation of pond samples has indicated that they are likely to be mostly brucite. In the case of the system analysed by Maher et al.⁷, it was concluded that it was likely that some of the particles are brucite, since there are Mg-rich particles that appear to contain little carbon, indicating that for the research by the author of this thesis, a $Mg(OH)_2$ based material as a waste analogue is likely appropriate.

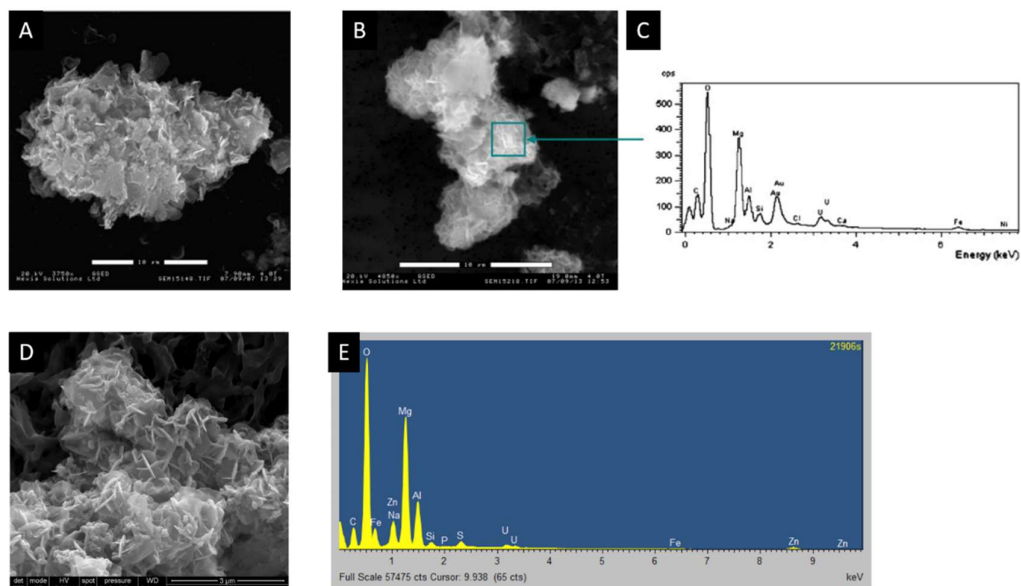


Figure 2.2: A & B) Environmental scanning electron microscopy (ESEM) images¹⁰⁰ and C) corresponding EDX spectra of Mg rich hydroxalcite species found in the SIXEP holding tank¹⁰⁰ D) Low magnification secondary electron images of particles isolated from SIXEP bulk storage tank liquor⁷, with E) associated energy dispersive x-ray (EDX) spectrum

$Mg(OH)_2$ powder dispersed in water has been a commonly used Magnox waste analogue in previous literature such as an investigation to the effects of zeta-potential and yield stress on filtration through a $Mg(OH)_2$ waste analogue bed by Biggs et al.²⁴. In the study by Biggs et al.²⁴, magnesium hydroxide was obtained from Pennine Darlington Magnesia Ltd. The physical properties for these particles were reported and are shown in Table 2.1.

Table 2.1: Physical properties on the Mg(OH)₂ radwaste analogue from Pennine Darlington Magnesia Ltd. used in the work of Biggs et al.²⁴. Including the particle density, the 50th cumulative percentile particle diameter (d_{50}), the specific surface area and porosity of the particles.

Physical property	Value
Density	2.38 g.cm ⁻³
Particle size (volume based d_{50})	3.58 μm
Surface area (BET)	15.43 m ² .g ⁻¹
Porosity (Mercury intrusion porosimetry)	66.2%

The Pennine Darlington Magnesia Ltd. Mg(OH)₂ powder is very fine, with a 50th cumulative percentile particle diameter (d_{50}) of 3.58 μm (dry) and a high specific surface area of 15.43 m².g⁻¹ as well as a noticeably high porosity of 66.2%. SEM micrographs shown in Fig. 2.3A from the work by Biggs et al.²⁴ show a platelet structure similar to those reported by Gregson et al.¹⁰⁰ and Maher et al.⁷ when investigating Mg-rich real pond samples at Sellafield. Biggs et al.²⁴ probed the zeta potential of the Pennine Darlington Magnesia Ltd. Mg(OH)₂ using an electroacoustic zeta-probe and particle suspensions of 10 wt.% were prepared in a background electrolyte of either 0.001 M potassium nitrate or 0.001 M sodium hydrogen carbonate. As the Pennine Darlington Magnesia Ltd. Mg(OH)₂ was found to be soluble and highly self-buffering at pH < 10 (with a natural pH of ~10.5), the pH of the suspension was altered using 0.5-5 M NaOH. The zeta-potential was found to be low (< 10 mV) even at low dosages of NaOH, indicating the presence of weak repulsion forces providing colloidal stability meaning that van der Waals driven aggregation is likely to be expected in these suspensions¹⁰². The iso-electric point was identified by gradually increasing the pH to be pH≈11 as shown in Fig. 2.3B. This suggests that the Mg(OH)₂ radwaste analogue is likely to be slightly cationic at natural alkali pH which will dictate the selection of polymeric flocculants later in this thesis.

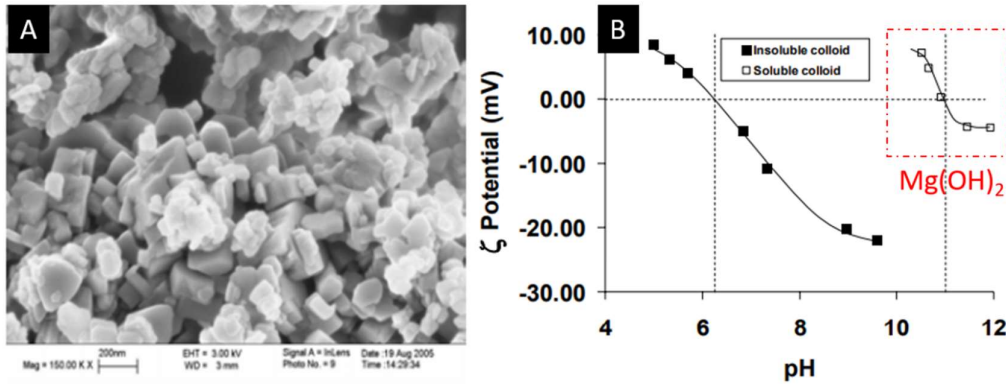


Figure 2.3: A) Scanning electron micrograph of Pennine Darlington Magnesia Ltd. $Mg(OH)_2$. B) The change in zeta-potential with increasing pH for titanium dioxide and $Mg(OH)_2$ (highlighted) by Biggs et al.²⁴.

A $Mg(OH)_2$ powder was used again as a radwaste simulant, but this time by Johnson et al.¹⁶ when investigating the sedimentation properties of $Mg(OH)_2$ powder produced by Rohm and Haas, U.S. called Versamag. A fine white precipitated powder with a density of 2.36 g.cm^{-3} and a solubility of 6.9 mg.l^{-1} . The particles were characterised using a range of imaging techniques including scanning electron microscopy (EVO MA15, Carl Zeiss, Germany), flow particle image analyzer (Sysmex FPIA-2100, Malvern Instruments, U.K.) and particle vision measurement (PVM) instrument (Mettler Toledo, U.S.). Additionally Johnson et al.¹⁶ also investigated the zeta-potential of the water suspended powder using the same methodology as Biggs et al.²⁴ and also *in situ* and *ex situ* particle sizing using focused beam reflectance measurement (FBRM) and static light scattering (SLS) techniques respectively.

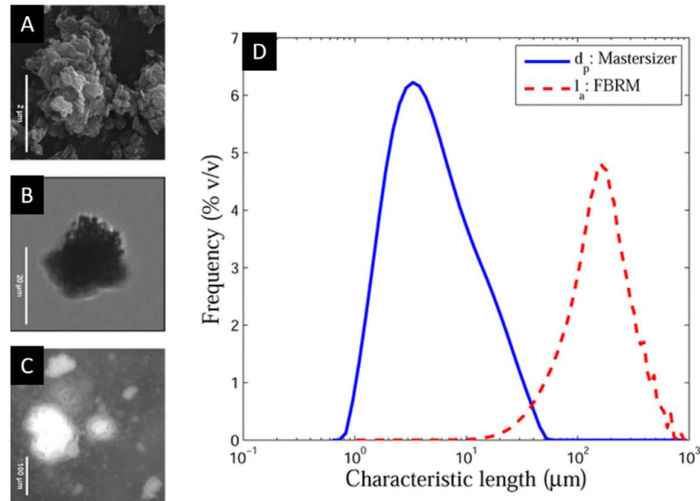


Figure 2.4: Johnson et al.¹⁶ images of Versamag Mg(OH)₂ at three scales: A) scanning electron micrograph at 2 μm. B) flow particle image analysis at 20 μm. C) Particle vision Measurement (PVM) at 100 μm. Particle size distribution measurements: D) Mg(OH)₂ at high shear using a Malvern Mastersizer 2000 and at low shear using a Mettler Toledo FBRM.

Johnson et al.¹⁶ reported a highly self-buffering nature of the Versamag similar to the Pennine Darlington Magnesia Mg(OH)₂ used by Biggs et al.²⁴ which demonstrated low but cationic zeta potential (0.5-3.2 mV). Fig. 2.4A-C show the particle images of Versamag Mg(OH)₂ using SEM, particle flow imaging and PVM respectively. Fig. 2.4A shows an image of the dry powder which reveals hexagonal platelets of brucite, these platelets are clustered into a small primary agglomerate of around 3 μm diameter. These agglomerates of hexagonal platelet crystals are consistent with similar images by Gregson et al.¹⁰⁰ and Maher et al.⁷ in Fig. 2.2A and 2.2D respectively and by Biggs et al.²⁴ in Fig. 2.3A. As a function of the Versamag's low cationic zeta-potential, particle aggregation in suspension was present and shear became an important variable in determining the particle size distribution of the suspension. Johnson et al.¹⁶ used a Malvern Mastersizer 2000E SLS instrument with a dispersion cell running an impeller at 2500 rpm to suspend and pump the pre-sonicated Versamag particles past the measurement window of the SLS instrument. This resulted in a considerably smaller particle size distribution than when measured *in situ* using the FBRM, which while recording chord lengths rather than particle diameters, was performed in a reactor vessel agitated with an overhead axial flow impeller at 250 rpm exposing the suspension to considerably less shear. As a result the FBRM recorded a particle size distribution considerably larger particle sizes that SLS with d_{50} of 152.4 μm and 4.2 μm respectively as shown in Fig. 2.4D. This indicates that shear conditions will

likely be important in any investigation of suspensions performed in the original work in this thesis and should be heavily considered in analysis and discussion.

In summary, Gregson et al.¹⁰⁰ and Maher et al.⁷ have analysed real samples from the first generation Magnox storage pond (FGMSP). Whilst there is some variation in the structure and incorporated impurities, the particulates seem to be primarily composed of Mg-rich hexagonal nanocrystalline platelets similar to brucite. Indicating brucite phase material will be a suitable analogue for radwaste dewatering when utilising polymeric flocculants to sediment and float suspensions to simulate dewatering operations on the Sellafield site. Biggs et al.²⁴ and Johnson et al.¹⁶ have used $\text{Mg}(\text{OH})_2$ radwaste simulants which also exhibit this platelet phase morphology. Both materials, though from different sources, exhibit slightly cationic surface charges, however, not strong enough to stabilise a colloidal suspension. With $\text{Mg}(\text{OH})_2$ suspensions actively aggregating in water and their resultant particle size distribution heavily influenced by shear conditions. Utilising a $\text{Mg}(\text{OH})_2$ simulant in this work will likely need to be subject to complimentary measurement techniques to take into account these effects. Furthermore, polymeric flocculants and surfactant species should be selected to be compatible with a weakly cationic surface charge, indicating a potential affinity to anionic reagents.

2.2) Polymers and particle interactions

2.2.1) Types of polymers and their interactions with particles

Polymers are a chain of organic molecules called monomers, which react together to form a long chain macromolecule, the polymer. If there is only one type of monomer in the polymer this is known as a homopolymer. If there are two or more different monomers in the polymer chain, this is known as a copolymer. These monomers can be arranged either randomly, known as a statistical copolymer where their structure is completely probabilistic, or they can be segregated into their component monomer species to form block copolymers (illustrated in Fig. 2.5)¹⁰³. There are other types of polymer such as structured or cross-linked polymers but they will not be discussed in this work. The design and structure of a polymer critically impacts its ability to flocculate a target particle, so the comonomer selection and structure of the polymer is critical in optimising a dewatering strategy for removing Magnox radwaste particulates from FGSMP supernatants.

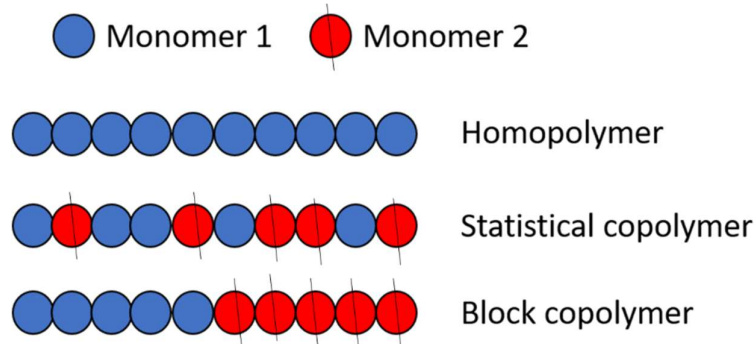


Figure 2.5: Illustration showing the differences in monomer arrangements for homopolymers, statistical (random) copolymers and block copolymers.

In an extensive review by Gregory and Barany³³, the types of polymer and their adsorption mechanics were summarised and included:

- Non-ionic
- Anionic
- Cationic

Cationic and anionic polymers have monomer species which ionise in water such as poly(acrylic acid) [PAA], poly-vinyl sulphate, poly(dimethylammonium chloride) [PDADMAC], diallyl dimethylammonium chloride [DDMAC] and polyethylene imine (PEI). For example, the acrylic acid (AA) in PAA dissociates a proton from the hydroxyl group to form an anionic charge on the acrylic acid species. As adsorption involves the attachment of many polymer segments to a particle surface, each individual segments adsorption only requires a small reduction in free energy (~ 0.3 kT per segment) to compensate for the entropy loss that occurs when the whole polymer adsorbs from the solution to the particle surface¹⁰⁴. In the case of anionic PAA, this free energy reduction can be achieved by electrostatic attraction to a cationic particle surface³³. For non-ionic polymers such as poly(acrylamide) [PAM] or polyvinyl alcohol [PVA], the dominating particle interaction mechanisms are either through hydrogen bonding for polar molecules, for example PAMs ability to form hydrogen bonds with silanol groups on silica¹⁷. Or by hydrophobic interactions, where non-polar segments will seek to reduce their free energy by adsorbing to a hydrophobic surface to increase entropy by 'freeing' a number locked water dipoles from their fixed orientation around the non-polar macromolecule¹⁰³, such as the adsorption of PVA onto silver iodide at high salt concentrations¹⁰⁵.

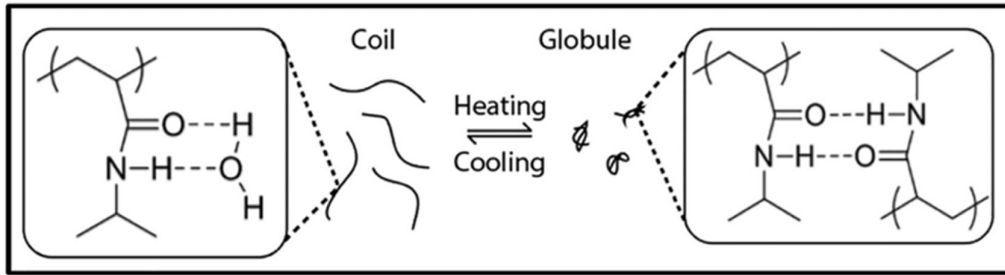


Figure 2.6: The reversible hydrophilic-to-hydrophobic transition of PNIPAM upon heating above 32 °C in water⁸⁴.

Recently, there have been developments of more complex polymers which are stimuli responsive. These consist of monomers which by altering pH or temperature, can switch from being hydrophilic to hydrophobic. An example of such polymers is poly(*n*-isopropyl acrylamide) [PNIPAM]. The hydrophilic-hydrophobic transition of PNIPAM originates from a balance of the enthalpy of mixing/solvency compared to the entropic cost of polymer-solvent interactions^{84,106}. Thus, at PNIPAM's lower critical solution temperature (LCST) the transition from a hydrophilic coil to a hydrophobic globule is driven by the breakage of hydrogen bonds between the polymer and surrounding water, and the formation of new bonds between the amide and carboxyl segments of the polymer, exposing the hydrophobic hydrocarbon backbone as shown in Fig. 2.6^{88,107}. This functionality is advantageous in sedimentation operations where above the LCST, hydrophobically driven flocculation can occur, improving sedimentation dynamics, and once the sediment is settled, the suspension can be cooled, terminating particle-polymer interactions (desorption) which reduce the bed yield stress allowing for further consolidation and improved dewatering⁸⁴. This same functionality has been achieved via pH switches using chitosan to flocculate 10 wt.% zircon suspensions resulting in a 10-45% bed volume reduction⁸⁹. However, as highlighted by Hastings et al.⁵, the nuclear industry would rather minimise any impact to processing streams and temperature or pH changes, so process condition changes in addition to an additive would likely face great regulatory scrutiny.

2.2.2) Polymer adsorption and the role of molecular weight and charge density

Polymer adsorption is a function of many variables, including but not limited to particle surface charge, hydrogen bonding, solution ionic strength and polymer concentration in solution. Here the structure of the polymer's impact of adsorption in particular shall be discussed. Generally polymers used in flocculation range from 10^4 to 10^7 g.mol⁻¹¹⁰³, whilst the length of the polymer will play a role in its flocculation mechanism and the resultant

floc structure (discussed below), there are thermodynamic implications for molecular weight increase. Mainly, the increased amount of polymer adsorbed with increasing molecular weight. This affect was observed by O'Shea et al.⁸⁵ when investigating a thermo-responsive PNIPAM flocculant to sediment alumina with varying molecular weights ($4.52-0.23 \times 10^6 \text{ g.mol}^{-1}$) as shown in Fig. 2.7A, where adsorption density of PNIPAM onto alumina increases as the molecular weight of the polymer increases. The enthalpic term which drives adsorption, consists of contributions from the polymer-surface bond energy and the solvent/polymer interaction term. It is the polymer-surface bond energy which is primarily responsible for the increased adsorption of polymer in good solvent with increasing molecular weight which increases as the number of polymer segments increase^{30,85,104}.

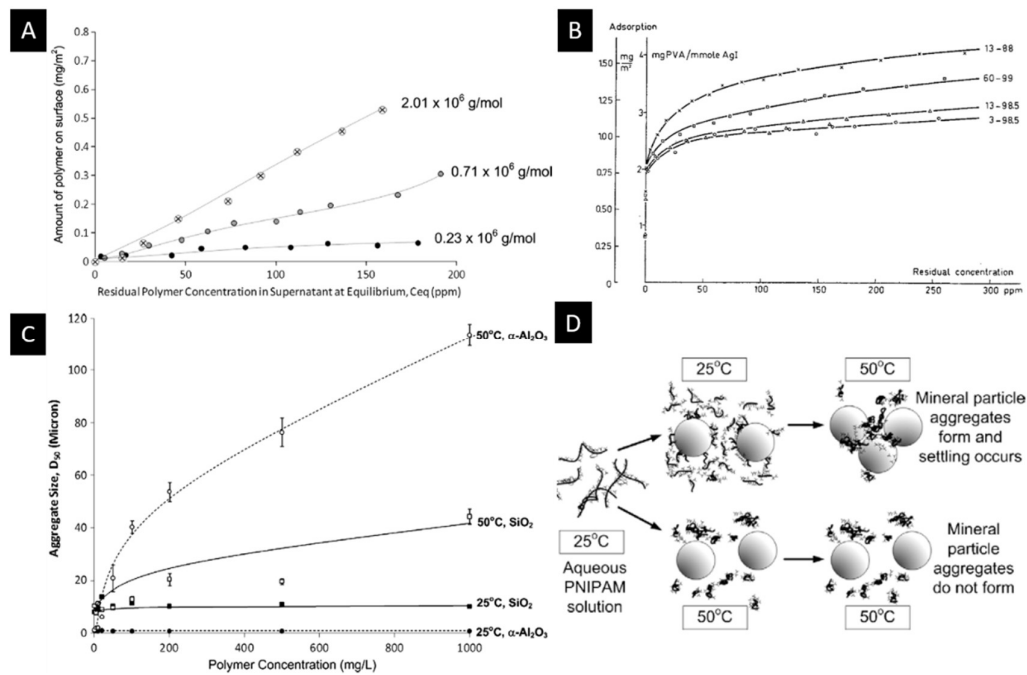


Figure 2.7: A) Amount of PNIPAM (mg.m^{-2}) on the alumina surface at 25 °C (48 h) with polymer molecular weight (g.mol^{-1}) [86]. B) The adsorption of polyvinyl alcohol on silver iodide sol. Conc. = 50 mmols.l^{-1} . Where 3-98.5, 13-98.5, 60-99 and 13-88, have molecular weights of 15,000, 56,000, 101,000 and 63,000 g.mol^{-1} respectively[106]. C) d_{50} volume weighted aggregate particle sizes (μm) with polymer dosage of alumina at 25 °C; alumina at 50 °C; silica at 25 °C; and silica at 50 °C. High-molecular weight polymer was used: $3.0 \times 10^6 \text{ g.mol}^{-1}$. The primary particle size of the alumina ($\sim 1 \mu\text{m}$) used was much smaller than silica ($\sim 10 \mu\text{m}$) [86]. D) PNIPAM adsorbs as individual molecules at 25 °C. Upon heating to 50 °C, phase separation and additional polymer deposition causes aggregation. PNIPAM molecules added at 50 °C self-associate before they can deposit onto the surface, resulting in little aggregation [86].

This relationship between molecular weight and increased polymer adsorption onto particle surfaces is also true for hydrophobic adsorption. However, the arguments are reversed, where hydrophobic polymers are enthalpically unfavourable in open free rotating structures

in water, so adsorption onto a hydrophobic surface reduces the number of entropically locked water dipoles forming a cage around the hydrophobic particles and polymer. As the hydrophobic chain length increases, the number of water dipoles required to orientate themselves to reduce free energy increases. Driving adsorption of the hydrophobic polymer onto hydrophobic surfaces to reduce free energy, as observed in Fig. 2.7B showing as the molecular weight of PVA increases so does the PVA adsorption onto silver iodine particles¹⁰⁵. However, O'Shea et al.⁸⁵ investigated the adsorption of PNIPAM above its LCST (hydrophobic conditions) without previous adsorbing PNIPAM to the alumina surface (hydrophilic). In this study it was more thermodynamically favourable for the PNIPAM to self-assemble into globules as shown by the dynamic light scattering study as a function of temperature in Fig. 2.7C and illustrated in Fig. 2.7D. Once heated above the PNIPAM LCST, Fig. 2.7C shows that the aggregate size of the polymer increases indicating PNIPAM self-association into a globular structure from individual PNIPAM chains and O'Shea et al.⁸⁵ reported little adsorption to alumina under the same conditions. Indicating that unless first adsorbed to the alumina surface in PNIPAMs hydrophilic state initially, the segment-segment hydrophobic interaction above the PNIPAM LCST is more favourable than adsorption and uncoiling onto the alumina surface, likely due to the requirement of water to diffuse into the hydrophobic globule core to facilitate uncoiling which would increase the free energy of the system. Whereas once initially adsorbed to the surface of the alumina through electrostatic means, the PNIPAM exists in an semi-uncoiled state during the hydrophilic-hydrophobic transition during heating above the LCST thus remaining attached to the alumina surface¹⁰³.

For ionic monomer species in polymer chains interacting with a charged particle surface, polymer segment conformation to a flatter more consolidated state occurs more quickly than in hydrophobic interactions due to the electrostatic attraction of the functional groups to the charged particle surface. This means that an ionic homopolymer will conform as flat as possible to a particle surface, to maximise the free energy reduction from each of the charged polymer segments interacting with the particle surface³³. However, for statistical copolymers of ionic and non-ionic species, this conformation is more complex. As polymers are randomly coiled thus entangled and rotate around their carbon-carbon bonds through Brownian motion in solvent³⁰, where the polymers state (radius of gyration) in solution is a function of segment-segment forces at play (van der Waals/hydrophobic attraction vs electrostatic repulsion). Thus, the electrostatic attachment of an ionic

monomer group anchoring to the particle surface will be followed by an uncoiling and re-conformation to the particle surface, which is a sluggish process illustrated in Fig. 2.8A^{33,103}. This results in the ionic segments in the statistical copolymer anchoring to the particle surface resulting in (if the polymer is of great enough molecular weight $\sim >10^5$ g.mol⁻¹) loops, trains and tails being formed on the particle surface until re-conformation can be achieved facilitating flatter equilibrium coverage¹⁰³ (see Fig. 2.8B). This process is complex and subject to many variables including the segment Kuhn length (stiffness of a polymer chain affecting conformation), degree of dissociation of ionic segments, the pH and type/concentration of electrolyte ions in the bulk solution¹⁰³.

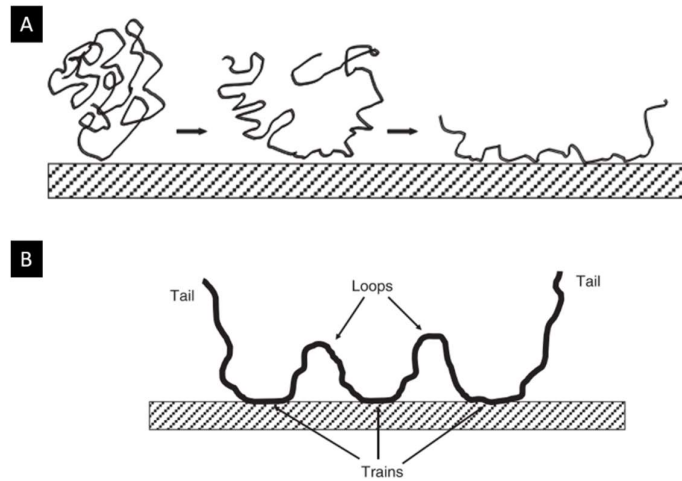


Figure 2.8: A) Re-conformation of an adsorbed polymer chain from first contact with a surface until adsorption equilibrium is achieved. B) Equilibrium conformation of an adsorbed polymer chain³³.

2.2.3) Flocculation mechanisms and non-equilibrium effects

As previously characterised by Johnson et al.¹⁶ and Biggs et al.²⁴ in Section 2.1, Mg(OH)₂ carries a low but cationic surface charge. Therefore this work will discuss flocculation mechanism of hydrophilic surface compatible flocculant systems. For charged particles in suspension, the behaviour of the particles is governed by Derjaguin, Landau, Verwey and Overbeek (D.L.V.O) theory. Where the spontaneity of particulate dispersion to aggregate is described as a balance of van der Waals attractive forces and electrostatic repulsive forces^{102,103,108}. The zeta potential of the Mg(OH)₂ surface attracts co-ions and repels counter-ions in solution forming an electrical double layer consisting of a fixed Helmholtz (or Stern) layer of ions strongly bound to the surface, and a diffuse and relative more mobile layer of co-ions and counter-ions. Where the double layer results in electrostatic screening of the particle surface charge to reduce Gibbs free energy¹⁰². The distance from the charged

particle surface, where the electrical double layer provides electrostatic screening, is known as the Debye screening length ($1/k$) and is a function of the ion concentration in bulk solutions, the valency of the ion and the vacuum and relative static permeabilities of the solution (illustrated in Fig. 2.9). The repulsive interaction energy is a balance between the particle surface potential and the ionic strength of solution, where a reduction in surface potential or an increase in ionic strength result in a depletion of the Debye screening length. As the total interaction potential is the sum of repulsive and attractive interaction energies, which are ultimately a function of inter-particulate distance, then as the Debye length is reduced, the particles may approach close enough for van der Waals forces to become dominant resulting in aggregation^{102,108}. As $\text{Mg}(\text{OH})_2$ has reported semi-solubility and low reported zeta-potential (0.5-3.2 mV) it is unsurprising that Johnson et al.¹⁶ has reported Versamag $\text{Mg}(\text{OH})_2$ readily aggregates in suspension.

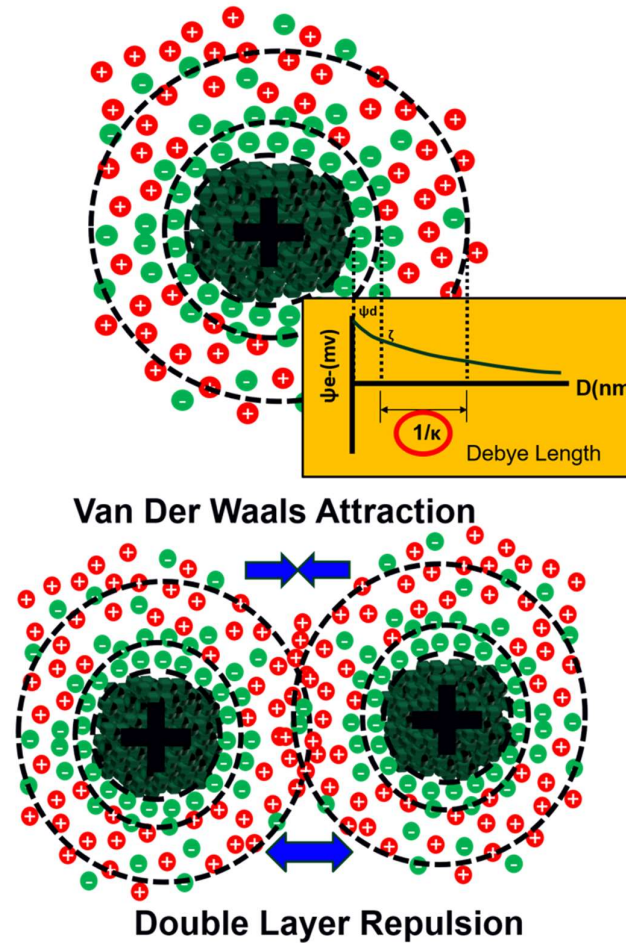


Figure 2.9: Illustration showing the electrical double layer structure and effect of electrostatic screening of electrostatic potential as a function of inter-particulate distance. Where D is the interparticle distance (nm), ψ_e is the electrostatic potential (mV), ψ_d is the electrostatic potential at the particle surface, ζ is the zeta potential (mV) and $1/k$ is the Debye screening length.

The flocculation mechanism of a particle-polymer system is strongly dependent on the polymer charge density and polymer molecular weight, where the adsorption mechanisms described in Section 2.2.2 play an important part in the resultant floc structure. For anionic homopolymers, or high charge density copolymers ($\sim 80\%$ ionic monomer), polymer adsorption will be flatter and tighter to the $\text{Mg}(\text{OH})_2$ particle surface. As a result, there will be patches of concentrated anionic point charges on the surface of the weakly cationic $\text{Mg}(\text{OH})_2$ surface. This results in not only localised charge neutralisation but patches of charge reversal on the $\text{Mg}(\text{OH})_2$ particle surface. This effect was reported by Barany et al.¹⁰⁹ who measured the change of zeta potential of bentonite particles as an increasing concentration of varying charge density polyelectrolytes when adsorbed onto bentonite particle surfaces shown in Fig. 2.10A^{33,109}. Where the high charge density cationic polymer

resulted in strong charge reversal on the bentonite surface from an anionic to cationic surface potential. This means if this partially anionic homopolymer covered $\text{Mg}(\text{OH})_2$ collides with another $\text{Mg}(\text{OH})_2$, the localised patches of positive and negative charges will attract resulting in 'charge-patch' or 'patch-wise' flocculation as illustrated by Hubbe¹¹⁰ in Fig. 2.10B showing the patch wise flocculation of cellulosic particles.

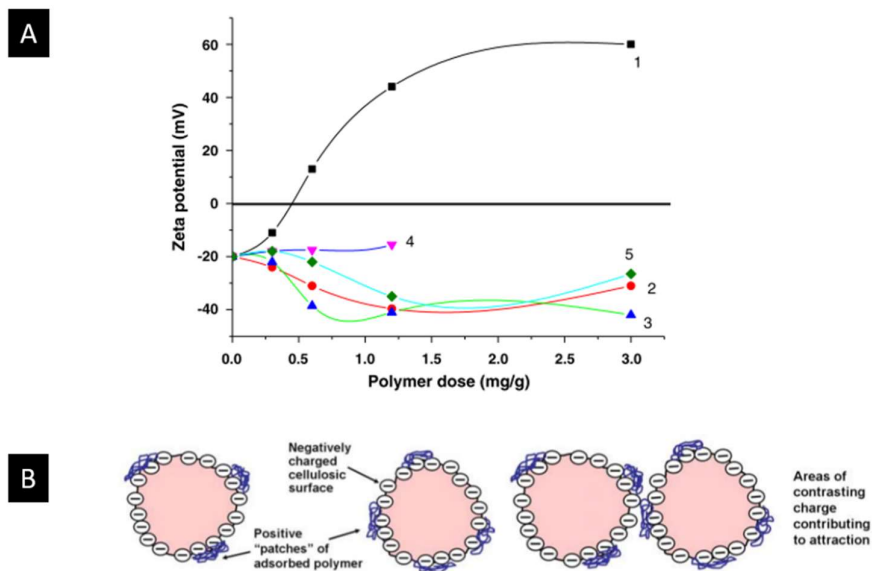


Figure 2.10: A) Showing the variation of the zeta-potential of bentonite particles with concentration of polyelectrolytes. 1) strongly charged cationic; 2) medium charged anionic; 3) after adding 0.65 mg.g^{-1} of cationic polymer to particles pre-treated with anionic polymer; 4) after adding 0.65 mg.g^{-1} of anionic polymer to particles pre-treated with cationic polymer; 5) the case of simultaneous addition of cationic and anionic polymers^{33,109}. B) Flocculation And Redispersion Of Cellulosic Fibre Suspensions: A Review Of Effects Of Hydrodynamic Shear And Polyelectrolytes¹¹⁰.

Unlike the charge patch flocculation mechanism facilitated by high charge density polymers, lower charge density copolymers which have slower conformation to the $\text{Mg}(\text{OH})_2$ particle surface displaying loops, trains and tails as shown in Fig. 2.8B are more effected by the molecular weight of the polymer. As anionic functional groups will not be as densely adsorbed in a localised patch on the $\text{Mg}(\text{OH})_2$ surface to facilitate charge reversal, the copolymer must have loops and tails which can extend beyond the $\text{Mg}(\text{OH})_2$ Debye length. If the copolymer chain length does not extend beyond the Debye length, the copolymer chains will not be able to bridge across and adsorb to the surface of an approaching particle as the particle will be repelled upon approach by double layer osmotic pressure forces as illustrated in Fig. 2.11A. If the copolymer loops and tails extend beyond the $\text{Mg}(\text{OH})_2$ Debye length, then 'bridging flocculation' can produce larger, more open structured flocs in comparison to charge patch flocculation. Such as those observed by Ng et al.¹⁰⁷ using *in situ* FBRM and PVM to monitor the change in chord length of a flocculated

chalcopyrite-quartz mixture when using copolymers of PNIPAM and xanthate with varying molecular weights (see Fig. 2.11B). The chord length distributions of the xanthate-PNIPAM copolymers of chain lengths $1.5 \times 10^6 \text{ g.mol}^{-1}$ and $0.15 \times 10^6 \text{ g.mol}^{-1}$ show that the larger copolymer flocculated the chalcopyrite-quartz mixture to a greater degree than the smaller copolymer. Where greater chain length polymers have greater extension beyond the Debye length, resulting in the ability to form more anchor points with an adjacent particle to develop larger, stronger flocs^{33,107}.

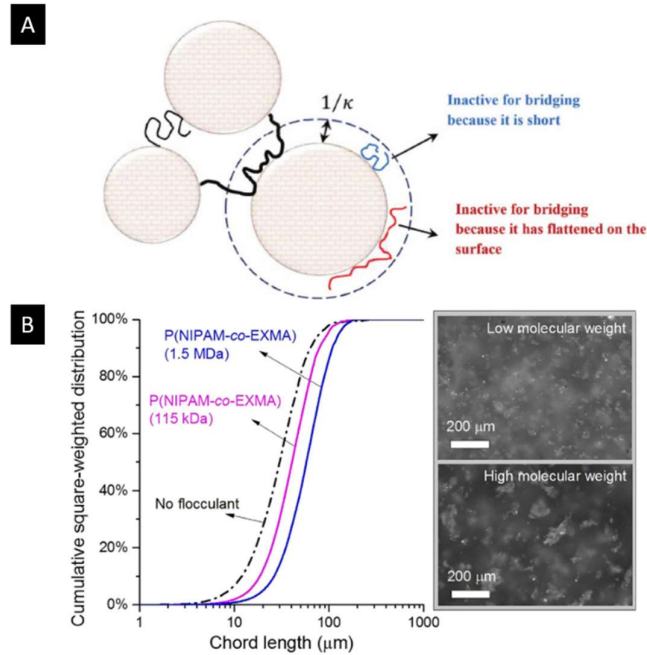


Figure 2.11: A) The concept of bridging flocculation of submicron particles by high molecular weights polymers. The double layer thickness is estimated as reciprocal Debye length, $1/\kappa$. Small polymer chains do not give access to bridging. The polymer chains that have flattened on the surface, before a contact is made with another particle, also lose their bridging capacity (as the case with some polyelectrolytes)^{33,111}. B) FBRM cumulative square-weighted chord length distributions comparing the aggregate sizes at 50 °C for the chalcopyrite-quartz mixture between short- and long- chain P(NIPAM-co-EXMA) at 300 g.t⁻¹, following polymer addition at 25 °C. The effective shear rate was 200 s⁻¹ at 25 °C, increasing to 250 s⁻¹ at 50 °C, due to the change in viscosity of water with temperature. The images on the right show that at 50 °C the aggregates formed in the presence of the short-chain P(NIPAM-co-EXMA) are much smaller than those found with the higher molecular weight P(NIPAM-co-EXMA)¹⁰⁷.

Due to the slow kinetics of polymer adsorption, non-equilibrium effects can drastically effect the structure of a resultant floc. The polymer relaxation process is slow and further relaxation occurs once a polymer becomes anchored to a particle surface, though often on time scales longer than the flocculation process. Additionally, for more complex systems such as the adsorption of cationic and anionic polyacrylamides onto kaolinite by Nasser and James¹⁷, multiple polymer-particle interactions may occur. Kaolinite which was anionic at pH 7, showed a great affinity for the cationic charged polymers, with the greater

charge density and greatest molecular weight polymer showing the greatest adsorption as a function of polymer concentration as shown in Fig. 2.12A. The cationic polymers adsorbed using a combination of both electrostatic interactions between the cationic polymer functional groups and anionic surface charge on the kaolinite particles, and hydrogen bonding between the polyacrylamide amide functional groups and the silinol and aluminol O-H surface groups. Whilst displaying a lower adsorption density due to the like-like repulsion from the anionic kaolinite surface (proportional with increasing anionic charge density) and once the polymer is hydrogen bonded to the kaolinite surface, the same like-like repulsion of the anionic PAM segments cause the polymer loops and tails to extend beyond the Debye to a greater extent than the counter-charge pairing resulting in greater floc sizes and faster sedimentation rates as shown in Table 2.2¹⁷. Indicating the potential for hydrogen bonding as a potential polymer adsorption mechanism for polyacrylamide backbone copolymers as brucite $Mg(OH)_2$ species also display compatible hydroxyl (O-H) surface groups¹¹².

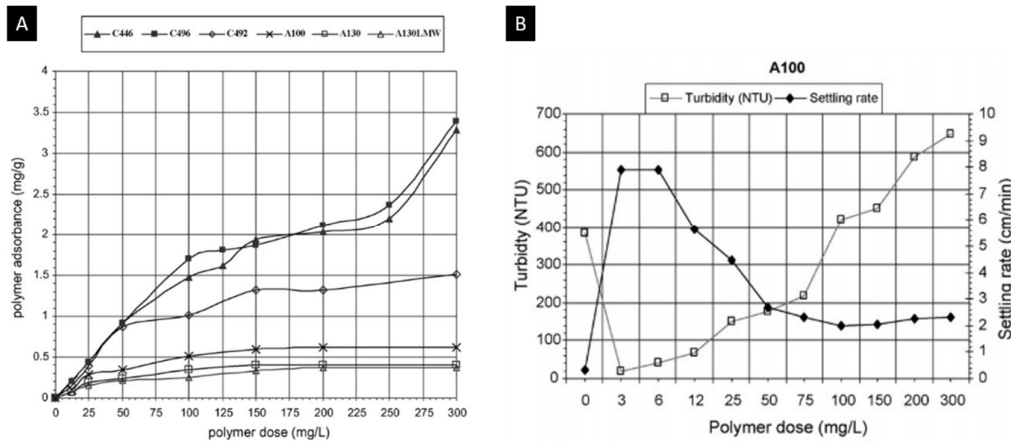


Figure 2.12: Adsorption isotherms for 50 g.l⁻¹ (2% volume fraction) of kaolinite in 10⁻³ M NaCl solution as a function of polymer dose at pH 7¹⁷. For polymer properties see Table 2.2.

Excessive adsorption of polyelectrolytes (charged polymers) onto particle surfaces is detrimental to flocculation¹⁰³. Greater polyelectrolyte surface coverages result in steric and electrostatic stabilisation of dispersions, as loops and tails, which are sufficiently extended beyond the Debye charge screening thickness, cannot electrostatically adsorb on to the surface of adjacent, high polymer surface coverage particles. This was observed in the study by Nasser and James¹⁷, where they found an optimum settling rate polymer dosage, and beyond this point, the settling rates and resulted turbidity reduction reached a point of inflection and became less effective as shown in Fig. 2.12B. It also be noted that the

polymers, cationic or anionic, performed better with lower charge densities for equivalent dosages, as these has lower surface adsorptions (see Fig. 2.12A) resulting in greater floc sizes and better sedimentation rates as loops and chains extended further into the aqueous medium and could interact with adjacent particles with lower polymer surface coverages more effectively. This is an important consideration for Sellafield, as overdosing with polyelectrolytes may actually stabilise brucite suspensions with incorporated radionuclides reducing the effectiveness of sedimentation as a dewatering strategy.

Table 2.2: Floc structure parameters obtained from dilute settling rate data at pH 7¹⁷.

Polymer	Molecular weight (g.mol ⁻¹)	Charge density (%)	Floc Size (µm)	Max settling rate (cm.min ⁻¹)
C 446	3-4 × 10 ⁶	+35	127	4.1
C 496	5-7 × 10 ⁶	+35	153	4.8
C 492	5-7 × 10 ⁶	+10	163	5.7
A130MW	3-4 × 10 ⁶	-35	141	4.6
A130	10-12 × 10 ⁶	-35	167	5.8
A100	10-12 × 10 ⁶	-10	184	7.9

Another important example is the utilisation of amphiphilic block copolymers, which have been found to utilise a combination of polymer-particle interaction mechanisms to facilitate flocculation. Amphiphilic block copolymers are important surface active macromolecules which are compatible with flotation operations and are discussed in further detail in Section 2.5. An investigation by O'Shea et al.¹¹³ into the flocculation of cationic alumina mineral particles using temperature responsive block-copolymers of PNIPAM and PAA-co-PtBA (poly(t-butyl acrylate)), found that the anionic PAA chain showed an affinity for alumina below the PNIPAMs LCST, resulting in minor flocculation. Upon heating to the PNIPAM LCST, hydrophobic forces dominated. Resulting in greater adsorption densities (see Fig. 2.13A) on the alumina and facilitating flocculation in combination with electrostatic interactions and charge neutralisation effects illustrated in Fig. 2.13B. Unlike the temperature sensitive statistical copolymers investigated by O'Shea et al.⁸⁵, the block-copolymers do not require to be adsorbed to the surface of the alumina then sequentially be heated to above its LCST to prevent flocculation hindering self-assembly. Block copolymers form micelles rather than globules due to the segregated polar and non-polar segments of the block-copolymer, meaning as the anionic segments from the corona of the micelle still spontaneously adsorb onto the surface of the cationic alumina. Even to a greater

degree than an ionically comparable statistical copolymer above the LCST (see Fig. 2.13C)¹¹³.

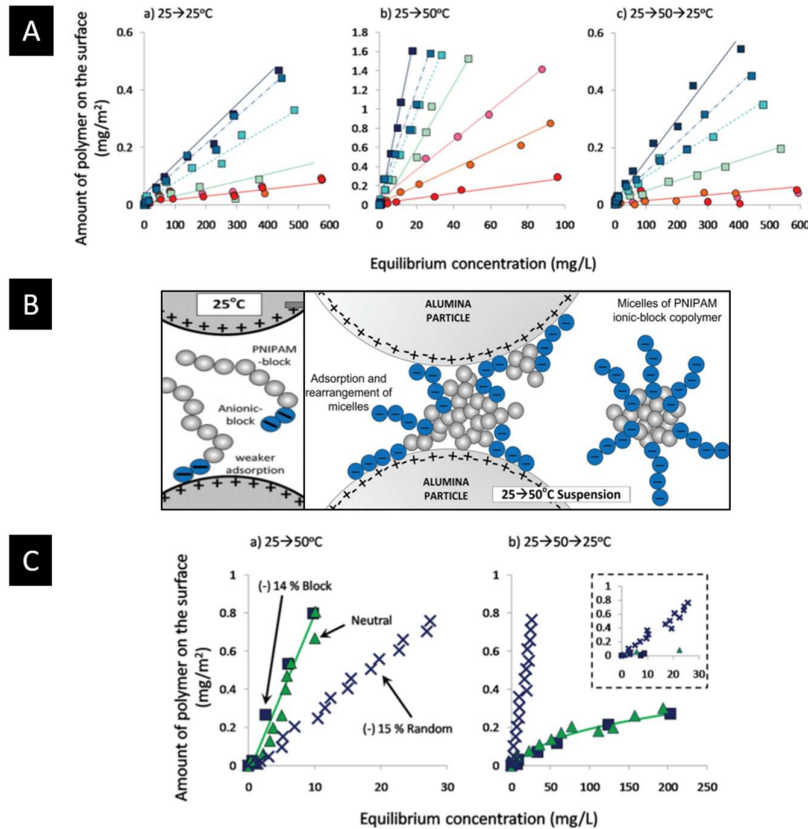


Figure 2.13: A) [a] Adsorption (mg.m⁻²) of block-PNIPAM onto alumina after equilibrating at 25 °C for 48 h. [b] Deposition (mg.m⁻²) of block-PNIPAM onto alumina after heating to 50 °C and holding for 48 h. [c] Polymer remaining on surface (mg.m⁻²) of block-PNIPAM onto alumina after heating to 50 °C for 24 h and then cooling to 25 °C and holding for 24 h. Block PNIPAM compared: red circle, (+)30%; orange circle, (+)15%; pink circle, (+)4%; green square, (-)1%; teal square, (-)4%; blue square, (-)9%; and dark blue square, (-)14%. Lines are drawn to guide the eye. B) Schematic of suspension stability and adsorption at 25 °C of shorter length anionic blocks of PNIPAM block copolymers onto positively charged alumina particles (pH 5). The PNIPAM block segments shrink to the surface when the suspensions is heated to 50 °C and flocculation results through a combination of charge-patch attraction, charge neutralization, and hydrophobic attraction mechanisms. C) Deposition (mg.m⁻²) of PNIPAM onto alumina after [a] heating from 25 to 50 °C and holding for 48 h and (b) cooling from 50 to 25 °C and holding for 24 h with low concentration detail showed in the inset. Polymers are denoted as: blue box, (-)14% block PNIPAM; blue, (-) 15% random PNIPAM; and green triangle, neutral PNIPAM. Lines are drawn to guide the eye [114].

2.2.4) Floc growth and breakage

The flocculation process proceeds through a number of steps, as the polymeric flocculant is added to a dispersion, the polymer adsorbs to particles and by one of the aforementioned flocculation mechanisms begins to promote aggregation of particles depending on the system. Flocs grow in size, observed as an increase in the average floc diameter with time as more polymer is adsorbed from solution to the particle surface. The dispersion particle

size distribution reaches a point of floc maxima, at this point the initial flocculation of particles through the adsorbed polymer's slow relaxation onto the particle surfaces ceases to be the dominant process and the inertia of vessel mixing begins to break down flocs through shear forces. Flocs will break down until the rate of floc reformation equilibrates with the rate of floc breakage, usually a function of shear in the flotation cell^{55,114,115}.

Non-equilibrium effects also inform the equilibrium floc size, the crucial parameter is the relative rate of particle collision and polymer re-conformation³³. As flocs break down under shear and polymer chains detach from adjacent particles, they re-conform to the surface of the particle reducing the loops and tails degree of extension beyond the Debye length meaning if subsequent collisions are infrequent enough, polymers will form smaller, denser flocs until the flocs develop the mechanical strength to resist further breakage as illustrated in Fig. 2.14A⁵⁵. Flocculation utilising charge neutralisation is however is more resistant to irreversible floc breakage, as polymer conformation rates are less influential on floc structure due to localised charge reversal resulting in aggregation³³. This initial flocculation, floc maxima, floc breakage and equilibria process is shown by Fig. 2.14B by using online *in situ* FBRM to monitor changes in particle size distributions with time of the flocculation of mature fine tailings using poly(vinylbenzyl trimethylammonium chloride) by Vajihinejad and Soares⁵⁵. Where the peak of the floc maxima decreases with increasing shear rate as the inertia forces of mixing break larger more delicate floc structures equilibrating at smaller floc sizes.

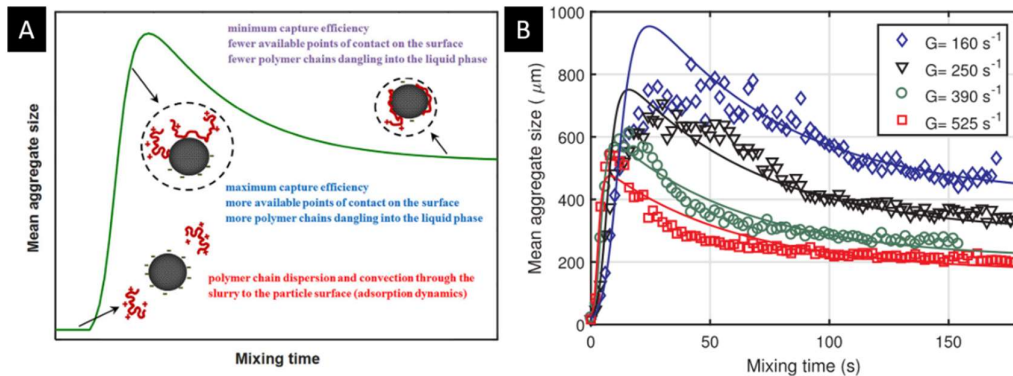


Figure 2.14: A) Typical FBRM response of mature fine tailing flocculation of poly(vinylbenzyl trimethylammonium chloride). B) Effect of shear rates on the evolution of mean aggregate size of mature fine tailings particles (3 %wt) over time flocculated with a partially hydrophobic cationic flocculant [poly(vinylbenzyl trimethylammonium chloride)-Molecular weight=7940 kDa] batch flocculant, flocculant dosage=5000 ppm (mg polymer/kg dry particle), pH=8.6. Model is continuous line and experimental data are symbols. ⁵⁵

In summary, there are multiple ways cationic $\text{Mg}(\text{OH})_2$ can be flocculated to increase particle sizes to improve sedimentation rates and decrease supernatant turbidity thus improving the performance of dewatering strategies at waste treatment facilities such as Sellafields SPP1. The weakly cationic surface charge of the $\text{Mg}(\text{OH})_2$ radwaste analogue materials investigated by Johnson et al. and Biggs et al. suggest that anionic polyelectrolytes could be implemented as either low charge density, high molecular weight bridging flocculants or lower molecular weight, high charge density electrostatic patch flocculants. The former would likely produce larger flocs with better settling dynamics, but as discussed in Section 2.2.4, once the floc is broken up by shear and the polymer chains re-conformed and relaxed, this will prohibit floc regrowth reducing sedimentation performance. This is an important consideration in the presence of high shear conditions or if settled sludge beds require to be disturbed regularly. The addition of more polymer to resettle suspended broken flocs may lead to steric stabilisation due to excessive surface coverage.

Additionally, due to the $\text{Mg}(\text{OH})_2$ -O-H surface groups¹¹², polyelectrolytes utilising a poly(acrylamide) ‘backbone’ may hydrogen bond due to the PAM amide functional groups, meaning that like-like charge polyelectrolytes may effectively promote bridging flocculation (if of sufficiently low enough charge density to reduce segment repulsion). This may result in comparatively larger flocs than when using counter-charge anionic polymers (of equal molecular weight) such as the system previously discussed by Nasser and James¹⁷ when flocculating anionic kaolinite with anionic polymers. Additionally, it may be also be viable to utilise amphiphilic block copolymers with an anionic segment and hydrophobic segment such as the system investigated by O’Shea et al.¹¹³. Where the anionic segment will electrostatically adsorb to $\text{Mg}(\text{OH})_2$ and the hydrophobic block will promote an additional hydrophobic aggregation driving force in addition to charge patch and charge neutralisation mechanisms.

2.3) Quantifying floc structure

2.3.1) Visualising floc structure

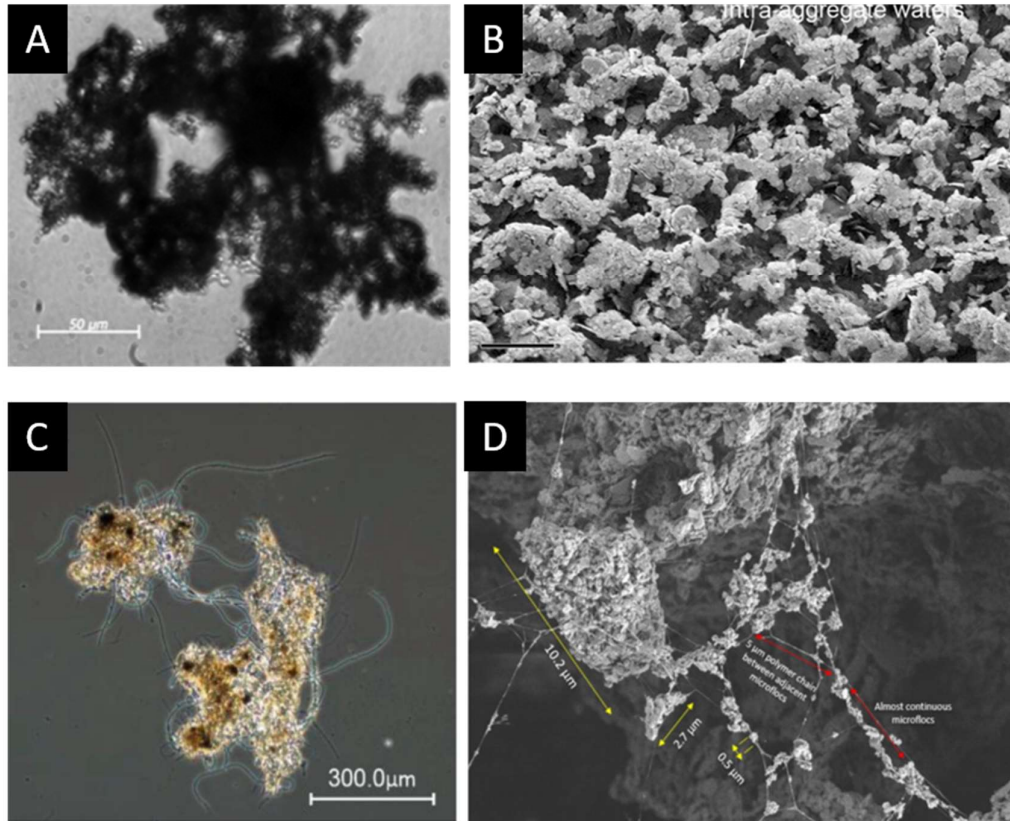


Figure 2.15: A) Projected 2D images of the floc using 3D-doctor software⁵⁰. B) Floc microstructures before shear within Unimin kaolin slurries at pH 8 with 0.04 dry weight% PEI Mw 750,000. Magnifications at 10,000 \times and scales at 5 μm . The black areas depict frozen waters trapped within floc aggregates⁴³. C) Phase contrast image of floccular sludge. The scale bars in images a and c are 400 μm in length³⁵. D) Microstructure of kaolinite floc as revealed by cryo-SEM. The microflocs containing primary kaolinite nanoparticles vary in size from 0.5 μm to 10 μm (highlighted in yellow). The microflocs could be almost continuous or have a significant length of polymer chain in between adjacent microflocs (highlighted in red)⁴¹.

Floc structure has been qualitatively observed using a range of microscopy techniques, ranging from simple optical to cryogenic-scanning electron microscopy (Cryo-SEM). Vahedi et al.⁵⁰ used microscopy to investigate the structure of lime softening flocs, using a 3D doctor software to build a 3d representation of the structures which were found to be highly porous, non-spherical as shown in Fig. 2.15A. Similarly, Avadiar et al.⁴³ investigated the floc structures of Unimin kaolin structures which were flocculated with polyethylenimine (PEI) using Cryo-SEM as shown in Fig. 2.15B. In the investigation by Avadiar et al.⁴³ the kaolin suspension was adjusted to pH 8, where unlike charge attractions,

hydrogen bonding and van der Waals forces of attraction, occurred between the free and available sites on pre-flocculated Unimin kaolin aggregates and PEI molecules. However, due to the low positive charge densities on PEI molecules and as a result, weak electrostatic attractive forces between PEI molecules and kaolin particles, PEI molecules would adsorb weakly onto kaolin particle sites and would not lie flat on these particle sites at pH 8. This resulted in a more open structure due to the great projection of loops and tails of the PEI into suspension resulting in an open and porous macro-aggregate structure composed of double layer depletion driven sub-aggregates⁴³. These observations by Vahedi et al.⁵⁰ and Avadiar et al.⁴³ imply that there will be an increase volume occupation by polymeric flocs due to the observed open structures which has implication for sedimentation with the flocs consisting of a compounded density of primary particles and water, shown in Eqn. 2.1, where ρ_s is particle density, ρ_w is the density of water, ρ_f is the density of the flocs and φ_s is the volume fraction of solid particles in a floc.

$$\rho_f = \varphi_s \rho_s - (1 - \varphi_s) \rho_w \quad (\text{Eqn. 2.1})$$

This open structure is visualised in Figs. 2.15C and 2.15D, where contrast phase microscopy and cryo-SEM images taken by Krysiak-Baltyan et al.³⁵ and Sharma et al.⁴¹ respectively show the individual polymer chains bridging between particles and flocs resulting in an open macro-structure hypothesized by the slow polymer-surface relaxation process discussed in Section 2.2. The intricate complex porous structures indicate that there will be complex hydrodynamic interactions which may occur during sedimentation and compression of suspensions, especially as inter-aggregate spacing approaches intra-aggregate spacing where the flow of fluid through the porous microstructure may relieve drag and aid in compressive dewatering as observed by Johnson et al.¹⁶, Xiao et al.⁴⁵ and Nasser and James.¹⁷. It's important when designing dewatering processes at Sellafield to remove Mg(OH)₂ particulates that the impacts of these complex microstructures on the macro-properties of the settling suspensions are considered. Therefore a quantitative measure of the floc porosities must be applied.

2.3.2) Mandelbrot's Fractal dimension for aggregates

Mandelbrot's fractal mathematics have received considerable attention as an alternative to understanding complex, chaotic and disordered systems which have been previously unquantifiable by conventional geometric approaches⁶³. The simplest mathematical

expression to embody the characterisation of fine particles, mathematically binding them to an invariable scaling dilatational symmetry, is shown in Eqn. 2.2. Where ‘ M ’ is the mass of the particles, ‘ B ’ is a linear measure of size (e.g. particle diameter) and ‘ d_f ’ is the mass fractal dimension^{44,46}.

$$M \propto B^{d_f} \quad (\text{Eqn. 2.2})$$

For aggregates (of diameter ‘ D_f ’) constructed of monodisperse, and even polydisperse spherical primary particles (of diameter ‘ D_p ’), the mass fractal dimensions and number fractal dimension are equivalent due to their embedded invariable scaling property with only a difference in proportionality constant ‘ k_o ’ known as the structure pre-factor. The aggregate scaling on a number basis is expressed in Eqn. 2.3⁴⁴.

$$N = k_o \left(\frac{D_f}{D_p} \right)^{d_f} \quad (\text{Eqn. 2.3})$$

The fractal dimension power law relationship is related to the structure of the open porous flocs shown in the micrographs in Figs. 2.15A-D, where the solid volume fraction, φ_s , is shown to be a function of the number of primary particles, N , in an aggregate or floc and the ratio of the volume of an individual primary particle, V_s , and the volume of the resultant floc, V_f , shown in Eqn. 2.4. Expanding the floc density relationship in Eqn. 2.1 by substituting Eqn. 2.4 for the solids volume fraction, φ_s , gives the floc density as a function of primary particles in a floc which is in turn determined by the floc fractal dimension.

$$\varphi_s = \frac{V_s N}{V_f} \quad (\text{Eqn. 2.4})$$

$$\rho_f = \frac{(NV_s \rho_s) - (V_f - V_s N) \rho_w}{V_f} \quad (\text{Eqn. 2.5})$$

A fractal dimension for an aggregate or floc manifests itself as a number between 1 and 3, where a fractal dimension of 3 represents a structure approaching a solid sphere. As the fractal dimension tends from 3 to 1, the structure becomes increasingly open and planar. Floc and aggregate structures have been previously modelled using techniques such as the 3D kinetic growth models embedding space and associated fractal dimensions such as those

computationally visualised by Friedlander¹¹⁶ in Fig. 2.16. The structures of reaction-limited, diffusion-limited and ballistic flocculation mechanisms for both cluster-cluster and particle-cluster aggregation mechanisms as a function of fractal dimension clearly demonstrate the tending towards more open porous flocs with decreasing fractal dimension. As shown in Fig. 2.16, particle-cluster aggregation results in more densely packed floc structures (with fractal dimensions ranging from 2.5-3). However, practically it is generally agreed that cluster-cluster flocculation mechanisms are more likely through probable collisions in agitated suspensions. This interaction is particularly likely for a polymerically flocculated $Mg(OH)_2$ suspension such as the system of interest for Sellafield Ltd. Johnson et al.¹⁶ reported that the $Mg(OH)_2$ freely aggregated in water (due to $Mg(OH)_2$ low cationic zeta potential), the freely aggregating suspension will likely form sub-aggregates which will be polymerically bridged to adjacent clusters such as the PEI-kaolin system shown in Fig. 2.15B by Avadiar et al.⁴³. Thus for bridging flocculation of $Mg(OH)_2$ using long chain lower charge density copolymers, fractal dimensions in the region of ~ 2.09 are expected.


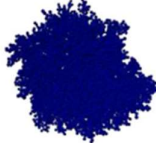
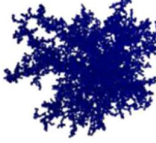

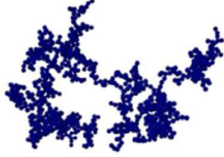

	Reaction-limited	Ballistic	Diffusion-limited
Particle-cluster	 $D_f=3.00$	 $D_f=3.00$	 $D_f=2.50$
Cluster-cluster	 $D_f=2.09$	 $D_f=1.95$	 $D_f=1.80$

Figure 2.16: Kinetic growth models in a 3D embedding space and fractal dimensions associated (based on Friedlander¹¹⁶)¹¹⁷.

2.3.3) Determining fractal dimension

There are a range of techniques which have been investigated to quantify the fractal dimension of aggregates and flocs. The development of image analysis techniques has progressed from area/perimeter analysis of 2D floc shapes to being able to quantify multiple fractal dimensions such as the non-homogenous fractal analysis of lime softening floc formation carried out by Vahedi and Gorczyca¹¹⁸. Whilst the methodology allows for greater insight into the nuances of floc formation, non-homogenous distribution of fractal structures in a floc and how fractal dimension varies with floc size, the techniques are still

very computationally intensive, which is inappropriate for industrial deployment. The use of 2D perimeter/area fractal dimension quantification requires the estimate projection of a 3D fractal dimension required for mass and number systems, which are more appropriate for structure quantification such as the relationship used by Vahedi and Gorzyca which was suggested by Maggi and Winterwerp¹¹⁹. However, this further calculation step introduces additional error. Additionally, it is highlighted by the authors that more research is required to investigate how to best utilise the information obtained from the multifractal spectra, to incorporate the variable floc density and nonhomogeneous mass distribution of flocs into the floc settling models¹¹⁸. Though, development of this technique should be monitored closely to capture the non-homogenous distribution of clusters in reaction limiter cluster-cluster aggregation for polydisperse particle size distributions.

It is more appropriate for this work to focus on the application of direct mass/number fractal dimension analysis techniques to quantify floc structures for direct incorporation into floc settling models (discussed in next section). Popular techniques for determining the mass fractal dimensions for floc structures is settling and static light scattering (SLS) techniques. Glover et al.⁴⁸ directly compared the two techniques when investigation the sedimentation of alumina particles flocculated with a low charge density anionic polyacrylamide settling aid. For determination of fractal dimension from flocs settling under gravity, the proportionality in Eqn. 2.6 was utilised. Where ‘ U_T ’ is the terminal velocity of an individual floc, ‘ g ’ is acceleration due to gravity and ‘ μ_w ’ is the dynamic viscosity of water. As this proportionality relates settling velocity to fractal dimension, the settling velocity is used to calculate the dry mass equivalent of solids shown in Eqn. 2.7, where ‘ $M(D_f)$ ’ is the mass of a floc which is a function of the floc diameter.

$$U_T \propto \frac{gD_f^2(\rho_s - \rho_w)}{18\mu_w} \left(\frac{D_f}{D_p}\right)^{d_f-1} \quad (\text{Eqn. 2.6})$$

$$M(D_f) = \frac{\pi D_f^3 \rho_p (\rho_f - \rho_w)}{6(\rho_p - \rho_w)} \quad (\text{Eqn. 2.7})$$

$$\text{Log}(M(D_f)) \propto d_f \log(D_f) \quad (\text{Eqn. 2.8})$$

Using the proportionality in Eqn. 2.6, the terminal settling velocity of individual flocs can be experimentally recorded as they were by Glover et al.⁴⁸ as a function of floc size, which in turn is converted to a floc mass using Eqn. 2.7. Taking logarithms of both sides of Eqn. 2.6 will allow one to fit a trendline, where the gradient would determine the fractal dimension of the flocs as shown in Eqn. 2.8. The fractal dimension of alumina flocculated with anionic polyacrylamide was determined using this method. Where Fig. 2.17A shows the logarithmic relationship between settling velocity and floc size, and Fig. 2.17B shows the same relationship, where settling velocity is related to aggregate mass producing a trendline gradient and thus fractal dimension of 1.8. This settling analytic technique for determination of fractal dimension has the advantage of being able to directly visualise aggregates, and can measure larger aggregates often outside the scope other analytical techniques. It is also suitable for aggregates formed of polydisperse particulates. However, measurements are time consuming and not suitable for small aggregates which are susceptible to vibrations. Porous flocs may allow flow through the particulate which is not captured by the settling relationship resulting in inaccurate determination of the fractal dimension. Aggregates which restructure may change their configuration to reduce drag as they settle and due to the variation in diameter with settling rate being integral to the calculation methodology, this technique is not suitable to monodisperse or pseudo-monodisperse systems. Additionally, for ‘hot’ samples from SPP1, a relatively large sample size would need to be taken to ensure statistical significance. The amount of material and increased time to record measurements would result in increased worker dose as well as an increase in analysis time for residence time determination, making the technique unsuitable as it does not conform with keeping worker radiation dosages ALARP.

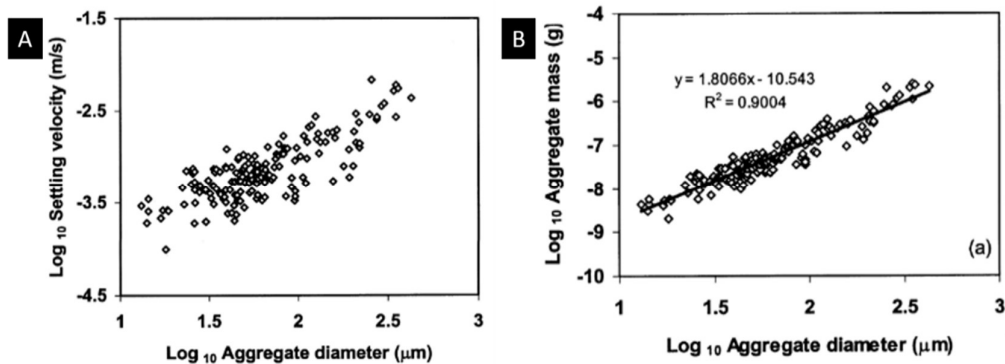


Figure 2.17: A) Experimental settling velocity versus equivalent sphere diameter for the bridging flocculated aggregates. B) Aggregate dry solid mass versus equivalent sphere diameter for the bridging flocculated aggregates⁴⁸.

A common technique which requires low volume samples to quantify floc fractal dimensions is static light scattering (SLS). In SLS analysis, the scattering intensity is a function of the magnitude of the scattering wave vector, Q , a reciprocal of the particle size, where n is the refractive index, λ is the wavelength of the incident light in vacuo and θ_s is the scatter angle shown in Eqn. 2.9.

$$Q = \frac{4\pi n}{\lambda} \sin\left(\frac{\theta_s}{2}\right) \quad (\text{Eqn. 2.9})$$

For determination of the fractal dimension, a particle that satisfies the Rayleigh-Gans-Debye criteria⁴⁸, the scattering intensity $I(Q)$ is given by Eqn. 2.10:

$$I(Q) = kP(Q)S(Q) \quad (\text{Eqn. 2.10})$$

Where k is the scattering constant, $P(Q)$ is the single particle form factor and is related to the shape of the primary particle, and $S(Q)$ is the interparticle structure factor which describes the interference proposed by the primary particles within the aggregate. For a detailed analysis of light scattering theory within aggregates, see Sorensen⁶³. Therefore, the fractal dimension of the flocs can be determined by plotting $\log I(Q)$ with respect to $\log Q$ ⁶³ as per the following proportionality in Eqn. 2.11 and illustrated in Fig. 2.18A⁵³.

$$I(Q) \propto S(Q) \propto Q^{-d_f} \quad (\text{Eqn. 2.11})$$

Fractal data were obtained over a $\log(Q)$ range of $\text{Log}[D_f^{-1}]$ to $\text{Log}[D_p^{-1}] \mu\text{m}^{-1}$ illustrated in Fig. 2.18A, where in this case, D_f is the minimum repeating floc size and D_p is the size of the primary particles. The fractal dimension was determined by linear fitting optimised for the greatest coefficient of determination (R^2) to determine the boundaries of the linear region corresponding to D_f and D_p values, where the gradient is the fractal dimension (d_f). As fractal structures are assumed self-similar, this scaling approach from the average smallest repeating floc structure is assumed to be consistent across the floc population⁶³. In Fig. 2.18A, N represents the scattering number/ number of primary particles in a floc, which is described in Eqn. 2.3. The scattering on the surface of the floc is described with N_s and the proportionality constant k_o , which is commonly referred to as being the structure prefactor and is of the order unity. Values of the prefactor, k_o , have been proposed to depend

on the type of aggregation method¹²⁰, such as the relationship between k_o and d_f for $1.5 \leq d_f \leq 2.75$, as shown in Eqn. 2.12¹²¹:

$$k_o = 0.414d_f - 0.211 \quad (\text{Eqn. 2.12})$$

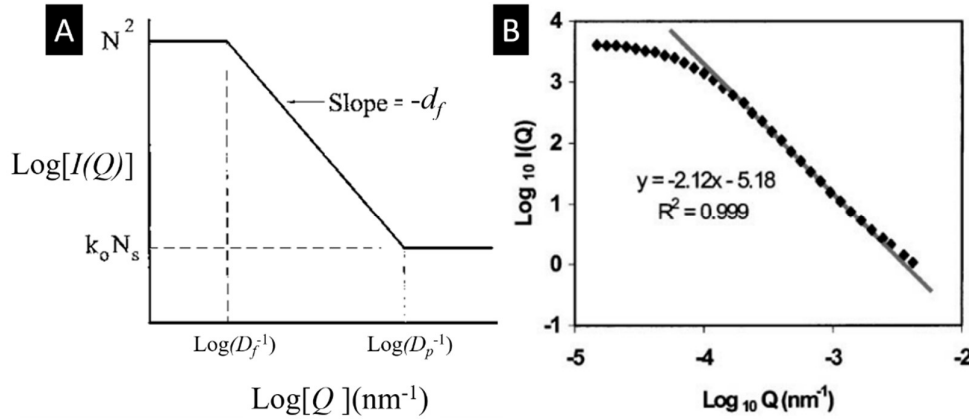


Figure 2.18: A) Log-log plot of the scattered intensity $I(Q)$ versus Q , i.e. Eqn. 2.11, for a system of N point scatterers separated by $2D_p$ thus in a region of size D_f with fractal dimensions d_f , respectively. There are N_s scatterers on the surface of the region. The constant k_o is defined in Eqn. 2.3. Note, the figure has been modified from the original to include the nomenclature utilised in this thesis⁶³. B) Experimental data obtained by Glover et al. showing $\text{Log}_{10}[I(Q)]$ vs $\text{Log}_{10}[Q]$ for determination of the fractal dimension, 2.12, for alumina flocculated with anionic polyacrylamide⁴⁸.

SLS was used to compliment the settling technique used by Glover et al.⁴⁸ to determine the fractal dimension of alumina flocculated with anionic polyacrylamide. Interestingly, the SLS methodology computed a greater fractal dimension associated with reaction limited cluster-cluster aggregation, whereas the settling method computed a fractal dimension of 1.8 which as shown in Fig. 2.17B, demonstrates more diffusion limit cluster-cluster behaviour¹²². There are assumptions in the SLS analysis methodology which vary from the settling method, such as the primary particles are assumed to be monodispersed. However, as discussed previously, these open structure flocs have been shown to have intra-aggregate spacing large enough for fluid to flow through their structures⁴⁵, and due to their delicate nature, likely reconfigure to reduce drag which may induce some error in the sedimentation methodology⁴⁸.

SLS has been shown to be a particularly powerful tool at identifying the differences in flocs structures as a function of copolymer molecular weight and charge density. Zhou and Franks¹⁹ investigated using SLS to characterise three cationic polymers with molecular

weights and charge densities of $3.0 \times 10^5 \text{ g.mol}^{-1}$ and 10%, $1.1 \times 10^5 \text{ g.mol}^{-1}$ and 40%, and $1.2 \times 10^5 \text{ g.mol}^{-1}$ and 100%. The three cationic polymers were chosen as flocculants to aggregate silica particles (90 nm), under various conditions, including change in polymer dosage, particle concentration, background electrolyte concentration, and shear rate. SLS demonstrated that as polymer chain length and charge density increased and decreased respectively. Lower fractal dimensions of ~ 2.3 were observed as shown in Figs. 2.19A and 2.19D, showing the SLS fractal dimension data and the particle size distribution of the flocculated dispersions with varying NaCl salt concentrations respectively, indicating more open structured and larger flocs associated with reaction limited cluster-cluster aggregation typical of bridging flocculation. For the shorter, 100% charge density homopolymer, greater fractal dimensions of ~ 2.6 were observed, typical of more particle-cluster driven flocculation mechanisms associated with charge patch flocculation. Which as discussed in Section 2.2, is facilitated with a patch wise particle by particle addition of particles to a floc structure, resulting in denser, smaller, more closed structure flocs as observed in Figs. 2.19C and 2.19F, showing the SLS fractal dimension data and the particle size distribution of the flocculated dispersions with varying NaCl salt concentrations respectively. Where Figs. 2.19B and 2.19E show intermediate floc structures respectively in terms of fractal porosity and size respectively as function of intermediate molecular weight and cationic charge density.

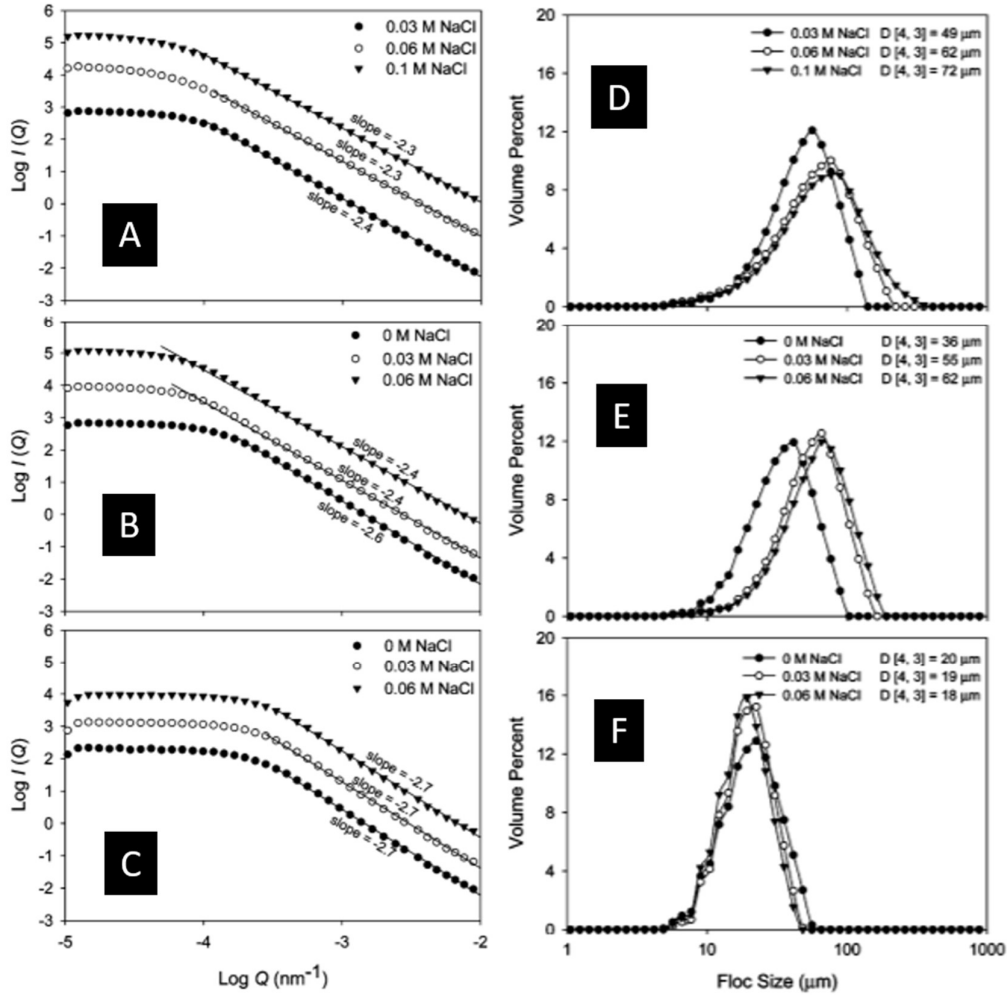


Figure 2.19: The left column of figures shows the effect of background electrolyte concentration on typical scattering patterns of silica flocculated with A) 10% charged polymers under the optimum polymer dosage of 12 mg/g and at [NaCl]) 0.03 M, B) 40% charged polymers under the optimum polymer dosage of 12 mg/g silica, and C) 100% charge polymers under the optimum polymer dosage of 2 mg/g silica, respectively. The right column of figures shows the effect of background electrolyte concentration on typical floc size distributions and volume average ($d[4, 3]$) floc sizes of silica flocculated with D) 10% charged polymers under the optimum polymer dosage of 12 mg/g silica and at [NaCl]) 0.03 M, E) 40% charged polymers under the optimum polymer dosage of 12 mg/g silica, and F) 100% charge polymers under the optimum polymer dosage of 2 mg/g silica, respectively¹⁹.

In summary, fractal dimension is a powerful quantification for floc structure which has demonstrated a capability to integrated into sedimentation models as a density modifier as shown in Eqn. 2.6⁴⁸. The internal porosity of flocs will induce complexities to sedimentation dynamics and intra-aggregate fluid flow has been demonstrated through modelling and visualisation and is key to incorporate in sedimentation models to predict SPP1 residence times⁴⁵. Fractal dimension has been shown through 3D space kinetic growth modelling to aid in identifying flocculation mechanisms¹¹⁷, which has been related

to the polymer molecular weight and chain length. SLS is likely a powerful tool to quantify floc fractal dimensions, requiring small volume samples, providing both size and structure characterisation while keeping radiation dosages to workers ALARP.

2.4) Sedimentation analysis and modelling

2.4.1) The role of polymers in improving settling rates

The sedimentation of $Mg(OH)_2$ radwaste analogues were performed by Johnson et al.¹⁶ at two test scales, litre and milli-litre (Turbiscan). The interfacial mudline of the settling sludge was measured with time to determine the initial sedimentation rate of Versamag as a function of solids concentration as shown in Fig. 2.20A at a litre scale. As the solids concentration increased, the interfacial settling rate decreased due to hindered settling effects. The sedimentation rate for 2.5 vol.% (max SPP1 transfer concentration⁶) Versamag was recorded as being $\sim 0.2 \text{ cm}\cdot\text{min}^{-1}$ shown in Fig. 2.20B at Turbiscan scale. Improvement of this sedimentation rate will critically reduce SPP1 residence time, increasing the rate of sludge removal from FGMSP. In Section 2.2, it was shown that literature indicated polymeric flocculants could be deployed to increase the size of aggregates in suspension, which have been shown to be beneficial to increasing sedimentation rates of suspensions, provided surface coverage is low enough to prevent steric stabilisation^{17,103}. Once the optimum polymer species and process operation is determined, the sedimentation should be modelled to produce a predictive capability resilient to varying feed compositions for Sellafield to assign SPP1 residence times for batch sedimentation scheduling, which results in an appropriately clarified supernatant liquor to be returned to FGMSP.

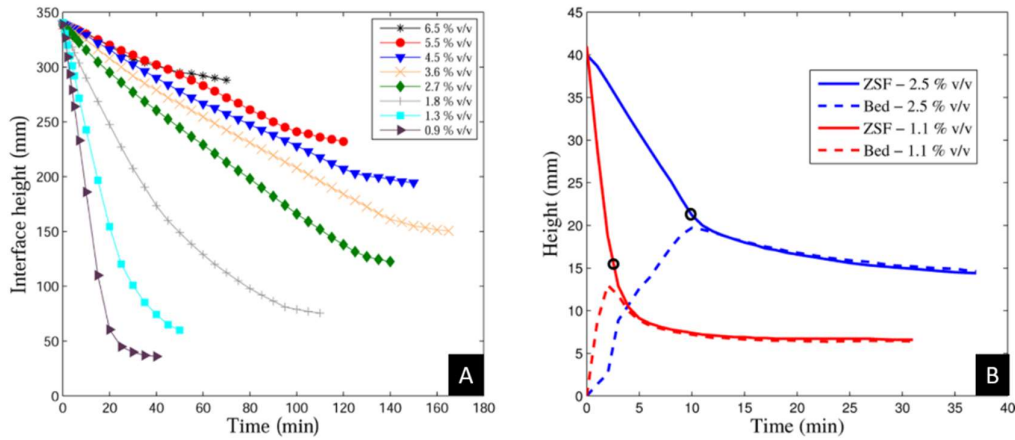


Figure 2.20: Example settling profiles for aqueous Mg(OH)₂ suspensions at two test scales. The transition point from linear settling to compressional dewatering. A) Litre scale settling test scale. B) Turbiscan lab expert scale experiments¹⁶.

2.4.2) Stokes Law and multiple fractal particle modifications

As individual particles settle, they displace fluid immediately beneath them. For multiple particles in a batch/suspension concentration cell (such as SPP1), where this fluid displacement hinders settling in the system by producing up flow and turbulence in the compressing suspension bed. Thus, the Stokes law of terminal settling velocity may be modified by Eqn. 2.12 to include a hindering function²¹:

$$U_i = U_T \times f_s \quad (\text{Eqn. 2.12})$$

The terminal velocity of an individual particulate, U_T , is calculated using Stokes law which determines the terminal settling velocity of a singular particle of diameter, D_m . Whereas the velocity of the sediment interface (or zonal settling front/mudline) in hindered settling systems, U_i , is determined as a product of a dimensionless function proportional to the permeability of the particle network suspended in the medium (referred to here as the dimensionless permeability number, f_s), and the individual particulate sedimentation velocity under terminal conditions shown in Eqn. 2.13.

$$U_i = \frac{g(\rho_p - \rho_w)D_m^2}{18\mu_w} f_s \quad (\text{Eqn. 2.13})$$

As discussed in Section 2.3, various microscopy techniques^{41,43,50} and modelling^{116,117} have shown that the floc structures are of a fractal nature and ultimately porous, indicating that the density of the primary particles is not appropriate for settling models. It was shown that this structure can be quantified using the fractal dimension which could be established using SLS. Adachi and Tanaka¹²³ and Adelman et al.¹²⁴ used a modified terminal settling rate equation that incorporated the fractal nature of the settling flocs shown in Eqn. 2.14:

$$U_i = \frac{g(\rho_p - \rho_w)\overline{D_f^2}}{18\mu_w} \left(\frac{D_f}{D_p}\right)^{d_f-3} f_s^* \quad (\text{Eqn. 2.14})$$

Where $\overline{D_f}$ represents the value of a floc diameter selected to represent the polydisperse floc population (i.e. d_{50} or d_{90}) which is determined from the respective particle size distributions (PSDs). This is an important consideration as there are multiple ways to represent an entire size distribution with a single number. f_s^* is the fractal modified dimensionless permeability number. Richardson and Zaki⁴⁰ suggested the following relationship in Eqn. 2.15, for multiple spherical particles settling in laminar flow conditions. Stating that the traditional particle dimensionless permeability number of the suspended medium, f_s , is a function of the particulate volume fraction, and the Richardson-Zaki exponent, n , which is traditionally also a function of Reynolds number^{16,125} and normally taken as equal to 4.65 in laminar conditions for spherical assumptions.

$$f_s = (1 - \phi_p)^n \quad (\text{Eqn. 2.15})$$

Here ϕ_p is the volume fraction of the settling particle species. While originally determined for discrete objects, the hindered settling model has been expanded, as originally described by Michaels and Bolger¹²⁶ to account for the effective fractal volume fraction of aggregate flocs, with respect to the dispersed particles. This modification is given Eqn. 2.16.

$$\phi_f = \phi_p \left(\frac{D_f}{D_p}\right)^{3-d_f} \quad (\text{Eqn. 2.16})$$

Finally, Eqns. 2.15 and 2.16 can be combined substituting ϕ_f for ϕ_p to derive the fractal modified dimensionless permeability number f_s^* shown in Eqn. 2.17 .

$$f_s^* = (1 - \phi_f)^n = \left(1 - \phi_p \left(\frac{D_f}{D_p}\right)^{3-d_f}\right)^n \quad (\text{Eqn. 2.17})$$

An overall Fractal Modified Richardson-Zaki model (referred to as the FMRZ model from hereon), can now be derived by combining Eqns. 2.14 and 2.17 as used by Heath et al.(2006) and Hunter et al.(2020), in Eqn. 2.18:

$$U_i = \frac{g(\rho_p - \rho_w)\overline{D_f^2}}{18\mu_w} \left(\frac{D_f}{D_p}\right)^{d_f-3} \left(1 - \phi_p \left(\frac{D_f}{D_p}\right)^{3-d_f}\right)^n \quad (\text{Eqn. 2.18})$$

Heath et al.¹⁸ utilised the FMRZ model when investigating polymer flocculation of calcite suspensions using an acrylate/acrylamide 30% anionic charge density copolymer. The calcite was flocculated in turbulent pipe flow and measured *in situ* using FBRM to establish a particle size distribution. The flocculated suspension then flowed into vertical column used to measure the hindered settling velocity. The fractal dimension was experimentally determined to be 2.4 and particles were assumed to be monodisperse and spherical meaning $n=4.65^{21}$. The FMRZ model was then used to predict settling rates and validated against experimental settling data shown in Fig. 2.22. Fig. 2.22 shows the experimentally observed hindered settling rates compared against the settling rates predicted using the FMRZ model in Eqn. 2.18, where points converging on the line $x=y$ show increasing agreement with model predictions. Fig. 2.21 therefore indicated that for fractal hindered settling systems that the FMRZ model in Eqn. 2.18 could be used as an effective model to determine SPP1 residence times to optimise FGMSP dewatering assuming drag forces are negligible.

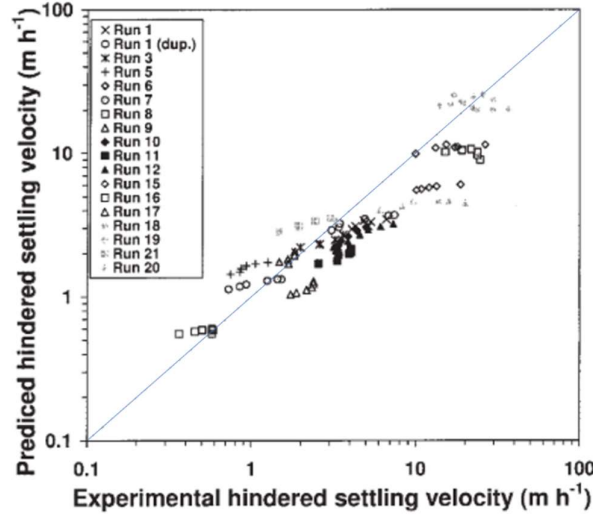


Figure 2.21: Comparison between measured and predicted (Eqn. 2.18) hindered settling velocities¹⁸.

Heath et al.¹⁸ made an assumption the permeability of the flocs, in conjunction with the high particulate packing (inter-aggregate spacing approaching intra-aggregate spacing) in hindered settling offset reductions in settling rates caused by shape affects and drag, resulting in neglecting the inclusion of a Reynolds number (Re) into the correlation in Eqn. 2.18. This mathematical functionality is often incorporated into models which predict the individual settling rate of flocs, or where solids concentrations are lower so that the ratio of fluid viscous forces and particle inertia forces is negligible and is a function of water density, ρ_w , particle diameter, D_p , particle settling velocity, U_T , and the viscosity of the water, μ_w , shown in Eqn. 2.19. Stokes law is constructed of a force balance of gravitational, buoyant and drag forces, and the coefficient of drag is introduced in the derivation of Stokes law and is often a function of Re , resulting in the terminal settling rate relationship shown in Eqn. 2.20, where η is a non-sphericity factor as suggested by Winterwerp¹²⁷.

$$Re = \frac{U_T \bar{D}_f \rho_w}{\mu_w} \quad (\text{Eqn. 2.19})$$

$$U_T = \frac{\eta(\rho_p - \rho_w)g}{18\mu_w} D_p^{3-d_f} \frac{\bar{D}_f^{d_f-1}}{1 + 0.15Re^{0.687}} \quad (\text{Eqn. 2.20})$$

Vahedi and Gorczyca¹²⁸ utilised the relationship in Eqn. 2.20 (originally proposed by Winterwerp¹²⁷ in 1998) to predict the settling rates of fractal structured lime softening flocs and much like the hindered settling experiments by Heath et al.¹⁸ found very strong

agreement to the model as indicated in Fig. 2.22. The findings of this research indicate that the settling velocity of lime flocs can be modelled by equations developed for predicting the settling velocity of natural sediments using Eqn. 2.20. However, knowledge of aggregation mechanisms of lime flocs was the key parameter required, fractal dimensions for the modelled flocs were generated assuming that for a specific floc size multiple fractal dimensions can exist as discussed in Section 2.2 regarding flocculation mechanism and in Section 2.3 regarding flocculation mechanisms consequence on fractal dimension. Consequently, same size flocs can have a range of different settling velocities. Vahedi and Gorczyca¹²⁸ found that Stokes' law significantly overestimated the settling velocities of lime flocs and that the settling velocity of flocs appeared to be mainly controlled by aggregation mechanisms and forming large flocs does not guarantee improved sedimentation on an individual basis, unsurprising given that the $\left(\frac{D_f}{D_p}\right)^{d_f-3}$ term in creeping flow conditions, where drag is negligible, acts as a floc density modifier.

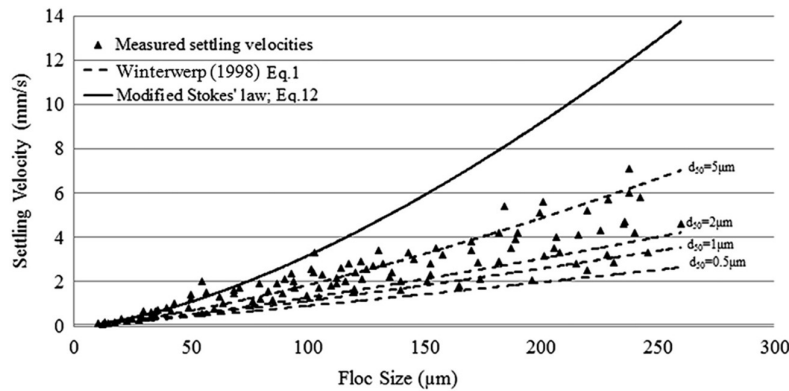


Figure 2.22: Lime floc settling velocities predicted based on experimentally determined fractal dimensions. Where Winterwerp Eq.1 is referred to as Eqn. 2.20 in this thesis¹²⁸.

The fractal modified Stokes Law proposed by Winterwerp¹²⁷ in Vahedi and Gorczyca¹²⁸ work on predicting settling velocities of multi-fractal dimension lime softened flocs in Eqn. 2.20 can be incorporated into the batch settling model similar to the drag negligent terminal settling velocity component suggested by Heath et al.¹⁸ in the FMRZ model (Eqn. 2.14). The model would maintain the same functional permeability number, f_s^* , to give Eqn. 2.21 which is referred hereon as the DRAG model. It is important to understand the floc structure and the influence of fractal dimension on the functional permeability number. Heath et al.¹⁸, assumed that due to the inter-aggregate spacing approaching intra-aggregate spacing that the floc permeability would relieve boundary layer separation due to floc permeability and

thus drag forces could be considered negligible. However, if inter-aggregate spacing is greater than intra-aggregate spacing (i.e. flow around flocs rather than through, manifesting as a larger f_s^* value), then the balance of inertia and viscous forces needs to be incorporated into the model. This inter-aggregate spacing is important for Sellafield Ltd. to understand when selecting their sedimentation model to predict SPP1 residence times and will be a function of flocculation mechanism and by extension fractal dimension¹²⁸. It should be noted that the product of Eqns. 2.17 and 2.20 to compute Eqn. 2.21 to incorporate drag effects into the fractal modified hindered settling model has not previously been utilised in the literature to the authors knowledge.

$$U_i = \frac{\eta(\rho_p - \rho_w)g}{18\mu_w} D_p^{3-d_f} \frac{\overline{D}_f^{d_f-1}}{1 + 0.15Re^{0.687}} \left(1 - \phi_p \left(\frac{D_f}{D_p} \right)^{3-d_f} \right)^n \quad (\text{Eqn. 2.21})$$

2.5) Surface active molecules and macromolecules (SAMs)

2.5.1) Amphiphilic surfactants and block copolymer properties

As discussed in Section 2.2.3, amphiphilic molecules such as block copolymers and surfactants consist of a segregated hydrophobic and hydrophilic component. The hydrophobic section is generally a lipophilic tail (usually a similar form non-polar hydrocarbon/polymer chain) and the hydrophilic segment is a general solubilising structure which can be¹²⁹:

- Anionic- sulphates, sulphonates, carboxylates or poly(acrylic acid) ABC blocks etc.
- Cationic- quaternary amines and poly(dimethylammonium chloride) ABC blocks.
- Non-ionic- polyoxyethylene and polyacrylamide ABC blocks
- Amphoteric- zwitterionic species such as Betaines

Water molecule dipoles cause water to form isotropic weakly hydrogen-bonded tetrahedral structures in the bulk solution. However, at the air water interfaces water molecules adopt less balanced, asymmetrical hydrogen-bonded structures resulting in excess surface energy¹²⁹. The presence of amphiphilic molecules result in an increase in surface energy regarding the water molecules immediately surrounding the hydrophobic organic chain, rearranging their structure asymmetrically to form entropically unfavourable ‘cages’ around the lipophilic tail to arrange their dipoles away from the non-polar alkyl chain.

Thermodynamically, it is unsurprising that adsorption of these amphiphilic molecules to air-water interfaces so that their hydrophobic tails are facing outwards into the air results in a decrease in entropy. Water molecule dipoles are both freed from their energetically unfavourable ‘cage’ arrangement around these lipophilic tails, as well as the displacement of water molecules from the air-water interface, lowering the surface energy of the solution.

The adsorption of amphiphilic molecules at the air-water interface increases with increasing amphiphilic molecule concentration until a molecular monolayer at the air-water interface is formed. Because amphiphilic molecules display this surface activity, from here-on amphiphilic molecules will be referred to as surface active molecules (SAMs). Once SAMs achieve a monolayer adsorption, the remaining SAMs in the bulk suspension display a phenomena known as self-assembly. Where the SAMs arrange themselves so that their hydrophobic tails orientate themselves so the they are facing each other and their hydrophilic headgroups face outwards into the bulk suspension to reduce the number of water molecules orientating themselves into asymmetrical high surface energy ‘cage’ structures. This SAM self-assembled structure is known as a micelle, and the concentration at which this occurs (i.e. above monolayer concentration) is known as the critical micelle concentration (CMC), illustrated in Fig. 2.23^{102,108,129,130}.

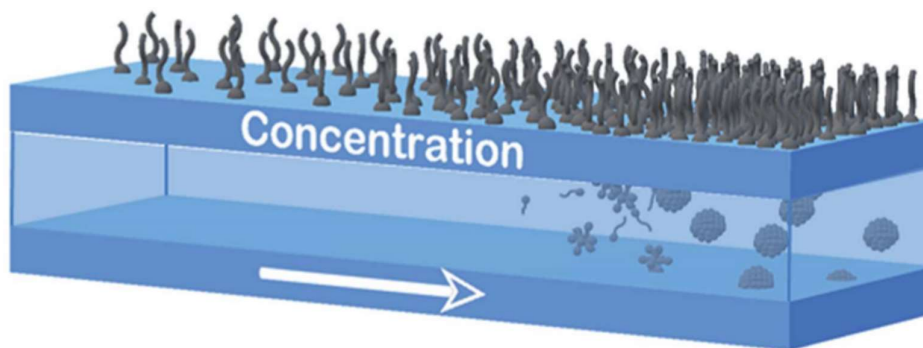


Figure 2.23: Scheme of micelle formation as the concentration of surfactant at the surface increases¹³⁰.

2.5.2) Surface tension and dilational viscoelasticity

A consequence of SAMs adsorption to the air-water interface (AWI) and the resultant displacement of high surface energy water molecules is a reduction in surface energy with increasing SAM concentration until a monolayer (the CMC) is formed. For example, sodium lauroyl isethionate is an anionic surfactant ubiquitous to the personal goods industry and is constructed of an acid-ester sulphate head-group and an alkyl hydrophobic

tail. As a result, the increase in SLI concentration resulted in an adsorption to the AWI and reduction in surface tension of deionised water until reaching its CMC (5.36 mM) with a plateaued surface tension of $38 \text{ mN}\cdot\text{m}^{-1}$ as shown in Fig. 2.24 by Jeraal et al.¹³¹.

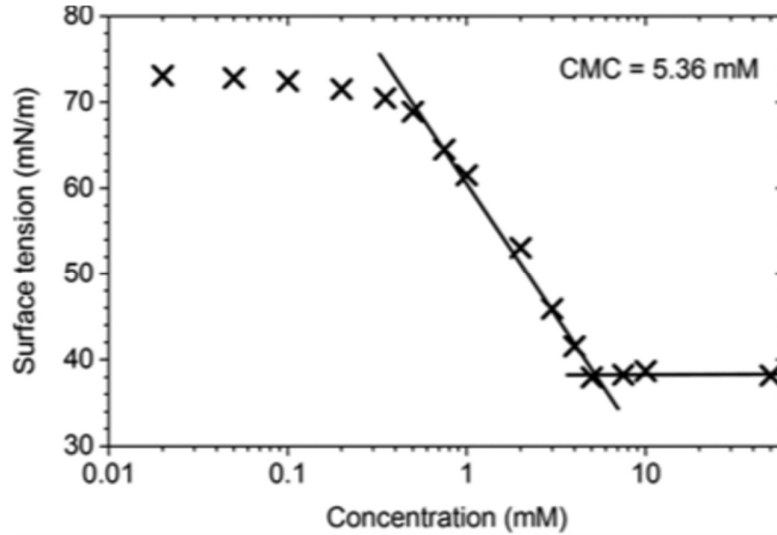


Figure 2.24: Surface tension as a function of the purified SLI concentration in water. The surface tension was determined by pendant drop analysis at 20 °C. Equilibrium surface tension values were obtained by fitting the droplet shape to the Young–Laplace equation. Reported values are an average of 30 consecutive images (1 fps)¹³¹.

For amphiphilic block copolymers (ABCs) the degree to which the surface tension is modified is more complicated. Whilst known for their comparatively low surface activity when compared to surfactants, their stability and adsorption to AWIs is a function of many variables, including but not limited to their hydrophilic/hydrophobic block species, the relative length of the two blocks and ionic strength of the aqueous medium. Garnier and Laschewsky⁹² investigated a range of ABCs with poly(butyl acrylate) as a common hydrophobic block and varied the hydrophilic component with an anionic, cationic and four non-ionic blocks of various compositions and degrees of hydrophilicity. The longer the hydrophobic block, the shorter the hydrophilic block, and the less hydrophilic the monomer of the hydrophilic block is, the lower the surface tension was found to be as shown in Fig. 2.25. Where Fig. 2.25A shows the 7 block species investigate arranged in degrees of hydrophobicity/hydrophilicity.. Fig. 2.25B(i) shows the change in surface tension as a function of two reference surfactants, SDS and P1 (with their CMCs marked with arrows). Fig. 2.25B(ii) shows ABC poly(M1)₈₁-*b*-poly(M7)₁₀₅ and poly(M1)₈₁-*b*-poly(M7)₅₅ changes in surface tension with increasing polymer concentration. Where the ABC shorter hydrophilic group, poly(M1)₈₁-*b*-poly(M7)₅₅, displayed marginally greater changes in

surface energy manifesting as a greater reduction in surface tension with concentration likely due to a lower degree of image charge repulsion. Fig. 2.25B(iii) shows the change in surface tension with ABC concentration for two cationic ABCs, poly(M1)₈₁-*b*-poly(M6)₁₃₆ and poly(M1)₈₁-*b*-poly(M6)₅₈. Where similarly to the cationic ABCs in Fig. 2.25B(ii), the short poly(M6) chain was identified as a marginally more surface active macromolecule. Finally Fig. 2.25B(iv) displays the change in surface tension with increasing ABC concentration of poly(M1)₈₁-*b*-poly(M5)₉₅, poly(M1)₈₁-*b*-poly(M6)₁₃₆ and poly(M1)₈₁-*b*-poly(M7)₁₀₅ from Figs. 2.25B(iii) and 2.25B(ii) respectively. Whilst the non-ionic M5 block displays lower hydrophilicity than M6 and M7(see Fig. 2.25A), the comparatively lower M5 chain-length hydrophilic block results in a more pronounced reduction in surface tension, indicating a convolution of these different parameters. Where M1 is poly(butyl acrylate), M5 is poly(oligo(ethyleneglycol)methyl ether acrylate), M6 is poly(2-acrylamide-2-methyl(proponesulphonic acid) and M7 is poly(3-acrylamidopropyltrimethylammonium chloride).

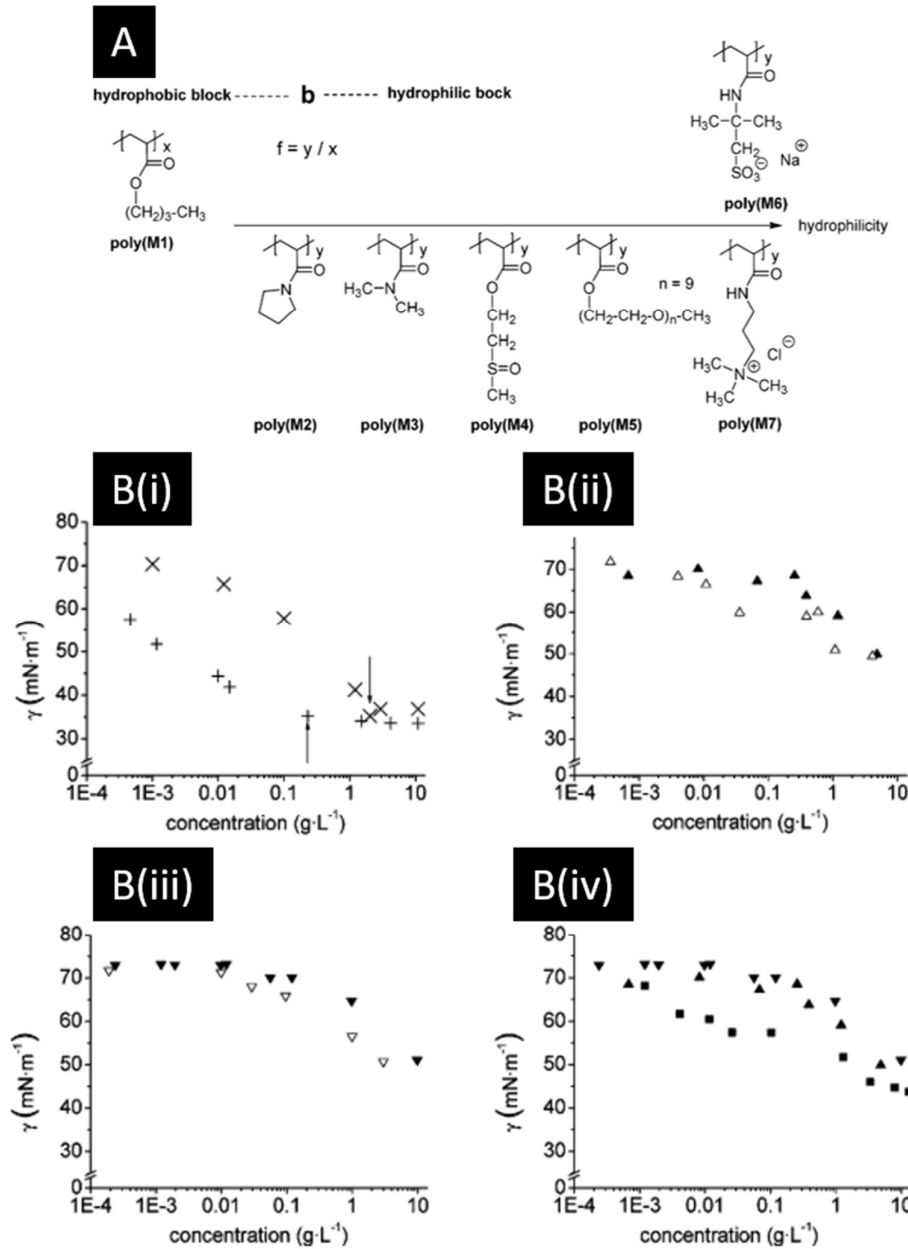


Figure 2.25: A) Polymer structures used and labelled in the work by Garnier and Laschewsky⁹². B(i) Surface tension γ vs concentration of aqueous solutions of reference surfactants SDS and P1. B(ii) Block copolymers poly(M1)- b-poly(M7). B(iii) Block copolymers poly(M1)-b-poly(M6). B(iv) Block copolymers with various hydrophilic blocks. The arrows indicate the CMC of SDS and of P1 according to DLS studies. (×) SDS, (+) P1, (▲) poly(M1)₈₁-b-poly(M7)₁₀₅, (Δ) poly(M1)₈₁-b-poly(M7)₅₅, (▼) poly(M1)₈₁-b-poly(M6)₁₃₆, (▽) poly(M1)₈₁-b-poly(M6)₅₈ and (■) poly(M1)₈₁-b-poly(M5)₉₅.

For Mg(OH)₂ radwaste suspensions displaying cationic surface charge, it is likely that an anionic hydrophilic block will have an affinity for Mg(OH)₂ surface adsorption. Conversely to Garnier and Laschewsky⁹², Ghosh et al.⁹¹ investigated the effects of the relative hydrophobic block length on surface activity and micellization of ABCs of poly(n-butyl

acrylate)-*b*-poly(3-(methacryloyloxy)ethyl)trimethylammonium chloride) referred to as (PBA-*b*-PDMC). As the hydrophobic chain length increased, a notable reduction in surface activity was observed, with the smallest chain length hydrophobic block, PBA₈-*b*-PDMC₆₀, shown in Fig. 2.26A displaying almost surfactant like adsorption to the AWI. Figs. 2.26B and 2.26C show ABCs PBA₂₅-*b*-PDMC₆₀ and PBA₅₀-*b*-PDMC₆₀ respectively indicating gradual decreases in surface activity manifesting as least pronounced reductions in surface tension as a function of ABC concentration where Fig. 2.26D (PBA₇₅-*b*-PDMC₆₀) shows no surface activity. An interesting observation is that the presence of 0.1 M NaCl results in an increase in surface activity for each of the four observed ABCs in Figs. 2.26A to 2.26D. It is likely that the addition of electrolyte reduced image charge effects preventing adsorption at the air-water interface which has been previously reported by Eghbali et al.¹³². Eghbali et al.¹³² investigated the surface activity and micellization of PAA₁₅₀-*b*-PnBA₁₀₀ (Which displayed surfactant like surface activity) ABCs observing that the addition of NaCl salt neutralised the image charge repulsion of PAA segments which reduced surface adsorption and lowered the CMC of the ABC similarly to the observations in Figs. 2.26A to 2.26D by Ghosh et al.⁹¹.

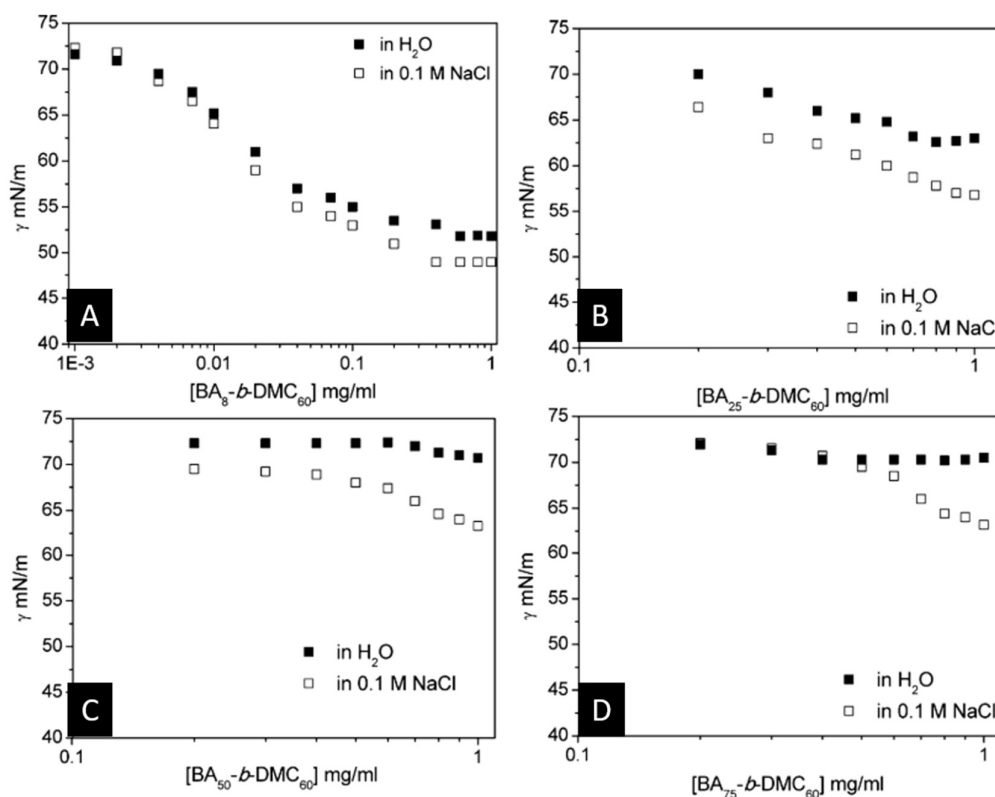


Figure 2.26: Surface tension (γ) as a function of the concentration of PBA-*b*-PDMC polymer. (A), (B), (C), and (D) are BA₈-*b*-DMC₆₀, BA₂₅-*b*-DMC₆₀, BA₅₀-*b*-DMC₆₀, and BA₇₅-*b*-DMC₆₀, respectively. Filled square is in water, and open square is in 0.1 M NaCl⁹¹.

ABCs reduce the surface tension much less than standard low-molar-mass surfactants and form micelles at much lower comparative concentrations (See Fig. 2.25⁹²). The resultant formability is a function of surface activity where Fig. 2.26A shows an investigation by Garnier and Laschewsky⁹² of the foamability of non-ionic and ionic ABCs displayed in Fig. 2.27A benchmarked against surfactants CTAB, P1 and Brij 56. Where the surfactants display significantly greater foam stability when compared to the ABCs which is unsurprising given their much greater surface activity reflected in Figs. 2.27B(i) to 2.27B(iv). Figs. 2.27B and 2.27C compare the formability of ABCs of 4 different hydrophobic chain lengths without and with 0.1 M NaCl respectively where (i) BA₈-*b*-DMC₆₀; (ii) BA₂₅-*b*-DMC₆₀; (iii) BA₅₀-*b*-DMC₆₀; (iv) BA₇₅-*b*-DMC₆₀. Much like the surface tension data also presented by Ghosh et al.⁹¹ in Fig. 2.26, the increase in poly(butyl acrylate) results in a decrease in foamability, however in the presence of electrolyte, image charge effects are reduced resulting in a marginal increase in AWI adsorption resulting in an increase in foamability compared to pure water. A key advantage for nuclear waste

management deploying ABCs in lieu of surfactants is the lower degree of foamability exhibited by ABCs as shown in Fig. 2.27, resulting in a lower degree of entrained water in the foam lamella thus reducing water volumes which will be required treatment to remove radionuclides before sea discharge.

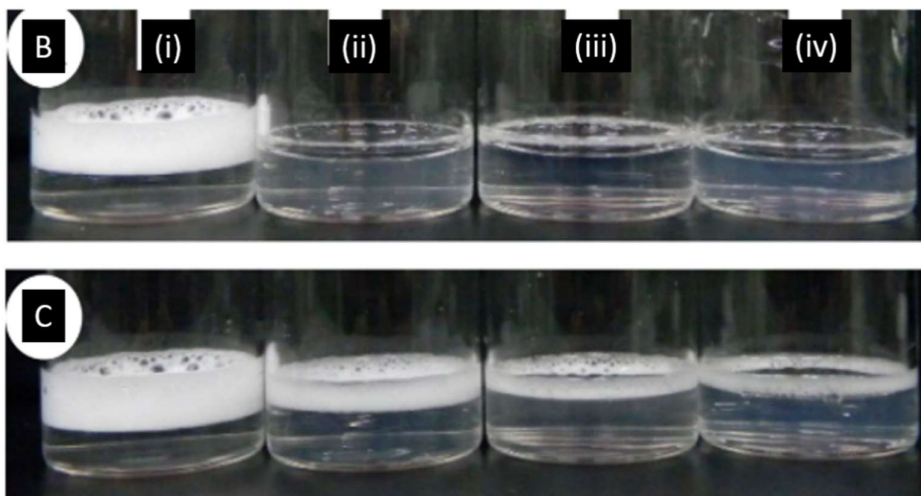
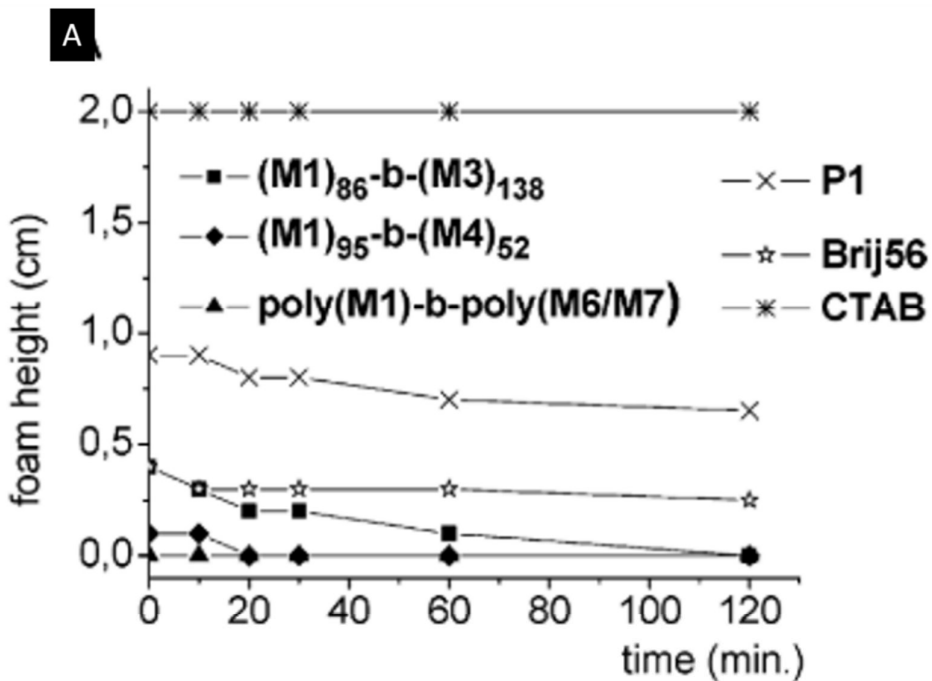


Figure 2.27: A) Foam height vs time for aqueous solutions of pure amphiphilic diblock copolymers and reference surfactants (see Fig. 2.25A for polymer identities)⁹². Photo observation of foam formation behaviour of 1 mg.ml⁻¹ of PBA-*b*-PDMC polymer in water (B) and 0.1 M NaCl (C) (5 min after shaking): (i) BA₈-*b*-DMC₆₀; (ii) BA₂₅-*b*-DMC₆₀; (iii) BA₅₀-*b*-DMC₆₀; (iv) BA₇₅-*b*-DMC₆₀⁹¹.

Another key property of interest regarding amphiphilic molecules is their effect on the elasticity of the resulting foams generated from entrained air. The adsorption of amphiphilic

molecules at the AWI reduces the work needed to expand the surface area of the AWI, as the AWI is perturbed, amphiphilic molecules are required to move from the bulk solution to the AWI to displace water molecules to reduce the increasing surface energy¹²⁹. The rate of this molecular exchange determines the elasticity of the generated foam and often related to the foams mechanistic strength to breakage. Low molecular weight surfactants generally have good elastic properties as they are not sterically inhibited from adsorbing to the surfaces. However for long chain macromolecules such as ABCs, their relaxation kinetics at perturbed AWIs are comparatively much slower, resulting in poorer elasticity promoting properties¹³³. A simple test to observe viscoelasticity of films is to dilate a pendant drop at a specified frequency. Mechanically perturbing an air-water-interface by oscillating the internal pressure at a known frequency, the rate of change of the principle radii of curvature and by extension the surface tension of the pendant droplet (through the Young-Laplace equation) will determine the dilational viscoelasticity of the droplet¹²⁹. Zhang et al.¹³⁴ investigated the dilational viscoelastic properties of two surfactants in water fuel interfaces, Monoolein and pentaerythritol oleate (PETO-B), where PETO-B not only had a greater molecular weight but is also a branched hydrocarbon structure. Fig. 2.28A shows the change in elastic modulus as a function of surfactant concentration for three oscillation frequencies (01, 0.25 and 0.5 Hz). The greater molecular weight branched PETO-B displays lower elastic modulus for all observed concentrations compared to the monoolein system. This was due to the comparatively low migration rates of PETO-B to the perturbed AWI compared to monoolein as shown in Fig. 2.28B, which was determined by Zhang et al.¹³⁴ to be a function of the steric hindrance of the PETO-B branched structure preventing quicker molecular exchanges at the AWI.

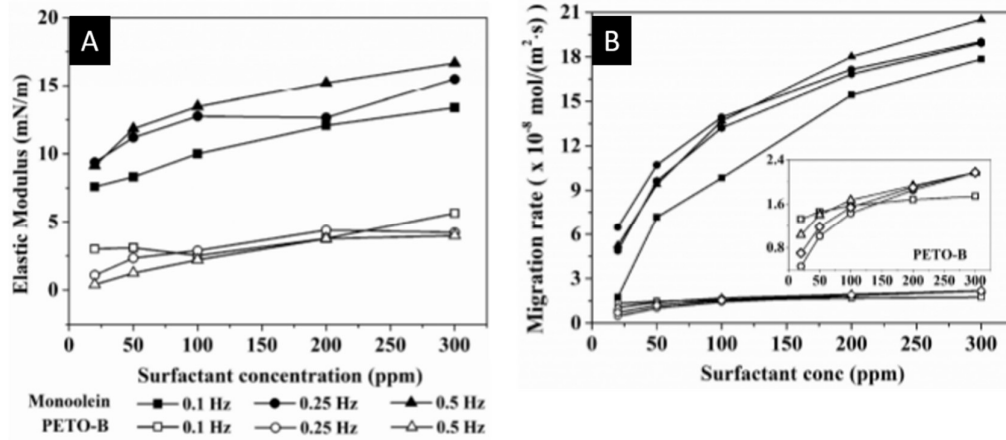


Figure 2.28: A) Elastic moduli of fuel/water interfaces consisting of monoolein and PETO-B under different oscillation frequencies. B) Average migration rate of monoolein and PETO-B at static and oscillation states with frequency of 0.1–0.5 Hz¹³⁴.

Due to the low surface activity and elasticity of the ABCs, it is likely that a ‘frother’ will have to be applied to Mg(OH)₂ suspensions to allow the formation of foams for particle recovery using flotation as a dewatering strategy. A frother is a chemical additive that alters the foamability of water but does not interact with any of the particles in suspension¹²⁹. Though if a sedimentation only dewatering strategy is pursued for SPP1, the low surface activity of the ABCs are advantageous as they will not cause severe foaming in aggressive sludge transport to downstream operations at Sellafield meaning they can be likely deployed solely as settling aids.

2.6) Flotation

2.6.1) Flotation in nuclear and bubble attachment factors

Flotation cells have very variable mechanical designs with various deployment strategies which have different advantageous and disadvantages. Jameson cells are widely deployed in the minerals industry and are praised for having high throughput in a small area, are easy to operate and tune for feed variations, conduct stable operation with minimal operator involvement, require minimal maintenance due to few moving parts, are easy to install and commission and have flexible cell designs⁷⁴. These are very attractive characteristics when cross-examining with the nuclear technology regulatory specifications highlighted in Section 1.2 by Hastings et al.⁵. Jameson cells come in multiple configurations and can occupy geographical footprints as small as 0.19m². Additionally, modular designs are

attractive to the nuclear industry so that these technologies can be retrofit into existing facilities, such as the mobile flotation cell design by Ortiz-Oliveros et al.⁷⁵ shown in Fig. 2.29 occupying a 4m² footprint which was proposed as a separation process response to radiological post-emergencies of nuclear power plants or environmental emergency responses associated with oil spills. The drive for smart processing has promoted sustainable development of such flotation cells. Particularly the need to reduce water consumption, a goal of interest to desert mining operations and a key requirement for the viability of large scale extra-terrestrial beneficiation¹³⁵.

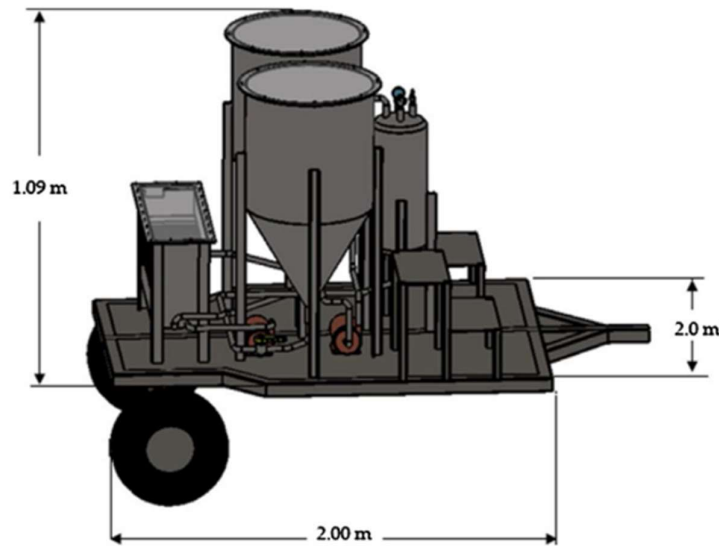


Figure 2.29: The schematization of the mobile dispersed air flotation cell with a high rate for the treatment of liquid radioactive waste⁷⁵.

A key aspect of flotation performance in all cell configurations is a particulates ability to attach to air bubbles in the cell for transport to the extractable foam phase. A review of bubble attachment models by Wang et al.⁷⁸ who looked at three classifications of models; force balanced, energy balanced and empirical and Gontijo et al.⁸³ who investigated the limits of fine and coarse particle flotation discussed common factors influencing bubble detachment. Bubble detachment factors include but are not limited to capillary forces, particle detachment vortex force, gravitational force and buoyancy forces, which could be rearranged to calculate the maximum particle size (D_{max}) indicated in Eqn. 2.22. Where θ is the detachment contact angle, γ is the surface tension of the suspension and a_v is the acceleration of the particle due to detachment vortex force. Eqn. 2.22 highlights some interesting hydrodynamic implications for flotation of polymerically flocculated flocs

which display porous, fractal properties which will be discussed further in Section 2.7. Additionally, the detachment vortex force is determined by the selected cell configuration and will only be practically appreciated at full scale operation and is therefore beyond the scope of this thesis. However, it should be noted that as discussed in Section 2.2.4, turbulence generated shear associated with vortex force in the cell will reduce the floc size distribution. Thus reducing the floc population above the upper limits of flotation and should be investigated in future work. The remaining major factors are the contact angle of the particle-bubble attachment (see Fig. 2.30) and the resultant surface tension of the suspension. As discussed in Section 2.5, ABCs should have very little influence on the resultant surface tension and this will be affected primarily by the frother concentration. Therefore the two factors which ABCs will have a major effect on are hydrodynamic considerations and contact angle modification.

$$D_{max} \approx \sqrt{\frac{6\gamma \sin^2(\theta/2)}{(\rho_f - \rho_w)g + \rho_f a_v}} \quad (\text{Eqn. 2.22})$$

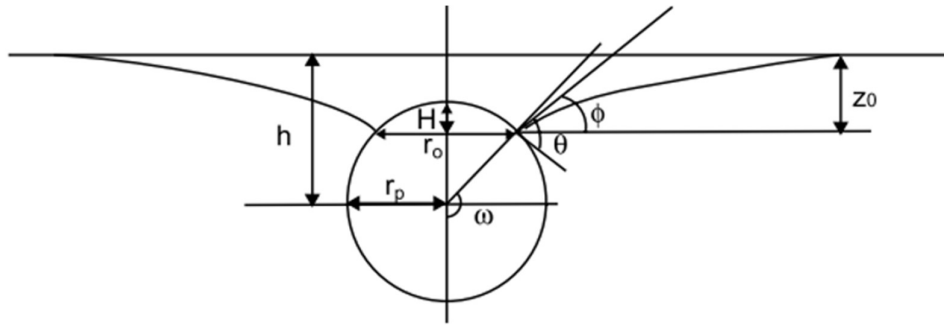


Figure 2.30: Spherical particle located at the liquid/gas interface. r_p is the particle radius, r_o is the radius of the three-phase contact line, h is the immersion depth of the particle, H is the height of the spherical cap above the meniscus; z_o is the height of the meniscus above the three-phase line (deformation of the liquid meniscus at the solid surface), θ is the particle contact angle, Φ is the polar angle, i.e., the angle between the surface tension direction (the tangent of the meniscus at the three-phase line) and the horizontal, ω is the central angle at the particle, i.e., the angle between the surface tension direction and the vertical downwards, γ is the liquid-gas surface tension⁸³.

2.6.2) Surface coverage and hydrophobisation

Particle hydrophobicity is generally measured as a function of its contact angle. Displayed two-dimensionally (see Fig. 2.30), the contact angle allows a measurement of effectively how ‘immersed’ a particle is within a bubble, where contact angles $<90^\circ$ indicate a partially hydrophobized particulate where the majority of its surface area is within the bulk liquid phase. Above 90° , a particle is considered strongly hydrophobic with the majority of its

surface area inside the bubble (i.e. the gas phase). Most particles in nature, including $\text{Mg}(\text{OH})_2$, have a mostly hydrophilic surface which enables them to be dispersed in water and therefore do not attach to bubbles very well¹²⁹. Hydrophilic particles have very low contact angles and therefore lower detachment energies. Hydrophilic particles such as silica which also display -O-H surface groups similar to $\text{Mg}(\text{OH})_2$, can have their contact angles increased by irreversibly chemically grafting non-polar short-chain alkyl silane or ester coupling agents to their surfaces. This same hydrophobising effect can be reversibly achieved by physio-adsorbing counter-ionic amphiphilic molecules to the $\text{Mg}(\text{OH})_2$, where the solubilising hydrophilic headgroup has an affinity for the $\text{Mg}(\text{OH})_2$ surface meaning the high surface energy non-polar tails face outwards into the bulk liquid as a corona.

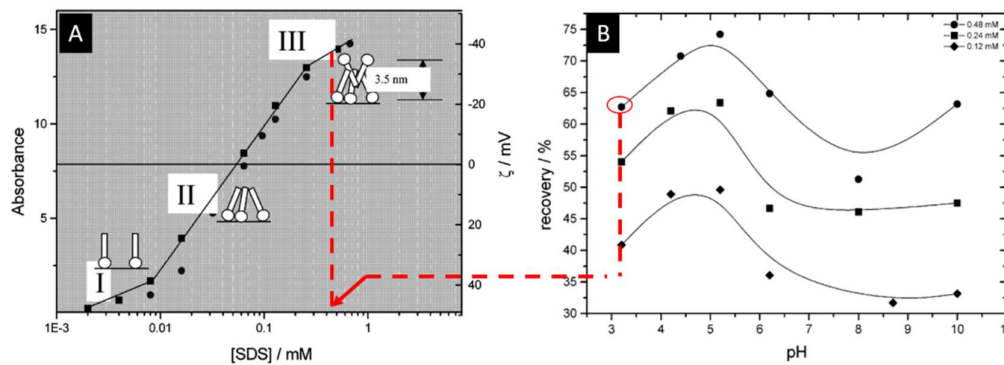


Figure 2.31: A) Adsorption and zeta (ξ)-potential (mV) isotherms for colloidal hematite: squares obtained from zeta-potential at pH 3.12 and a temperature of 20 °C; circles obtained from ATR absorbance measurement at pH 3.6 and a temperature of 20 °C. B) Effect of SDS concentration on flotation recovery (values refer to initial SDS concentrations)⁸⁰.

As the surface coverage of these hydrophobising surface modifiers increases, by extension the contact angle increases making the particles increasingly compatible with bubble attachment assuming liquid-air surface tension and particle size remain constant. An *in situ* mechanistic study of SDS adsorption on hematite with the purpose of optimising froth flotation operations was performed by Bai et al.⁸⁰ using an attenuated reflectance Fourier transform infrared (ATR-FTIR) technique to measure collector adsorption. The SDS adsorption was found to be sensitive to pH where low pHs induced precipitation of SDS and high pHs (specifically above the iso-electric point of hematite at 7.3) resulted in little to no adsorption of SDS. This effect of pH will likely be of little importance in the $\text{Mg}(\text{OH})_2$ suspension due to its reported self-buffering behaviour and slight cationic surface potential at the equilibrated pH of ~ 10 ¹⁶. In the study by Bai et al.⁸⁰, an adsorption isotherm (at pH 3.6) was determined shown in Fig. 2.31A, where two adsorption regimes are identified, a

monolayer region of SDS coverage and a bilayer. The greater surface adsorption was related to superior flotation performance indicated by Fig. 2.31B with 0.48 mM SDS performing better at pH 3.2 than lower dosages. However, the given that the optimum Flotation performance is shown in Fig. 2.31B to be at pH 5, and adsorption density was found to decrease with increasing pH, it was assumed that a partial monolayer coverage resulted in optimum flotation performance, though likely to be approaching maximum monolayer adsorption density.

$$q_e = \frac{q_e^* K_l C_e}{1 + K_l C_e} \quad (\text{Eqn. 2.23})$$

$$q_e = K_f C_e^{\frac{1}{n}} \quad (\text{Eqn. 2.24})$$

Adsorption of surfactants onto mineral surfaces are quantified using adsorption isotherms. Typically utilised isotherms include the Langmuir (Eqn. 2.23) and Freundlich (Eqn. 2.24) adsorption isotherms. The Langmuir isotherm applies to monolayer adsorption on a homogeneous surface of a finite number of identical site, where maximum monolayer adsorption density, q_e , is a key element of the equation. K_l is the Langmuir adsorption equilibrium constant, q_e is the amount of surfactant adsorbed onto the particle surface and C_e is the equilibrium supernatant concentration. The Freundlich adsorption isotherm is related to adsorption capacity (Where K_f is the Freundlich adsorption equilibrium constant) and adsorption intensity, n , and is derived assuming an exponentially decaying sorption site energy distribution and occurs on heterogeneous surfaces by multilayer adsorption¹³⁶.

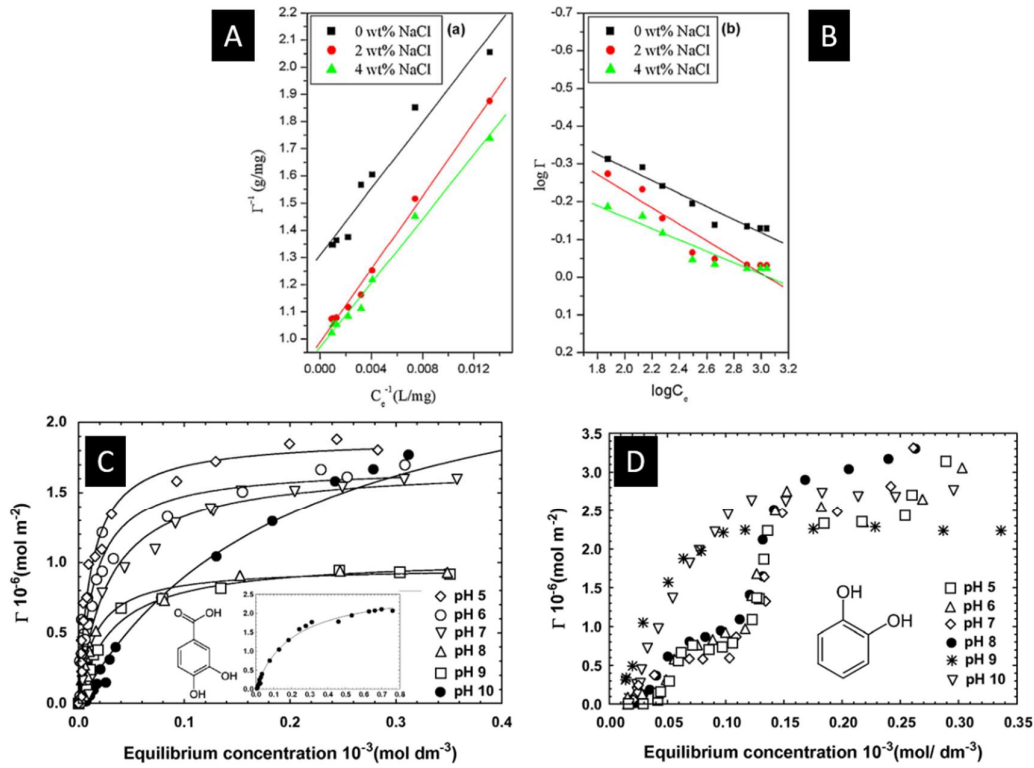


Figure 2.32: Adsorption isotherms of SDS at different NaCl salt concentrations at 303 K: (A) Langmuir equation fitting; (B) Freundlich equation fitting¹³⁷. Adsorption isotherms of (C) 3,4-dihydroxybenzoic acid onto hematite surface at pH 5–10 and 298.15 K. Inset: Adsorption isotherm, Γ_{max} (g_e) vs. equilibrium concentration, of 3,4-DHBA onto hematite surface at pH 10 under above experimental conditions and (D) 1,2-dihydroxybenzene onto hematite surface at pH 5–10 and 298.15 K. NaCl(aq) = 0.05 mM, hematite = 0.5 g, V = 15 ml. Solid lines represent Langmuir adsorption isotherms for A and C and Freundlich adsorption isotherms for B. Langmuir adsorption isotherms could not be applied to D as it displays multilayer adsorption behaviour¹³⁸.

Bera et al.¹³⁷ investigated the adsorption of a cationic (CTAB), anionic (SDS) and non-ionic (tergiol 15-S-7) surfactants onto sand surfaces. The adsorption density was determined differentially using the equilibrium supernatant chemical oxygen demand measurements with and without sand particles after 24 hours of agitation at 303 K. Fig. 2.32A and 2.32B show logarithmically linearised Langmuir and Freundlich adsorption models fit to experimental data respectively. Adsorption of the surfactants onto sand particles proceeded in a monolayer manner and the Langmuir adsorption had the strongest coefficient of determination. As discussed previously in the adsorption isotherm computed by Bai et al.⁸⁰ in Fig. 2.31A, it is possible for bilayers to form on target particulate surfaces which when related to the flotation data in Fig. 2.31B showed detrimental effects for flotation performance with corona of solubilised polar head groups decreasing surface energy. Bilayer adsorption is subject to multiple factor regarding the adsorbing species. For example, a study by Saikia et al.¹³⁸ of the adsorption of 3,4-dihydroxybenzoic acid and 1,2-

dihydroxybenzene onto hematite. The former showed a monolayer surface coverage exhibiting Langmuir adsorption behaviour and the latter displayed bilayer adsorption shown in Figs. 2.32C and 2.32D respectively. The presence of the -COOH group on the 3,4-dihydroxybenzoic acid below pH 9 is responsible for adsorption, but above pH 9 the phenolic acid -OH groups undergo deprotonation mimicking the behaviour of the 1,2-dihydroxybenzene which displayed bilayer adsorption onto the hematite surface due to van der Waals forces and desorption of water in the pH range 5-8. It should be added that amphiphilic molecules such as surfactants or ABCs will form *hemimicelles* structures to reduce free energy by concealing their non-polar hydrophobic tails from dielectric media such as water^{80,139}. Whereas above pH 9, 1,2-dihydroxybenzene undergoes aggressive deprotonation increasing adsorption through electrostatic interactions¹³⁸. Importantly, the adsorption mechanism of collector agents onto Mg(OH)₂ is important as the formation of a bilayer has been shown to be detrimental to flotation performance. Additionally, in the presence of bilayer formation, Langmuir adsorption isotherms have been shown to be inapplicable and multilayer models such as Freundlich adsorption isotherms should be applied.

2.6.3) *Role of particles in foam stabilisation*

A key factor in flotation performance is the stability of the resultant foam forming at the top of the flotation cell, as foam breakages and drainage may result in the loss of recovered particulates back into the bulk suspension. As discussed in Section 2.6.2 as per Eqn. 2.22, increased hydrophobisation of a particulate surface the resultant increase in contact angle makes the particulates more energetically stable when adsorbed to a bubble interface, assuming particle size (no hydrophobic driven agglomeration) and surface tension remains constant. Whilst high contact angles (>90°) improve particle-bubble attachment, high contact angles have been proven to be detrimental to foam stability. As particles with contact angles above 90° are interpreted from the 2D diagram of bubble attachment in Fig. 2.30 as existing with most of their surface area in the air phase, this results in strongly hydrophobic particles opposing bending energies leading to the breakage of foams¹²⁹. This may be a factor as to why Bai et al.⁸⁰ reported that the optimum flotation performance of hematite recovery using SDS occurred at a partial monolayer coverage (see Fig. 2.31A and 2.30B) where hydrophobisation effects were slightly limited improving foam stability. This is unsurprising given that optimum froth stabilising contact angles have been reported to

be in the region of $60-70^\circ$ where particles exist with the majority of their surface area in the bulk liquid phase to aid in sterically prohibiting drainage from the film^{129,140}.

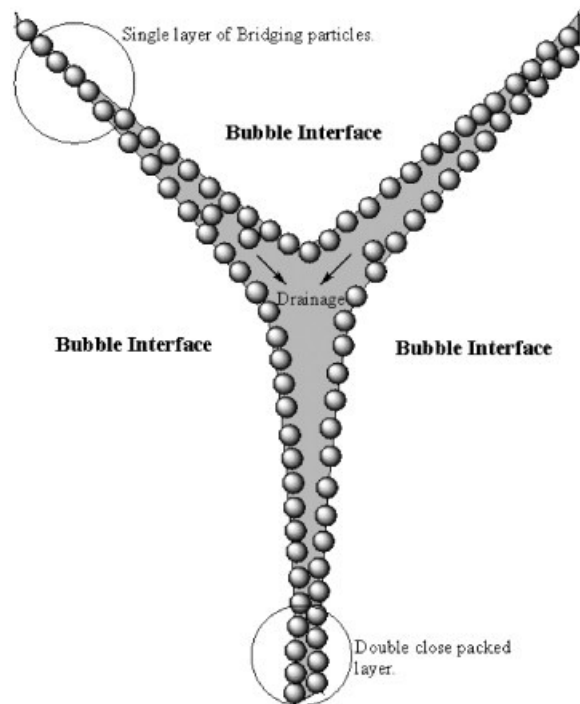


Figure 2.33: Particle stabilised foam¹⁴⁰.

The stability of three-phase foams is a function of many variables. Hunter et al.¹⁴⁰ comprehensively reviewed the role of particle in stabilising foams. The presence of particulates at air-water interfaces have been found to stabilise foams through various mechanisms, including: steric resistance to bubble coalescence, increasing capillary pressure of coalescence and particle-particle interactions. The high concentrated adsorption of fine particulates at the air-water interface have been shown to create a steric barriers preventing/retarding film drainage as shown in Fig. 2.33 where bridging of particles between bubbles (circled and labelled double packed layer in Fig. 2.33) stabilise foams as they dry¹⁴⁰. The shape and state of the particles are important when considering steric barriers, and the aggregated state of $Mg(OH)_2$ structure made up of aggregates of pseudo-hexagonal platelets forming a fused nanocrystallite platelet arrangement could result in hysteresis. Additionally, the irregular shape and tendency to aggregation could result in piercing the film and rupturing the foam¹²⁹. However, there has been evidence to suggest that weakly coagulated particles aid in foam stability due to their polydispersity. The variation particle size allows for more compact monolayer packing on at the air-water

interface preventing film drainage and aggregating particles at the air-water interface have even been found to produce complex chain and meso-structures resisting film drainage.

2.6.4) *Quantifying foam stability: dynamic foam stability index*

A key measurement to quantify foam stability is the gas retention in the foam phase. Stable froths and foams will retain gas to a greater degree than less stable foams which will bleed gas as interfacial films drain and rupture. This phenomena has been linked to determining the optimum aeration conditions for flotation cell banks by Hadler et al.¹⁴¹ who reported that as the fraction of air entering a flotation cell that overflows the cell lip as unburst bubbles peaks a maxima, particle recovery was found to be maximised in a range of industrial flotation cells. Air recovery has been shown to be a reliable, non-intrusive technique that yields valuable information on the behaviour of the overflowing froth. The non-intrusiveness is attractive to the nuclear industry as previously discussed in Section 1.2, visual observation is limited as this results in increased worker radiation dose which is not ALARP⁵. As the lost air from the foam will likely have to undergo monitoring and HEPA filtration to remove aerosolised radionuclides, the recovered air volume in the foam phase could be determined differentially.

$$t_r = \frac{\Delta H_f}{\Delta u} \quad (\text{Eqn. 2.25})$$

A common technique for measuring foam stability is the Bickerman column test which has been performed by a number of authors including Gupta et al.¹⁴², Laskowski and Cho^{69,143}, Hunter et al.¹⁴⁴ as well as Hadler and Cilliers¹⁴⁵. The test consists of an open top fritted glass column and a suspension of particulates and SAMs (collector and or frother) is agitated. Air is the flowed through the bottom of the column at varying air flow rates and the equilibrium height of the resultant foam is recorded. The gas retention time (t_r) is experimentally established from the slope of the linear part of the dependence of the total gas volume in solution and foam, plotted with respect to gas flow rate (for increasing frother or collector concentrations). As the diameter of the Bikerman column is constant, measurements can be reduced to changes in foam height (H_f) and superficial air velocity (u) as shown in Eqn. 2.25. Laskowski and Cho¹⁴³ investigated the effect of the frothers (MIBC, di-ethoxy mono-propoxy hexanol [DEMPH] and DF-1012) on bubble size and foam stability in potash ore flotation systems utilising the Bickerman column test to

determine gas retention of DEMPH initiated foams as shown in Figs. 2.34A and 2.34B in the presence of water and brine.

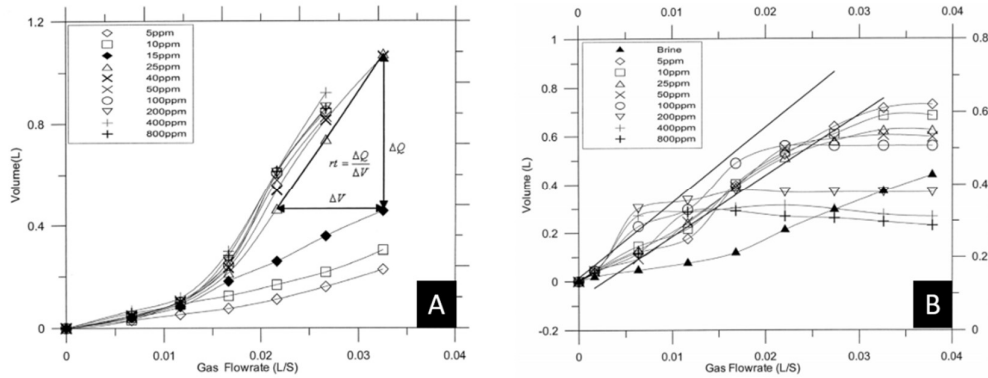


Figure 2.34: A) Effect of DEMPH concentration in A) water and B) brine on gas retention time¹⁴³.

An issue with gas retention alone is that it is a function of concentration, and therefore must be normalised in order to give an effective comparison of surfactant and or frother performance. The dynamic foamability index (*DFI*) allows comparison of collector and frother foamabilities independent of concentration, for a more robust assessment of flotation performance than retention time alone. The *DFI* is obtained from the t_r values as a function of the dosed concentration (C_d) limiting slope, as C_d approaches 0, shown in Eqn. 2.26. Laskowski and Cho¹⁴³ utilised the *DFI* concept to compare the frothers directly independently of concentration. The presence of brine reduced the frother MIBC's ability to produce foams as stable as pure water (see Fig. 2.35A) whereas the frother DEMPH displayed a resistance to brine inhibiting its foamability shown in Fig. 2.35B.

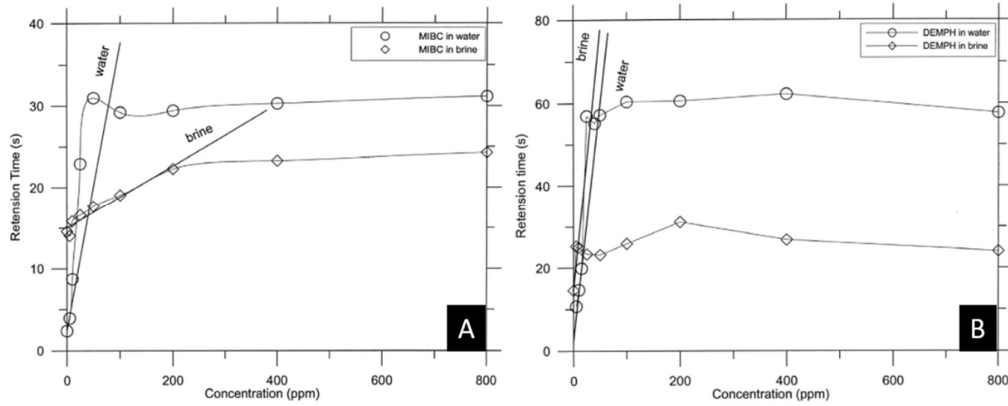


Figure 2.35: Dependence of retention time on A) MIBC and B) DEMPH frother concentration¹⁴³.

The dynamic stability of foams produced by flotation operations is an important factor to compare when selecting appropriate SAMs to float $Mg(OH)_2$ radwaste suspensions and will directly affect water retention in the foam which may decrease dewatering capacities of the process. Additionally, Hadler and Cilliers¹⁴⁵ have shown that adsorption of ballotini particles modified with trimethyltetradecylammonium bromide (TTAB) to the air-water interface resulted in more pronounced increases in gas retention times when compared to TTAB systems alone and this effect increased with increased particle loading in the suspension pulp (see Fig. 2.36). This suggests more effective collectors will produce increasingly more stable foams/froths as a function of greater collection efficiency where particles stabilise foams through the aforementioned steric and capillary pressure mechanisms. This suggests that flotation maybe even more effective at dewatering more concentrated sludges from ponds and silos at Sellafield if the need arises as well as the 2.5 vol.% feed to SPP1.

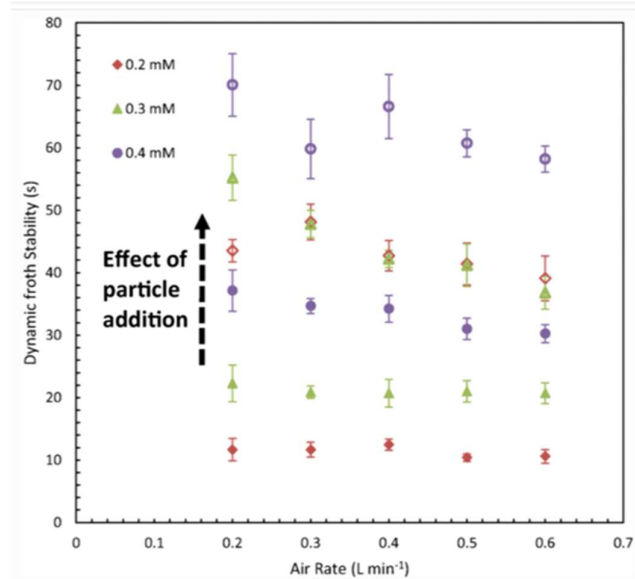


Figure 2.36: Froth gas retention time (s) on the y-axis as a function of air rate and TTAB concentration; solid markers represent two-phase system, hollow markers represent the three-phase system. Note gas retention time is referred to as dynamic froth stability in the work by Hadler and Cilliers¹⁴⁵.

2.6.5) Dewatering efficiencies

As water is retained in the bubble film structure due to steric barriers created by increasing particle loaded foams¹⁴⁵, it is important to understand the dewatering efficiencies of flotation processes, specifically the ratio of recovered particles to entrained water. Prajitno et al.⁷¹ investigated the effect of cationic surfactant Ethylhexadecyldimethylammonium bromide (EHDA-Br) and the concentration of frother MIBC on floating clinoptilolite. Where clinoptilolite is an ion exchange media used at Sellafield to recover radionuclides such as Cs-137 and Sr-90, which is notably the downstream process handling process water decontamination from FGMSP and SPP1. Prajitno et al.⁷¹ used a water reduction ratio as a measure of water remaining in the cell shown in Eqn. 2.26. Where WRR is the water reduction ratio, V_0 is the initial volume of water in the cell and V_e is the remaining volume of fluid in the cell. Where a decreasing WRR indicates increase fluid loss from the cell decreasing the dewatering capacity of the flotation cell. As shown in Fig. 2.37, as the frother MIBC concentration increases, the WRR decreases indicating fluid loss. However, there is a noticeable increase in clinoptilolite recovery with increasing MIBC concentration and fluid loss. There is likely entrainment occurring aiding in additional particulate recovery withing the foam lamella. This is an important consideration when utilising flotation operations with collectors above monolayer coverage. As excess collector will increase the

foaming in the cell which may lead to excessive water loss and a mistaken increase in particulate recovery. Where the increased particulate recovery is due to entrainment rather than hydrophobic attachment to an air-water interface. Therefore, collection efficiency should be measured as a ratio of particles to fluid recovered to include dewatering capacity, which can in turn be related to the dosed collector concentration to determine optimum surface coverage and by extension optimum collector-particle ratios for low water recovery of radwaste particulates in SPP1.

$$WRR = \frac{V_0}{V_0 - V_e} \quad (\text{Eqn. 2.26})$$

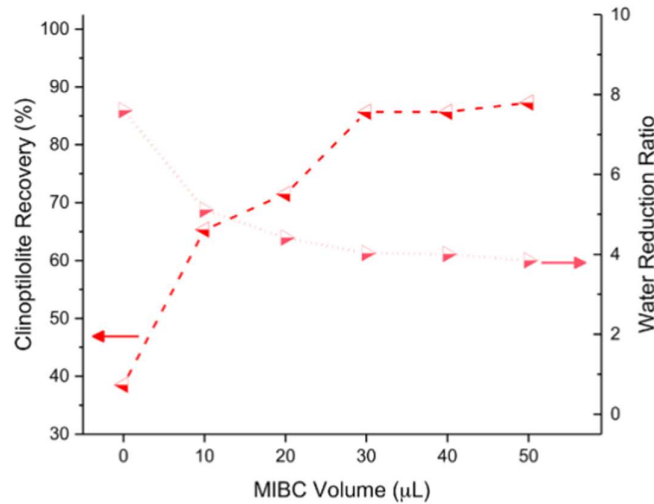


Figure 2.37: The effect of different added MIBC volumes on flotation recovery of clinoptilolite (LHS) and associated water reduction ratio (RHS) with fixed 0.5 mM CPC concentration. Connecting dashed line is to guide the eye for clinoptilolite recovery and dotted line is to guide the eye for water reduction ratio⁷¹.

2.7) Polymers as collectors for flotation

2.7.1) Hydrodynamic considerations and aggregation advantages

As discussed in Section 2.6.1, Gonjito et al.⁸³ modelled the hydrodynamic limits of flotation. Previously the role of contact angle was discussed in depth. However, hydrodynamics have a vital role in flotation, where fine particles lack the inertia to overcome the slipstreams generated by rising bubbles and larger particles have high bubble detachment energies. A gap in the literature (to the authors knowledge) is the application of these bubble detachment energy models to polymerically flocculated particulates, as the

fractal structure of these flocs results in them having an invariable scaling dilatational symmetry and lower density with increasing size (Eqn. 2.5, Section 2.3.2). This lower material density has implications for the largest floatable floc size being greater than non-porous particles of equivalent contact angles. However, for fine particles, polymeric flocculants whose hydrophobicity can be triggered via pH or temperature switches (such as Chitosan⁸⁹ or PNIPAM^{87,88,146} respectively) have been shown to improve the collection of fine particulates (see Fig. 2.38). This fines target agglomeration and recovery is of particular importance to the nuclear waste management industry in the UK as americium and plutonium association with $Mg(OH)_2$ based colloidal corrosion products due to their high surface-area to volume ratio⁷ (see Section 2.1).

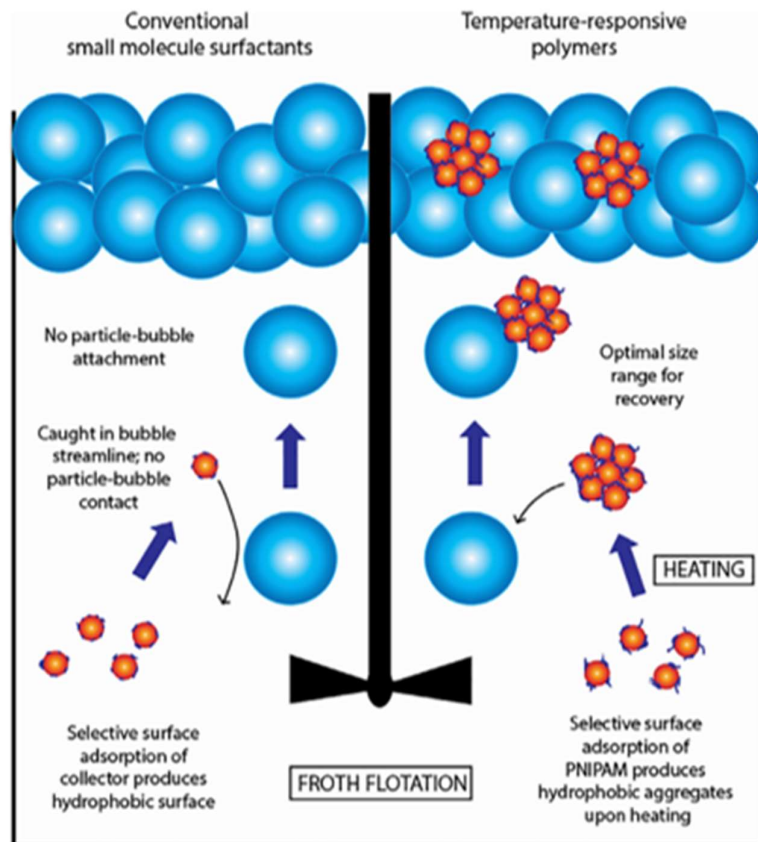


Figure 2.38: The temperature-responsive flocculation-flotation mechanism of PNIPAM, as a polymer with LCST behaviour (on the right), compared to conventional collectors (on the left). The thermo-responsive nature of the polymer is used to produce particle aggregates within the optimal flotation range, improving the recovery⁸⁴.

The application of these temperature-sensitive polymers to flocculate and float various minerals was reviewed in depth by Ng et al.⁸⁴. Forbes et al.⁸⁸ investigated the application of 15 mol% anionic and cationic statistical copolymers of PNIPAM with poly(acrylic acid)

and poly(dimethylamino ethyl quaternary chloride) respectively to selectively float a mixture of anionic quartz and cationic alumina. The resultant temperature-sensitive copolymers displayed LCSTs of 32°C and a solids to polymer ratio of 1000 g.t⁻¹ was used. The changes in zeta-potential with application of the cationic and anionic copolymers were first investigated with a background electrolyte solution of 10⁻² M KCl at 50 °C. Counterion affinity was observed (see Fig. 2.39A) where cationic poly(dimethylamino ethyl arylate quaternary chloride)-*co*-PNIPAM adsorbed almost exclusively onto quartz resulting in a reduction in zeta-potential from ~43 mV to ~-27mV with negligible effect on alumina. In the presence of anionic poly(acrylic acid)-*co*-PNIPAM quartz zeta-potential remained mostly unaffected (though a small increase in anionic surface charge was observed, and the cationic alumina zeta-potential was reduced to within error of point zero charge conditions though marginally reversed. When used to float mixtures of alumina and quartz, both copolymers showed selectivity characteristics as a function of their adsorption affinity. With the cationic copolymer floating ~65% of the quartz, and the anionic copolymer floating ~79% of the alumina. Though both systems noted entrainment of up to ~20% gangue material shown in Fig. 2.39B.

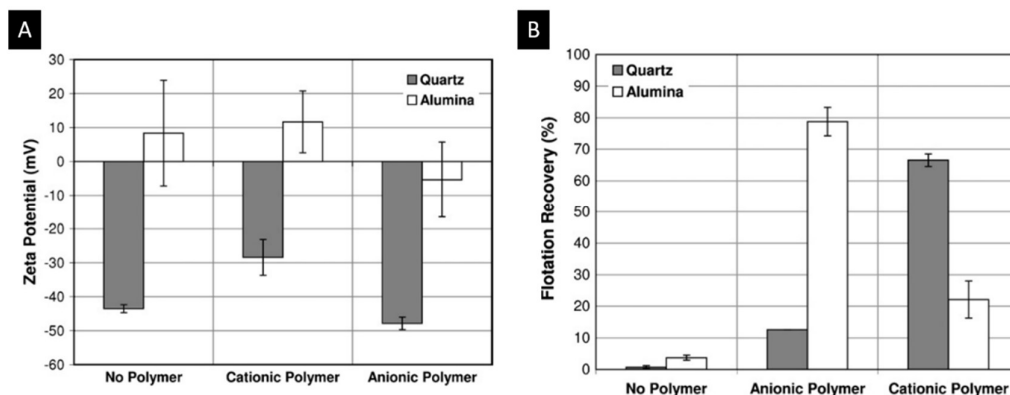


Figure 2.39: A) Zeta potential of quartz and alumina particles at 50 °C in 10⁻² KCl solution at pH 8, in the presence and absence of 400 g.t⁻¹ of different types of PNIPAM. B) Flotation recovery of quartz and alumina particles after 5 min of flotation at 50 °C in 10⁻² M KCl solution at pH 8, in the presence and absence of 1000 g.t⁻¹ of different types of PNIPAM⁸⁸.

Attempts to probe polymer-aggregated hydrodynamics have been made by Ng et al.⁸⁷ who investigated the effect of shear and temperature on the flotation behaviour of a xanthate-functional temperature-responsive polymer, P(NIPAM-*co*-ethyl xanthate methacrylate (EXMA)), in the recovery of copper sulphide from a natural mixed-mineral ore where the xanthate polymer contains only 5% of the xanthate moiety. The temperature-sensitive

copolymer was benchmarked against commercial collector potassium amyl xanthate (PAX). The poly(NIPAM)-*co*-poly(EXMA) outperformed the PAX collector in high shear (1000 s^{-1}) mechanical flotation cells and performed on par with PAX in low shear (200 s^{-1}) column flotation cells. Particles were segregated into coarse, mids and fines. The enhanced shear in the mechanical cell resulted in fragmentation of larger flocs and was shown to improve the recovery of fines when compared to the low shear cell, though flocculation was observed to be a greater degree in the low shear cell due to less fragmentation of larger flocs. Indicating that cell shear conditions are important for deployment at Sellafield, where inadequate agitation may result in poor flocculation of fine $\text{Mg}(\text{OH})_2$ which has been identified as incorporating alpha emitting radionuclides⁷.

2.7.2) *Minerals vs nuclear*

A key difference between the requirements of the minerals industry, which has previously been the most driven vehicle for flocculated-flotation research, and the nuclear waste management industry is the focus on selectivity as a primary metric for successful deployment. Whereas the nuclear waste management aims to utilise this technology as a solid-liquid separation technique to dewater radwaste sludges. As discussed in depth in Section 2.2.3, statistical copolymers of PNIPAM hydrophobise above their lower critical solution temperature (LCST). However these statistical PNIPAM copolymers require adsorption to the target particle initially otherwise they form globules which indicated very little adsorption to particle surfaces. When these PNIPAM copolymers were synthesised as block copolymers they formed micelles above their LCST. But due to their corona of ionic block groups still adsorbed to surfaces even if applied to suspensions above the LCST without prior adsorption below the LCST. Whilst there has been progress in reducing the LCST of temperature-sensitive polymers by increasing the ratio of hydrophobic groups or decreasing hydrophilic moiety fraction^{84,147}, for nuclear industry regulatory appraisal the removal of the need for these temperature switches altogether is preferable.

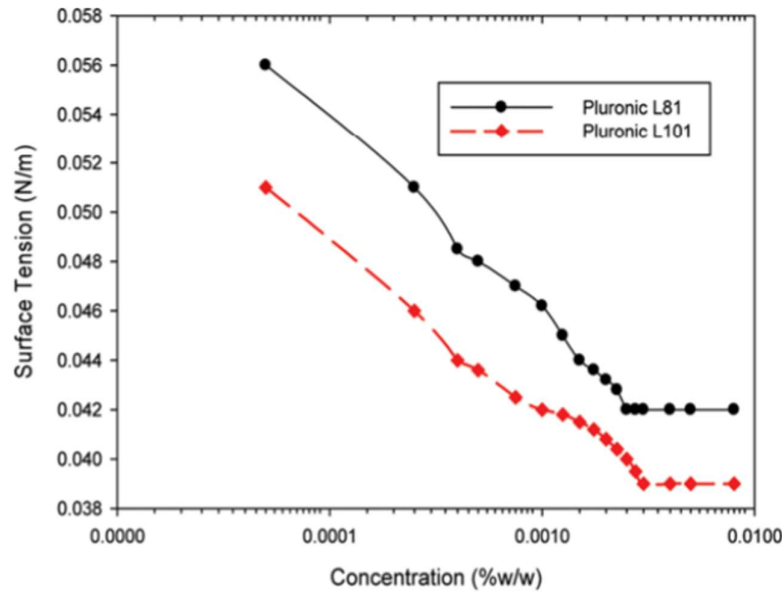


Figure 2.40: Surface tension as a function of concentration of Pluronic L81 and L101¹⁴⁸.

The presence of block copolymers utilised as flotation aids in literature is sparse. In fact to the authors knowledge, non-temperature-responsive block copolymers have only been utilised for the flotation of coal¹⁴⁸ and deinking of paper¹⁴⁹ in the form of a tri-block copolymers of poly(ethylene oxide)-*b*-poly(propylene oxide)-*b*-poly(ethylene oxide) known commercially as Pluronic polymers. Though unlike some amphiphilic block copolymers discussed in Section 2.5.2, the tri-block polymers utilised by Ofori et al.¹⁴⁸ significantly reduced the surface tension of water (see Fig. 2.40), which as discussed in Section 2.6.5, may lead to excessive water loss. Therefore, given the macrosurfactant and flocculation properties of amphiphilic diblock copolymers it is reasonable to investigate their utilisation in both flotation and flocculation operation. As highlighted by the investigation by Ng et al.⁸⁷ into the effects of shear on dual collector-flocculation aids such as poly(NIPAM)-*co*-poly(EXMA), the remaining suspension sedimentation in the cell post flotation should be examined, as it is known that a reduction in volume fraction in hindered settling improves sedimentation dynamics¹⁶ and flotation may be primarily hydrodynamically limited. A combination of both flotation to target fine material at low water recovery cost, then subsequent sedimentation of lower solids content, coarser particle size distribution suspensions may provide optimum dewatering capacities of Mg(OH)₂ based radwaste suspensions.

Part 2
Original research

Chapter 3:

Structure and sedimentation characterisation of sheared $\text{Mg}(\text{OH})_2$ with anionic polymers

3.1) Introduction

The application of polyelectrolyte based settling agents in solid-liquid separation operations has received considerable research interest^{17–20,32,48,60,150–152}. From applications in the minerals industry to water treatment and nuclear decommissioning, the reliability of suspension clarification with these additives is recognised as a low cost, simple method for optimizing turbidity reduction, driving sedimentation throughput and reducing the separation process residence time^{153,154}. Designing optimum gravity driven separation processes involves an in-depth understanding of the sedimentation dynamics of the system in question, particularly the role that floc structure plays in hindered settling regimes, and ultimately, which size of flocculated aggregates (or ‘flocs’) are most influential for determining the interfacial settling rate of these suspensions.

For example, the relationship between suspension concentration and Stokes settling rate, as originally suggested by Richardson and Zaki⁴⁰, is often determined from the 50th percentile cumulative (d_{50}) aggregate size of the floc population. While this is a reasonable assumption if there are negligible interactions between flocs as they settle, it is known that larger flocs may encompass smaller ones into their structure as they sediment, which is an effect observed in sweeping flocculation systems^{155–157}. Greater influence of larger flocs on sedimentation has important implications on the nature of predictive equations, as they generally require only a single number to represent aggregate populations. Given the impact of this value in settling rate prediction, it is still largely unclear for many systems which average diameter is the most appropriate value to use in settling rate estimations (for example, 50th or 90th percentiles). Additionally, the competing effects of fractal dimension versus floc diameter on zonal settling rates requires further attention, as while denser flocs with lower effective floc volume fractions theoretically should sediment at a greater rate, literature shows that floc size is often the dominating factor^{17,18}.

It has also been suggested that fractal aggregates, whilst occupying a greater volume than non-fractal equivalents (due to more open structures of lower fractal dimension) may

actually produce a vector for fluid flow through their porous microstructure reducing boundary layer separation and drag^{16,18,45,54}. Furthermore, it has been found experimentally that microflow channels exist large enough to encompass smaller agglomerates resulting in aggregate densification¹⁶. Additionally, given the fractal nature of flocs, the effects of the structural complexities and resultant floc density from the number and spatial distribution of particles must also be accounted for in such predictive equations. Developments in techniques such as static light scattering^{48,53,62,63} have allowed for quantification of such floc characteristics, so that fractal dimension may be mathematically accounted for in predictive equations. Whilst these low volume *ex situ* sampling techniques for determining fractal dimension are advantageous for industries where large volume sampling is uneconomic or hazardous, complete removal of risk rather than mitigation is preferable. Thus, there is increasing industrial interest in the development of online or *in situ* monitoring techniques, such as focused beam reflectance meters (FBRM), to inform on floc structure and size for prediction of zonal settling rates, reducing risk to the workforce and aiding process optimisation.

Polymeric flocculation of suspended particles using charged polyelectrolytes, firstly requires the adsorption of the polymer onto the particle surface, where the mechanism is dependent on the overall charge of the polymer functional groups relative to the particle surface. In cases of like-like charge, the adsorption process is often hydrogen bonding driven, as the particle surface repels the like charged functional groups on the polymer flocculant. These interactions lead to conformational extension of the polymer chains into the aqueous medium, resulting in a number of loops and tails and the formation of large and open structures in bridging flocculation utilising polymers with molecular weights in the order of 10^6 g.mol^{-1} ¹⁷. For opposing charged particle-polymer systems, greater charge density polymers of similar chain length (with identical functionality) are expected to produce smaller, denser flocs due to their comparatively faster polymer-surface conformation kinetics with a greater fractal dimension than lower charge density counterparts¹⁹. Additionally, an increased charge density results in greater charge neutralisation, thus reducing particle-particle electrostatic repulsions and lowering adsorption free energy, which also allows denser flocs to form, as documented in previous literature^{17,19,34,158}. When considering solely the implications of fractal modified Stokes equations, higher charge density polymers are in theory expected to also dominate in

hindered settling systems, due to the weighting of density and neglect of particle-particle interactions in most sedimentation models¹⁸.

For this study, the influence of bridging polymers of varying charge density (30% and 40%) on the flocculation size, structure and sedimentation of fine magnesium hydroxide ($\text{Mg}(\text{OH})_2$) is investigated, based on their successful use in previous work on mineral systems^{17,18,22,28,38,49,60,89}. While the effect of polymer settling aids on the sedimentation dynamics of $\text{Mg}(\text{OH})_2$ suspensions have received relatively little attention from researchers, it is an area of significant interest to the nuclear industry. In particular, large amounts of magnesium hydroxide based sludge wastes are produced from the corrosion of magnesium alloy fuel cladding, which have been stored outdoors in water cooled facilities, such as with the First Generation Magnox Storage pond, at Sellafield in the U.K.^{4,8,25,159}. This corrosion product is required to be gravimetrically separated for ultimate containment⁷. Given the expected slight cationic properties of this material's surface^{16,24}, anionic polymer settling aids are likely compatible candidates for optimising dewatering operations being undertaken⁶.

To understand the polymer flocculation efficiency, several complimentary techniques are used within to fully confirm size, morphology and structural properties of the aggregates. Floc growth and shear breakdown are measured *in situ*, using focused beam reflectance measurement (FBRM) a technique utilised to investigate the kinetics of such systems in other literature⁵⁵⁻⁶⁰. Static light scattering (SLS) is also used to confirm floc size and structural properties (e.g. fractal dimension) with further direct comparisons to optical microscope measurements, which have been previously applied to investigate the 2D properties of flocs in large statistical populations ($> 20,000$)¹⁶⁰⁻¹⁶³. Complimentary cryogenic scanning electron microscopy (Cryo-SEM) is additionally performed, a technique which has allowed for an insight in polymer induced floc microstructures and internal porosity^{35,41,164}. Importantly, the sedimentation performance of flocculated systems for various polymer doses is then measured and coupled with the obtained structural data, to evaluate the performance of settling rate predictions, utilising a fractal modified Richardson-Zaki (FMRZ) approach. Here, measured fractal dimensions are used to estimate overall floc density and volume fractions from non-flocculated $\text{Mg}(\text{OH})_2$ particle density and volume fractions for use in a fractal modified Richardson-Zaki model, with calculated sedimentation rates compared to those measured using d_{50} and d_{90} particulate

sizes. Critically, a detailed sensitivity analysis of the settling model at a fixed $\text{Mg}(\text{OH})_2$ concentration is also performed, which comprehensively investigates the relative influence of particle size and fractal dimension on overall predicted sedimentation rates.

3.2) Theory

3.2.1) Fractal dimension

The structural information for aggregate flocs (which are an agglomeration of two or more primary particles) were established using SLS. In this section, the mathematical procedure to determine these values is discussed and variables defined (see also Nomenclature section). The average volume fraction of solid particles within a floc decreases as the floc grows according to Bushell et al.⁴⁴, where the number of particles within a floc can be calculated using Eqn. 3.1.

$$N = \psi \left(\frac{D_f}{D_p} \right)^{d_f} \quad (\text{Eqn. 3.1})$$

Here, N is the number of particles in an aggregate, ψ is the structure prefactor (a proportionality constant of order unity) which is suggested to be a function of the packing factor and the ratio of the shape factors of the aggregate and the primary particles^{63,117}. D_f is the diameter of the aggregate or floc and D_p is the diameter of the primary particles (where $D_f/D_p > 1$), while d_f is the fractal dimension. It is important to note that the D_f and D_p values are determined from SLS data, which are calculated from the reciprocal microns of the wave scatter vector to determine floc structure properties (see Section 3.3.3) and are not representative diameters of polydisperse systems. In particular, D_f is referred to in this work as the ‘minimum repeating floc size’, which represents the unit cell floc structure assumed to be uniform across all flocs in the polydisperse system independent of size. Values of the prefactor, ψ , have been proposed to depend on the type of aggregation method¹²⁰, such as the relationship between ψ and d_f for $1.5 \leq d_f \leq 2.75$, as shown in Eqn. 3.2¹²¹:

$$\psi = 0.414d_f - 0.211 \quad (\text{Eqn. 3.2})$$

The floc density, ρ_f , can be calculated from the average volume fraction of the particles in the floc, Φ_s , the average volume fraction of water in the floc being the porosity, $1 - \Phi_s$, and the solid and liquid densities (ρ_p and ρ_w) as per Eqn. 3.3⁴⁴:

$$\rho_f = \Phi_s \rho_p + (1 - \Phi_s) \rho_w \quad (\text{Eqn. 3.3})$$

The density of the floc, ρ_f , can then be evaluated in terms of particle number per floc and volume of components as displayed in Eqn. 3.4:

$$\rho_f = \frac{(NV_p \rho_p) + (V_f - NV_p) \rho_w}{V_f} \quad (\text{Eqn. 3.4})$$

Where V_p is the volume of the primary particles (thus NV_p is the total volume of solid components in a floc) and V_f is the volume of the minimum repeating floc diameter D_f , including the internal trapped liquid¹²⁰.

3.2.2) Modified Stokes law

Floc settling rates for suspensions of intermediate concentration have been widely investigated^{16,29,165-167}. As particles settle, they displace fluid below them in a batch settling regime, where this fluid displacement may hinder settling in the system. Thus, the Stokes law of terminal settling velocity may be modified by Eqn. 3.5:

$$U_i = U_T \times f_s \quad (\text{Eqn. 3.5})$$

The terminal velocity of an individual particulate, U_T , is calculated using Stokes law which determines the terminal settling velocity of a singular particle of diameter, D_m . Whereas the velocity of the sediment interface (or zonal settling front) in hindered settling systems, U_i , is determined as a product of a dimensionless function proportional to the permeability of the particle network suspended in the medium (referred to here as the dimensionless permeability number, f_s), and the individual particulate sedimentation velocity under terminal conditions, U_T , as displayed in Eqn. 3.6, where additionally 'g' is acceleration due to gravity and μ_w is the viscosity of water.

$$U_i = \frac{g(\rho_p - \rho_w)D_m^2}{18\mu_w} f_s \quad (\text{Eqn. 3.6})$$

Adachi and Tanaka¹²³ and Adelman et al.¹²⁴ used a modified terminal settling rate equation that incorporated the fractal nature of the settling flocs shown in Eqn. 3.7:

$$U_i = \frac{g(\rho_p - \rho_w)\overline{D_f^2}}{18\mu_w} \left(\frac{D_f}{D_p}\right)^{d_f-3} f_s^* \quad (\text{Eqn. 3.7})$$

Where $\overline{D_f}$ represents the value of a floc diameter selected to represent the polydisperse floc population (i.e. d_{50} or d_{90}) which is measured by SLS, FBRM and optical microscopy and determined from their respective particle size distributions (PSDs). f_s^* is the fractal modified dimensionless permeability number (see explanation below). Richardson and Zaki⁴⁰ suggested the following relationship in Eqn. 3.8, for multiple spherical particles settling in laminar flow conditions, stating that the traditional particle dimensionless permeability number of the suspended medium, f_s , is a function of the particulate volume fraction and an exponent, which is traditionally also a function of Reynolds number^{16,125} and normally taken as equal to 4.65 in laminar conditions.

$$f_s = (1 - \phi_p)^{4.65} \quad (\text{Eqn. 3.8})$$

Here ϕ_p is the volume fraction of the settling particle species. While originally determined for discrete objects, the hindered settling model has been expanded, as originally described by Michaels and Bolger¹²⁶ and a number of proceeding authors^{16,18,49,168} to account for the effective fractal volume fraction of aggregate flocs, with respect to the dispersed particles. This modification is given Eqn. 3.9, where ϕ_f is the effective volume fraction of the aggregate floc.

$$\phi_f = \phi_p \left(\frac{D_f}{D_p}\right)^{3-d_f} \quad (\text{Eqn. 3.9})$$

Finally, Eqns. 3.7- 3.9 can be combined (substituting ϕ_f for ϕ_p to derive the fractal modified dimensionless permeability number f_s^*) giving an overall Fractal Modified Richardson-

Zaki model (referred to as the FMRZ model from hereon), as used by Heath et al.¹⁸ and Hunter et al.²², in Eqn. 3.10:

$$U_i = \frac{g(\rho_p - \rho_w)\overline{D_f^2}}{18\mu_w} \left(\frac{D_f}{D_p}\right)^{d_f-3} \left(1 - \phi_p \left(\frac{D_f}{D_p}\right)^{3-d_f}\right)^{4.65} \quad (\text{Eqn. 3.10})$$

3.3) Materials and methodology

3.3.1) Materials

Versamag Mg(OH)₂ (Martin Marietta, US) was used for all experiments. Versamag is a fine, white precipitated powder with a solubility of 6.9 mg.l⁻¹ at pH 10.1 in water¹⁶⁹. Initial characterization of the dry and suspended Mg(OH)₂ was completed to understand the non-flocculated size and morphology. Detailed methodology is provided within Appendix A including a scanning electron micrograph of the dry Mg(OH)₂ and energy dispersive X-ray (EDX) analysis of Mg(OH)₂ in Appendix Figs. A1 and A2 respectively. The 50th percentile cumulative particle size, zeta potential, Brunauer–Emmett–Teller (BET) surface area, bulk suspension pH and average fractal dimension (see SLS data in Appendix Fig. A3) are provided in Table 3.1. It is noted that the high equilibrium pH is due to the self-buffering nature of magnesium hydroxide because of its partial solubility. The powder is present as particles of fused nanocrystallite platelets, as described previously¹⁶ which gives rise to the large relative surface area in terms of that expected from spherical equivalent estimations¹⁷⁰. Thus, there are many potential interaction sites with the charged anionic polymers for a given volume fraction, although the low magnitude of the zeta potential may reduce the interaction strength. A fractal dimension of 1.97 suggests that the raw Mg(OH)₂ aggregate via a ballistic cluster-cluster aggregation mechanism¹¹⁷.

Table 3.1: Physical characteristics of Mg(OH)₂ suspensions; 10th, 50th and 90th cumulative percentile particle diameters (*d*₁₀, *d*₅₀, *d*₉₀), zeta potential, surface area and equilibrium pH.

<i>d</i> ₁₀ (μm)	<i>d</i> ₅₀ (μm)	<i>d</i> ₉₀ (μm)	ζ -Potential (mV)	BET Surface Area (m ² g ⁻¹)	pH	Fractal dimension [<i>d</i> _f]
~0.85	~2.5	~6.4	~12	~8	~10.1	1.97

The polymers used in the study were water soluble anionic polyacrylamide-poly(acrylic acid) copolymers, AN934SH and AN945SH (SNF® Ltd) of similar molecular weight (approximately 1.4×10^6 g.mol⁻¹, as provided by supplier) with charge group densities of 30% and 40% respectively. 1 g of the powders provided were dissolved in 1 litre deionised water batches to produce stock polymer solutions of 1000 ppm that could be sampled and diluted accordingly. In this work, the polymers AN934SH and AN945SH will be referred to as '30%σ' and '40%σ' respectively, as a reference to their charge density.

3.3.2) *Production of flocculated particle suspensions*

Two suspension-polymer systems were characterised using various analytical techniques, where the Mg(OH)₂ particle concentration was set at 2.5 vol.% in all cases, to reflect the typical particle loading of sludge transfers from legacy nuclear waste spent fuel ponds. Additionally previous investigation of Mg(OH)₂ settling by Johnson et al.¹⁶ have shown Mg(OH)₂ gel points ($5.4 \pm 1.6\%$ v/v) to be greater than the solids concentration used in this work providing an initial linear settling profile^{6,22}. Added 30%σ and 40%σ polymer dosages were varied, ranging from 5 ppm to 20 ppm (mg of polymer per litre of suspension) as these dosages are consistent with much literature on the flocculation of minerals using similar charge density polymers^{17,18,60}. In particular, the same polymers have been used successfully to flocculate calcium carbonate suspensions²², which have similar size distributions and surface charge¹⁷⁰. Flocculated suspensions were prepared in a 1 litre reactor vessel 25 cm in diameter with four baffles and mixed using a four-blade axial flow impeller of 50 mm diameter, and 60° pitch, which was located 2 cm from the base of the reactor vessel. Impeller rotation rate was at 300 rpm, as this was determined to be a sufficient agitation rate to keep flocs suspended and prevent sedimentation, while reducing shear degradation experienced with higher mixing rates. The required polymer was then added in 5 ml aliquots via a calibrated micropipette over a period of no more than 10 seconds at the centre of the suspension, to ensure an even distribution throughout the system.

For determination of reactor vessel residence time, a study of the *in situ* floc growth kinetics was conducted using a Lasentec® Focused Beam Reflectance Measurement (FBRM) model PI-14/206 instrument (Mettler-Toledo) in macro mode. The reactor was set-up with the FBRM probe mounted at a 45° angle to the impeller shaft and 10 cm from the reactor vessel base within the mixing zone, to ensure representative flow of suspended particles

past the measurement window¹⁷¹. A schematic of the mixing reactor with inserted FBRM is given within the appendix (Appendix Fig. A4). The chord length distribution (CLD) of the system was monitored by taking measurements every 5 seconds for 1 hour, and subsequently processed to produce a number percentage based d_{50} chord length with time. Chord length number distributions were then computationally translated to volume percentage spherical equivalent diameters, assuming floc sphericity, as outlined by Rhodes²¹ similar to techniques used by Li and Wilkinson¹⁷². For a number based cumulative frequency distribution as function of floc diameter, F_N , and corresponding frequency distribution f_N (or $\frac{dF_N}{dD_f}$), conversion to a volume based cumulative frequency distribution (F_V) can be computed by the relationship suggested by Rhodes²¹ shown in Eqn. 3.11. Therefore, the cumulative volume based distribution of flocs obtained from FBRM analysis can be determined from the number based distribution using Eqn. 3.11²¹. These data were then used to determine a suitable reactor residence time to produce stable flocs for sedimentation performance and structural characterisation.

$$F_V = \frac{\int_0^{\bar{D}_f} \bar{D}_f^3 f_N d\bar{D}_f}{\int_0^{\infty} \bar{D}_f^3 f_N d\bar{D}_f} \quad (\text{Eqn. 3.11})$$

3.3.3) Size and structural characterization

Static light scattering (SLS) was used to measure both the size distributions of the flocculated suspensions and determine their fractal dimension. Here, 1 litre suspensions of $\text{Mg}(\text{OH})_2$ were flocculated with 20 ppm of 30% σ and 40% σ polymer for 1000 seconds, as described in Section 3.3.2. The suspension was then transferred to a 1 l measuring cylinder and inverted 5 times to meet the shear conditions in the sedimentation tests (detailed below). A 5 ml aliquot was then drawn from the measuring cylinder and added to a Mastersizer 2000E (Malvern Panalytical Ltd) using a Hydro 2000SM aqueous dispersion cell (external dimensions of 140 × 175 × 390 mm and sample volumes between 50 - 120 ml). The dispersion unit was prefilled with 120 ml of deionized water dosed with a polymer solution background, providing a polymer concentration gradient to prevent desorption of polymer from the particle surface. Importantly, the unit was sheared at 900 rpm to ensure consistent flow of suspensions through the vertical optical window and to prevent particle deposition, meaning that there was some potential for additional shear degradation of the generated flocs. Over the initial measurement time, this degradation would be most likely

attributed to floc breakdown, while densification may also occur over longer timescales¹¹⁵. To help understand these changes, additional measurements of average floc diameter and fractal dimension were taken for the flocculated suspensions over 300 s (data averaged in 30 s bins). Also, it is noted that whilst SLS has a natural bias to oversize particulates, the observed influence of shear on floc diameter is significant enough that the bias is likely negligible¹¹⁵. Floc size distribution data were generated from the Mastersizer 2000E as Mie theory based SLS, using a 683 nm He-Ne laser via Eqn. 3.12. For each experiment, the scattering intensity is a function of the magnitude of the scattering wave vector, Q , a reciprocal of the particle size, where n is the refractive index, λ is the wavelength of the incident light in vacuo and θ is the scatter angle.

$$Q = \frac{4\pi n}{\lambda} \sin(\theta/2) \quad (\text{Eqn. 3.12})$$

For determination of the fractal dimension, a particle that satisfies the Rayleigh-Gans-Debye criteria⁴⁸, the scattering intensity $I(Q)$ is given by Eqn. 3.13:

$$I(Q) = kP(Q)S(Q) \quad (\text{Eqn. 3.13})$$

Where k is the scattering constant, $P(Q)$ is the single particle form factor and is related to the shape of the primary particle, and $S(Q)$ is the interparticle structure factor which describes the interference proposed by the primary particles within the aggregate. For a detailed analysis of light scattering theory within aggregates, see Sorensen⁶³. Therefore, the fractal dimension of the flocs can be determined by plotting $\log I(Q)$ with respect to $\log Q$ ⁶³ as per the following proportionality in Eqn. 3.14⁵³.

$$I(Q) \propto S(Q) \propto Q^{-d_f} \quad (\text{Eqn. 3.14})$$

As noted, there was some potential for additional shear degradation (breakage and densification) of the generated flocs^{19,114}. Therefore, an initial investigation of floc degradation rate was undertaken, observing average floc size and changes in fractal dimension within the Mastersizer dispersion cell over 9000 seconds to assess the impact of densification in the presence of shear. To reduce the effect of floc breakdown on skewing the d_{50} and d_{90} average floc size producing additional noise in the data, one measurement

was taken for multiple aliquots of the flocculated suspension, measuring the first recorded floc size after the induction period and averaged, rather than taking multiple measurements of the same sample which would progressively undergo shear, reducing floc size over the measurement period. Fractal data were obtained over a $\log(Q)$ range of $-1.84 \mu\text{m}^{-1}$ to $0.96 \mu\text{m}^{-1}$ corresponding to sizes of $69.2 \mu\text{m}$ to $0.11 \mu\text{m}$ respectively. The fractal dimension was determined by linear fitting optimised for the greatest coefficient of determination (R^2) to determine the boundaries of the linear region corresponding to D_f and D_p values, where the gradient is the fractal dimension. As fractal structures are assumed self-similar, this scaling approach from the average smallest repeating floc structure is assumed to be consistent across the floc population⁶³.

Visual microscopy was also utilised to confirm the size and morphology of aggregates produced from suspensions dosed with 20 ppm polymer concentration, using a Morphologi G3 (Malvern Panalytical Ltd.) automated single element microscope. Floc samples were prepared in the same manner as described above, whereupon samples were placed onto 4 microscope slides and analysed optically with 3 repeats. The number of flocs analysed ranged between 40,000 and 60,000 for each system to gain statistical significance. Data were analysed both in terms of circular equivalent diameters and aspect ratio.

The morphology of aggregate flocs was also confirmed using cryogenic scanning electron microscopy (Cryo-SEM). Again, samples were prepared in the same manner as described, before being sampled. Flocculated suspensions were then cryogenically frozen using liquid nitrogen, then sublimed for 10 minutes to remove the frozen liquid and reveal the floc structures. The cryogenically frozen samples were then coated in iridium to reduce charging effects and analysed using an EVO MA15: variable pressure W SEM (Carl Zeiss AG).

It is finally noted that zeta potential measurement using electrophoresis were also attempted to understand the change in surface charge with polymer adsorption. However, the polymer flocculation led to sedimentation of flocs in the test cell resulting in poor correlation function fittings. Additionally, it was not deemed critical analysis for this current study, due to the focus on the overall influence of floc structures on sedimentation, rather than the surface chemistry changes from polymer-particle interactions.

3.3.4) Gravimetric sedimentation performance

Visual observation of suspension-supernatant boundary level change with time was used to measure the influence of polymer concentration on hindered settling rates. Again, 2.5 vol.% $Mg(OH)_2$ suspensions were prepared in the agitated 1 litre baffled reactor, as described in Section 3.3.2, with variable concentrations of the two polymers (5 – 20 ppm). Flocculated suspensions were then transferred to 1 litre measuring cylinders of 61 mm diameter. The cylinders were inverted 5 times to evenly re-suspend flocs and the interfacial height was measured over time. The turbidity of the resultant supernatant was taken after 30 minutes of settling, at 5 cm below the air water interface, using a TN-100 turbidity meter (Eutech Instruments).

3.4) Results and discussion

3.4.1) Size and structure characterization of flocculated $Mg(OH)_2$

Fig. 3.1 A(i) and A(ii) show the *in situ* floc growth kinetics of $Mg(OH)_2$, with addition of 5, 10 and 20 ppm 30% σ and 40% σ polymers respectively, where the converted FBRM volume based 50th percentile cumulative particle size (d_{50}) is presented over time. The data display several distinct flocculation events; being initial floc growth upon addition of polymer, a floc size maxima size at intermediate times, which then leads to a dominant floc breakage process under shear and dynamic floc growth-breakage equilibrium, as acknowledged by previous literature⁵⁵⁻⁶⁰. For both polymer suspensions, 1000 s was selected as the reactor residence time to be used for all further testing, being a time beyond the floc maxima, where the aggregate d_{50} were relatively stable. While such periods of shear are greater than would normally be employed in water treatment operations, for example, the 1000 s time period is also consistent with expected operational regimes in nuclear waste treatment⁶. It is evident therefore that some significant shear degradation of the polymer flocs occurs with these conditions, though it is also clear that the 20 ppm polymer systems led to significantly larger aggregates than for lower concentrations, which is generally consistent with previous literature on similar polymers^{17,18,22,60,89}. Fig. 3.1B shows the cumulative frequency distribution of the floc population at 1000 s, for suspensions without polymer and with 20 ppm of 30% σ and 40% σ polymer. Both flocculated suspension distributions are similar, although sizes are slightly larger overall for the 30% σ system.

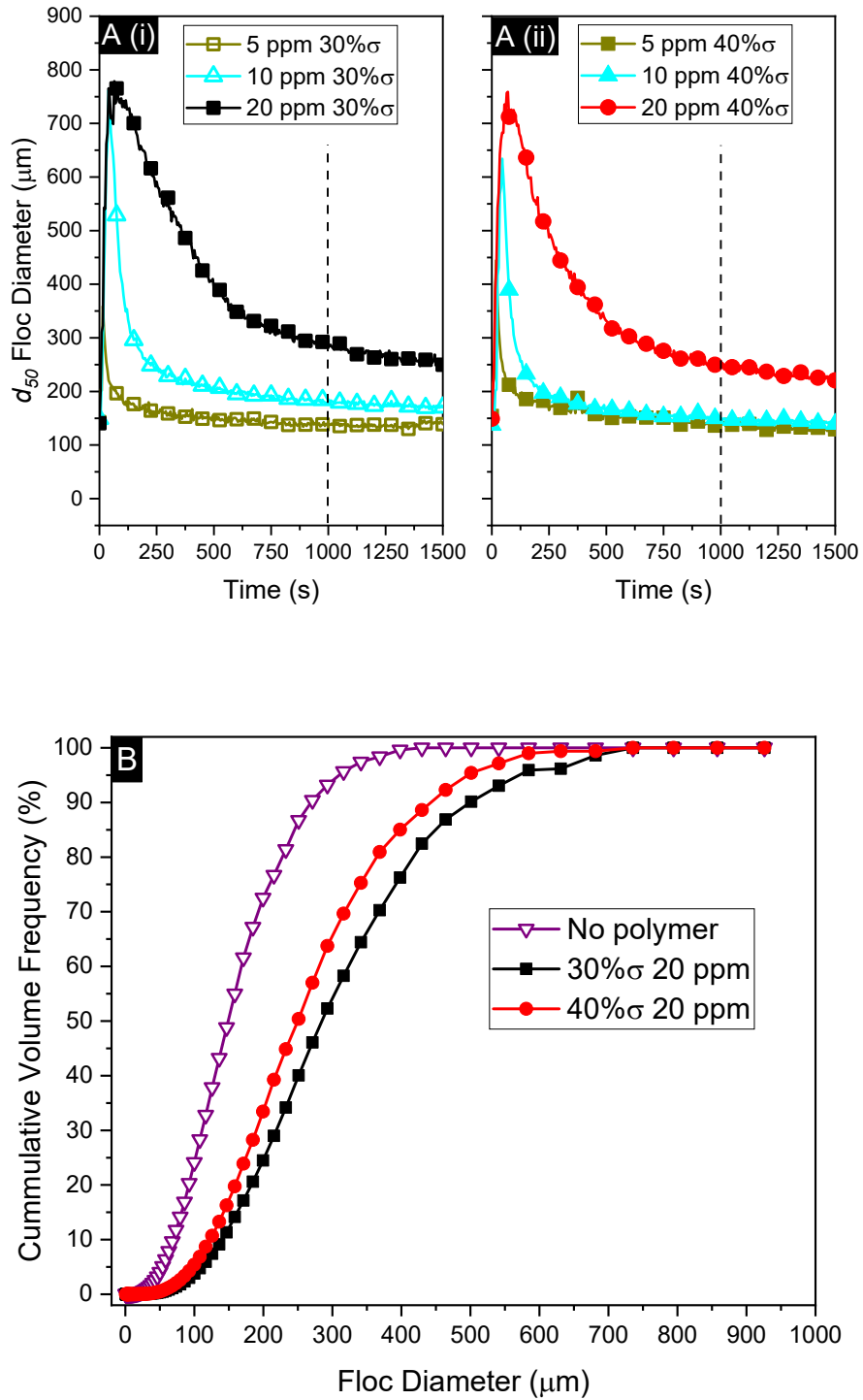


Figure 3.1: A (i) & A (ii) Median volume weighted particle size (d_{50}) over time, measured with a focused beam reflectance meter (FBRM), for 2.5 vol.% $\text{Mg}(\text{OH})_2$ suspensions agitated at 300 rpm, flocculated with 30% σ and 40% σ anionic polymers respectively, dosed at 5, 10 and 20 ppm. Dashed vertical lines at 1000 s indicate mixing time used for equilibrium studies. B) Cumulative volume distribution of floc sizes for the same systems dosed at 20 ppm, measured by FBRM after 1000 s.

Fig. 3.2A presents the SLS PSD of the suspensions with no polymer, as well as addition of 30% σ and 40% σ polymers at 20 ppm. Consistent with the FBRM data, both flocculated suspensions have similar size distributions, although again, the 30% σ system is larger. Fig. 3.2B shows SLS data displaying the log of the wave vector against the log of scattering intensity. The diameters of the minimum repeating floc diameter and corresponding primary particles within the structure, were determined using the procedure outlined by Sorenson⁶³. D_f and D_p are represented by the upper and lower limits of the linear regime in Fig. 3.2B, determined by linear fitting optimised for the greatest coefficient of determination (R^2). As shown in Table 3.2, D_f and D_p were determined to be 6.74 μm and 0.28 μm respectively for the 30% σ 20 ppm system and 8.01 μm and 0.34 μm respectively for the 40% σ 20 ppm system. Using the linear regime of Fig. 3.2B and the proportionalities highlighted in Eqn. 3.14, the fractal dimensions of the 30% σ and 40% σ systems were determined from the gradient of the linear fitting to be 2.07 and 2.09 respectively. Using Eqn. 3.2, the structure prefactor was then determined to be ~ 0.65 (to 2 sig. figs.) for both systems, and the number of primary particles in a floc calculated using Eqn. 3.1 to be 467 and 487 for the 30% σ and 40% σ systems respectively. Finally using Eqns. 3.3 and 3.4, the densities of the flocs were determined to be $\sim 1045 \text{ kg.m}^{-3}$ and $\sim 1049 \text{ kg.m}^{-3}$ for the 30% σ and 40% σ systems respectively, thus highlighting a very open structure (given the particle phase density is 2340 kg.m^{-3}). Such values are again consistent with similar flocculated dispersions previously investigated^{17,18,20,48,60} and are indicative of a highly fractal structure in both cases.

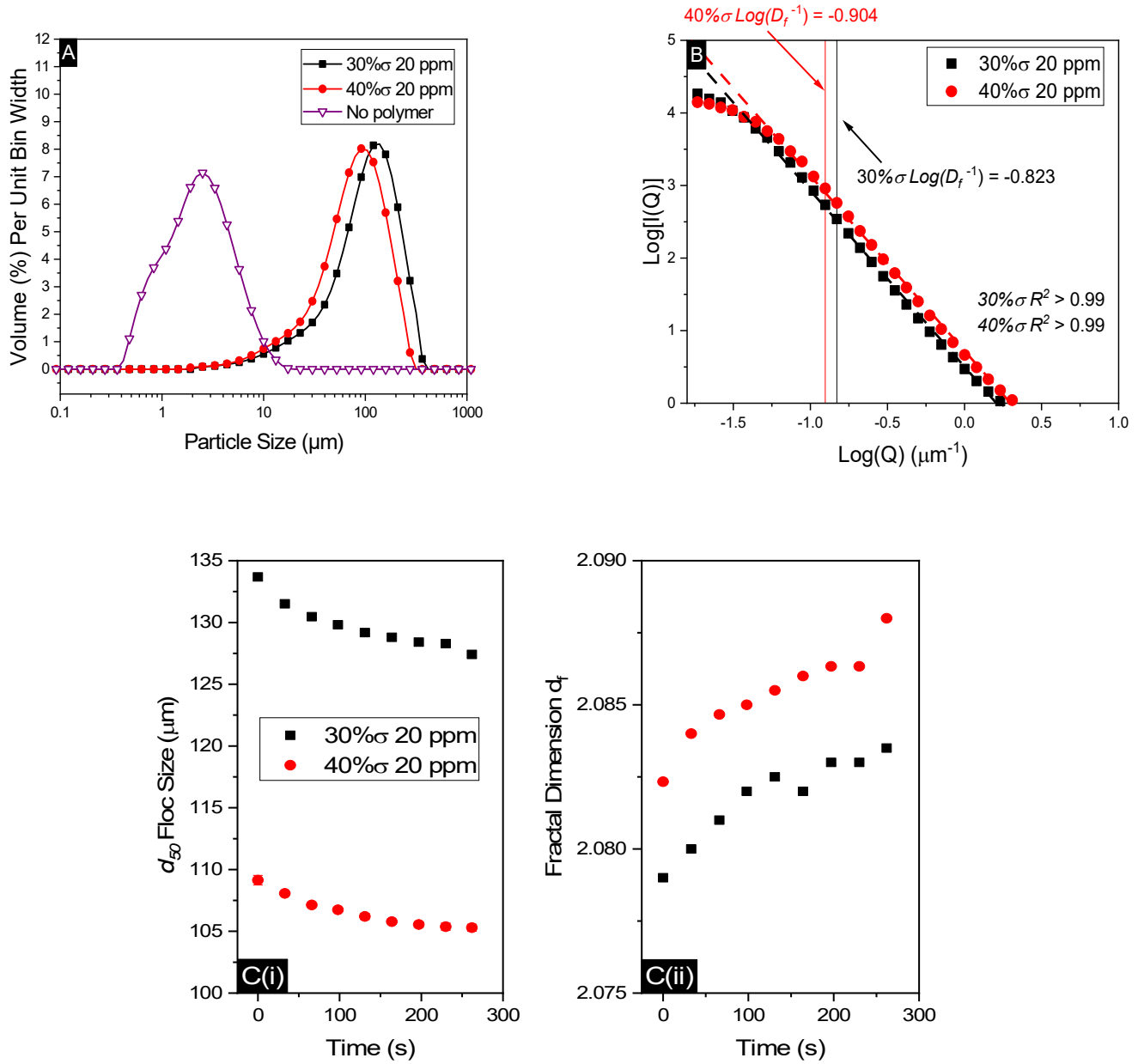


Figure 3.2: A) Static light scattering (SLS) particle size distributions of 2.5 vol.% Mg(OH)₂ suspensions with addition of 20 ppm 30%σ and 40%σ polymers, compared to sonicated Mg(OH)₂ with no polymer. Represented are continuous distributions for measurement bin sizes $\pm 6.25\%$ of the floating particle means. B) SLS fractal dimension analysis of 2.5 vol.% Mg(OH)₂ suspensions with 30%σ and 40%σ polymer. C) Kinetics of floc shear from shear degradation, showing (i) change in median diameter d_{50} with time and (ii) densification of Mg(OH)₂ with 20 ppm 30%σ and 40%σ polymers. All samples prepared in a reactor vessel at 300 rpm for 1000 s, then subsampled into the Malvern Mastersizer 2000E dispersion cell at 900 rpm. All points repeated in triplicate.

It should be noted that when SLS is used to identify fractal structure, it only identifies the fractal structure of the smallest repeating flocs in the system, the fractal dimension then being assumed to be the same throughout the entire floc population, regardless of floc

size⁶³. Previous Work has investigated the application of multifractal floc analysis of lime softening floc formation¹¹⁸, although whilst the methodology allows for greater insight into the nuances of floc formation and how fractal dimension varies with floc size, the techniques are still very computationally intensive. Additionally, it is highlighted by the authors that more research is required to investigate how to best utilise the information obtained from the multifractal spectra, to incorporate the variable floc density and nonhomogeneous mass distribution of flocs into the floc settling models¹¹⁸.

Table 3.2: Calculated floc structural properties established from the minimum floc diameter (D_f) and the corresponding primary particle diameter (D_p) obtained from SLS (Fig. 3.2B). D_f and D_p were found by extracting the wave scatter vector (Q) reciprocals from the upper and lower limits of the linear regime (determined by linear fit) of $\log(IQ)$ vs. $\log Q$, where the fractal dimension (d_f) is the gradient of the linear trendline, indicated in Eqn. 3.14. The structure prefactors (ψ) were calculated using Eqn. 3.2, number of primary particles (N) in a floc were calculated using Eqn. 3.1 and the volume fraction of particles in a floc (Φ_s) and floc densities (ρ_f) were calculated using Eqns. 3.3 and 3.4.

Properties determined from SLS data in Fig. 3.2B	30% σ 20 ppm	40% σ 20 ppm
Diameter of primary particle [D_p] (μm)	0.28	0.34
Diameter of minimum repeating flocs [D_f] (μm)	6.74	8.01
Floc fractal dimension [d_f]	2.07	2.09
Floc structure prefactor [ψ]	0.65	0.65
Number of particles in a floc [N]	469	487
Volume fraction of the particles in a floc [Φ_s]	0.034	0.037
Floc density [ρ_f] (kg.m^{-3})	1045	1049

Fig. 3.2C(i) shows the kinetic changes to the 50th percentile floc diameter and Fig. 3.2C(ii) the simultaneous densification indicated by the increasing fractal dimension over time for the same flocs. While some reduction is evident, further changes over longer times were considered relatively small, with the d_{50} for both flocculated systems reducing only on the order of 5% (with a corresponding increase in fractal dimension, indicating minor densification). However, it is noted that measurements were averaged over 30 second periods, after a certain induction time (typically >1 min) from when the suspension was added in order to give the appropriate obscuration (amount of light blocked or scattered by the particles), which indicated the concentration of flocs was within the operating envelope of the Mastersizer. Thus, there was some potential for aggregate breakdown to occur before the initial measurement could be taken (within 30 - 60 s of adding flocculated samples to the Mastersizer cell). There are also some very minor discrepancies between the fractal dimension computed from the slope of Fig. 3.2B, and the fractal dimension reported in Fig. 3.2C(ii), which may be due to slight differences in sampling preparation. For Fig. 3.2B, sub-samples were taken from the settling cylinders after inversion (prior to settling

analysis) while samples were taken directly from the flocculation reactor for the kinetics study (Fig. 3.2C). Thus, there may have been some variance in shear experienced by the samples, although the same trends regarding how polymer charge density affects floc structure are observed. It is also noted again that only the initial 10 s average was used for fractal measurements in Fig. 3.2B (representing the 'zero' timepoint in Fig. 3.2C).

Fig. 3.3 presents quantified microscopy data (while Fig. 3.4 shows an example micrograph for 30% σ flocs) with fig. 3.3A giving the aspect ratio distributions of the 30% σ and 40% σ polymer suspensions, demonstrating almost identical median aggregate aspect ratios of ~ 0.70 and ~ 0.69 respectively. Similar 2D morphologies have been previously reported⁵² and are indicative of their fractal shape factors, given that for lower fractal dimensions, flocs assume a less symmetrical shape with elongation along a single plane (termed drag induced prolated flocs)⁵². It is noted though, that their 2D shape factors will not necessarily be indicative of their 3D aspect ratios, due to flattening that can occur during drying on the microscopy slides.

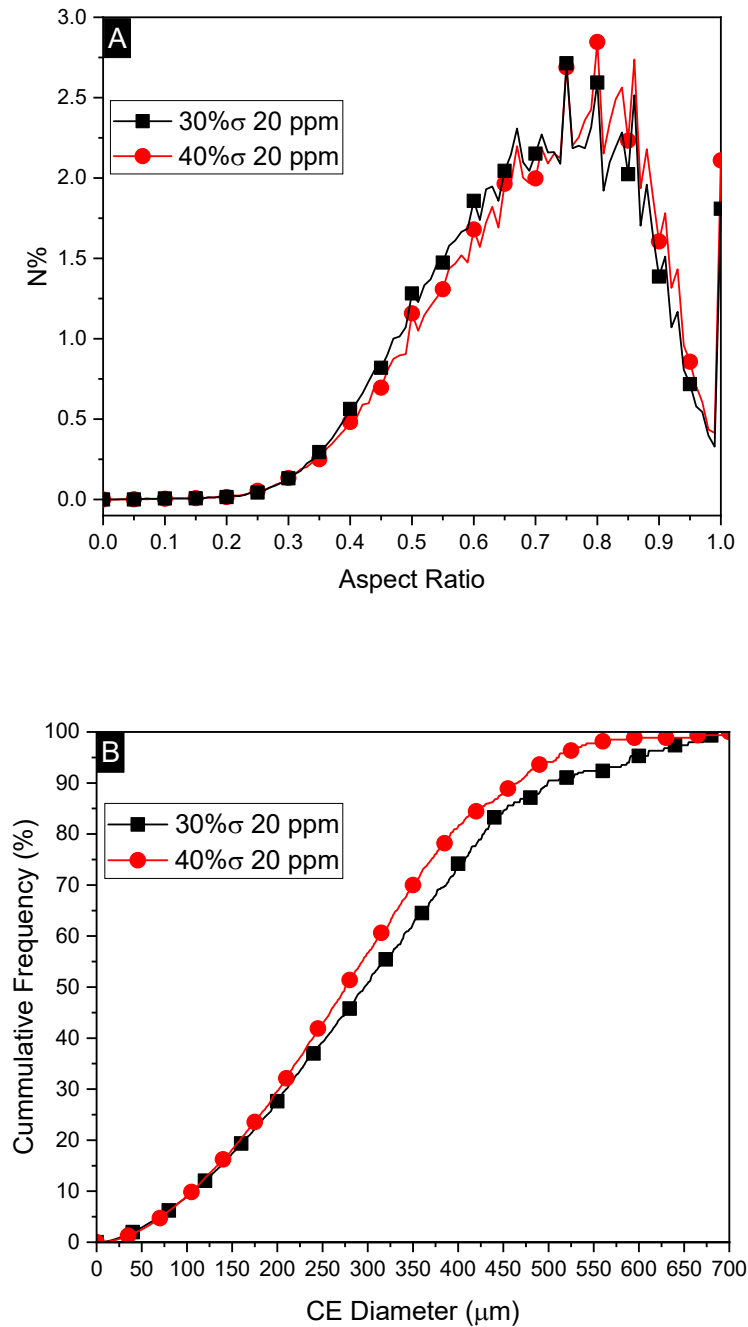


Figure 3.3: A) Aspect ratio distribution and B) cumulative frequency distribution, for optical image analysis of 2.5 vol.% Mg(OH)₂ suspensions agitated for 1000 s at 300 rpm with 30%σ and 40%σ polymers dosed at 20 ppm.

The deviation from sphericity raises the question as to whether the aspect ratios influence shape effects (especially on fluid drag) (see also Paul et al.¹⁷³ and Winterwerp¹²⁷), and in turn compromise the validity of the proposed FMRZ model. If so, a shape factor variable

may have to be introduced in predictive sedimentation equations (e.g., Eqn. 3.10), such as the coefficient used by Winterwerp¹²⁷. For dilute sedimentation, a number of correlations exist to modify the drag coefficient for non-spherical particles (e.g. as used by Benn et al.⁶⁰), but for hindered settling additional drag manifests as differences in the Richardson-Zaki exponent, n (typically assumed as 4.65). For example, exponents >10 have been reported for high aspect ratio colloidal particles¹⁷³, due in part to achieving stable orientation with the flocs longest axis normal to the settling direction rather than parallel thus increasing fluid drag. However, for most systems of irregular particles with relatively low aspect ratio, exponent values of 5 – 6 are more common¹⁷⁴. Given that the measured values of circularity in the flocs (of ~ 0.7) do not suggest highly asymmetrical form factors, it is likely therefore that any enhancement to the hindered settling exponent value would be relatively minor. In fact, Johnson et al.¹⁶ investigated the effect of altering the exponent value on predictions of coagulated magnesium hydroxide aggregate sizes from settling data, where it was shown to be a mathematically weak dependency (with predicted sizes changing by $< 9\%$ as n was increased from 4.65 to 6). Further, it is important to emphasize the differences between discrete particles of a given shape and the greater volume occupation of fractal aggregates observed in zonal settling, which increases floc-floc perimeter interaction, thus enhancing drag to a significantly greater extent than particle shape factors¹⁷³.

Fig. 3.3B shows the cumulative frequency distribution of circular equivalent diameters from microscopy, while Table 3.3 gives the d_{50} and d_{90} values obtained from FBRM, SLS and optical microscopy methods. Table 3.3 also shows the calculated number of particles in the flocs measured by the aforementioned techniques based on the self-similar properties of the fractal flocs⁴⁴. The solid particle volume fraction of the minimum repeating flocs (Φ_s) calculated using SLS data from Fig. 3.2B (~ 3.4 vol.% and ~ 3.7 vol.% for the 30% σ and 40% σ 20 ppm systems respectively) was used to calculate the number of particles from the measured polydisperse floc diameters by scaling up the number of particles in a minimum repeating floc in Table 3.2 using Eqn. 3.15. Where \overline{N}_f is the number of particles

in a measured polydisperse floc and \overline{V}_f is the spherical equivalent volume of measured polydisperse floc diameters (\overline{D}_f).

$$\overline{N}_f = (\overline{V}_f / V_p) \Phi_s \quad (\text{Eqn. 3.15})$$

The calculated polydisperse floc particle numbers (\overline{N}_f) in Table 3.3 aid comparisons between the 30% σ and 40% σ 20 ppm systems, with regards to floc size and solid particle components. For a given size, an increase in particle number will increase the density of the floc, although as settling rate is a function of the square of floc size, increases in size will influence the measured rate to a greater degree. Importantly also, it is emphasised that a less dense floc with lower particle number (for a given size) infers a greater effective volume fraction of the flocs (see Eq. 3.15) which itself will enhance hindered drag, potentially reducing settling rates. The microscopy data are consistent with FBRM and SLS measurements discussed, indicating that the lower charge density 30% σ polymer suspensions produced consistently larger flocs (and larger particle numbers) than the 40% σ polymer. Importantly also, whilst the differences in values of d_{50} are relatively small, there is a greater variation for the d_{90} floc diameter averages. This deviation between distribution values aligns with the research conducted by Nasser and James¹⁷, Zhou and Franks¹⁹ and Franks et al.⁸⁹, who found that lower charge density polymers produce larger, less dense flocs, although differences in size and fractal dimension values are normally more pronounced in previous literature^{19,48}. Generally, it has been shown that lower charge density polymers may conform on particle surfaces at a slower rate^{17,19,20}, producing larger flocs from the lower electrostatic driving force between the polymer functional groups and the particle charged surface. However, it appears in the current case, that the relatively small difference in polymer charge density results in relatively small overall differences in floc sizes, although, given the greater increase in d_{90} values for the 30% σ polymer systems, such differences may be great enough to produce variations in sedimentation behaviour.

In terms of instrumental variation, data in Table 3.3 show that SLS analysis measured considerably smaller d_{50} and d_{90} values for both systems, while values from FBRM and optical microscopy were similar. The differences in size for the SLS data are likely due to the shear occurring in the measurement cell, which demonstrate partial floc size degradation with time during agitation. As described, to prevent particle deposition and

bubble formation, the SLS dispersion unit circulation rate was required to be a minimum of 900 rpm, which increases the shear from the baffled reactor system that the flocs were prepared in (300 rpm). While this enhanced shear did not appear to lead to pronounced size reduction over long time periods (as discussed in relation to Fig. 3.2C(i)) it is important to note, as detailed, that each measurement represents 10 second averages and does not include the induction time required to produce acceptable obscuration in the cell. Hence, it is likely that the majority of the shear breakdown of the flocs occurred very rapidly, within the initial measurement time window.

Table 3.3: Comparison of the 50th (d_{50}) and 90th (d_{90}) percentile equivalent polydisperse floc diameters, \overline{D}_f , using focused beam reflectance measurement (FBRM), static light scattering (SLS) and optical microscopy (Opt) techniques, for 30% σ and 40% σ polymer- Mg(OH)₂ systems at 2.5 vol.% dosed at 20 ppm polymer concentration. The calculated number of particles in the measured polydisperse flocs, \overline{N}_f , is also listed and calculated using Eqn. 3.15. These data are complemented with aspect ratios obtained via optical microscopy.

Measurement	30% σ 20 ppm		40% σ 20 ppm	
	\overline{D}_f (μm)	\overline{N}_f (10^7)	\overline{D}_f (μm)	\overline{N}_f (10^7)
d_{50} (FBRM)	285	~3.6	245	~1.4
d_{90} (FBRM)	501	~19	437	~7.9
d_{50} (SLS)	134	~0.4	110	~0.1
d_{90} (SLS)	258	~2.6	214	~0.9
d_{50} (Opt)	295	~3.9	275	~2
d_{90} (Opt)	508	~20	463	~9.4
Aspect ratio (Opt)	0.7		0.69	

The consistency between FBRM and optical microscopy data gives confidence that measured polydisperse floc sizes closely represent the actual aggregate distributions within the suspensions, and additionally highlights the stability of flocs to sampling. The close correlation is particularly important, given the limitations of each individual technique. For the optical system, flocs are laid out on one plane which may affect their orientation and thus maximum diameter, while subjecting them to capillary forces on the microscope slide. Alternatively, it is emphasized again that the FBRM actually measures particle chord lengths, rather than true diameters. Thus, results suggest the translation employed to convert sizes to volume averaged diameters is a very close fit to the data¹¹⁵.

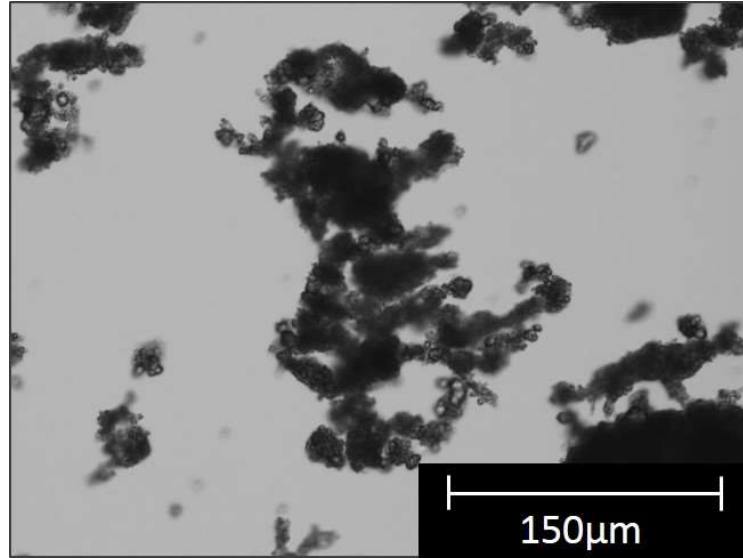


Figure 3.4: Example optical microscope image of Mg(OH)₂ suspensions mixed with 20 ppm 30%σ polymer.

Optical microscopy images of the 30%σ polymer-Mg(OH)₂ floc dosed at 20 ppm, enable the fractal structure of the flocs to be inferred, and demonstrate the deviation from circularity, as quantified in Fig. 3.3A. Furthermore, closer observation indicates the presence of individual detached primary particles that can be seen around the flocs. Whilst particle detachment is likely in the transfer to microscope slides, if they occur within the suspension they may potentially generate increased turbidity if small enough to separate from the bulk suspension, as suggested by Johnson et al.¹⁶ in previous work on the sedimentation of Mg(OH)₂. Cryogenic scanning electron micrographs of a 40%σ polymer-Mg(OH)₂ floc (Fig. 3.5), highlight far more detailed structures than the optical microscopy. The primary particles in the floc structures can be seen to be submicron platelets, as indicated by SEM imaging of the raw Mg(OH)₂ in Appendix Fig. A1. These structures resemble computational simulation designs of flocs of similar fractal dimensions (≈ 2.09)⁴⁸ in reaction limited cluster-cluster aggregation mechanisms of flocculation^{45,117}. In this process, large clusters of aggregated particles interact to form an even larger network floc, as opposed to particle by particle addition of the diffusion limited cluster-cluster aggregation mechanism¹⁷⁵. Given that Fig. 3.3A demonstrates similar aspect ratio and fractal dimension for both the 30%σ and 40%σ systems that also agree with aspect ratios found by Xiao et al.⁴⁵ in computer simulated designs, it is likely that the reaction limited cluster-cluster aggregation mechanism is dominant in both 30%σ and 40%σ systems.

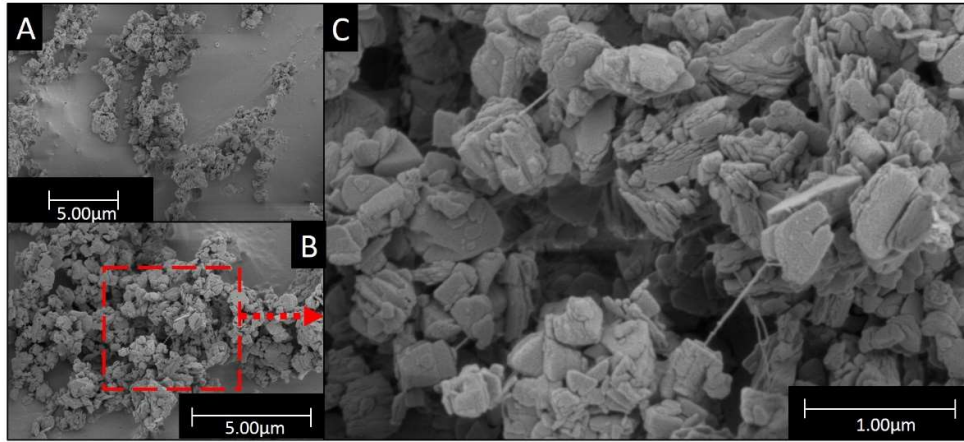


Figure 3.5: Cryo-SEM images of 2.5 vol.% Mg(OH)₂ suspensions mixed with 20 ppm 40%σ polymer. A) 19982× magnification, B) 35000× magnification and C) 99959× magnification.

The similar and significant porosity observed in Figs. 3.4 and 3.5, suggest that liquid permeability within the floc structures may be large enough to encompass smaller primary particle phases and axiomatically allow fluid flow through these micro channels in a similar manner to previous reports^{16,45}. Moreover, polymer chains linking the primary particles are present in the Cryo-SEM images, consistent with work completed by Sharma et al.⁴¹. Capturing images of cryogenically frozen polymer chains is generally very difficult, because of the sensitivity of the organic materials to electron bombardment⁴¹. Even at low voltages, this damage can be extensive. The chains found in the images are sparse on the particle surface and represent ‘surviving’ polymer chains that are much thicker than expected for single polymer segments. Sharma et al.⁴¹ have hypothesised that the variation in polymer chain dimension could be due to the stacking of fine polymer chains, giving rise to thicker structures, or due to the presence of poorly dissolved polymer, where the loss in water due to cryogenic freezing and sublimation leads to collapse and aggregation of the polymer network.

3.4.2) Measurement and prediction of floc sedimentation rates

Figs. 3.6A(i) and 3.6A(ii) present the change in the zonal interface height (mud-line) with time, for varying concentrations of both 30%σ and 40%σ polymers respectively, while Fig. 3.6B shows the average linear settling rate against varying polymer concentration for both systems. These data are also complemented with supernatant turbidity values after 30 minutes of sedimentation taken from 5 cm below the air-water interface (Fig. A5 within Appendix A) where it was found that the 30%σ system reduced supernatant turbidity to a

greater extent than the 40% σ system, although both produced very low turbidity values inferring efficient separation. As expected, the increase in polymer concentration resulted in a greater settling rate for both 30% σ and 40% σ polymers. This result also correlated to changes in aggregate size from FBRM (Fig. 3.1A) where the increase was most pronounced for the 30% σ system at 20 ppm concentration.

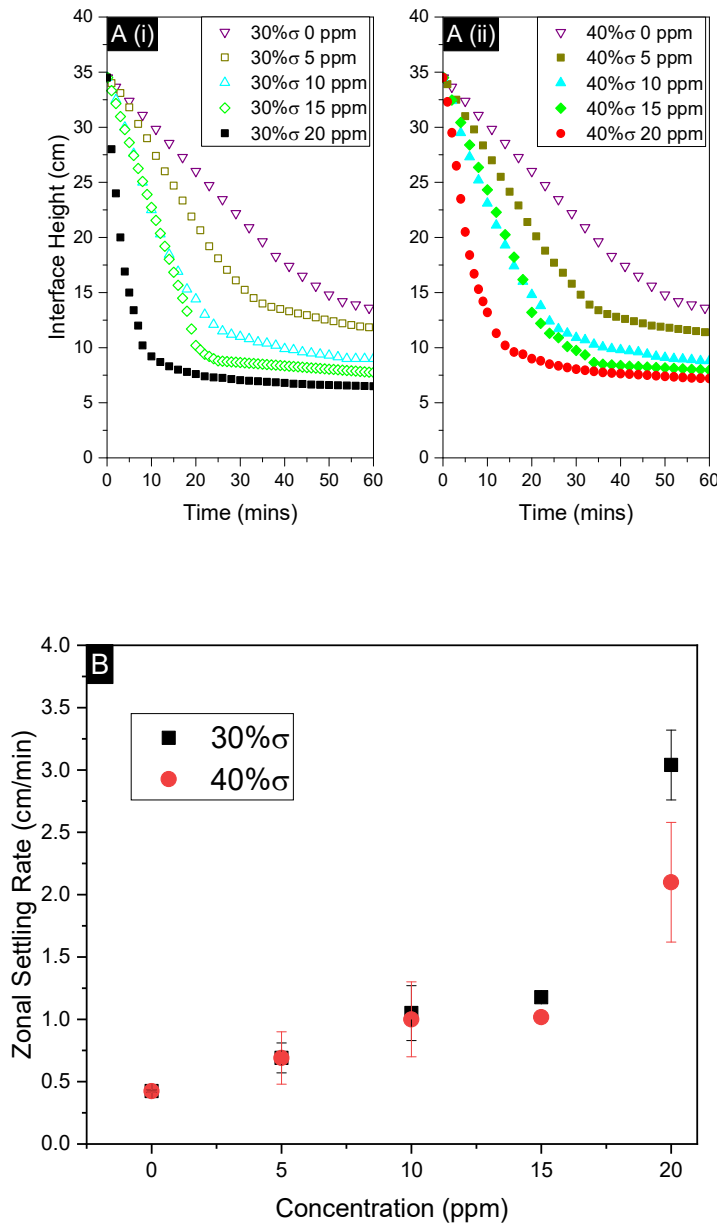


Figure 3.6: A) Interface height versus time for flocculated 2.5 vol.% Mg(OH)₂ with varying concentrations of (i) 30% σ and (ii) 40% σ polymer, prepared in a reactor agitated at 300 rpm for 1000 s. B) Linear zonal settling rate versus polymer concentrations for the same systems.

The validity of the FMRZ model (Eqn. 3.10) was demonstrated by comparing experimentally determined settling rates for the 20 ppm dosed 30% σ and 40% σ systems (Fig. 3.7A), to those predicted using measured d_{50} and d_{90} sizes from FBRM, SLS and optical microscopy, with fractal dimensions estimated from SLS data in Fig. 3.2B. The zonal settling rate predictions determined by the FMRZ model are also shown for comparison in Appendix Figs. A6A and A6B, for the 30% σ and 40% σ 20 ppm system respectively. The same comparisons for a 10 ppm dose of both polymers are given in Appendix A, Fig. A7 (without the addition of optical microscopy measurements). Interestingly, the measured d_{50} values underpredicted the actual settling rates considerably in each case, where additionally, calculations based from SLS size data were poor, due to the assumed aggregate breakup. Settling rate predictions from FBRM and optical microscopy were much closer to experimental values when using the 90th percentile (d_{90}) values, especially for the 30% σ system. The same trends are evident for the 10 ppm data (Appendix Fig. A7) although, in general, the settling rate predictions are lower than the measured values (perhaps due to lower size measurement resolution, from the smaller particle sizes present). It is also noted that as the settling rate scales to the diameter squared, small deviations in size measurements will lead to large apparent errors in estimated settling rates. With both 10 and 20 ppm systems, critically, results suggest that the population of flocs that occupy only the top 10% of the total systems by size dominate the settling mechanics. A likely explanation for this behaviour is the ‘netting’ effect observed in sweeping flocculation^{155–157}. As larger, faster setting flocs sediment in the vertical plane, they may encompass slower settling, smaller flocs in their microstructure (possible given the size of such voids observed in microscopy data in Figs. 3.4 and 3.5) leading to densification and integration of the agglomerates¹⁶.

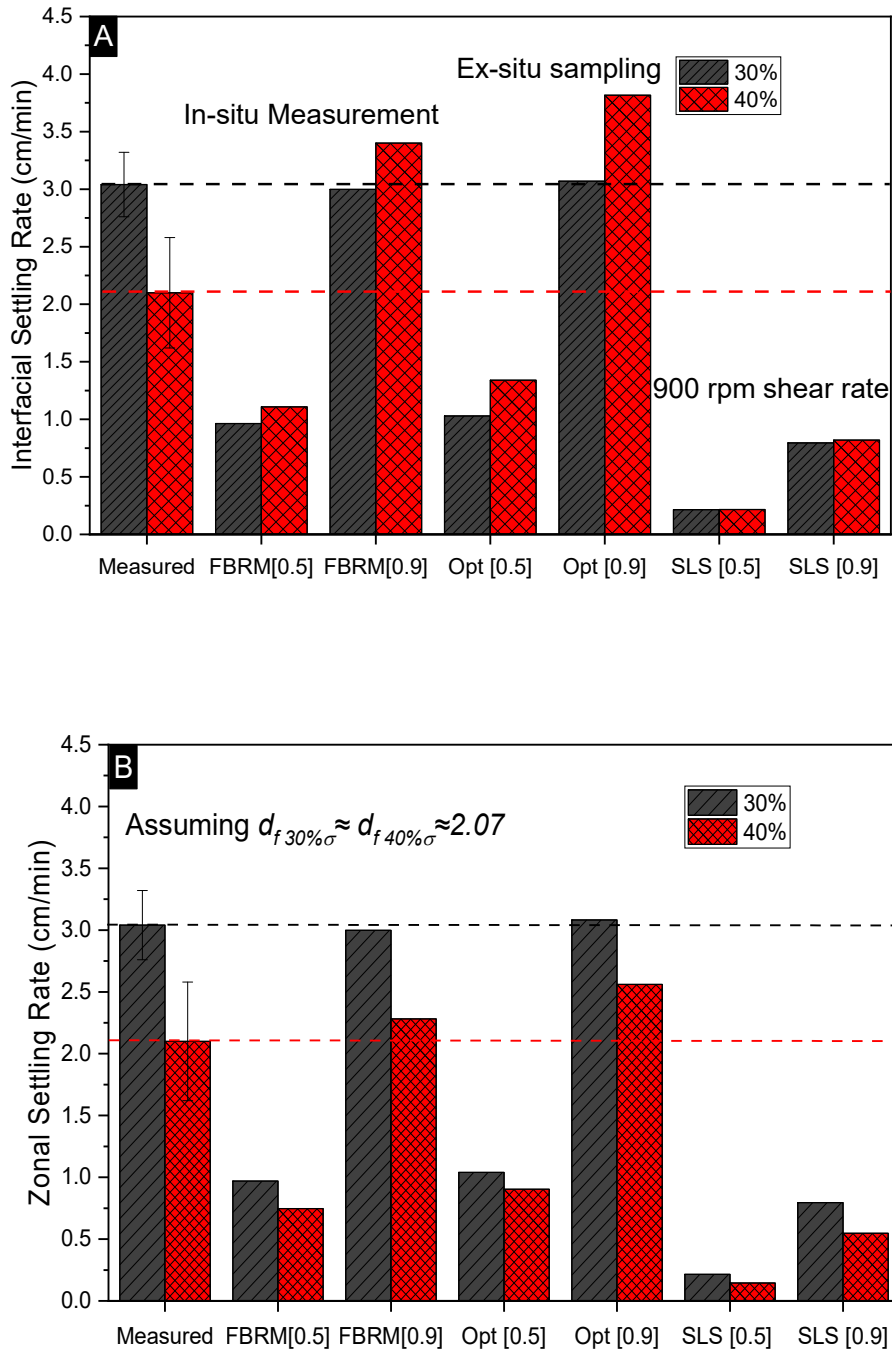


Figure 3.7: A) Comparison of measured (actual) zonal settling rates (dashed lines) for flocculated 2.5 vol.% Mg(OH)₂ suspensions mixed with 20 ppm 30%σ ($d_f = 2.07$) and 40%σ ($d_f = 2.09$) polymer, to those predicted by the fractal modified Richardson-Zaki equation (Eqn. 3.10). Comparisons using median [0.5] and 90th percentile [0.9] sizes measured by *in situ* focused beam reflectance meter (FBRM), *ex situ* optical microscopy (Opt) and *ex situ* static light scattering (SLS) that incorporated a 900 rpm agitated feed-cell. B) Comparison of measured and predicted data as A), assuming identical fractal properties for both flocculated polymer systems ($d_f = 2.07$).

Previous studies that also found larger (d_{90}) sized flocs had a greater effect on sedimentation performance^{17,18}, have examined a number of other mechanisms that may explain the observed behaviour, in addition to ‘netting’ interactions. What may also be important in high solid fraction systems, is the increased porosity of fractal aggregates, which may allow for microflow channels to relieve hydrodynamic stress across the projected surface of the floc, by producing a vector for fluid to flow through the fractal structure⁴⁵. Such effects would be greater in larger flocs (and so more important for the d_{90} versus d_{50} sizes) as fractal floc densities may reduce with size, due to potential variability of fractal dimension with floc diameter. Any such variation would not be captured by SLS measurements, which assume self-repeating fractal structures^{48,50,63,118,128}. Computational investigations by Xiao et al.⁴⁵ into aggregates displaying a fractal dimension of 2.13, demonstrated such high levels of intra-aggregate permeability that the internal flow through the microstructure increased the settling rate of the bulk suspended solids significantly when compared to non-permeable controls. Further, studies by Johnson et al.¹⁶ on naturally coagulated $Mg(OH)_2$ also found evidence for the influence of fluid flow through rather than around settling aggregates. They observed that there was a sudden reduction in the hindered settling exponent at intermediate particle concentrations (indicative of reduced drag) which was hypothesized to occur when inter-aggregate spacing approached that of intra-aggregate spacing, due to the low density of particles within an aggregate. In such cases, the assumption by Heath et al.¹⁸ that the magnitude of hindrance due to aggregate shape effects is negligible when compared to that of average hindered settling interactions due to the floc volume, is likely valid. Further in Table 3.3, the calculated number of particles within the measured floc diameters is also recorded.

Comparing the floc diameters and particle numbers for the d_{90} optical microscopy data, while the 30% σ system is ~10% larger by diameter than the 40% σ system, it contains more than twice the number of primary particles. Therefore, it would be expected that the larger, more particle loaded 30% σ flocs would sediment at a faster rate, due primarily to its increased floc density, as experimentally measured. However, in terms of the model prediction, this is not the case (as shown in Fig. 3.7A) where the predicted sedimentation rate for the 40% σ is actually greater. This disparity suggests that the hindering functionality of the FMRZ model (described by the fractal dimensionless permeability number, f_s^*) is particularly sensitive to small changes in fractal dimension, due to the significant weight that the FMRZ model in Eqn. 3.10 places on fractal dimension values which is modelling

flow around flocs. While measured values for the 40% σ systems are slightly larger, differences between the flocs are minor (with $d_f = 2.09$ for 40% σ and 2.07 for 30% σ systems) but these differences correlate to relatively large differences in both predicted sedimentation rates and the calculated number of particles within a floc.

Thus, to test the influence of the fractal dimension, settling rate predictions were recalculated, assuming both floc systems had a fractal dimension of 2.07, as per the 30% σ systems (given predictions were closer in this case). From this FMRZ modelling (Fig. 3.7B) it is evident that the 40% σ system predictions are now below that of the 30% σ system and align much closer to the experimental rates (at least for those estimated on the d_{90} sizes). In terms of floc particle numbers, assuming the fractal dimension is lower than measured, and using the fractal dimension 2.07 in lieu of 2.09 (assuming a fixed D_f/D_p ratio) results in a decrease to the number of particles in a minimum repeating floc. Indeed, the resultant polydisperse floc number for the 40% σ system is reduced from $\sim 9.4 \times 10^7$ to $\sim 8.8 \times 10^7$ (a 6% reduction), which in turn translates to a $\sim 33\%$ reduction in zonal settling rate. This result highlights that the actual fractal dimensions of the two flocculated systems are remarkably similar, but also, that model predictions are extremely sensitive to fractal dimension values. Therefore, it is extremely important that fractal dimensions can be estimated accurately and use of a low-shear dispersion cell would be recommended for future work.

To further understand the influence of FMRZ model parameters on output predictions, a multivariate analysis of the FMRZ model was conducted, as shown in Fig. 3.8A demonstrates how both changes in floc diameter and fractal dimension affect the predicted zonal settling rates, where measured SLS and Opt d_{50} and d_{90} data (for both 30% σ and 40% σ systems) have been added onto the FMRZ surface plot for comparison. Fig. 3.8B presents the variation of polydisperse floc particle number with fractal dimension, for arbitrary floc diameters of 100, 500 and 900 μm , selected to cover the experimental range. The limits of the fractal analysis are also briefly noted, for Eqn. 3.9, the effective floc volume fraction, ϕ_f , must also be less than 1. Therefore, the fractal dimension limit for Eqn. 3.9 to be valid, was determined by fitting of the calculated change in effective volume fraction for different fractal dimension values (see Appendix Fig. A8). Here, $\phi_p = 0.025$ and D_f and D_p are fixed for their respective charge density polymer systems shown in Table 3.2, and was found to be $1.84 \leq d_f$.

It is evident from Fig. 3.8A (as also highlighted in Fig. 3.7B) that even small increases in fractal dimension result in considerable changes to settling velocity, and those effects are much more significant than changes to aggregate size (noting fractal dimension is only varied between 1.85 and 2.1, while floc sized is increased from 100 – 500 μm). The reason for this functional influence, is due to the non-linear effects on the effective volume fraction, ϕ_f , of the flocs. The isolated function representing the change in the dimensionless permeability number, f_s^* , with increasing fractal dimension, was found to be highly non-linear (see, Appendix Fig. A9). Conversely, large changes in the fractal dimension (1.85-2.75) were less impactful on the particle number within flocs, than the changes to the overall floc sizes (see Fig. 3.8B) consistent with the order reported experimentally in Table 3.3. Only in the case where the fractal dimension, d_f , approaches 3 (resulting in the effective volume fraction, ϕ_f , approaching the initial particle volume fraction, ϕ_p) does the impact of the measured floc diameter, \overline{D}_f , and thus the Stokes function of the FMRZ model, become dominant in determining the settling rate of the suspension.

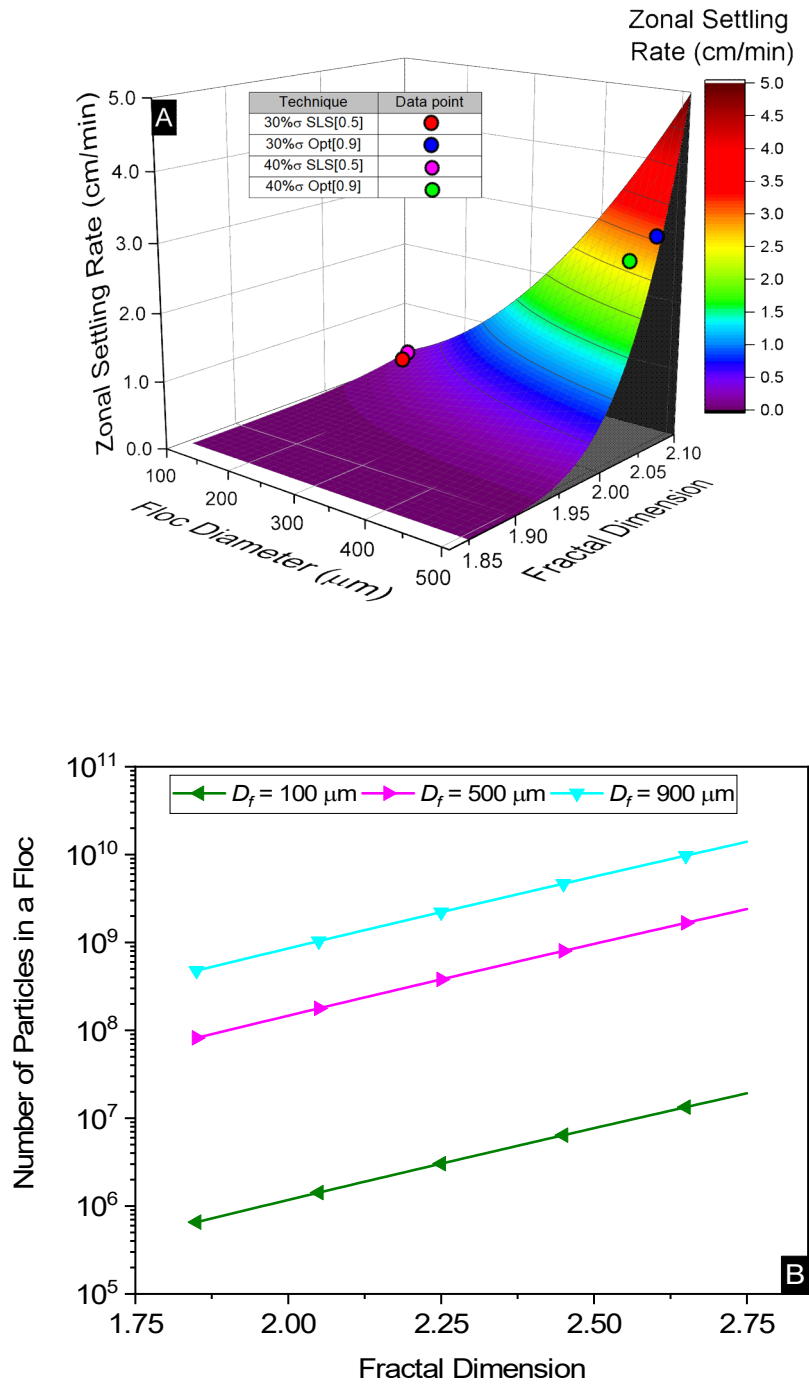


Figure 3.8: FMRZ model prediction of the zonal settling rate of 2.5 vol.% Mg(OH)₂ suspensions mixed with 20 ppm 30%σ polymer, for various input floc sizes, \bar{D}_f , and fractal dimensions, d_f , based on the fractal modification of the Richardson-Zaki equation (Eqn. 10). Here, $\rho_p=2340.6 \text{ kg.m}^{-3}$, $\rho_w=1000 \text{ kg.m}^{-3}$, $g=9.81 \text{ m.s}^{-2}$, $\mu_w=8.9 \times 10^{-4} \text{ kg.m}^{-1}.\text{s}^{-1}$, $D_f=6.74 \mu\text{m}$ and $D_p=0.28 \mu\text{m}$. B) The change in the floc particle number, \bar{N}_f , as a function of floc diameter and fractal dimension for $\bar{D}_f = 100, 500$ and $900 \mu\text{m}$, selected to cover the experimental range.

Furthermore, Table 3.4 displays analysis conducted to determine the corresponding predicted fractal dimension values for each of the measured floc diameters in Table 3.3 (using the FMRZ model) to produce the experimentally determined zonal settling rates in Figs. 3.6A and 3.6B. The inverse was also computed in Table 3.4 to give floc size predictions for the measured fractal dimensions (in Fig. 3.2B). These data further highlight the non-linear influence of the fractal dimension, when considering the d_{50} (SLS) data measured in Table 3.3, which represents the furthest departed prediction from the experimentally measured zonal settling rates for both the 30% σ and 40% σ 20 ppm systems.

Table 3.4: Interpolated fractal dimensions from the FMRZ model (Eqn. 3.10) for experimentally obtained floc diameters (in Table 3.3) to project the experimentally obtained zonal settling rates in Figs. 3.6A and 3.6B. Also given is the corresponding interpolated floc diameters required to project the experimental zonal settling rates, based on the experimentally obtained fractal dimension data (Fig. 3.2B).

Measurement	Corresponding modelled fractal dimension	
	30% σ 20 ppm	40% σ 20 ppm
d_{50} (FBRM)	2.15	2.14
d_{90} (FBRM)	2.07	2.07
d_{50} (SLS)	2.31	2.31
d_{90} (SLS)	2.17	2.17
d_{50} (Opt)	2.14	2.13
d_{90} (Opt)	2.07	2.06
Corresponding modelled floc diameter	505 μm	357 μm

For the 30% σ system, the FMRZ modelled sedimentation rate based on the SLS experimentally obtained d_{50} floc diameters and fractal dimensions, is over 20 times lower than the experimentally observed zonal settling rate. When extracting the corresponding polydisperse floc diameter from the FMRZ model based on the experimentally obtained fractal dimension of 2.07 to predict the experimentally obtained zonal settling rate, the SLS d_{50} diameter in Table 3.3 is increased almost fivefold from 134 μm to 505 μm (shown in Table 3.4). However, when performing the inverse, where the corresponding fractal dimension is extracted from the measured d_{50} SLS floc diameter to predict the experimentally obtained zonal settling rate, only an increase of 2.07 to 2.31 (or $\sim 10\%$) was required to achieve the same zonal settling rate increase. In terms of changes to floc particle numbers between these two scenarios, increasing the particle size to the estimated 505 μm results in a particle number increase from 0.37×10^7 to 20×10^7 (calculated using Eqn. 3.15). Alternatively, altering the fractal dimension to 2.31 would produce floc particle numbers in the order of just 0.92×10^7 . The comparative increase in zonal settling rate when

comparing the change in the number of particles in flocs as a function of floc size and fractal dimension independently (Fig. 3.8B) further demonstrates that the zonal settling rate is greatly dependent on the fractal modified dimensionless permeability number (f_s^*). Small increases in fractal dimension non-linearly increase the dimensionless permeability number (see Appendix Fig. A9) producing greater zonal settling rates than increasing floc size. Essentially, increases in permeability number is reflective of decreases to the effective volume fraction of the dispersion. A high permeability number indicates the flocs take up a small effective volume, significantly decreasing overall drag from hindered settling. This influence of fractal dimension mathematically is considerably more influential on estimated settling rates than increased floc weight granted by greater particle loading or larger floc sizes. However, as previously discussed, the dominance of fractal dimension is not reflected in the experimental work in Figs. 3.6A and 3.6B or by previous literature, where it has been observed that floc size is usually dominant in sedimentation performance^{17,18}

For the FMRZ model, when $\phi_p \left(\frac{D_f}{D_p}\right)^{3-d_f} \ll 1$, f_s^* is close to unity, and \overline{D}_f has a greater influence on zonal settling rate. Conversely, when $f_s^* \ll 1$, $\phi_p \left(\frac{D_f}{D_p}\right)^{3-d_f}$ is close to unity, and the zonal settling rate is much more sensitive to values of d_f . The FMRZ model indicates that the 30% σ and 40% σ systems have f_s^* values of 0.05 and 0.07 respectively, suggesting that they are in a strongly hindered settling regime and more sensitive to fractal dimension than floc size. Since this was not strictly observed experimentally (with measured sedimentation rate being most dependent on d_{90} sizes) it indicates that the hindering effects are reduced in comparison to model estimates.

In particular, the FMRZ model does not take into account any specific factors, for example, the effects of floc microstructure and internal porosity, as previously discussed. Aggregate porosity may provide a means of intra-aggregate flow, thus increasing the effective permeability number, f_s^* , closer to unity, enhancing the relevance of \overline{D}_f on zonal settling rates. Particularly, as suggested by Johnson et al.¹⁶, whilst the external perimeters of the flocs may interact through increased inter-aggregate packing, microflow channels in the flocs may prevent increased drag and boundary layer separation providing a vector for dewatering processes to dominate. Further, internal floc permeability hindering relief effects may be captured by theoretical models on aggregate densification and their impact on thickener performance, as suggested by Usher et al.¹⁷⁶, which has been applied to batch

settling and thickening scenarios similar to this work¹⁷⁷⁻¹⁷⁹. Nevertheless, given these limitations, the correlation between predicted and experimental settling rates demonstrated in Fig. 3.7B and Fig. 3.8A, highlights that the FMRZ model still provides a very close first approximation to experimental aggregate sedimentation rates.

It is lastly evident that the volume translation of the *in situ* FBRM measurements provided a very close size estimate, indicating the potential to couple inline measurements with the FMRZ model predictions, for process optimization and control of industrial solid-liquid separators. While, currently, there are no standard *in situ* techniques to easily measure aggregate fractal dimensions, it may simply be sufficient in most circumstances to evaluate fractal dimension using FMRZ model predictions from batch sedimentation data (as completed in Table 3.4) providing robust estimates of floc structures for full scale operations. There may also be the potential to combine model predictions with other *in situ* techniques, such as acoustic backscatter systems, to gain both size and structure information, completely negating the need for sampling¹⁸⁰. The sensitivity analysis of the FMRZ model presented in Fig. 3.8, is also critical for accurate integration into CFD simulations of clarifiers and thickeners, where similar fractal models are often used to simplify solid-liquid separation physics. The influence of uncertainties with fractal dimension values has, in particular, been shown to impact the accuracy of CFD predictions in simulations of large-scale flocculated calcite separation²².

3.5) Conclusions

This study investigated the flocculation of magnesium hydroxide dispersions with 30% and 40% charge density polyacrylamide-poly(acrylic acid) flocculants and resultant sedimentation behaviour. Static light scattering (SLS), focused beam reflectance measurement (FBRM) and automated optical microscopy found relatively small differences in resultant floc density, shape and size (although, SLS underpredicted floc sizes in all cases). Additionally, the 30% charge systems were measured to be slightly larger under all techniques, which was potentially thought to be due to a lower electrostatic driving force between polymer functional groups and the particle surface, resulting in slower conformation kinetics when compared to the 40% charge density system. Cryogenic scanning electron microscopy was also used to investigate floc microstructure, displaying porosity at multiple length scales.

Measured sedimentation rates were compared to estimations from a fractal modified Richardson-Zaki settling model (FMRZ model), to assess the role of floc size dominance in hindered sedimentation. It was found that the 90th cumulative percentile (d_{90}) floc sizes predicted settling rates more accurately than the d_{50} sizes, which was assumed to be due to netting effects. A full sensitivity study of the FMRZ model was also performed, indicating the valid fractal dimension range, and most importantly, the relative influence of floc size and fractal dimension parameters (along with associated particle number density in each floc). The correlation of settling rate predictions to experimental values (when using the d_{90} floc size) highlighted the advantages of the FMRZ model as a relatively simple method to achieve close first approximations, even though shape and internal porosity effects are not included. Additionally, the close estimates of FBRM size data converted from a number-based distribution to a volume-based distribution, indicated its suitability as an *in situ* sizing technique to couple with FMRZ model estimations, for online prediction of industrial clarifiers and thickeners. Nevertheless, due to heavier weighting on floc compactness rather than the comparative floc particle loading - settling rate predictions were found to be overly sensitive to fractal dimension values from multivariate analysis, and likely above the sensitivity of the actual measurements. This result draws attention to the need for improved *in situ* methods of fractal dimension characterisation.

3.6) Nomenclature for Chapter 3

Scripts

d	Fractal dimension	-
D	Diameter	m
D_f	Minimum repeating floc unit diameter	m
\overline{D}_f	Diameter of a polydisperse floc in a measured PSD	m
D_m	Singular particle diameter	m
D_p	Primary particle diameter	m
d_{50}	Cumulative 50% point of diameter in a PSD	m
d_{90}	Cumulative 90% point of diameter in a PSD	m
F_N	Number based cumulative frequency	-
f_N	Number based frequency distribution	-
F_V	Volume based cumulative frequency	-

f_s	Dimensionless permeability number	-
f_s^*	Fractal dimensionless permeability number	-
g	Gravitational acceleration	m.s^{-2}
$I(Q)$	Scattering intensity	-
k	Scattering constant	-
n	Refractive index	-
N	Number of particles in a minimum repeating floc	-
\bar{N}_f	Number of particles in a measured polydisperse floc	-
$P(Q)$	Single particle form factor	-
Q	Scattering wave vector	μm^{-1}
$S(Q)$	Interparticle structure factor	-
U	velocity	m.s^{-1}
V	Volume	m^3
V_f	Minimum repeating floc volume	m^3
\bar{V}_f	Measured PSD polydisperse floc volume	m^3
V_p	Volume of a floc primary particle	m^3
θ	Scattering angle	degrees
λ	Wavelength of incident light	μm
μ	Dynamic viscosity	$\text{m}^2.\text{s}^{-1}$
ρ	Density	kg.m^{-3}
Φ_s	Volume fraction of particles within floc	-
ϕ	Volume fraction within whole suspension	-
ψ	Structure prefactor	-
ζ	Zeta potential	mV

Subscripts

f	Floc
i	Interfacial
	Primary
p	particle
T	Terminal

w Water

Chapter 4:

Flotation using anionic surfactants for rapid dewatering of $Mg(OH)_2$ radwaste suspensions

4.1) Introduction

There is a critical need for new flexible and efficient dewatering systems to aid in decommissioning of the abundance of legacy Nuclear reactor facilities worldwide. However, critical challenges that exist to the transfer and treatment of radwaste sludges in risk and hazard reduction operations^{8,159,181}. Challenges from particulate suspensions are ubiquitous in radioactive waste (radwaste) management, with broad particle size distributions (PSDs) ranging from fine colloidal material to coarse particles and even fuel fragments^{4,6,7,101}. It is extremely difficult to optimise dewatering processes for the separation of radwaste suspensions, due to their heterogeneity, especially when operations are subject to additional regulatory requirements, such as no moving parts and reduction of secondary waste generation¹⁸².

A common regulatory driven approach for radwaste dewatering is gravitational thickening, where suspensions are subject to sedimentation, with the less turbid supernatant liquor being pumped back into storage ponds and the separated thickened sludges are stored and finally encapsulated^{6,16}. Whilst sedimentation is safe and straightforward, it is also slow, with considerable residence times being required in the thickening zones to remove finer particles¹⁵². Given the strict timelines that most governments have for the processing and storage of legacy nuclear wastes, optimisation of these dewatering operations is thus a priority for the nuclear industry. To accelerate dewatering, there is current interest in the application of polymeric flocculants to enhance suspension zonal settling rates, which have been shown to significantly decrease residence times in thickening operations^{20,107,146,183}. However, these processes have a number of drawbacks, in terms of their modification to waste structure and related downstream issues¹⁸¹. In particular, the resultant fractal nature of these polymeric flocs can increase settled bed volumes, which may reduce the solid waste capacity of intermediate level waste containers for final geological disposal when a site becomes available^{60,84}.

As an alternative to gravitational separation, flotation has received increasing interest from researchers investigating radwaste separation, as it has been shown to be an extremely rapid

dewatering technique, and is already commonly utilised in the minerals, water treatment and paper industries^{65,73,79,80,129,140,144,184,185}. Previous investigators have studied a range of variables that affect flotation performance, including but not limited to particle contact angles^{58,83,186}, bubble size distribution^{69,129}, foam stability^{142-144,187,188}, suspension/collector concentration^{58,71,172}, collector adsorption density^{67,71,79,81}, collector hydrophobicity¹⁸⁹⁻¹⁹¹, particle coagulation and hydrodynamic consequences of variable PSDs^{83,88,113,146}. Research into flotation of $\text{Mg}(\text{OH})_2$, a corrosion product of the fuel cladding alloy at Sellafield^{4,8}, has received little interest, but similar mineral particulates with positive surface charges have been shown to be effectively separated using flotation facilitated with anionic surfactant collectors, such as alkyl sulphates including sodium dodecyl sulphate (SDS)^{65,67,192}.

It is thus critical that before the deployment of flotation as a dewatering strategy to separate magnesium hydroxide based radwastes, research is undertaken to establish efficient collectors that are effective at hydrophobising $\text{Mg}(\text{OH})_2$ particles to allow adsorption onto foam interfaces. Additionally, the objective of flotation for dewatering purposes is not only to successfully remove particles through hydrophobic interactions, but to avoid excess water carry over, which would require secondary waste treatments. Therefore, flotation must be optimised for both particle removal and high dewatering ratios. Additionally, the adsorption dynamics of surfactant collectors onto $\text{Mg}(\text{OH})_2$ surfaces must be further understood to adapt for varying solid feed concentrations, as it would be expected that monolayer surfactant coverage conditions facilitate optimum recovery of $\text{Mg}(\text{OH})_2$. Given the impact of collectors and frothers on the foam stability and flotation performance in many mineral systems^{143,187,193}, a wide range of collector agents have been previously investigated. However, sodium lauroyl isethionate (SLI), which is an anionic surfactant consisting of an acid-ester sulphonate head group compared to the SDS sulphate head group¹³¹, has not previously been used as a collector in flotation. Thus, it is proposed that an understanding of the differences in collector adsorption, particle coagulation and foamability between two anionic surfactants (SDS and SLI) is key in tailoring a flotation process for effective $\text{Mg}(\text{OH})_2$ radwaste dewatering.

Here, fine magnesium hydroxide ($\text{Mg}(\text{OH})_2$) suspensions were used as a radwaste analogue to UK legacy wastes composed of corroded magnesium alloy fuel cladding⁶. The adsorption of SDS and SLI surfactants onto particle surfaces were characterised using total organic carbon analysis and fitted to heterogeneous Freundlich isotherms, as used in

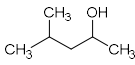
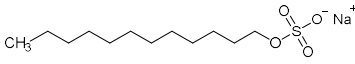
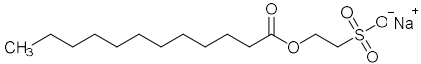
previous studies investigating the adsorption of surfactants onto mineral surfaces^{81,194-196}. The coagulation kinetics of sonicated Mg(OH)₂ suspensions were also investigated using static light scattering and compared to their surfactant driven aggregation with increasing SDS and SLI concentrations, to determine the collector's effect on particle size distributions. The foamability of particle stabilised suspensions was investigated using the well-established Bikerman column test^{143,191,197}, to calculate the gas retention time and dynamic foamability indices (*DFIs*) of the particle-surfactant systems, in comparison to non-ionic Methyl isobutyl carbinol (MIBC) frother. Finally, the flotation performance of the two surfactant systems was analysed using particle and water mass recovery metrics to calculate residual cell concentrations post-flotation, using a collection efficiency factor incorporating dewatering ratios. The flotation was then holistically analysed by comparing the monolayer surface coverage and resultant hydrophobicity to particle coagulation, foamability and the dewatering efficiency through flotation.

4.2) Experimental

4.2.1) Materials

Versamag Mg(OH)₂ (Martin Marietta, US) was used for all experiments has been previously characterised in Chapter 3. Anionic surfactants were selected as collectors as they have been shown to have an affinity to electrostatically adsorb to the surface of positively charged particles^{80,129,192,198}. Solid Sodium dodecyl sulphate (SDS) (TOKU-E, ≥99% pure), with a reported critical micelle concentration (CMC) of 8.2mM¹³¹, was dissolved in 0.5 l of Milli-QTM water to make up a stock solution of 16.4 mM. This solution was stored in cleaned polypropylene containers and diluted with further Milli-QTM water accordingly for experiments, as used in various previous flotation studies^{65,67,80,81}. Sodium lauroyl isethionate (SLI) (>98% purity), with a recorded CMC of 5.4mM¹³¹, was synthesised and crystallised via the methodology outlined by Jeraal et al.¹³¹. It was then dissolved in Milli-QTM water to make a stock solution of 10 mM, which was stored and sampled for various experiments similarly to the SDS. A stock solution of 100 ppm 4-methyl-2-pentanol (MIBC) (Sigma-Aldrich, 98%, density: 0.802 g.ml⁻¹) was also utilised in experiments. MIBC is commonly used as a frothing agent for foamability and dispersed air flotation tests^{142,199}. SDS, SLI and MIBC chemical formulas and structures can be found in Table 4.1.

Table 4.1: List of chemicals used in flotation with their corresponding purposes, chemical formulas and skeletal structures.

Chemical	Formula	Purpose	Structure
Methyl isobutyl carbinol (MIBC)	C ₆ H ₁₄ O	Frother	
Sodium dodecyl sulphate (SDS)	NaC ₁₂ H ₂₅ SO ₄	Collector	
Sodium lauroyl isethionate (SLI)	NaC ₁₄ H ₂₇ SO ₅		

4.2.2) Particle size analysis

20 ml suspensions were prepared using 2.5 vol.% Mg(OH)₂ suspensions, and were dispersed using an ultrasonic bath (Clifton Sonic) for 20 minutes to breakup any preformed aggregates. The suspensions were then added to a Mastersizer 2000E (Malvern Panalytical Ltd) static light scattering instrument, using a Hydro 2000SM aqueous dispersion cell (external dimensions of 140 × 175 × 390 mm and sample volumes between 50-120 ml). The suspension PSDs were then monitored as a function of time at 900 rpm with KNO₃ (Sigma Aldrich) background electrolyte at doses of 0, 1×10⁻³ and 1×10⁻² M KNO₃, to observe the effect of salt concentration on Mg(OH)₂ aggregation formation. The investigation time was intrinsically limited as the Malvern Mastersizer 2000E instrument has an obscuration envelope in which particle size measurements are validly taken. As particles aggregate, the overall number of particles and thus concentration decreases, which reduces obscuration eventually to numbers below the instrument lower limit. To observe the effect of adsorbed collectors on particle aggregation, varying concentrations of collector between 0 and 1000 μM were then added to 2.5 vol.% Mg(OH)₂ suspensions and agitated using a magnetic stirrer for 20 minutes. The Mg(OH)₂-collector suspensions were then added to the dispersion unit at 900 rpm, to ensure constant shear rates on the aggregated particulates, which could then be compared to the initial aggregation data without collector.

4.2.3) FBRM measurement

As per the previous methodology for performing FBRM analysis used in Chapter 3, *in situ* aggregate size determination was conducted using a Lasentec® Focused Beam Reflectance Measurement (FBRM) model PI-14/206 instrument (Mettler-Toledo) in macro mode. The reactor was set-up with the FBRM probe mounted at a 45° angle to the impeller shaft and 10 cm from the reactor vessel base within the mixing zone, to ensure representative flow of suspended particles past the measurement window¹⁷¹. The chord length distribution (CLD) of the system was monitored after allowing a 1 l suspension of 2.5 vol.% Mg(OH)₂

to equilibrate under agitation at 300 rpm for 5 minutes. Chord length number distributions were then computationally translated to volume percentage spherical equivalent diameters, assuming floc sphericity, as outlined by Rhodes²¹ and used in Chapter 3.

4.2.4) Collector adsorption onto $Mg(OH)_2$

Suspensions of 2.5 vol.% $Mg(OH)_2$ and varying concentrations of collector ranging from 0.82 μM to 1000 μM , were prepared in centrifuge tubes of 15 ml with the required collector concentration of SDS or SLI diluted from the stock solutions. The suspensions were then agitated using a carousel mixer (Compact Star CS4) for 24 hours, to ensure equilibrium adsorption of the anionic collectors on the $Mg(OH)_2$, before being centrifuged at 500 rpm for 4 hours to separate the particulates from the supernatant liquor. The supernatant liquor was then sampled using a needle and syringe through a 0.45 μm syringe filter to ensure no fine suspended material remained in the liquid. Remaining organic carbon concentration was determined using an IL550 Total Organic Carbon (TOC) analyser (Hach-Lange) and was translated to SDS and SLI concentrations using the stoichiometric ratios (see Table 4.1). Concentrations were quantified by comparing to pure collector solutions as benchmarks, where the difference in collector concentration was used to determine the amount of collector adsorbed onto the $Mg(OH)_2$.

Surfactant adsorption was analysed using the Freundlich adsorption isotherm, which is commonly used to measure the adsorption of collectors onto the surface of particles¹⁹⁴⁻¹⁹⁶. The linear form is shown in Eqn. 4.1, where q_e is the adsorption density of the collectors onto the $Mg(OH)_2$ surface, and in this study was calculated in units of both $mg.g^{-1}$ and $\mu mol.m^{-2}$ (by dividing through by the relative molecular mass of the collector (M_r) and the specific surface area (A_s) of the particles, with $A_s = 8 m^2.g^{-1}$). C_e is the equilibrium concentration of collector in the aqueous medium, $1/n$ is the Freundlich constant, and is related to the adsorption energy, while k_d is the adsorption affinity and essentially relates to the adsorption limit at infinitely small surfactant concentrations.

$$\text{Log}(q_e) = \text{Log}(k_d) + \frac{1}{n} \text{Log}(C_e) \quad (\text{Eqn. 4.1})$$

4.2.5) Foamability tests

Dynamic foam stabilities of Mg(OH)₂ collector mixtures and MIBC frother were investigated using a fritted glass burette with 19 mm internal diameter and 400 mm height, analogous to the Bikerman column experimental designs implemented by Gupta et al.¹⁴², Laskowski and Cho^{69,143} and Hunter et al.¹⁴⁴. MIBC foamability tests were conducted by preparing five 35 ml samples of MIBC at dosages of 2, 10, 25, 50 and 100 ppm with 2.5 vol.% Mg(OH)₂ suspensions without collectors initially to determine a baseline foamability of the MIBC in the electrolyte background provided by the Mg(OH)₂ semi-solubility. Foamability analysis was performed by combining frother (at 1 ppm) with 2.5 vol.% Mg(OH)₂ suspensions, along with SDS or SLI at various concentrations and superficial gas flow rates from 0 ml.min⁻¹ to 250 ml.min⁻¹ at fixed 50 ml/min intervals. The height of the foam layer was recorded after reaching equilibrium, and the airflow was then increased. After the system re-equilibrated, the foam height from the liquid-foam interface was again measured, and the process was repeated until the foam height began to grow non-linearly against flow rate.

Experiments were undertaken with varying dosed concentrations of SDS from 0.82 µM to 9.84 µM and SLI from 1 µM to 40 µM (noting these represented initial added concentrations) and were completed in triplicate. The retention time (t_r), which is often referred to as the Bikerman coefficient^{200,201}, is established from the slope of the linear part of the dependence of the total gas volume in solution and foam, plotted with respect to gas flow rate (for increasing frother or collector concentrations). As the diameter of the Bikerman column is constant, measurements can be reduced to changes in foam height (H_f) and superficial air velocity (u) as shown in Eqn. 4.2. The dynamic foamability index (DFI) can then be determined using the procedure used by previous authors^{142,143}. The DFI allows comparison of collector and frother foamabilities independent of concentration, for a more robust assessment of flotation performance than retention time alone. The DFI is obtained from the t_r values as a function of the dosed concentration (C_d) limiting slope, as C_d approaches 0, shown in Eqn. 4.3.

$$t_r = \frac{\Delta H_f}{\Delta u} \quad (\text{Eqn. 4.2})$$

$$DFI = \left(\frac{\partial t_r}{\partial C_d} \right)_{C_d=0} \quad (\text{Eqn. 4.3})$$

4.2.6) Flotation experiments

A bespoke flotation cell (210 ml, 65 mm ID; Fig. 4.1) was manufactured with an air inlet and a fritted glass base similar to the designs used by Zhang et al.¹⁹⁹ and Prajitno et al.⁷¹. 12.31 g of Mg(OH)₂ was added to a measuring cylinder and dosed with 98 µM of MIBC as per this previous work^{71,199}, along with the required dose of SDS, and then made up to 210 ml with Milli-Q® water. The cell was stirred for 20 minutes at 250 rpm to facilitate adequate adsorption of SDS to Mg(OH)₂ surfaces. The airflow rate into the bottom of the cell was set at 0.1 l.min⁻¹ resulting in a superficial gas velocity of 5 cm.s⁻¹, which was set low to prevent over foaming of the surfactant loaded suspension. The agitator speed was reduced to 100 rpm to minimise turbulence in the cell, preventing bubble disengagement. Froth generated above the air-water interface was collected through the outlet at the top of the vessel, and into an oven for 24 hours to evaporate the water component of the foam, leaving behind the recovered particulates. The recovered solids were then weighed to determine a number of performance indicators.

The Mg(OH)₂ particle recovery percentage was measured, as shown in Eqn. 4.4, where the recovery percentage, $P_{\%}$, from Mg(OH)₂ suspensions was calculated using a mass balance approach, as suggested by Zhang et al.¹⁹⁹. It is the percentage of the mass of Mg(OH)₂ recovered from the initial suspension in the foam phase, where $M_{r,p}$ is the recovered mass of Mg(OH)₂ from the foam phase and $M_{T,p}$ is the total initial mass of Mg(OH)₂ in the suspension.

$$P_{\%} = \left(\frac{M_{r,p}}{M_{T,p}} \right) \times 100\% \quad (\text{Eqn. 4.4})$$

The percentage of fluid remaining in the cell, $W_{\%}$, was also calculated from the measured mass of the water in the foam phase, $M_{r,w}$, extracted from the flotation cell. It was obtained differentially from the mass of the aluminium collection container before and after evaporation, and divided by the total initial mass of water in the cell $M_{T,w}$, as given in Eqn. 4.5.

$$W_{\%} = \left(\frac{M_{T.w} - M_{r.w}}{M_{T.w}} \right) \times 100\% \quad (\text{Eqn. 4.5})$$

The $\text{Mg}(\text{OH})_2$ particle concentration remaining in the flotation cell, $C_{\%}$, can then be determined from mass balance principles, as shown in Eqn. 4.6.

$$C_{\%} = \left(\frac{M_{T.p} - M_{r.p}}{M_{T.w} - M_{r.w}} \right) \times 100\% \quad (\text{Eqn. 4.6})$$

The performance of the collectors were then compared using a collector efficiency factor, ξ , shown in Eqn. 4.7, which is a ratio of the percentage fraction of the particles-to-fluid recovered from the flotation cell. When $\xi > 1$, there are more $\text{Mg}(\text{OH})_2$ particles recovered than water by mass, when $\xi = 1$ there is equal particle-fluid extraction (entrainment) and when $\xi < 1$ there is more fluid being extracted than $\text{Mg}(\text{OH})_2$ particles (indicative of overly wet froths). The collection efficiency factor can then be used to determine the optimum dose of collector to maximise solid-liquid separation.

$$\xi = \frac{P_{\%}}{100 - W_{\%}} \quad (\text{Eqn. 4.7})$$

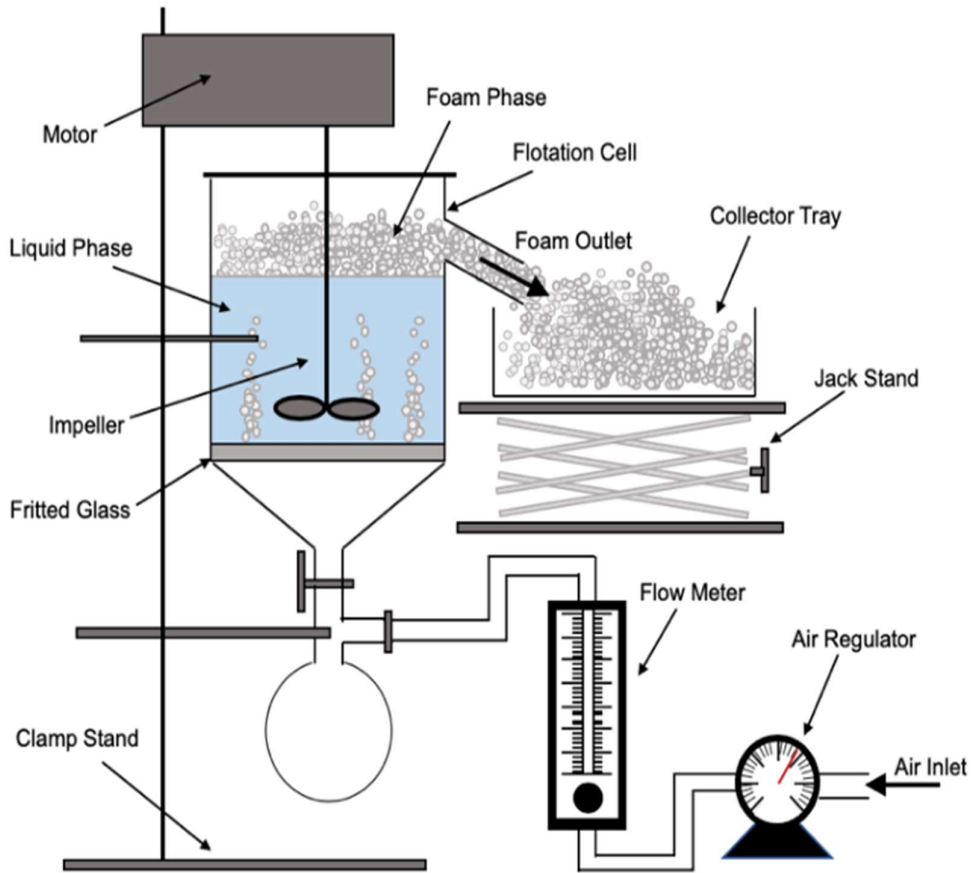


Figure 4.1: Schematic of batch flotation cell used for dispersed air flotation tests.

4.3) Results and discussion

4.3.1) Natural aggregation characterisation

Scanning electron micrographs of $\text{Mg}(\text{OH})_2$ reveal a structure made up of aggregates of pseudo-hexagonal platelets as shown in Fig. 4.2A, similar to those reported by Johnson et al.¹⁶ and Maher et al.⁷, and in Chapter 3. This fused nanocrystallite platelet arrangement, gives rise to the large relative surface area in terms of that expected from spherical equivalent estimations¹⁷⁰, which is an important factor to consider when evaluating the adsorption density of collectors to the $\text{Mg}(\text{OH})_2$ surface¹⁹⁸. The $\text{Mg}(\text{OH})_2$ specific surface area was investigated in Chapter 3 using a Brunauer–Emmett–Teller (BET) approach, and was found to be $\sim 8 \text{ m}^2 \cdot \text{g}^{-1}$. Whilst this could be considered to be a high specific surface area, for particle agglomerates of micron size, Biggs et al.²⁴ have observed similar $\text{Mg}(\text{OH})_2$ material as having a specific surface area of $15.43 \text{ m}^2 \cdot \text{g}^{-1}$, due to its fractal nature and high internal porosity⁴⁸. Similar mineral pseudo-hexagonal platelet material, such as

aluminium hydroxide, have also been found to have correspondingly high BET surface areas, ranging from $1.5 \text{ m}^2 \cdot \text{g}^{-1}$, as observed by Adekola et al.²⁰², up to $91 \text{ m}^2 \cdot \text{g}^{-1}$ measured by Rosenqvist²⁰³.

The low surface potential of magnesium hydroxide (of $\sim 12 \text{ mV}$, as noted in the methodology in Chapter 3) has implications when considering colloidal stability of particulates, suggesting they may naturally aggregate¹⁰⁸. Aggregation may affect the accessible surface area in aqueous media, resulting in consequences for adsorption density¹⁹⁸. Additionally, increases in particle size distributions (PSDs) may potentially lead to hydrodynamic limitations in the flotation process^{83,146}. Therefore, a series of measurements were performed to understand particle size changes in dispersions. Fig. 4.2B shows the differences in PSDs of sonicated $\text{Mg}(\text{OH})_2$, using static light scattering, where the sample was dispersed in a small distribution cell at 900 rpm, with an approximate median particle size (d_{50}) of 2-3 μm . Also shown in Fig. 4.2B is a non-sonicated dispersion, measured *in situ*, using the focused beam reflectance measurement (FBRM) technique, which presents a considerably larger range, with comparative $d_{50} = 149 \mu\text{m}$. Whilst these techniques are different (and noting the FBRM represents a volume based conversion from raw chord length distributions in Chapter 3) the significant disparities in PSDs indicate that $\text{Mg}(\text{OH})_2$ suspensions will naturally further aggregate under low shear conditions, due to their low zeta potential¹⁰⁸. Previous work by Johnson et al.¹⁶ on the same type of $\text{Mg}(\text{OH})_2$ also found naturally coagulated aggregates in the range of 150 μm , consistent with the FBRM data.

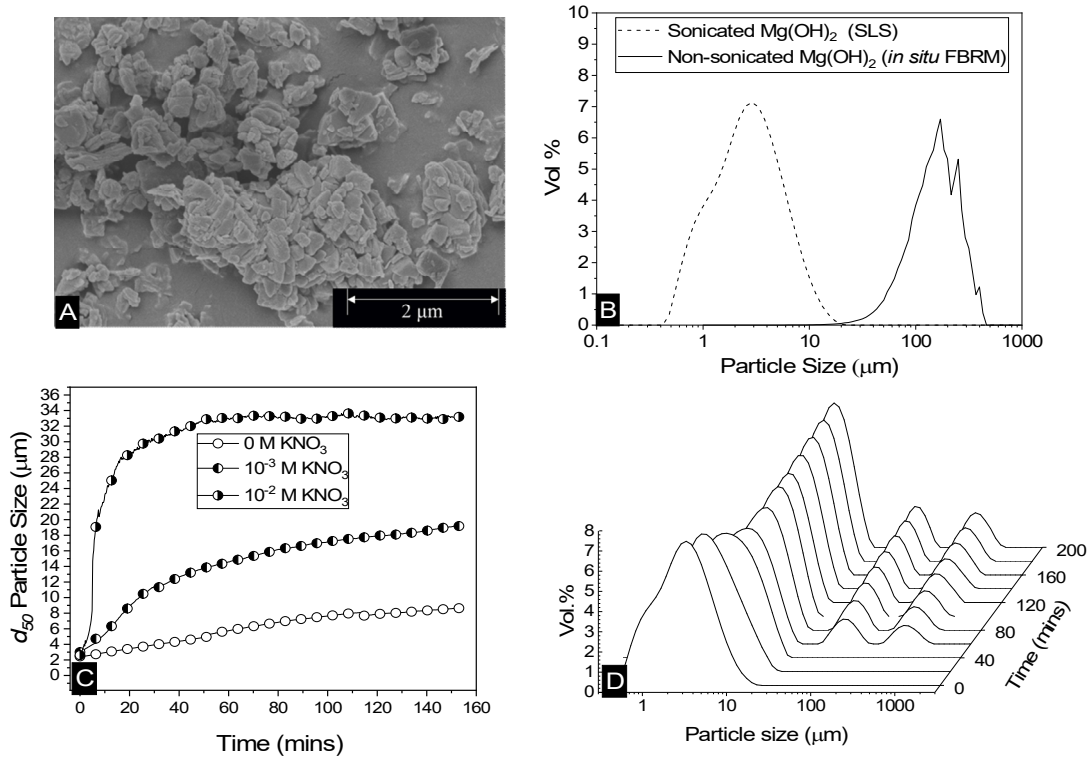


Figure 4.2: A) Scanning electron micrograph of dry Mg(OH)₂ powder. B) Particle size distributions of sonicated Mg(OH)₂ dispersions agitated at 900 rpm measured using static light scattering, and non-sonicated agitated at 300 rpm measured *in situ* using focused beam reflectance measurement. C) Change in the 50th cumulative percentile (*d*₅₀) particle size with time of Mg(OH)₂ dispersions agitated at 900 rpm, along with the addition of 10⁻² M and 10⁻³ M KNO₃ at 900 rpm. D) The change in the volume based (vol.%) particle size distribution of Mg(OH)₂ agitated at 900 rpm with time.

The change in the 50th cumulative percentile (*d*₅₀) particle size with time of Mg(OH)₂ suspensions is shown in Fig. 4.2C; these were also sonicated for 20 minutes to break up any preformed aggregates. The post-sonication re-aggregation of the sonicated sample can be observed by the change in *d*₅₀ with time when added to the Mastersizer dispersion cell at 900 rpm, along with KNO₃ electrolyte backgrounds of 10⁻³ M and 10⁻² M. For all datasets, the *d*₅₀ increased with time indicating different degrees of particle aggregation. The role of electrolytes in electric double layer compression, resulting in greater aggregation is well documented in previous literature^{155,165,195,204}, with the data in Fig. 4.2C following expected trends, where an increase in KNO₃ concentration results in a greater degree and rate of aggregation^{165,205}.

The impact of aggregation on polydispersity is shown in Fig. 4.2D in the form of PSDs of sonicated suspensions evolving over time. It is often difficult to completely understand the aggregation process when considering a single number to represent a whole particle size distribution, such as the d_{50} . Therefore, an insight into the change in particle size dispersity and PSD transition to polymodality can provide important information on the aggregation mechanism. For times up to 40 minutes, there is a gradual shift in the PSD peaks to the right, indicating a gradual size increase (similar to that captured by Fig. 4.2C in increasing d_{50} values). At 40 minutes however, the emergence of two additional peaks in the region of ~ 100 - $1000 \mu\text{m}$ is evident. The magnitudes of these additional peaks (vol.%) increases with time, accompanied by a continuing shift to the right of the initial peak (~ 0.1 - $20 \mu\text{m}$). The emergence of the two additional peaks (~ 100 - $1000 \mu\text{m}$) does not visibly impact the trajectory of the d_{50} size increase with time (in Fig. 4.2C) as their relative magnitudes are much lower than that of the initial peak, and they also do not lead to significant skewing of d_{50} value (highlighting the limitations of using this single value). It is additionally noted that the relatively high shear rate in the instrument cell (900 rpm) may lead to continual aggregate breakage, reducing the development of these larger size peaks. It is also likely why large single macro-aggregate peaks are not observed, as evidenced with the *in situ* FRBM data (as these measurements were gained in a larger 300 rpm low-shear cell).

What is particularly important regarding the emergence of these additional peaks at ~ 100 - $1000 \mu\text{m}$ at intermediate times, is the inference of the distinctive development of a new aggregation mechanism. The initial peaks ($t < 40$ minutes) indicate a particle-cluster aggregation mechanism, where the dispersed $\text{Mg}(\text{OH})_2$ gradually aggregates by a particle wise addition to developing $\text{Mg}(\text{OH})_2$ clusters. As time elapses and more of these clusters are formed, this results in more probabilistic cluster-cluster macro-aggregation^{117,206}, represented by the additional two peaks after 40 minutes. As time develops, these peaks overlap as can be observed in the 10^{-2} M KNO_3 system in the Appendix B, Fig. B1, which displays more advanced aggregation within the time observed, due to the depletion of the electric double layer from the KNO_3 electrolytes²⁰⁵. Finally, the PSD reaches an equilibrium, which is a function of the shear rate in the dispersion cell (i.e. greater shear reduces equilibrium particle size)^{55-57,59,60}.

4.3.2) Collector adsorption and effect on particle aggregation

The specific adsorption of SDS and SLI onto $\text{Mg}(\text{OH})_2$ as a function of concentration is shown in Figs. 4.3A(i) and 4.3A(ii) presented as the logarithmic adsorption capacity, $\log(q_e)$, plotted against the logarithmic collector equilibrium concentration, $\log(C_e)$, for SDS and SLI respectively. The linear form of the Freundlich adsorption isotherm (Eqn. 4.1) was fitted to the data in two clear regions, which were assumed to represent monolayer and bilayer (ad micelle) regions respectively, commonly found with charged surfactant adsorption on solid surfaces^{71,207}. The associated Freundlich adsorption coefficients were extrapolated from the linear fittings and are displayed in Table 4.2. The intercept of the monolayer and bilayer Freundlich adsorption isotherms represents the collector equilibrium concentration, where the monolayer to bilayer transition is assumed to represent the maximum monolayer coverage adsorption density (denoted C_e^* and q_e^* respectively).

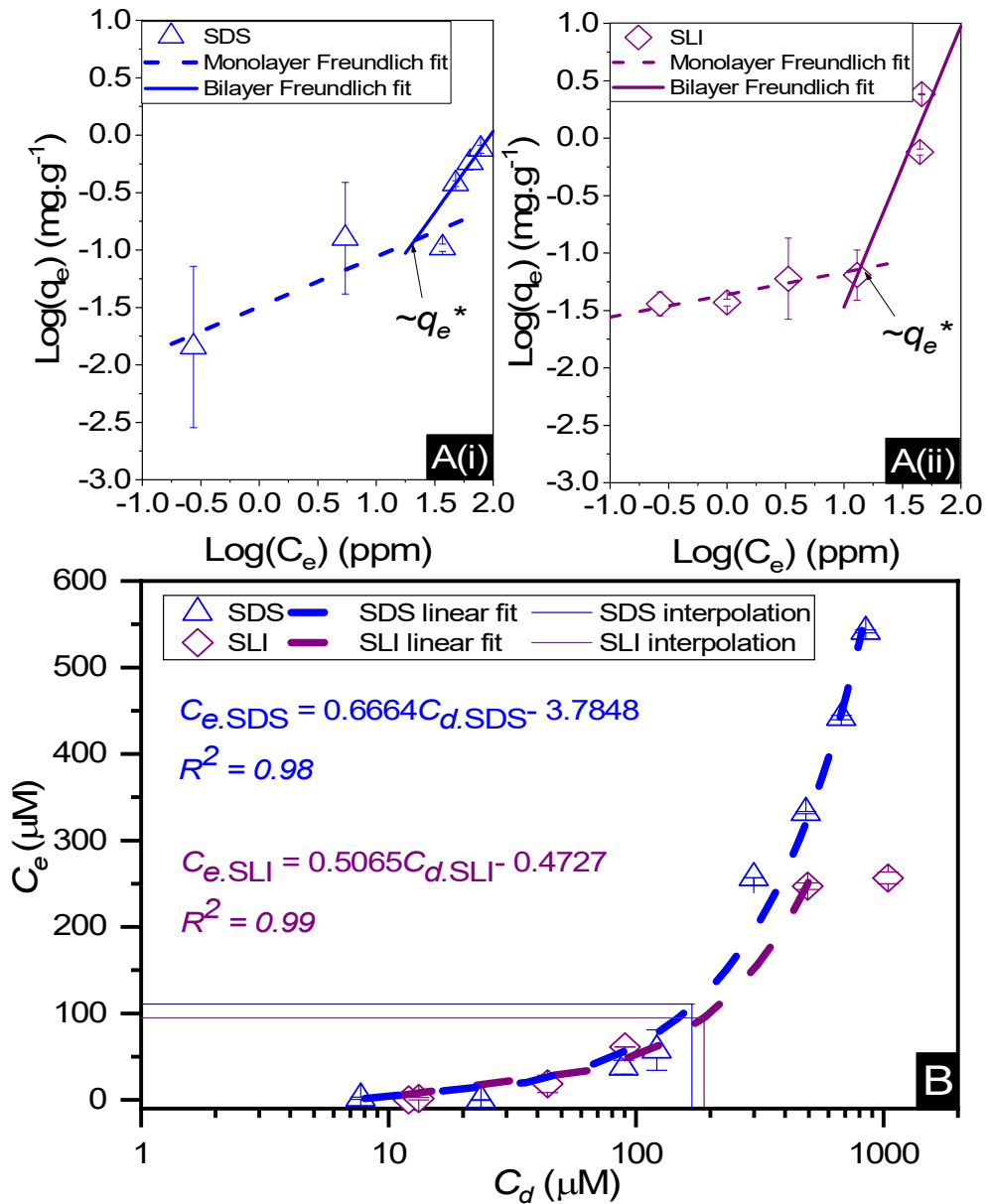


Figure 4.3: A) Two region fitted Freundlich adsorption isotherm including both monolayer and bilayer adsorption profiles for i) sodium dodecyl sulphate and ii) sodium lauroyl isethionate collectors on $\text{Mg}(\text{OH})_2$. It is noted that q_e^* is the maximum monolayer collector adsorption density (monolayer to bilayer transition point). B) Calculated equilibrium concentration, C_e , established from the dosed collector concentration (C_d) minus the amount of surfactant adsorbed. The monolayer-bilayer transition concentration is shown for both surfactants by interpolation.

The corresponding initial collector dosage concentration representing this transition, C_d^* , can be interpolated from the plot of initial dosed collector concentration, C_d , and the

collector supernatant equilibrium concentration, C_e , (shown in Fig. 4.3B). The Freundlich adsorption isotherms have relatively good fits with R^2 values ranging from 0.87 to >0.99, although the fits were notably better for the bilayer adsorption regimes, which is likely due to the lower experimental uncertainty of carbon concentration analysis at higher collector concentrations. A feature of the Freundlich adsorption model is that it is derived by assuming an exponentially decaying adsorption site energy distribution. As the Freundlich constant ($1/n$) that based on adsorption density increases, this represents a greater adsorption intensity on the $Mg(OH)_2$ surface occurs with the bilayer¹⁹⁶.

Table 4.3: Freundlich adsorption isotherm coefficients for sodium dodecyl sulphate (SDS) and sodium lauroyl isethionate (SLI) monolayer and bilayer adsorption profiles determined from linear fittings in Fig. 4.3A(i) and 4.1A(ii). Here, K_d and $1/n$ are the Freundlich coefficients related to the adsorption affinity and intensity respectively, q_e^* is the maximum monolayer collector adsorption density (i.e. monolayer to bilayer transition point), C_e^* and C_d^* are the collector supernatant equilibrium and initial dosed concentration respectively at the monolayer to bilayer transition point.

Isotherm value	Sodium dodecyl sulphate (SDS)		Sodium lauroyl isethionate (SLI)	
	Monolayer	Bilayer	Monolayer	Bilayer
<i>Freundlich R²</i>	0.89	0.99	0.87	0.96
<i>K_d</i> (mg.g ⁻¹)	3.21×10^{-2}	1.60×10^{-3}	4.43×10^{-2}	1.21×10^{-4}
<i>K_d</i> (μmol.m ⁻²)	1.39×10^{-2}	6.94×10^{-4}	1.61×10^{-2}	4.39×10^{-5}
<i>1/n</i>	0.43	1.41	0.2	2.44
<i>n</i>	2.30	0.71	5.10	0.41
<i>q_e[*]</i> (μmol.m ⁻²)		~0.11		~0.05
<i>q_e[*]</i> (mg.g ⁻¹)		~0.24		~0.14
<i>C_e[*]</i> (μM)		~111		~95
<i>C_e[*]</i> (mg.g ⁻¹)		~0.03		~0.03
<i>C_d[*]</i> (μM)		~172		~188
<i>C_d[*]</i> (mg.g ⁻¹)		~0.05		~0.03
<i>Linear R²</i>		0.98		0.99

By comparing the monolayer adsorption profiles for SDS and SLI, it is apparent that the adsorption intensity is greater for SDS than SLI, with corresponding $1/n$ values of 0.43 and 0.2 respectively. These $1/n$ values are similar to those observed by Yekeen et al.¹⁹⁵ who investigated the adsorption of SDS onto kaolinite in the presence of Al_2O_3 and SiO_2 nanoparticles. The maximum monolayer adsorption capacities (q_e^*) determined from the intercept of the monolayer and bilayer Freundlich adsorption isotherms of the SDS and SLI are ~0.11 and ~0.05 μmol.m⁻² respectively. These values are slightly higher than those observed by Yekeen et al.¹⁹⁵, who found maximum SDS adsorption onto Al_2O_3 nanoparticles to be ~0.04-0.08 μmol.m⁻² (5.102 mg.g⁻¹, where $A_s=230-400$ m².g⁻¹¹⁹⁵) where it is assumed the Al_2O_3 particles are similarly charged to the magnesium hydroxide (although specific chemical affinities may be different).

When comparing SDS to SLI, it is noted that due to the acid-ester sulphonate head group, SLI has a lower hydrophilic head electron cloud density than SDS, which is due to the difference in chemical structure (see Table 4.1). The reduced electron density is due to SLI having an additional ethyl chain between the S and O (ergo isethionate functional group) unlike in the SDS (which has a sulphate head group). The increased hydrophilic head group size will act in conjunction with the longer hydrophobic chain length (which may induce steric hindrance) to overall reduce the maximum monolayer adsorption density compared to SDS, as observed in Figs. 4.3A(i) and 4.3A(ii).

When considering the bilayer adsorption regimes, a critical characteristic is the adsorption intensity is greater than the monolayer regime, but contrary to the monolayer regime, the adsorption is noticeably greater for SLI than SDS in the bilayer region, likely due to its longer carbon chain leading to a greater degree of hydrophobicity. The sudden increase in adsorption intensity is caused from the formation of surface aggregates of the monolayer (*hemimicelle*) that are derived from the lateral interaction of hydrocarbon chains. This lateral attraction generates an additional driving force to superimpose the existing electrostatic attraction, causing a sharp increase in adsorption, due to the reduction in free energy that occurs by reducing the degree of H₂O dipole orientation around exposed collector hydrophobic tails, thus forming a bilayer at a greater intensity than the initial monolayer^{102,108,137,196,208–210}.

The effect of surfactants on the aggregation of sonicated Mg(OH)₂ dispersions is presented as the volume based PSDs for Mg(OH)₂ suspensions (initially sonicated to break up any preformed aggregates) dosed with collector concentrations ranging from 0-820 μM for SDS and 0-1000 μM for SLI (below both SDS and SLI CMCs) in Fig. 4.4. There are distinctive changes in the PSDs with varying doses, most noticeably at concentrations above the q_e^* max adsorption density (monolayer-bilayer transition point) values (determined in Fig. 4.3A for both systems, at ~172 μM and ~188 μM for SDS and SLI respectively).

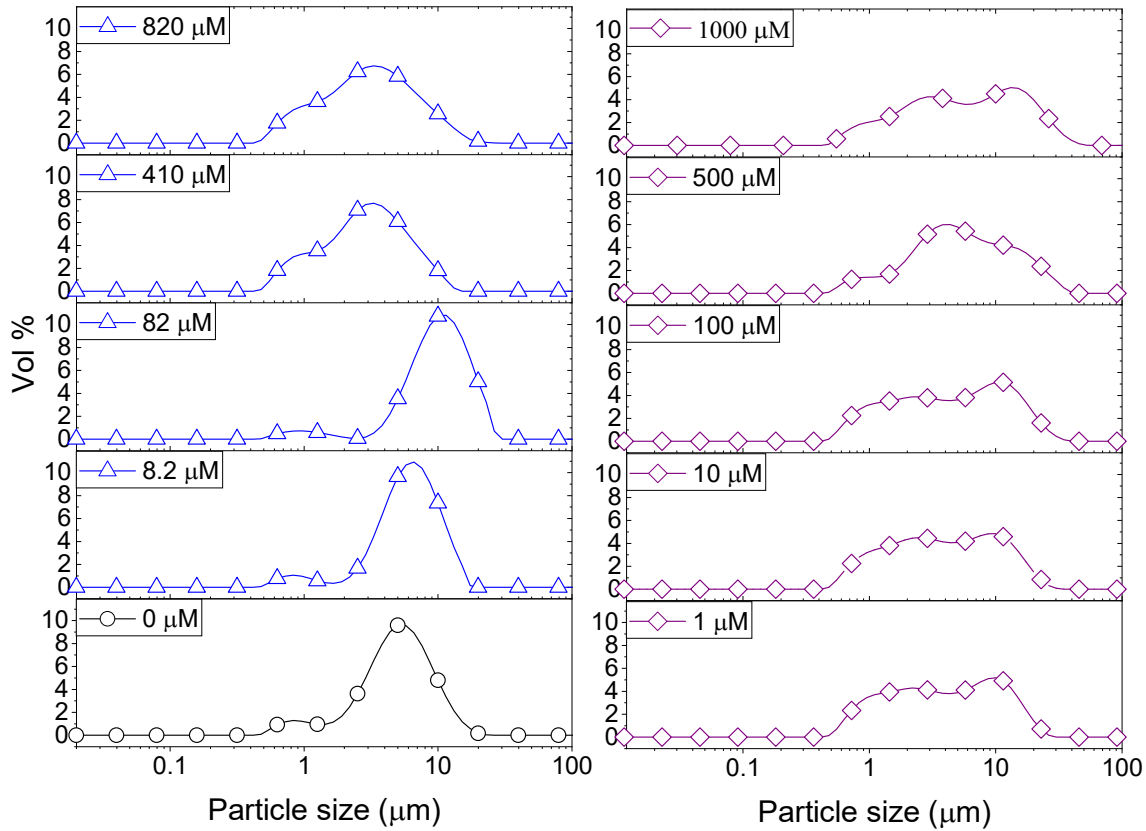


Figure 4.4: Particle size distributions for $Mg(OH)_2$ suspensions sonicated for 20 minutes, dosed with 0-820 μM of SDS and 0-1000 μM of SLI and stirred for 20 minutes, before analysis with static light scattering using a 900 rpm flow cell.

For 0 μM collector dose, the PSD may be considered as pseudo-bimodal, with a small peak at 0.3-2 μm of magnitude ~ 2 vol.% and a major peak at 2-20 μm of magnitude ~ 8 vol.%. The smaller peak is likely the size of the primary particles, which were determined in Chapter 3 to be ~ 0.3 μm via SLS, whereas the larger peak is likely the equilibrium particle size achieved by sonication (with some initial particle-cluster aggregation as discussed in Figs. 4.2C and 4.2D). When considering the SDS systems, when $C_d < C_d^*$, there is a visible shift of the larger peak to the left accompanied by gradual peak broadening, indicating an increase in particle size from enhanced aggregation conditions. When $C_d > C_d^*$, the particle size distribution reduces again, back towards the 0 μM distribution (although, with a broader monomodal peak). Potentially, the high concentration of SDS may have resulted in some aggregation of the primary particles in the smaller peak size range (0.3-2 μm), but it should be noted that the span of the PSD does not explicitly show any increase, which may indicate that the particle size maxima are shear rate dependent. Alternatively, the greater surface coverage of SDS may stabilise smaller nucleation clusters similar to how

surfactants stabilise nanoparticle systems^{188,211,212}, preventing the initial cluster-cluster aggregation processes from developing into those observed in Fig. 4.2D at 40 minutes. The SLI system shows similar trends to SDS, however, there is greater PSD dispersity at $C_d < C_d^*$ and the overlap of the primary particle size range (0.3-2 μm) and the main peak (2-20 μm) is visible as an emerging peak at \sim 2-8 μm above 100 μM SLI doses (i.e. $C_d > C_d^*$). The SLI also displays a less clear trend of particle size reduction in the bilayer region, suggesting a reduced dispersant property for the SLI in comparison to the SDS at high concentrations.

Prajitno et al.⁷¹ investigated the effect of Ethylhexadecyldimethylammonium bromide and Cetylpyridinium chloride collectors adsorbed onto clinoptilolite on suspension dispersity using SLS. Whilst Prajitno et al.⁷¹ observed no significant shift in the clinoptilolite PSD d_{50} with collector adsorption, increased polydispersity was observed similar to the SDS and SLI systems in this work. Similar to the SDS and SLI, the hydrophilic head group (in this case cationic) of the surfactants investigated by Prajitno et al.⁷¹ adsorbed onto the anionic clinoptilolite particle surface, resulting in the clinoptilolite particles having greater hydrophobicity at monolayer coverage (similar to SDS and SLI in Fig. 4.3A). The greater hydrophobicity resulted in a greater surface energy in the water environment, reducing stability leading to aggregation, although not to a significant enough extent to facilitate considerable flocculation⁷¹. Like this system, the adsorption of SDS and SLI should not present any significant issues regarding the suspension's dispersion stability⁷¹, indicating that the PSD of suspension in the flotation is likely best represented by the *in situ* measurements taken in Fig. 4.2B.

4.3.3) Foamability

The change in foam height versus surfactant or frother concentration found in the Bikerman column tests for SDS, SLI and MIBC respectively (all in 2.5 vol.% magnesium hydroxide suspensions) are shown in Fig. 4.5A-C. For each of these investigations, the volume of foam increases linearly at lower air flowrates, before entering an unstable non-linear region, indicative of airflow turbulence in the burette^{69,142,144,201,213}. Also, for the SDS and SLI collector systems, the maximum experimental concentrations presented represent the transition point before the foam became significantly unstable (and no accurate measurements at higher concentrations were possible). The upper relative concentrations of SDS and SLI are within the regions for monolayer surfactant coverage (see Fig. 4.3)

where significant hydrophobization of particles is assumed to occur. It was observed visually that $\text{Mg}(\text{OH})_2$ particles in this concentration region for both surfactants were transported into the foam phase, causing a heterogeneous froth, where less particle dense regions collapsed, forming cavities in the foam structure preventing further foam volume expansion (see Appendix Fig. B2). The SDS had a lower boundary concentration for this effect than SLI, with maximum experimental concentrations of $9.84 \mu\text{M}$ and $40 \mu\text{M}$ respectively (see Table 4.4). This difference is likely related to the greater adsorption intensity of SDS onto $\text{Mg}(\text{OH})_2$ surfaces at lower concentrations (again, see Fig. 4.3). It is also noted that no such effects were evident with the uncharged MIBC frother, and it is assumed to not have any considerable interaction with mineral cationic surfaces. Therefore, MIBC tests were conducted over a much larger concentration range.

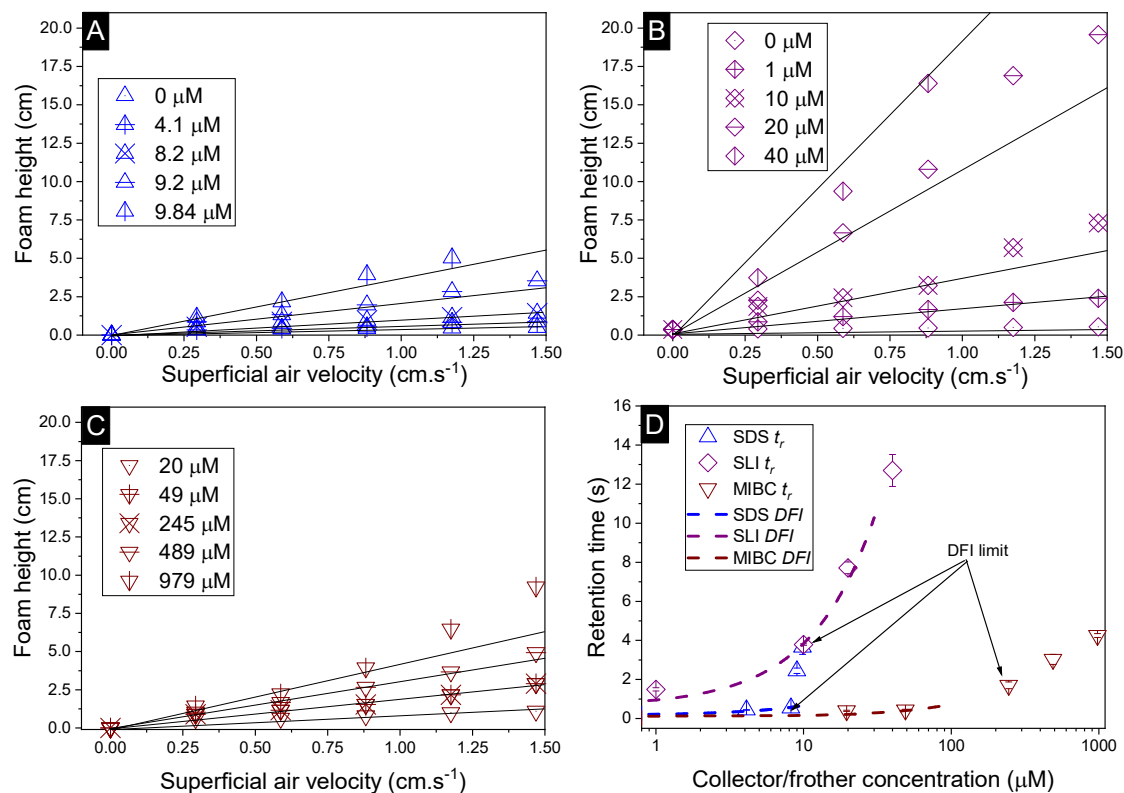


Figure 4.5: Change in foam height with superficial air velocity for A) SDS, B) SLI, and C) MIBC, all with 2.5 vol.% $\text{Mg}(\text{OH})_2$ suspensions. D) The retention time was calculated using Eqn. 4.2, with varying collector or frother concentration. Solid lines in A) to C) represent linear trendlines to determine the gas retention time (t_r). Dashed lines in D) represent the linear fit of the dynamic foam stability index (DFI) as per Eqn. 4.3. DFI limit defines the max collector/frother concentrations that are used to determine the DFI from Eqn. 4.3.

The retention time of the gas in the foam phase, with varying concentrations of each collector or frother (calculated using Eqn. 4.2) was measured and is presented in Fig. 4.5D. While the retention time does increase with surfactant concentration for all systems, it does not increase at the same rate, due to the impact of enhanced particle-stabilisation effects in the SDS system (with respect to the SLI-particle system) which complicates the use of retention time as a marker for foam stability in these mixed surfactant-particle cases. The MIBC system achieves greater retention times than the SDS-particle system at high concentrations, but again, this is likely from the concentration limits imposed by the additional foam-particle stability. Indeed, it is noted that in general, MIBC is used as an active frother that promotes stable foams over relatively short periods of time, allowing for high degrees of mineral separation, without long lasting froths that hinder breakdown in onward treatments²¹⁴.

Table 4.4: Maximum surfactant or frother concentration measurable in Bickerman foam tests, due to particle overstabilisation preventing foam development, and corresponding dynamic foamability index (*DFI*), calculated using Eqn. 4.3.

System	Max conc. (μM)	<i>DFI</i> (s.l.mol^{-1})
Sodium dodecyl sulphate	9.84	49×10^3
Sodium lauroyl isethionate	40	321×10^3
Methyl isobutyl carbinol	979	6×10^3

To compare the foamability with a measure independent of concentration, the dynamic foamability indices (*DFI*) were calculated using Eqn. 4.3 and are displayed in Table 4.4. The collector-particle systems displayed *DFIs* greater than that of the frother system, where SDS and SLI have *DFIs* of 49×10^3 and 321×10^3 s.l.mol^{-1} respectively. The MIBC frother displayed a *DFI* of 6×10^3 s.l.mol^{-1} , which is lower than previous work done by Gupta et al.¹⁴², Melo and Laskowski⁶⁹ and Laskowski et al.¹⁴³, who found *DFIs* of MIBC in the range of $34\text{-}37 \times 10^3$ s.l.mol^{-1} . However, in the study by Melo and Laskowski⁶⁹, they also investigated the effect of brine on the *DFI* of MIBC and found a much lower value of 3.9×10^3 s.l.mol^{-1} . This difference indicates that ion effects on frother activity may significantly impact the *DFI* of MIBC, and is important in the current systems because of the semi-solubility of $\text{Mg}(\text{OH})_2$, which at 2.5 vol.%, possess an ionic strength sufficient to alter the pH of suspensions to $>10\text{-}10.5$. In terms of the surfactant systems, a previous study with SDS by Khoshdast et al.¹⁹⁷, found the *DFI* to be 92×10^3 s.l.mol^{-1} , and so similar to the

value observed in this work (although, any comparisons must be made with caution, owing to the complication of SDS interactions with the $\text{Mg}(\text{OH})_2$ particles in the present case). As the *DFI* for SLI solutions (with or without particles) has not been recorded previously in literature (to the authors' knowledge) additional Bickerman column tests were completed with SLI only solutions (see Appendix Figs. B3A and B3B) where the *DFI* was calculated to be $324 \times 10^3 \text{ s.l.mol}^{-1}$, and so very similar to the particle stabilised SLI system in Table 4.4

The role of particles in foam stabilisation has been extensively researched, where Hunter et al.^{140,144} suggested that for strongly hydrophobic particles with contact angles approaching 90° , particles act as steric barrier to bubble coalescence due to their high particle-interface attachment energy. However, particles that are weakly hydrophobic may also stabilise foams through retarding film drainage in the lamella via film stratification^{129,190,215–217}, which is more important for dynamic wet foams found in flotation operations, and implies that they have greater water retention at their equilibrium lamella fluid drainage¹⁴⁴. Increased water retention is an important factor in flotation as it may lead to increased water carry-over reducing solid-liquid separation efficiencies. Given the greater *DFI* for SLI, which has lower collector monolayer adsorption densities, increased stabilisation via film drainage retardation may entrain greater amounts of water with less particles, potentially lowering the collection efficiency factor for the SLI system. The greater foam volume generated by SLI compared to SDS, combined with the lower adsorption density of the SLI onto the $\text{Mg}(\text{OH})_2$ particles, indicates that there is a greater water content in the foam. Combined with the potential for particle drainage or lower collection due to the comparatively subpar hydrophobization, SLI may result in inferior flotation conditions compared to the SDS system^{65,71,79–81,143,144,187}.

4.3.4) Flotation performance

Particle recovery as a mass percentage of the total $\text{Mg}(\text{OH})_2$ particles initially in the flotation cell as a function of collector concentration of SDS and SLI is presented in Fig. 4.6A. As the collector concentration increases, there is a clear increase in $\text{Mg}(\text{OH})_2$ recovery from the flotation cell using both collectors, which plateaued at 93% and 86% $\text{Mg}(\text{OH})_2$ recovery for SDS and SLI respectively. Excluding the first recorded point at $\sim 1 \mu\text{M}$ collector concentration, the SDS significantly outperforms the SLI in regards to $\text{Mg}(\text{OH})_2$ mass recovery. Fig. 4.6B compares the mass of water remaining in the flotation

cell as a function of collector concentration for SDS and SLI. Much like when considering the mass of $Mg(OH)_2$ recovered from the flotation cell, SDS outperformed the SLI again, with the region of greatest separation in performance located at the predicted region (data points enclosing 172-188 μM) for maximum monolayer coverage discerned from Fig. 4.3A and 4.3B. The combination of the mass of particles and water recovered from the flotation cell can be used to calculate the residual cell concentration from Eqn. 4.6, as shown in Fig. 4.6C. Consistent with the previous performance measures, again the SDS considerably outperforms the SLI system, achieving the lowest cell volumetric concentrations of 0.5 vol.% and 1.6 vol.% respectively (from initial suspension concentration of 2.5 vol.%). Once again, these optimum performances lay in the maximum monolayer coverage regions (calculated from the adsorption isotherms) as highlighted in Fig. 4.6A-C.

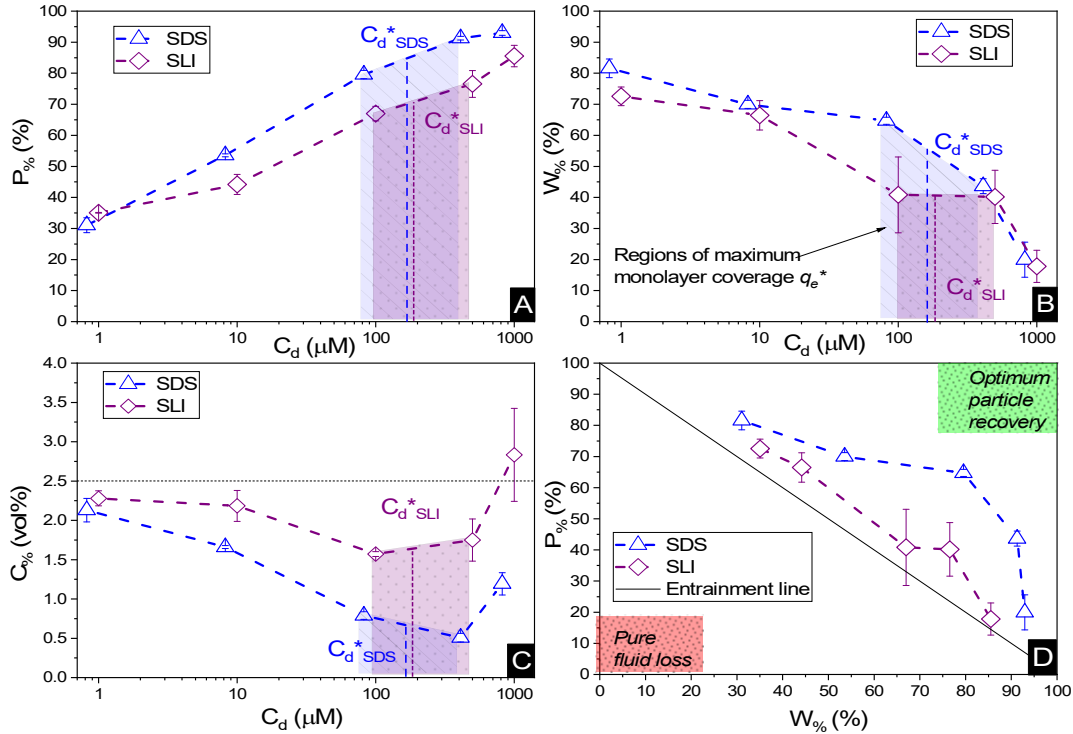


Figure 4.6: The flotation performance with increasing collector concentration for 2.5 vol.% suspensions, as a measure of A) mass percentage ($P\%$) of $Mg(OH)_2$ particles recovered, B) mass percentage of water ($W\%$) remaining in the cell, and C) the residual $Mg(OH)_2$ concentration ($C\%$) in the flotation cell post flotation. D) The corresponding mass percentage of water recovered with increasing mass percentage of $Mg(OH)_2$ particles recovered. Connecting lines are a visual guide.

For SLI, the residual cell concentration post flotation in the bilayer adsorption regime increased, likely due to the increase in fluid loss intensity shown in Fig. 4.6B when $C_d >$

C_d^* . For greater insight into performance, the fluid loss from the cell and particle recovery were plotted with respect to each other, along with an equal entrainment line ($P\% = W\%$) as shown in Fig. 4.6D. Values above the entrainment line represent a higher ratio of the mass percentages of particle recovery to water remaining in the flotation cell post flotation, i.e. greater collection efficiency. Conversely, values below this line represent a greater amount of water being recovered than particles on a mass basis. All data points for SDS and SLI lay above the entrainment line showing at all concentrations of collector dose there is successful particle-fluid separation to some degree, while the heightened performance of SDS is clearly evident across the concentration range.

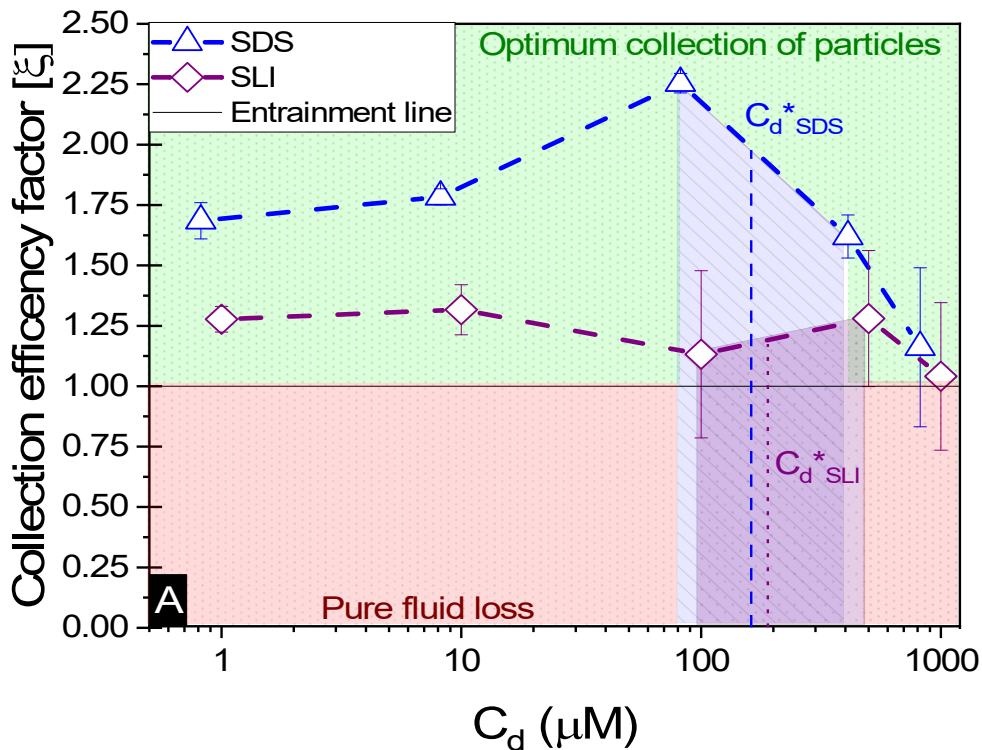


Figure 4.7: The effect of collector concentration on the collection efficiency factor in Eqn. 4.7, displayed with an equal entrainment line. Values above the line represent a greater proportion of particles being recovered and below the line represent greater fluid recovery.

A synthesis of the data from Fig. 4.6A-D is shown in Fig. 4.7, allowing scrutiny of collection efficiency as a function of collector concentration, and by extension, the adsorption data shown in Fig. 4.3A, for a holistic analysis of flotation performance. The ratio of the mass percentage of $\text{Mg}(\text{OH})_2$ particles and water recovered is displayed as the collection efficiency factor, ξ , as per Eqn. 4.7. The greater the value of ξ , the more efficient

the particle separation from water in the flotation cell, where values below 1 (the entrainment line) represent a greater recovery of water from the $\text{Mg}(\text{OH})_2$ suspension. The maximum ζ values coincide with maximum monolayer coverage regions calculated from Fig. 4.3A. Beyond this point, $C_d > C_d^*$, the collection efficiency tends back towards the entrainment line.

As the maximum monolayer coverage concentration, C_d^* , lies between data points, because of the low data resolution from the logarithmic concentration sweep, the performance factors of the highest performing collector concentrations recorded (by ζ) are shown in Table 4.5. Here one can assume that monolayer coverage is achieved, as the recorded adsorption capacities for these concentrations of SDS and SLI are 96% and 98% respectively of the maximum adsorption capacity q_e^* . SDS outperforms SLI at every measure, with greater proportion of $\text{Mg}(\text{OH})_2$ particles recovered, a greater proportion of water retained in the flotation cell and a lower residual concentration of $\text{Mg}(\text{OH})_2$ in the flotation cell. Not only does SDS perform better than the SLI by flotation performance metrics, but it is also more efficient on a molecular basis, requiring a lower concentration to achieve a greater collector adsorption density on the surface of the particles to achieve this superior performance. The comparison of flotation performance is illustrated in Fig. 4.8A and 4.8B for SDS and SLI respectively summarising each of the metrics in Table 4.5.

Table 4.5: Optimum performance data for SDS and SLI, based on their collection efficiency factor (ζ). Given is their corresponding mass percentage recovery ($P\%$), the mass percentage of water remaining in the flotation cell ($W\%$), the residual flotation cell concentration ($C\%$), the corresponding surface adsorption density (q_e , from Fig. 4.3A) and the percentage of maximum capacity adsorption (q_e^*) onto the $\text{Mg}(\text{OH})_2$ particles.

Collector	C_d (μM)	ζ	$P\%$ (%)	$W\%$ (%)	$C\%$ (vol.%)	q_e ($\mu\text{mol.m}^{-2}$)	$(q_e/q_e^*) \times 100\%$
SDS	82	2.3	80	64.7	0.8	0.1	96
SLI	100	1.1	67	40.8	1.6	0.049	98

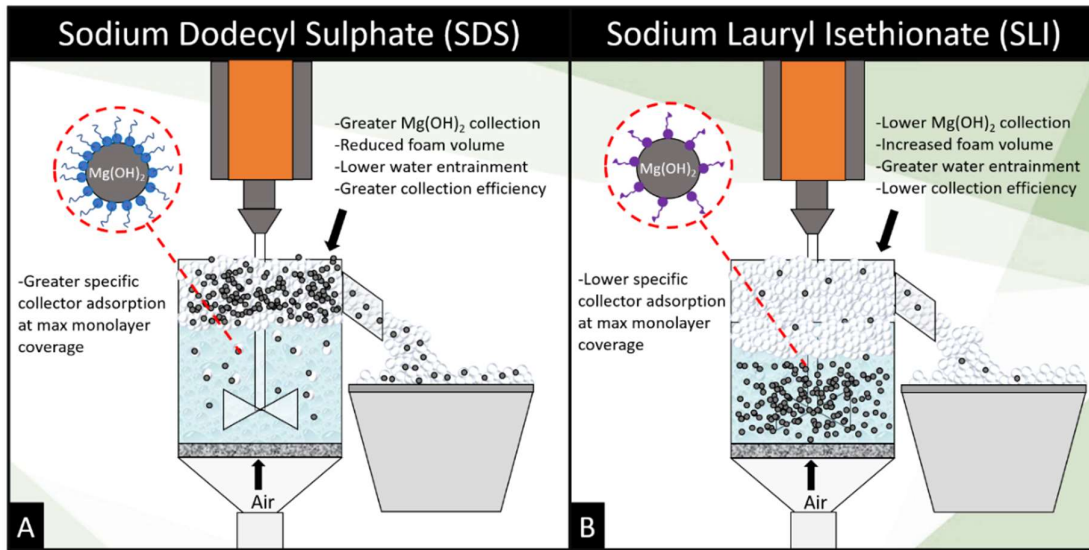


Figure 4.8: Schematic illustrating the mechanistic differences between A) sodium dodecyl sulphate and B) sodium lauryl isethionate collector flotation systems.

The importance of collector surface adsorption density and foamability on flotation performance are demonstrated clearly in the flotation data. The adsorption density of collectors on the $Mg(OH)_2$ aggregates is vital to increasing the surface hydrophobicity facilitating bubble attachment^{71,79–81,199}. SDS generated the greatest particle recovery in this investigation, forming very stable foams with lower water content than SLI (which displayed a significantly greater *DFI* in Table 4.3). This increased foamability of the SLI which captured more water in the lamella than the SDS system, and also recovered less particles due to the lower degree of particle hydrophobisation²¹⁸.

The role of collector hydrophobisation in flotation performance is highlighted further in the bilayer adsorption regime. At these concentrations, $C_d > C_d^*$, “hemimicelles” begin to form^{137,196,208}, where the second layer of collectors orientate their hydrophobic tails towards the corona of hydrophobic tails in the previously formed monolayer. This lowers the surface energy by reducing the surface area of hydrophobic tails exposed to water dipoles, meaning the bilayer adsorption is entropically driven¹⁹². As the polar head groups of the collectors are now facing out into the water, the particles hydrophobicity is decreased, which prohibits bubble attachment as the bilayer coverage increases. The effects of this increase in wettability are observed in the flotation efficiency analysis in Fig. 4.7, as the collection efficiency factors tend towards 1 when $C_d > C_d^*$. However, as observed, the

collection efficiency factors do not drop below 1 at any concentration, which is likely due to the homogeneous distribution of $\text{Mg}(\text{OH})_2$ in the well mixed flotation cell. Here, entrained fluid in the foam lamella also has a heterogeneous concentration distribution of $\text{Mg}(\text{OH})_2$. This means that even in the event of bubble coalescence and lamella drainage, the concentration does not change unless particles are successfully hydrophobically attached to air water interfaces in the foam, where the degree of air water interface adsorption decreases as the bilayer coverage increases, thus ζ approaches 1^{129,140,144,215}.

An important observation is that at 96% maximum monolayer adsorption capacity (q_e^*), SDS removed 80% of particles, meaning that 20% of particles remained in the flotation cell. For industrial applications, it would be likely that a second flotation cell operating in series would be required. At higher concentrations further particles were removed, but the efficiency analysis indicates this was through entrainment rather than hydrophobic separation. Previous work into the effect of the hydrophobic tail lengths in carboxylate soap collectors found that increasing the hydrophobic tail length increased the recovery yield in ion flotation¹⁸⁹. However, in the present case, the increase in chain length of the SLI did not enhance flotation, largely due to the reduced adsorption density from the larger headgroup as shown in the surfactant-particle adsorption density data in Table 4.2. Also, increasing the hydrophobicity of particles has a trade off with foam stability. Studies have found that particles with contact angles of $\sim 70^\circ$ are optimal for flotation, as greater hydrophobicity particles (contact angles of $>90^\circ$) have been shown to destabilise, dry and collapse foams due to the increased film drainage^{129,144}. Nevertheless, the low level of aggregation evident (e.g. Fig. 4.5) would suggest such high contact angles are not achieved through either SDS or SLI adsorption.

The relatively fine particle size distributions may additionally suggest a reduced flotation performance of the $\text{Mg}(\text{OH})_2$, because of the hydrodynamic limitations. Studies into the effect of fine and coarse particles on flotation have found that particles which are too small will lack the inertia required to overcome slipstreams created by the bubbles in turbulent foaming conditions for successful interactions at the air-water interface for particle-bubble attachment^{83,87,146}. While the magnesium hydroxide does aggregate to varying degrees (see Fig. 4.2) the majority of particles in well mixed conditions are $< 50\text{-}100\ \mu\text{m}$, with in particular, a high degree of $< 10\ \mu\text{m}$ fines that will be in the low inertial region. Conversely, aggregates that are too large, may detach from bubbles too easily, because of the greater

gravitational forces acting upon them against the buoyancy of rising bubbles⁸³. Although probably less of an issue in the current system, this is why the minerals industry has very high energy requirements for comminution of coarse particles to meet the operational envelope of subsequent froth flotation separation stages which is typically estimated as 10-150 μm ⁸³. The drive for smarter processing to increase recovery yields and decrease water use has driven innovation in this area to the development collectors, which have the dual functionality of flocculation agents and hydrophobic surface modifiers (usually copolymers)^{84,88,146}. However, the current stimuli triggers required to facilitate the switch between hydrophobic and hydrophilic behaviour is problematic for economical/process chemistry concerns, and as a result there is a drive for the development of dual flocculation-collector agents which circumvent the need for stimuli changes⁸⁴.

4.4) Conclusions

The aim of this work was to investigate the application of anionic surfactants, sodium dodecyl sulphate and sodium lauroyl isethionate, as collector agents to dewater $\text{Mg}(\text{OH})_2$ based radioactive waste suspensions using dispersed air flotation in the presence of a methyl isobutyl carbinol frothing agent. Sodium dodecyl sulphate (SDS) and sodium lauroyl isethionate (SLI) were found to both readily adsorb to the surface of $\text{Mg}(\text{OH})_2$. SDS was found to have a greater adsorption intensity and density in the monolayer regime, with a surface concentration double that of SLI. During bilayer formation, due to the greater surface energy associated with the long hydrophobic chain length, SLI demonstrated a greater adsorption intensity which was entropically driven. Upon sonication, $\text{Mg}(\text{OH})_2$ was found to readily aggregate, due to its low surface potential in a static light scattering kinetic study, where aggregation was further enhanced in the presence of KNO_3 salt from reduction of the electrical double layer. The influence of SDS and SLI on the $\text{Mg}(\text{OH})_2$ particle size distribution (PSD) as a function of collector concentration was investigated and compared to the baseline coagulation study. Whilst there was some moderate aggregation associated with the increased surface energy of monolayer coverage of collector molecules, there was no significant change in the $\text{Mg}(\text{OH})_2$ PSD. An interrogation of the $\text{Mg}(\text{OH})_2$ particle stabilised foam dynamics using a Bikerman column test showed that the SLI system dynamic foamability index (*DFI*) was greater than the SDS system. While foamability is necessary for flotation, increased foamabilities are associated with excess water recovery lowering solid-liquid separation efficiency. Flotation performance was analysed using a

batch flotation cell. Whilst mass and water recovery both increased with increasing collector doses, SDS outperformed SLI as a collector with superior $\text{Mg}(\text{OH})_2$ recovery, lowest water recover, lowest residual cell concentrations and the highest collection efficiency factors. The optimum recovery conditions for both SDS and SLI aligned with the maximum monolayer adsorption density collector concentrations and decreased back to entrainment concentrations in the bilayer regime, which was associated to the decreased hydrophobicity from hemi-micelle formation decreasing the particle surface energy. At the optimal conditions for particle-liquid separation with SDS, 80% of particles were recovered with an efficiency factor of 2.3, highlighting that flotation is a viable, rapid technique for the dewatering of legacy nuclear wastes, where further improvements may be gained by using a number of columns in series.

4.5) Nomenclature for Chapter 4

Scripts

A_s	Specific surface area	$\text{m}^2 \cdot \text{g}^{-1}$
	$\text{Mg}(\text{OH})_2$ concentration remaining in the flotation cell	vol.%
C_d	Initial supernatant collector concentration	μM
C_e	Equilibrium supernatant collector concentration	μM
DFI	Dynamic foamability index	$\text{s} \cdot \text{l} \cdot \text{mol}^{-1}$
H_f	Foam height	cm
k_f	Freundlich constant related to the adsorption capacity	$\text{mg} \cdot \text{g}^{-1}$
M_r	Relative molecular mass	$\text{g} \cdot \mu\text{mol}^{-1}$
M_{rp}	Mass of recovered particles in the collector tray	g
M_{rw}	Mass of recovered water in the collector tray	g
M_{Tp}	Mass of total particles initially in the flotation cell	g
M_{Tw}	Mass of total water initially in the flotation cell	g
n	Freundlich adsorption intensity-based coefficient	-
$P\%$	Mass% of $\text{Mg}(\text{OH})_2$ recovered from the flotation cell	%
q_e	Collector adsorption density on $\text{Mg}(\text{OH})_2$ surfaces	$\text{mg} \cdot \text{g}^{-1} / \mu\text{mol} \cdot \text{m}^{-2}$
t_r	Retention time	s

u	Superficial gas velocity	cm.s^{-1}
$W\%$	Mass% of water remaining in the flotation cell	%
ξ	Collector efficiency factor	-

Superscripts

	At maximum monolayer coverage onto $\text{Mg}(\text{OH})_2$
*	surface

Chapter 5:

Utilising amphiphilic block copolymer self-assembly for dual flocculation-flotation dewatering optimisation

5.1) Introduction

In Chapter 4, flotation was shown to be an effective process intensification technique, rapidly dewatering $Mg(OH)_2$ radwaste analogue suspensions using a surfactant collector agent. However, whilst there is a chemical robustness to variable feed compositions, flotation suffers from a limited hydrodynamic operational envelope^{83,186}. Particles that are below the lower limit of acceptance (fines) are too small, thus lacking inertia to overcome slip streams generated from rising bubbles in the flotation cell, preventing bubble attachment. Particles above the upper limit of acceptance (coarse particles), are too heavy for bubble buoyancy to facilitate adequate mass transfer to the foam phase, due to high particle-bubble detachment energies⁷⁸. Whilst the CFAs for flotation are dependent on several variables (particle density, bubble size distribution, contact angle etc.) the optimum hydrodynamic operational envelope of flotation is often approximated as 20-150 μm ^{83,99,146,186}.

Whilst surfactants are regularly used as collectors in industry due to their surface-active amphiphilic nature^{65,67,80,81,199}, they have been found to poor particle aggregators^{71,84}. Even though adsorption of surfactants should lead to the particles having greater hydrophobicity at monolayer coverages (from the hydrophobic tail group) and thus a greater surface energy in the water environment reducing colloidal stability⁷¹. Additionally, surfactants have been associated with greater water loss in flotation processes due to the high water content of foams generated, leading to poor dewatering ratios and low collection efficiency^{129,144,190,215-217}. Polymeric flocculants have proven to be highly effective at affecting particle size distributions (PSDs), increasing the 10th, 50th and 90th cumulative percentile particle diameters, d_{10} , d_{50} and d_{90} respectively, as shown in Chapter 3 and previous work^{17,19,20,29,38,114,115,156,219,220}. This will increase the fine particle diameters to be within the operational envelope of flotation. However, the diameters of particles across the distribution will also increase, meaning a larger proportion now exist above the operational envelope for successful flotation^{107,146}. Combining flotation with subsequent gravity driven

sedimentation can successfully remove non-floatable coarse particles, which is further aided by polymeric flocculation⁹⁹.

For flocculation of charged particles, polymeric flocculants are typically statistical (randomly configured) copolymers of high molecular weights (MWs) of $\sim 10^6$ g.mol⁻¹ such as those investigated in Chapter 3. These macromolecules have a non-ionic backbone with a charged monomer species with ionic functional groups responsible for particle attachment^{17,32,59,60,85,156}. The ratios of monomers in the flocculant macromolecule determine the overall charge density of the polymer. Where lower charge densities have shown to be more successful at improving the sedimentation rate of suspensions as they form larger, open structure, fractal flocs by utilising a ‘bridging’ flocculation mechanism^{17-20,22,59,60,85}. Additionally, not only do these polymers ‘over-flocculate’ suspensions so that they primarily exist above the hydrodynamic operational envelope for flotation, they are chemically poor hydrophobic surface modifiers (collectors). Lacking the contact angle modification for successful bubble attachment and separation in the initial flotation stage^{23,84}. Conversely, high charge density polymers conform tightly to the surface of particles, forming areas of localised charge reversal on the surface of particles, resulting a patch-wise adsorption of local colliding particles, a mechanism referred to as ‘charge patch’ flocculation^{17,19,32,33}. These flocs generally exhibit tighter, denser fractal structures, which while less favourable for improving sedimentation rate, yield greater settled bed densities and greater dewatering capacity²²¹. For charge patch flocculation, copolymers can have lower MWs (10^4 - 10^5 g.mol⁻¹) and greater charge densities (up to 100%). As detached polymer ‘tails’ or ‘loops’ are not required to expand past the Debye layer of the suspended particles due to the high localised charge density of the adsorbed copolymer, this allows for greater adsorption densities and charge neutralisation at lower surface coverages for charge patch flocculation^{33,222}.

Combining the aforementioned factors, the use of temperature responsive polymers have received a large amount of attention in recent years^{23,84,223-225,85-88,99,107,146,147}. These macromolecules function as a dual flocculation-collector agent. Where these macromolecules are hydrophilic below a transition temperature, known as the lower critical solution temperature (LCST), and above this temperature are hydrophobic. The behaviour of these macromolecules originates from a situation where the free energy component of enthalpy of mixing/solvency is close to the entropic cost of polymer- solvent interactions

required for solvency. Thus, small changes in temperature can result in segment-segment interactions being more thermodynamically favourable to segment-solvent interactions, marking the change from solvency to insolveny^{84,88}.

There have been several observed advantages to using these macromolecules including the ability to flocculate particles and use a ‘thermal switch’ to control bed sedimentation densities^{23,147,223,224}. These macromolecules can flocculate particles below their LCST, then when heated, thermo-responsive polymers, such as statistical copolymers of poly(N-isopropyl acrylamide) (PNIPAM), become hydrophobized on the particles surface, increasing the flocs contact angle so that it is compatible with flotation operations hydrophobically and hydrodynamically^{87,88,146}. Copolymers of PNIPAM are commonly researched as dual flocculation-flotation aids, as the transition from hydrophobic coil to hydrophilic globule is reversible⁸⁴. However, this thermal transition functionality is also a caveat to technological viability. Heating suspensions on industrial scales is highly energy intensive. Therefore, polymers such as PNIPAM must bond to particle surfaces in their soluble hydrophilic states, as they actively aggregate to form hydrophobic globules and precipitate from solution above their LCST²³. Whilst work has been completed on incorporating hydrophobic comonomers to lower the LCST, thus reducing energy requirements, a higher polymer dosage may be required to maintain a great enough degree of surface adsorption and coverage for flotation based on selectivity requirements of the minerals industry¹⁴⁷.

With industry focus shifting to ‘smart processing’, which aims to lower industry energy requirements and process water consumption, interest in the development of collectors which do not require heating and produce high particle load, low water content foams have increased. An alternative to temperature responsive polymers is to use amphiphilic block copolymers (ABCs). Unlike statistical copolymers which have a random configuration of comonomers, ABCs have segregated hydrophobic and hydrophilic blocks and effectively act as macrosurfactants^{92,226}. Like traditional surfactants, ABCs have self-assembly characteristics which are dependent on the relative length of their hydrophobic and hydrophilic blocks, which adsorbed onto solid substrates in unimer polymer forms (such as polymer brushes) or by micellar adsorption, and dosed concentration rather than stimuli triggers^{227–232}. An advantage is that ABCs have been shown to have little effect on surface tension at high hydrophobic chain length, with critical micelle concentrations (CMCs)

decreasing with increasing hydrophobic chain lengths which can be exploited to control water loss to maintain high collection efficiency^{90-93,233}. The hydrophilic block will have a high affinity to oppositely charged particle surfaces in suspension and adopt a tight patch-wise adsorption mechanism facilitating charge patch flocculation below the ABC CMC^{17,19,113}. Above the CMC, micellar adsorption has been shown to facilitate a pseudo-bridging flocculation mechanisms¹¹³. Effectively, allowing the ABCs to act as moderate flocculation agents and excellent hydrophobic surface modifiers below their CMC. But above the CMC, facilitate larger structures associated with the properties of excellent polymeric settling aids combining hydrophobic and charge modification flocculation mechanisms^{17,18,60}.

In this research, ABCs consisting of a hydrophilic poly(acrylic acid) block, and a hydrophobic poly(n-butyl acrylate) block were synthesised using reversible addition-fragmentation chain-transfer (RAFT) polymerisation. The relative lengths of the hydrophilic and hydrophobic blocks were varied to observe their relative effects on polymer solutions interfacial surface tension and dilational viscoelasticity, to probe the mechanical strength and resistance to coalescence of the generated foams in the flotation process. This is important as interfacial properties have been linked to flotation performance through mechanical stability and where air recovery has even been linked to optimum performance for flotation cell banks^{69,140,141}. ABC-particle surface adsorption was also investigated to determine the transition from unimer to micellar adsorption which may possess differing flocculation properties¹¹³. The floc density was also investigated using fractal mathematical approach combined with static light scattering (used in Chapter 3)^{44,48,63}, and compared to resultant zonal settling rates. The ABCs were then used as flotation aids in a batch flotation cell with methyl isobutyl carbinol frothing agent and the performance was measured against particle and water mass recoveries, comparing dewatering efficiencies with a collection efficiency factor. Mg(OH)₂ was selected as the valuable particle due to its cationic surface charge and our experience with this nuclear waste analogue in Chapter 4's surfactant driven flotation work, which the performance of the ABCs as collectors were benchmarked against. Given the drive for reduction in secondary waste generation in the form of unnecessary water consumption and robust salt contamination in these facilities, ABCs could be a chemically and hydrodynamically robust alternative to surfactant-based flotation water treatment and reduce residence times of polymerically aided sedimentation alone.

5.2) Materials and experimental methodology

5.2.1) Materials

Mg(OH)₂ (Versamag, Martin Marietta, US) was used for flocculation and flotation experiments¹⁶⁹. This work was completed using the same Mg(OH)₂ material utilised in Chapters 3 and 4 at a constant solids concentration of 2.5 vol.%. For the polymeric synthesis of the PAA-*b*-nBA amphiphilic block copolymers (ABCs), the monomers Acrylic acid (AA; Acros Organics 99.5% extra pure stabilised) and n-butyl acrylate (nBA: VWR >98%, stab. with up to 50ppm 4-methoxyphenol ml), were selected to form the hydrophilic and hydrophobic segments of the ABC respectively. These were polymerised in the presence of 3-(((1-carboxylethyl)thio)carbonothioyl)thio)propanoic acid (CCTP; Boron Molecular) which acted as a RAFT chain transfer agent.^{230,234} The polymerisation was initiated using 4,4'-Azobis(4-cyanovaleric acid) (ACVA: Merck ≥75%). Methanol (Sigma-Aldrich ≥99.6%) was selected as a compatible diluent for AA and nBA, allowing characterisation before the emulsion polymerisation stage as nBA is not soluble in water, preventing NMR spectroscopy of the reagents prior to polymerisation. For NMR spectroscopy analysis, the NMR standard, 3-(trimethylsilyl)-1-propanesulfonic acid sodium salt (TMS salt; Sigma Aldrich; 99%) was used as an internal standard to enable calculation of nBA conversion. For the flotation and interface modification investigations, sodium dodecyl sulphate (SDS) and 4-methyl-2-pentanol (MIBC) were utilised identically to the methodology in Chapter 4.

5.2.2) Synthesis and Characterisation of Poly(acrylic acid)-*b*-poly(*n*-butyl acrylate)

The ABC synthesis methodology elected the use of RAFT polymerization. PAA-*b*-PnBA ABCs have previously been successfully synthesized by Colombani et al.(2007) using Atom transfer radical polymerization. However, for this research, RAFT polymerisation was selected as it is an effective controlled radical polymerization process that features aspects of living polymerization, whilst also gaining from the versatility of a radical polymerisation process and is compatible with acids^{230,234}. The overall process in this work involved first synthesising a PAA macromolecular chain transfer (macro-CTA) by aqueous RAFT solution polymerisation of AA (see Fig. 5.1A) to produce macromolecular chain transfer agents, which were then subsequently chain-extended with n-butyl acrylate (nBA) chain via aqueous RAFT emulsion polymerisation. The latter process has been well reported recently and is beneficial in that it enables aqueous polymerisation of insoluble

monomers²³⁴. An array of three target ABCs were selected for synthesis for this work. Firstly, PAA was synthesised using AVCA as a thermal initiator and CCTP as the chain-transfer-agent (reaction A in Fig. 5.1). A target degree of polymerisation (P_d) of 160 was chosen for the macro-CTA, which represents a relative MW of $\sim 1.15 \times 10^4$ g.mol⁻¹. This is effective comparable order of magnitude of MW to polymeric flocculants, which utilise a ‘charge patch’ flocculation mechanism to successfully aggregate particles into tight compact flocs³². A solids concentration of 30 wt.% was selected for a lower aqueous macro-CTA solution viscosity for ease of manipulation.

Aliquots of the polymer solution were taken and analysed using a Magritek® Spinsolve Ultra 60 MHz benchtop NMR spectrometer to determine the achieved macro-CTA D_p . A conversion of 96 % was achieved and the reaction was quenched by introducing oxygen to the system to ensure high retention of terminal RAFT trithiocarbonate groups required for effective chain extension (See Fig. 5.1B). The PAA was then used as a macro-CTA for the RAFT emulsion polymerisation stage (reaction B in Fig. 5.1) of ABC synthesis. The polymerisation process was repeated using the macro-CTA *in lieu* of CCTP with the nBA monomer with target P_d 's of 25, 100 and 200. The RAFT polymerisation reaction was carried out till completion and NMR spectroscopy indicated monomer conversions of >99% (judged by near complete disappearance of the signals relating to the vinyl protons in the NMR spectrum). The solids concentration for the ABCs was also 30 wt.% for ease of manipulation. During the polymerisation, successful chain formation of ABCs was confirmed by an increase in turbidity of the samples due to in-situ self-assembly of the polymers to form polymer micelles. The three polymers, PAA₁₅₃-*b*-PnBA₂₅, PAA₁₅₃-*b*-PnBA₁₀₀ and PAA₁₅₃-*b*-PnBA₂₀₀ were then each diluted in Milli-Q water to make three stock solutions of 10000 ppm, which could be sampled and diluted as required for the experiments in this work. For full detail on the ABC synthesis methodology and polymer characterisation please refer to the Appendix C where Figs. C1 and C2 display the NMR spectra for initial and final reactor compositions of PAA and PAA-*b*-PnBA synthesis respectively. Unfortunately, the resulting polymers were insoluble in all available solvents used for gel permeation chromatography, meaning the molecular weight distribution could not be obtained.

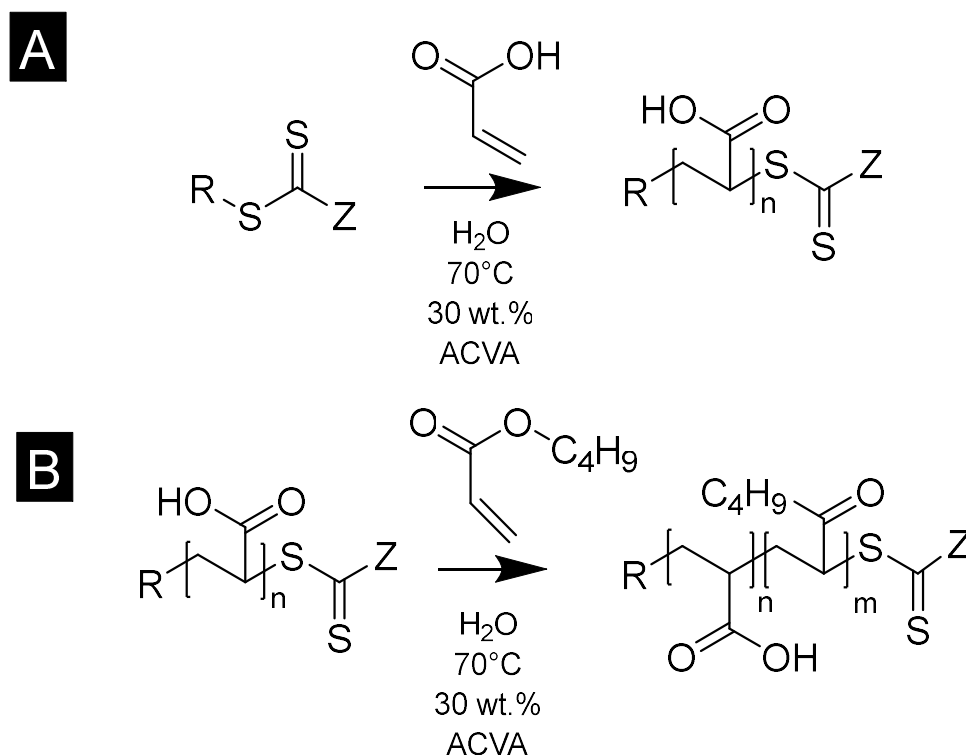


Figure 5.1: Amphiphilic block copolymer (ABC) RAFT reaction scheme where the top reaction (A) is the synthesis of the poly(acrylic acid) macro chain transfer agent and the bottom reaction (B) is the poly(n-butyl acrylate) diblock attachment reaction carried out in an inert N_2 atmosphere at $70^\circ C$. The reaction was carried out in a H_2O solvent media with ACVA initiator and CCTP chain transfer agent.

5.2.3) Interfacial tension and viscoelasticity characterisation

The interfacial surface tension and dilational viscoelasticity was determined using a PAT-1 tensiometer (SINTERFACE Technologies, Germany) instrument. Utilising image analysis of a pendant drop to determine the principle radii of curvature of the drop, the Youngs Laplace equation was used to calculate the dynamic interfacial surface tension²³⁶. The effect of concentration of this array of polymers on the surface tension and dilational viscoelasticity of aqueous polymer-water solutions was examined over the concentration range of 0-820 μM , 0-207 μM , 0-81 μM for SDS, PAA₁₅₃-*b*-PnBA₂₅ and PAA₁₅₃-*b*-PnBA₂₀₀ respectively, with each system repeated in triplicate to align with the concentration range of SDS systems investigated in Chapter 4. An oscillation period of 5 seconds and ten complete cycles with a pendant drop volume oscillation envelope of 9-11 μl was selected from previous investigations of surface tension and dilational viscoelasticity with the same instrument²³⁷⁻²³⁹.

5.2.4) Polymer-particle adsorption

Adsorption experiments were performed for both PAA₁₆₀-*b*-PnBA₂₅ and PAA₁₆₀-*b*-PnBA₂₀₀ polymers to represent the envelope of the hydrophobic block chain lengths investigated in this work across a range of concentrations of 10-655 μ M and 3-270 μ M respectively, completing three adsorption runs for each concentration and taking the averaged result. For each adsorption experiment at a desired polymer concentration, Mg(OH)₂ (117 mg) was weighed into a centrifuge tube (15 mL) and a given volume of Milli-Q water was added using a pipette. The centrifuge tubes were placed in a sonicator for 20 minutes to ensure the breakup of any preformed Mg(OH)₂ aggregates. Given volumes of the chosen polymer stock solutions were then added to the centrifuge tubes using a pipette to achieve the desired polymer concentration, giving a total sample volume of 10 ml. The centrifuge tubes were put on a carousel stirrer at 40 rpm for 24 hrs for adsorption to occur. The suspensions were then separated in a Megafuge 16R centrifuge at 8000 rpm for 30 minutes and the supernatant polymer solution was removed from the top into a separate sample vial using a pipette. Reference solutions were also made up for each desired polymer concentration but omitting Mg(OH)₂.

UV-visible (UV-VIS) spectroscopy was selected as a method for analysing supernatant polymer concentrations over the TOC technique utilised in Chapter 4 as the subsequent combustion of the trithiocarbonate group in the chain-transfer agent and capture of the resultant sulphate gas produced levels of sulphuric acid detrimental to the TOC analyser. The reference and adsorption solutions were then analysed using an Agilent Technologies (Stockport, Cheshire, UK) Cary 60 UV-VIS spectrometer. Initial calibration and optimisation of UV-vis operating parameters were first investigated and can be found in Appendix C (Fig. C3A-B). The UV-Vis spectroscope was run with simple scan controls at a medium scan speed, using plastic vials, and a baseline correction was run with Milli-Q water. To correlate the absorbance measured by the UV-vis spectroscope to the polymer concentration, calibration measurements were taken for samples of known polymer concentration for both PAA₁₆₀-*b*-PnBA₂₅ and PAA₁₆₀-*b*-PnBA₂₀₀. The relationship between initial dosed concentration of ABCs and the supernatant equilibrium concentration of the ABCs can be found in Appendix Fig. C3C. The adsorption of ABC onto the Mg(OH)₂ was then characterised using the same procedure as in Chapter 4, utilising a linear form of the Freundlich adsorption isotherm shown in Eqn. 4.1 (Section 4.2.4). The concentration where

the two isotherms fits intercept represents the unimer-micellar transition point. Where q_e^* , C_e^* and C_d^* are the adsorption density of ABC on the $\text{Mg}(\text{OH})_2$ particle surface, ABC equilibrium concentration and initial dosed ABC concentration at the unimer-micellar adsorption transition points respectively.

5.2.5) Floc structure characterisation

Floc structure characterisation was completed using a similar same procedure used in Chapter 4. Static light scattering (SLS) was used to measure the fractal dimensions of the flocculated suspensions. 20 ml suspensions were prepared using 2.5 vol.% $\text{Mg}(\text{OH})_2$ and Milli-Q water and then sonicated for 20 minutes to breakup any preformed aggregates. To observe the effect of adsorbed ABCs on the fractal structure of the flocs, varying concentrations of ABC up to 207 μM and 81 μM (comparable molar concentration to the benchmark SDS study) for PAA₁₅₃-*b*-PnBA₂₅ and PAA₁₅₃-*b*-PnBA₂₀₀ respectively were then added to a 2.5 vol.% $\text{Mg}(\text{OH})_2$ and Milli-Q water suspensions and agitated using a magnetic stirrer for 20 minutes. The suspension was then added to a Malvern Mastersizer 2000E (Malvern Panalytical Ltd) static light scattering instrument using a Hydro 2000SM aqueous dispersion cell (external dimensions of 140 × 175 × 390 mm and sample volumes between 50 - 120 ml). The unit was sheared at 900 rpm to ensure consistent flow of suspensions through the vertical optical window at concentrations within the instrument obscuration envelope. The obtained scattering intensity, $I(Q)$, and the scattering wave factor, Q , were then used to determine the fractal dimension of the ABC- $\text{Mg}(\text{OH})_2$ flocs, denoted as d_f . As the relationship between the scattering intensity and scattering wave vector is established by the same procedure utilised in Chapter 3 (see Section 3.3.3 for methodology) with each system repeated in triplicate shown in Appendix Figs. C4A and C4B.

The density of the flocs, ρ_f , can then be calculated using the same procedure as in Chapter 3 by determining the ratio of solid particles and water in a floc divided by the floc volume V_f . The number of particles (N) in a floc, shown in Eqn. 3.1 (Section 3.2.1), is established by using the ratio of the radius of gyration of the floc, D_f , and primary particles, D_p , raised to the power of the floc fractal dimension. Which is then normalised using a function of the packing factor and the ratio of the shape factors of the aggregate and the primary particles known as the structure prefactor ψ ^{63,117}. As discussed in Chapter 3, values of ψ have been proposed to depend on the relationship between ψ and d_f , such as the relationship suggested

by Gmachowski¹²¹, where the structure prefactor can be determined using $\psi = 0.414d_f - 0.211$ when $1.5 \leq d_f \leq 2.75$. The floc density can be determined by calculating the mass of particles in a floc which is a product of the number of particles, N , the volume of the primary particles, V_p , and the $\text{Mg}(\text{OH})_2$ density ρ_p . The mass of water trapped inside the floc is then established as the difference in the floc volume and total particle volume multiplied by the density of water ρ_w . Thus, the floc density is summarised in Eqn. 3.4 as suggested by Tang et al. (Tang et al., 2002).

Visual microscopy was utilised to confirm the size and morphology of aggregates produced from suspensions dosed with optimum ABC concentrations established through flotation performance screening. Two samples were set up for each polymer at different initial concentrations ($\text{PAA}_{153}\text{-}b\text{-PnBA}_{25}$ at 207 μM and 345 μM , and $\text{PAA}_{153}\text{-}b\text{-PnBA}_{200}$ at 41 μM and 81 μM). A Morphologi G3 (Malvern Panalytical Ltd.) automated single element microscope was used, floc samples were taken after 5 minutes of agitation in the flotation cell. A 4-slide plate was selected for dispersing the floc suspensions, a droplet of the sample was added to each slide, sealing with a cover slip. The microscope setting was optimised starting from the smallest magnification, taking images of each sample. A magnification of $\times 20$ was selected for $\text{PAA}_{153}\text{-}b\text{-PnBA}_{25}$ and $\times 5$ for $\text{PAA}_{153}\text{-}b\text{-PnBA}_{200}$. A differential z-stacking of 2 was selected to cover an appropriate depth of scanning, and the full scan area was selected to maximise sample size. Data were analysed and computed as a cumulative frequency distribution for comparison of floc population sizes. For the most effective ABCs, the floc sizes were compared pre-flotation directly from the flotation cell and post-flotation from the collector tray to establish the flotation separation floc size envelope and inform on post-flotation sedimentation results.

5.2.6) Sedimentation and flotation performance and analysis

Visual observation of suspension-supernatant boundary level change with time was used to measure the influence of ABC concentration on hindered settling rates. Again, 2.5 vol.% $\text{Mg}(\text{OH})_2$ suspensions were prepared and agitated in the bespoke flotation cell (210 ml, 65 mm ID; Fig. 4.1) used in Chapter 4, with variable concentrations of the two ABCs (35-245 μM and 14-81 μM for $\text{PAA}_{153}\text{-}b\text{-PnBA}_{25}$ and $\text{PAA}_{153}\text{-}b\text{-PnBA}_{200}$ respectively). Flocculated suspensions were then transferred to 1 litre measuring cylinders of 61 mm diameter. The cylinders were inverted 5 times to evenly re-suspend flocs and the interfacial height was measured over time. 12.31 g of $\text{Mg}(\text{OH})_2$ was added to a measuring cylinder and dosed

with 98 μM of MIBC, the required dose of ABC and then made up to 210 ml with Milli-Q water. The cell was stirred for 20 minutes at 250 rpm to facilitate adequate adsorption of ABC to $\text{Mg}(\text{OH})_2$ surface. Airflow into the bottom of the cell was set at $0.1 \text{ l}\cdot\text{min}^{-1}$ and the agitator speed was reduced to 100 rpm to suspend larger particulates but minimise turbulence in the cell preventing bubble disengagement. Foam generated above the air-water interface (AWI) poured through the outlet at the top of the vessel and into a pre-weighed aluminium collection container. This container was placed into an oven for 24 hours to evaporate the water component of the foam, leaving behind the recovered particulates. The container was then weighed to determine the performance indicators.

The flotation performance was scrutinised using the same metrics as Chapter 4 (Section 4.2.6) investigating the flotation performance of $\text{Mg}(\text{OH})_2$ using the ABCs *in lieu* of anionic surfactant collectors and benchmarked against the SDS collector performance. The $\text{Mg}(\text{OH})_2$ particle recovery percentage ($P\%$) is shown in Eqn. 4.4 and the percentage of fluid remaining in the cell, $W\%$, is calculated using Eqn. 4.5 using the same experimental procedure. The $\text{Mg}(\text{OH})_2$ particle concentration remaining in the flotation cell, $C\%$ can then be determined from mass balance principles and is defined as the mass of particles and mass of fluid remaining in the flotation cell shown in Eqn. 4.6. The performance of the collectors can then be compared using a collector efficiency factor, ξ , shown in Eqn. 4.7 which is a ratio of the percentage of the particles to fluid recovered from the flotation cell. When $\xi > 1$ there are more $\text{Mg}(\text{OH})_2$ particles recovered than water by mass, when $\xi = 1$ there is equal particle-fluid extraction (entrainment) and when $\xi < 1$ there is more fluid being extracted than $\text{Mg}(\text{OH})_2$ particles. The collection efficiency factor can then be used to determine the optimum dose of collector to maximise solid liquid separation and will be used to compare the ABCs to the SDS benchmark in this work.

5.3) Results and discussion

5.3.1) Interfacial tension and dilational viscoelasticity

Firstly, to understand the surface activity of the ABCs and to benchmark them against industry standard surfactants, the change in interfacial surface tension (γ) with changing ABC and SDS dosed concentration was investigated and the behaviour of the ABCs is displayed in Fig. 5.2A. $\text{PAA}_{153}\text{-}b\text{-PnBA}_{25}$ appears to be significantly more surface active than both $\text{PAA}_{153}\text{-}b\text{-PnBA}_{200}$ and SDS (in the observed concentration window which is at

max 10% of the reported SDS CMC of 8.2 mM¹³¹). The CMC cannot be determined from these γ vs C_d plots, and SDS is at dosed concentrations much lower than its reported CMC¹³¹ which has been reported to have CMC γ plateau values of ~ 33 mN.m^{-1131,240}. It has been reported that ABCs display much lower CMCs than short molecular surfactants such as SDS, and the CMC also decreases with increasing hydrophobic block length^{92,233}. This non-surface activity associated with ABCs was also observed when Ghosh et al.⁹¹ examined a range of comonomers ratios for their effect on surface activity/non-activity and found that there was a transition point of hydrophobic block length when ABCs became non-surface active.

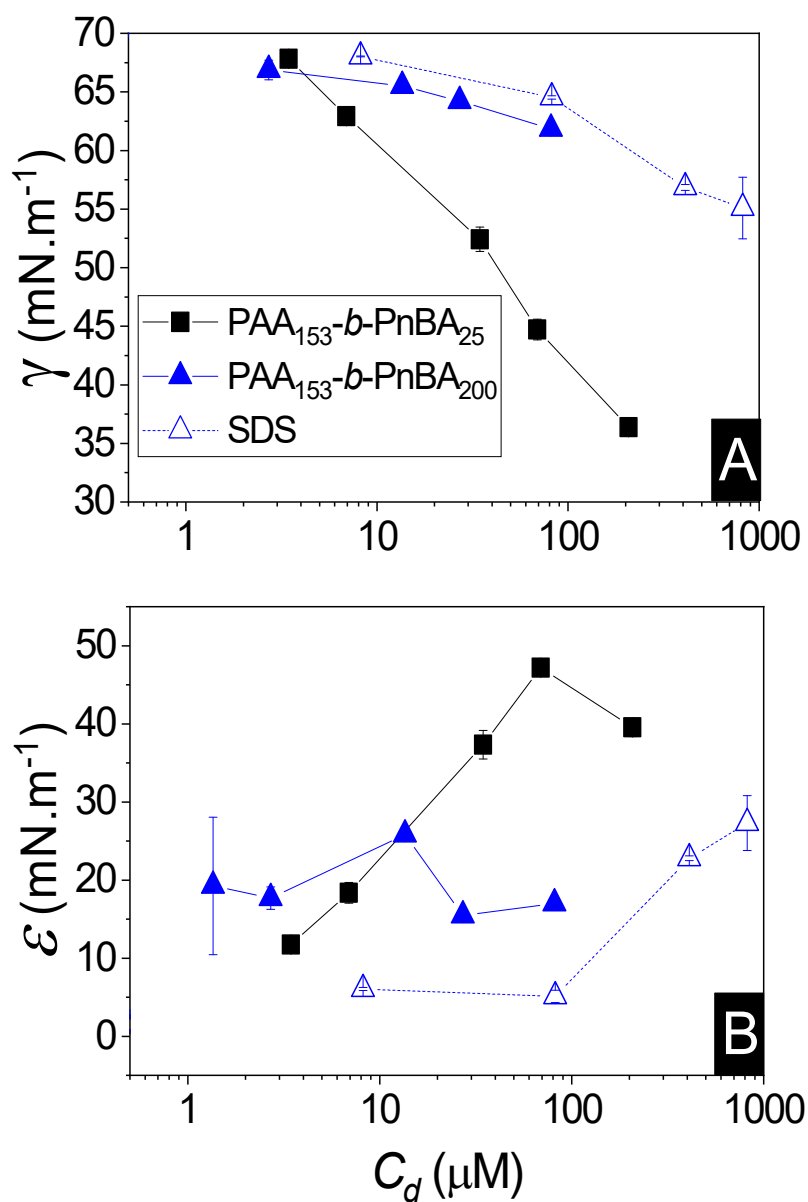


Figure 5.2: A) The change in interfacial surface tension (γ) with increasing concentrations of amphiphilic block copolymers (ABCs) PAA₁₅₃-b-PnBA₂₅, PAA₁₅₃-b-PnBA₂₀₀ and sodium dodecyl sulphate (SDS). B) Data showing the change in interfacial elasticity with increasing ABC and surfactant concentrations for PAA₁₅₃-b-PnBA₂₅, PAA₁₅₃-b-PnBA₂₀₀ and sodium dodecyl sulphate.

It has also been examined that the degree of hydrophilicity/hydrophobicity of the comonomers in an ABC play a role in the surface activity/non-activity, where weakly hydrophilic comonomers^{93,95-97} and strongly hydrophobic comonomers⁹⁸ would micellize without adsorption to the AWI. The degree of image charge repulsion from hydrophilic

polyions in ABCs has been found to destabilise ABCs adsorbed at the AWI, though as the hydrophobic PAA block length is constant, this effect will not likely be in play^{90,91,132,241}. This was observed by Eghbali et al.¹³² when investigating the surface activity and micellization of PAA₁₅₀-*b*-PnBA₁₀₀ ABCs, that the addition of NaCl salt neutralised the image charge repulsion of PAA segments which increased surface adsorption and lowered the CMC of the ABC, thus the semi-solubility of Mg(OH)₂ likely provides some stability regarding hydrophilic block image charge interactions through Debye screening effects. Conversely, Ghosh et al.⁹¹ found that when investigating the change in hydrophobic block length of comonomers 3-(Methacryloyloxy)ethyltrimethylammonium chloride (DMC) and nBA in PDMC-*b*-PnBA, the introduction of NaCl reduced the surface tension further in addition to the PDMC-*b*-PnBA. This surface tension reduction occurred even at longer chain hydrophobic blocks, indicating that both image charge effects in addition to hydrophobicity/ block length were factor in surface activity.

Like the systems analysed by Ghosh et al.⁹¹, who also investigated ABCs of PAA and PnBA of varying hydrophobic chain length, this work observed more significant surface activity for the PAA₁₅₃-*b*-PnBA₂₅ than by the observed PAA₁₅₃-*b*-PnBA₂₀₀ system in Fig 5.2A. Where the PAA₁₅₃-*b*-PnBA₂₅ showed a consistent decrease in surface tension with increasing dosed ABC concentration to similar degrees as the SDS system, whereas the greater MW PAA₁₅₃-*b*-PnBA₂₀₀ system had little effect on surface tension. This suggests there may be a relationship between decreasing hydrophobic chain length and its impact on surface tension reduction similarly observed in the PDMC-*b*-PnBA systems⁹¹. Additionally, Ghosh et al.⁹¹ found that the more surface-active ABCs were the most foaming. This has interesting consequences for the design of ABCs as collector reagents. As not only does the hydrophilicity/hydrophobicity and relative block length of the comonomers have an effect on their surface activity, but the selection of the hydrophilic group can suppress effects of salt on surface activity, which is an important consideration for highly contaminated feed compositions experienced in radwaste dewatering⁴. Whilst the effects of the relative hydrophobic length appear clear in the work to reduce the additional water losses associated with excessive foaming^{129,144,190,215-217}, the selection of hydrophilic length may also have an effect on the ABC surface adsorption density and flocculation behaviour of the ABC, which is important in optimising the hydrodynamic behaviour of the hydrophobized flocs^{17,19,32}.

Additionally, dilational viscoelasticity (ε ; $\text{mN}\cdot\text{m}^{-1}$) is an important consideration in flotation operations, as foams form and surface perturbation occurs, the transfer of surface-active molecules to the AWI will allow further AWI expansion in foaming processes, dynamically reducing AWI surface energy by substituting with anisotropic interfacial water molecules^{129,242}. The ε of the AWI is shown in Fig. 5.2B, where both PAA₁₅₃-*b*-PnBA₂₅ and PAA₁₅₃-*b*-PnBA₂₀₀ display differing magnitudes of ε which peaks then decreases with increasing molecular concentration. This is a characteristic of low and high MW surface active molecules^{31,133,134,242,243}. As the ε is a function of the bulk migration time of a surface active molecules to diffuse from the bulk solution to the AWI when the surface area of the AWI is perturbed from processes such as foaming²⁴³. The ε value is also dependent on adsorption and desorption kinetics at the AWI and it is known that ε increases with increasing dosed surface active molecule concentration. As the surface active molecules approach their respective CMCs, the total molecular diffusion time becomes fast and deletes the surface gradients created by the AWI perturbation²⁴³, beyond this point the ε begins to decrease as the formation of micelles to reduce free energy competes with diffusion of free surface active molecules to replace those at the perturbed AWI^{31,133,242}.

Low MW surfactants are known to have much faster molecular exchanges at the AWI than macromolecules due to macromolecules displaying slow conformational relaxation and tendency to form pre-micellar aggregates in the bulk phase^{31,133,134}. The systems observed in Fig 5.2B. follow these previous observations, where the PAA₁₅₃-*b*-PnBA₂₅ system increases in ε before peaking at $\sim 90 \mu\text{M}$, then decreasing again, which indicates the location of the ABC CMC. The same observation was made for the PAA₁₅₃-*b*-PnBA₂₀₀ ABC with the CMC peak at $\sim 11 \mu\text{M}$ and a slight decrease beyond this concentration with a much lower magnitude of ε . This agrees with observation that longer chain hydrophobic ABCs display lower CMCs and also display slower conformational and diffusional exchange at perturbed AWI indicating slower conformational relaxation^{31,92,133,134,233,242}. The peak of the SDS is not observed as it is investigated at concentration much below its CMC¹³¹, but displays sharp increases in ε due to its comparatively fast diffusional and AWI relaxation times¹³⁴. Other ABCs used in flotation such as pluronics, tri-block copolymers of poly(ethylene oxide) (PEO) and poly(propylene oxide) (PPO), which have previously been used in paper deinking¹⁴⁹ and coal flotation operations¹⁴⁸, have also been investigated in regard to their dilational viscoelasticity. Noskov et al.²⁴⁴ investigated the dilational viscoelasticity of PEO₇₆-*b*-PPO₂₉-*b*-PEO₇₆ and found a maximum spread film dilational

viscoelasticity of $\sim 20 \text{ mN.m}^{-1}$, similar to those observed by the $\text{PAA}_{153}\text{-}b\text{-PnBA}_{200}$ system in Fig. 5.2B. The lower molecular weight $\text{PAA}_{153}\text{-}b\text{-PnBA}_{25}$ displays elevated maximum dilational viscoelasticity of $\sim 50 \text{ mN.m}^{-1}$, whilst greater than those observed for pluronics by Noskov et al.²⁴⁴, investigations of nanoparticle stabilised film elasticities of latex stabilised hexane/water interfaces with adsorbed ABCs of poly(methyl methacrylate)-*b*-poly(2-(dimethylamino)ethyl methacrylate) have shown dilational viscoelasticities of 120-140 mN.m^{-1} ²⁴⁵.

5.3.2) Polymer-particle adsorption

Next, the polymer-particle interactions of the two varying MW ABCs was investigated, allowing the development of understanding of self-assembly and particle flocculation characteristics. The ABC adsorption affinity for the surface of Mg(OH)_2 particles is shown in Fig 5.3A. There is a distinct difference in the adsorption behaviour between the $\text{PAA}_{153}\text{-}b\text{-PnBA}_{25}$ and $\text{PAA}_{153}\text{-}b\text{-PnBA}_{200}$ systems. Firstly, there is the initial electrostatic adsorption and relaxation of unimer ABCs onto the particle surface. Followed by relaxation and hydrophobic adsorption of the hydrophobic PnBA tails to the charge neutralised sites on the particle surface reducing free energy which occurs below the ABC CMC^{17,23,33}. Secondly, there is micellar adsorption of ABCs to the surface, where the hydrophobic tails entangle and ABCs self-assemble to form densely hydrophobic cores which form a quasi-impenetrable adsorbed layer onto the Mg(OH)_2 . This has been observed by Volpert et al.⁹⁴ upon investigating the adsorption of hydrophobically associating polyacrylamides on clay surfaces, where they reported the bound water fraction in the adsorbed layers of different ABCs using H^1 NMR. Some ABCs were even reported to completely liberate water from these layers⁹⁴. This Micellar transition and adsorption was also observed by O'Shea et al.¹¹³ who found that above the LCST using dynamic light scattering that $\text{P(AA-co-BA)-}b\text{-PNIPAM}$ ABCs self-assemble. But unlike a previous investigation of a statistical copolymer PAA and PNIPAM by the same group⁸⁵, which self-assembled into globules above its LCST and showed little to no adsorption onto alumina surfaces, that ABCs conversely adsorbed onto the surface of alumina. This is likely due to the outward facing corona of P(AA-co-BA) having an electrostatic affinity to the alumina surface promoting micellar adsorption and flocculation of particles¹¹³. Where the act of heating $\text{P(AA-co-BA)-}b\text{-PNIPAM}$ above its LCST is analogous to the increasing concentration of $\text{PAA-}b\text{-PnBA}$ ABCs in this work above their CMCs promoting self-assembly. This unimer to micellar

adsorption regime transition of PAA-*b*-PnBA on Mg(OH)₂ is indicated in the Freundlich adsorption isotherm studies shown in Fig. 5.3B.

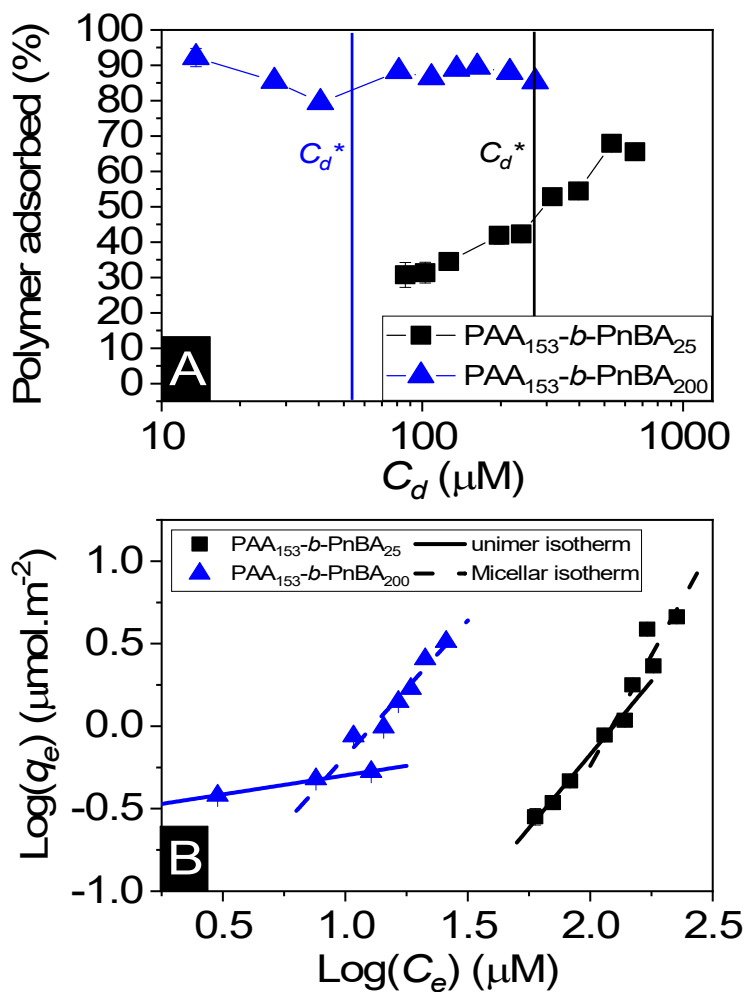


Figure 5.3: A) Data showing the percentage of ABC adsorbed to the surface of Mg(OH)₂ with increasing ABC concentration. Vertical lines indicate micellar transition points (C_d^*). B) Freundlich adsorption isotherm data for amphiphilic block copolymers (ABCs) PAA₁₅₃-*b*-PnBA₂₅ and PAA₁₅₃-*b*-PnBA₂₀₀ showing the variation in the surface adsorption per gram of Mg(OH)₂ (q_e) with increasing equilibrium concentration of ABC (C_e) with fitted ABC unimer and micellar adsorption regimes.

The greater MW PAA₁₅₃-*b*-PnBA₂₀₀ ABC shows a stable ABC adsorption percentage with increasing dosage of ABC, indicating an equilibrium of the proportional split between ABC at the surface and in the bulk solution (Fig. 5.3A). The greater MW PAA₁₅₃-*b*-PnBA₂₀₀ ABC has shown to have low surface activity and likely a comparatively lower CMC value than the lower MW PAA₁₅₃-*b*-PnBA₂₅ ABC indicated in Figs. 5.3A and 5.3B. Indicating

self-assembly and micellar adsorption may occur at lower comparative concentration than the lower molecular weight ABC. This is likely due to the greater CMC and molecular AWI adsorption observed for the lower MW system in Figs. 5.2A and 5.2B. For the lower MW PAA₁₅₃-*b*-PnBA₂₅ ABC, the percentage adsorption gradually increases with dosed ABC concentration as shown in Fig. 5.3A. The gradual increase in percentage of polymer adsorbed in the lower MW ABC system is likely due to the increase in free energy of ABC in the bulk solution as the AWI ABC adsorption approaches saturation with increasing ABC dosed concentration. Gradually the increasing osmotic pressure gradient with increasing ABC dosed concentration entropically drives the ABC adsorption on the Mg(OH)₂ particle surface to reduce free energy^{33,103}.

Table 5.1: Freundlich adsorption isotherm coefficients, K_f and n with corresponding coefficients of determination for amphiphilic copolymers (ABCs) PAA₁₅₃-*b*-PnBA₂₅ and PAA₁₅₃-*b*-PnBA₂₀₀ above and below their estimated critical micelle concentrations calculated from the data in Fig. 5.3B.

Isotherm value	PAA ₁₅₃ - <i>b</i> -PnBA ₂₅		PAA ₁₅₃ - <i>b</i> -PnBA ₂₀₀	
	Unimer	Micellar	Unimer	Micellar
<i>Freundlich</i> R^2	0.99	0.79	0.99	0.97
K_f ($\mu\text{mol.m}^{-2}$)	1.8×10^{-4}	2.5×10^{-6}	0.296	0.015
$1/n$	1.78	2.69	0.23	1.65
q_e^* ($\mu\text{mol.m}^{-2}$)	~0.92		~0.48	
C_e^* (μM)	~119		~8	
C_d^* (μM)	~269		~54.7	

Fig. 5.3B shows four Linear Freundlich adsorption isotherms, a unimer adsorption regime and micellar adsorption regime for both ABC systems, which describe the changing logarithmic Mg(OH)₂ surface adsorption density (Log q_e) with increasing logarithmic supernatant equilibrium concentration (Log C_e). The unimer and micellar adsorption regimes for the lower MW PAA₁₅₃-*b*-PnBA₂₅ ABC have much closer adsorption intensity values ($1/n$) than their greater MW counterpart (PAA₁₅₃-*b*-PnBA₂₀₀). However, both adsorption regime intensities are larger than the PAA₁₅₃-*b*-PnBA₂₀₀ equivalents. At the unimer-micellar adsorption transition point concentration (C_e^*) located at the isotherm intercept, there is a stark increase in the greater MW PAA₁₅₃-*b*-PnBA₂₀₀ ABC adsorption intensity between regimes. It should be noted that for both ABC systems, their C_e^* values align with the dilatational viscoelasticity peaks in Fig. 5.2B which is likely related to the ABC CMCs²⁴³. With greater MW PAA₁₅₃-*b*-PnBA₂₀₀ ABC and lower MW PAA₁₅₃-*b*-

PnBA₂₅ ABC displaying C_e^* values of 8 μM and 119 μM respectively as shown in Table 5.1 (along with other Freundlich isotherm fitting constants). This was then related back to the dosed concentration using the C_d vs C_e plot in Appendix Fig. C3C and the equivalent C_d^* ABC concentrations are shown in Table 5.1.

At the unimer-micellar adsorption transition point, the adsorption densities of the lower MW PAA₁₅₃-*b*-PnBA₂₅ ABC are greater than the greater MW PAA₁₅₃-*b*-PnBA₂₀₀ ABC with q_e^* values of ~ 0.92 and ~ 0.48 $\mu\text{mol.m}^{-2}$ respectively. There are two factors influencing these q_e^* values. Firstly, as the lower MW ABC axiomatically has a shorter chain length, it can more easily conform and relax to the Mg(OH)₂ particle surface. Additionally, the smaller hydrophobic chain will provide lower steric barriers to further adsorption of ABCs on the Mg(OH)₂ surface³³. Secondly, the unimer-micellar adsorption transition point occurs at a much greater concentration due to the comparative entropic stability of the lower MW ABC, meaning there is a greater concentration gradient of ABC in bulk solution to drive adsorption onto the Mg(OH)₂ particle surface, which is indicated by the greater $1/n$ values compared to both regimes for the greater MW ABC.^{31,92,133,134,233,242}

Our previous work in Chapter 4 investigated the adsorption densities of SDS on Mg(OH)₂ through its monolayer and bilayer adsorption regimes using Freundlich adsorption isotherms, and at the monolayer-bilayer transition concentration was found to have q_e^* value of 0.11 $\mu\text{mol.m}^{-2}$ which is lower than those observed for the ABCs in this Chapter. It was thermodynamically argued by O'Shea et al.⁸⁵ that macromolecules such as polyelectrolytes increase in adsorption density with increasing MW. The enthalpic term which drives adsorption to reduce free energy, consists of contributions from both the polymer-surface bond energy and the solvent/polymer interaction energy. It is the polymer-surface bond energy which is primarily responsible for the increased adsorption of polymer in good solvent with increasing MW. The adsorption – MW trend has been attributed by other authors, to an increase in the number of polymer segments (i.e. MW) which bond to the particle surface resulting in an increased total bond energy with increasing MW^{30,85,246}. As ABCs are much less stable, displaying lower CMCs than their low MW surfactant counter parts, there is a greater thermodynamic drive for adsorption^{92,233}.

5.3.3) Floc structure characterisation

The flocculation characteristics of the two ABCs were then investigated using SLS. Fig. 5.4A shows the change in the ratio of the minimum repeating floc size to primary particle size (D_f/D_p) with increasing ABC dosed concentration. As the ABC concentration increases there is an increase in the (D_f/D_p) ratio. Interestingly, whilst the hydrophobic segments are identical between the two ABC systems, the larger MW ABC produced moderately larger flocs at lower concentrations, which is likely due the greater surface coverage at lower ABC concentrations shown in the adsorption isotherm in Fig. 5.3A. As previously discussed, the PAA segment causes local neutralisation of surface charge reducing particle stability, and subsequent conformation of the PnBA segment on the particle surface then increases surface energy promoting flocculation⁸⁵.

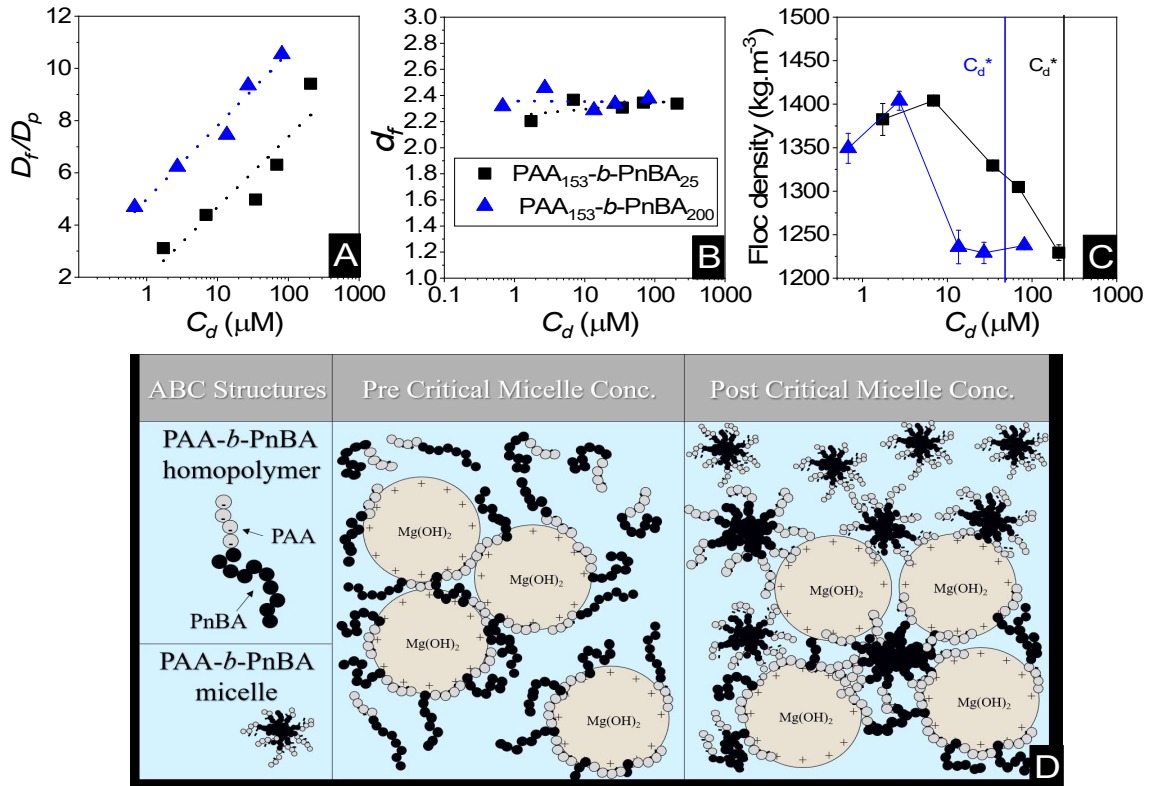


Figure 5.4: A) the change in the ratio of the smallest repeating floc unit diameter (D_f) to the primary particle diameter (D_p) with increasing ABC concentration determined through static light scattering. B) The change in fractal dimension (d_f) with increasing ABC concentration determined through static light scattering. C) The change in floc density with increasing ABC concentration determined via Eqn. 3.4. Vertical lines indicate micellar transition points (C_d^*). D) Illustration showing the change in adsorption and flocculation mechanisms pre and post critical micelle concentrations (CMC) of the amphiphilic block copolymers (ABC).

The gradient determined from the plot of linear region of $\text{Log}(IQ)$ *w.r.t* $\text{Log}(Q)$ shown in Appendix Fig. C4A and C4B, for varying dosed concentrations of ABCs for both systems, computes the fractal dimensions (d_f) of the resultant floc structures shown in Fig. 5.4B. The d_f values are stable with increasing ABC concentrations with both systems, displaying d_f values between 2.2-2.4. For high charge density polymeric flocculants (100% charge density) of intermediate MW of 10^4 - 10^5 $\text{g}\cdot\text{mol}^{-1}$, high fractal dimensions are generally recorded. Zhou and Franks¹⁹ recorded fractal dimensions of ~ 2.7 for a homopolymer poly(diallyldimethylammonium chloride) (PDMAC) used to flocculate silica particles, however for kaolin flocculated with polyaluminium chloride, fractal dimensions of 2.1-2.3 were recorded³⁷. Fractal dimension is a function of polymer charge density, particle

concentration and polymer conformation and these factors can affect the flocculation mechanism⁴⁴. These mechanisms have been modelled by various authors^{117,122} and generally quantify fractal dimensions of 2.2-2.4 as following an aggregation mechanism between diffusion limited particle-cluster aggregation and reaction limited cluster-cluster aggregation¹¹⁶.

Additionally, Bushell et al.⁴⁴ reported that bridging flocculation systems can display fractal dimensions of 1.75-2.5, which indicates an area of uncertainty regarding flocculation mechanism for structures of this intermediate fractal dimension 2.1-2.4. In fact, in addition to the PDMAC homopolymer, Zhou and Franks¹⁹ investigated a copolymer of PDMAC and polyacrylamide with a cationic charge density of 40% and found that the flocculation mechanism was likely a combination of charge patch and bridging flocculation mechanisms. This has interesting implications for the ABC systems as there is little known about their flocculation mechanisms regarding fractal dimension. In Chapter 3, very high MW (10^6 g.mol^{-1}) statistical copolymers of PAA and poly(acrylamide) (PAM) of 30% and 40% charge density were used to flocculate Mg(OH)_2 suspensions of the same solids concentration. This work reported fractal dimensions associated with open, porous bridging flocculation of 2.07 and 2.09 respectively and computed floc densities of $\sim 1045 \text{ kg.m}^{-3}$ and $\sim 1049 \text{ kg.m}^{-3}$ respectively, much lower than those in this work.

These pseudo-bridging flocs can display high particle agglomeration densities displayed in Fig. 5.4C compared with traditional reaction limited cluster-cluster flocculation^{117,122}. These are greater floc densities than the very high MW bridging flocculation system using the 30% and 40% charge density PAA-co-PAM indicating less porous, more closed structures. Fig 5.4C shows the computed floc densities using Eqn. 3.4 for both ABC systems. There is a decrease in floc density with increasing floc size/ ABC concentration. However, there is a sharp transition to a plateau at $\sim 1230 \text{ kg.m}^{-3}$ for the greater MW PAA₁₅₃-*b*-PnBA₂₀₀ ABC, whereas the lower MW ABC has a gradual decrease in floc density but also approaches $\sim 1230 \text{ kg.m}^{-3}$. The sharp and sudden density plateau for the greatest MW ABC occurs at approximately the unimer-micellar transition concentration, C_d^* . Indicating the formation of pseudo-bridging flocculation through micellar intermediates between particles (see Fig. 5.4D).

O'Shea et al.¹¹³ also noted that P(AA-co-BA)-*b*-PNIPAM ABCs could adsorb at particle surfaces facilitating flocculation with micellar intermediates between particles using a combination of charge-patch, charge neutralisation and hydrophobic attraction mechanisms. As these hydrophobic blocks have much shorter chain lengths than bridging flocculants, and the adsorption of high charge density hydrophilic blocks providing electrostatic charge neutralisation depleting the electrical double layer repulsion and thus Debye length of the particle³³. The transition to the plateaued floc densities of $\sim 1230 \text{ kg.m}^{-3}$ observed by the greater MW ABC system likely indicates the transition to this pseudo-bridging flocculation mechanism (i.e. unimer to micellar adsorption transition). Whereas for the lower MW ABC, there is a gradual transition to this mechanism as larger proportions of ABC are entropically driven to adsorb to the particle surface with increasing ABC dosed supernatant concentration and free energy. Whilst this occurs below the proposed unimer-micellar transition point concentration C_d^* in Table 5.1 for PAA₁₅₃-*b*-PnBA₂₀₀ ABC, it is known that highly unstable large hydrophobic ABCs form pre-micellar aggregates before full micelles^{31,133,134}, thus it is possible that the adsorption of the pre-micellar aggregates lowers the observable transition concentration below the ABC CMC.

5.3.4) Sedimentation and flotation performance

Fig. 5.5A shows the change in zonal settling rate with initial dosed ABC concentration. For both systems there is a clear increase in zonal settling rate from the non-flocculated baseline zonal settling rate. The greater MW PAA₁₅₃-*b*-PnBA₂₀₀ ABC system has a greater settling rate at lower dosed concentrations than the lower MW system. Initially, for the greater MW PAA₁₅₃-*b*-PnBA₂₀₀ ABC system, there is a plateaued sedimentation rate performance below the unimer-micellar transition dosed concentration C_d^* . Above this concentration there is a significant increase in zonal settling rate. For the lower MW PAA₁₅₃-*b*-PnBA₂₅ system however there is a gradual increase. Fig. 5.5B shows a photograph of the floc sizes with increasing ABC dosed concentration for the greater MW PAA₁₅₃-*b*-PnBA₂₀₀ ABC, and the change in floc size is clearly visible with increasing ABC concentration. However, substantial inter-aggregate spacing is visible at the highest doses, where the large particulates reduce the turbidity of the suspension due to reduced light scattering.

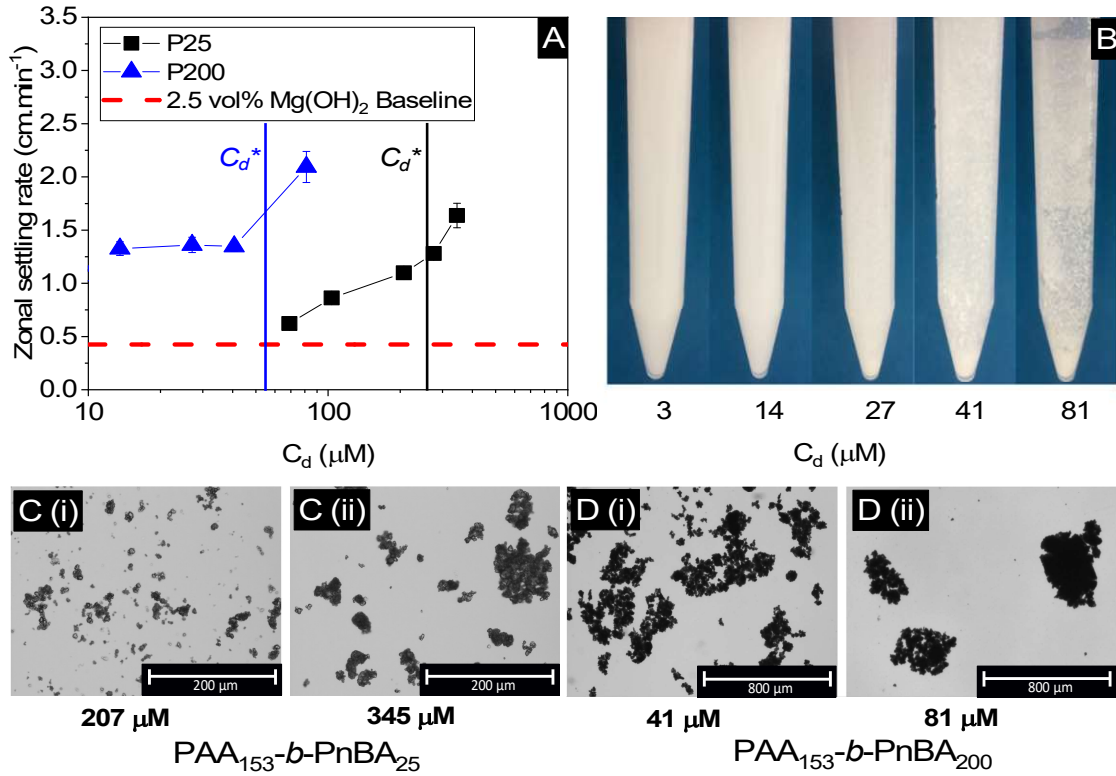


Figure 5.5: A) Data showing the sedimentation rate of amphiphilic block copolymers (ABCs) PAA₁₅₃-*b*-PnBA₂₅ and PAA₁₅₃-*b*-PnBA₂₀₀ flocculated Mg(OH)₂ as a function of ABC concentration. Vertical lines indicate micellar transition points (C_d^*). B) Shows an image of the ABC-Mg(OH)₂ flocs with increasing concentrations of ABC. C) Morphologi G3 single element microscopy images of PAA₁₅₃-*b*-PnBA₂₅ ABC-Mg(OH)₂ flocs at i) 207 μM and ii) 345 μM . D) Morphologi G3 single element microscopy images of PAA₁₅₃-*b*-PnBA₂₀₀ ABC-Mg(OH)₂ flocs at i) 41 μM and ii) 81 μM .

The change in zonal settling rate is function of a number of factors especially in hindered settling systems. In previous work (Chapter 3) the sedimentation dynamics of 2.5 vol.% Mg(OH)₂ flocculated with a statistical copolymer of PAA-*co*-PAM, the zonal settling rate was scrutinised using a fractal modified Richardson-Zaki sedimentation model (FMRZ model). The sedimentation dynamics of Mg(OH)₂ flocculated with PAA-*co*-PAM were found to be sensitive to floc size when inter-aggregate packing density was lower than the intra-aggregate packing density, where flow around the flocs was free and not restricted by floc-floc spacing permeability. When inter-aggregate packing densities approached intra-aggregate packing density the sedimentation rate was highly influenced by the fractal dimensions of the flocs, as floc permeability was suggested to be the main mechanism for water flux through the settling bed. As the two ABC floc systems in this work indicated more compacted floc densities, the same mathematical scrutiny was applied to the polymers

in this chapter to compare the suspension permeabilities and water flux capacity through the consolidating particulate bed.

$$f_s^* = \left(1 - \phi_p \left(\frac{D_f}{D_p}\right)^{3-d_f}\right)^{4.65} \quad (\text{Eqn. 5.1})$$

In Chapter 3, this inter-aggregate spacing consideration is mathematically defined as a dimensionless function proportional to the permeability of the particle network suspended in the medium, referred to as the fractal modified dimensionless permeability number, f_s^* ^{16,18,21}. f_s^* is a function of particle volume fraction, ϕ_p , smallest repeating floc unit diameter, D_f , the primary particle diameter, D_p and fractal dimension, d_f which are shown in Figs. 5.5A and 5.5B. The function, shown in Eqn. 5.1, is non-linear and the exponent which is traditionally a function of Reynolds number^{16,125} and normally taken as equal to 4.65 in laminar conditions²¹. The f_s^* values as a function of concentration are shown in Table 5.2, there is a decrease in f_s^* with increasing ABC dosed concentration for both ABC systems. This is a function of the decrease in floc density shown in Fig. 5.4C, resulting in the flocs physically occupying more space in terms of their outer boundaries. In our previous work (Chapter 3) using statistical copolymer PAA-co-PAM, the f_s^* values were calculated to be 0.05 - 0.07, substantially lower than those in Table 5.2 which are closer to order unity. This indicates that for the ABC systems, the floc size and density is dominant as inter-aggregate packing allows for substantial flow around these structures reducing hindering affects. However, drag and shape effects are likely influential on the zonal settling rates and suspension permeability effects are less important as the inter-aggregate packing density in the suspension is greater than intra-aggregate packing in the floc structures^{18,173}. This likely implies that floc-floc interaction effects are also less important, where it was found in our previous work in Chapter 3 that larger flocs were more influential on zonal settling rates due to netting effects¹⁵⁵⁻¹⁵⁷.

Table 5.2: The change in fractal modified dimensionless permeability number, f_s^* , with increasing dose of amphiphilic block copolymer concentration for both PAA₁₅₃-*b*-PnBA₂₅ and PAA₁₅₃-*b*-PnBA₂₀₀ systems calculated using Eqn. 5.1. using the data in Figs. 5.5A and 5.5B for a Mg(OH)₂ concentration of 2.5 vol.%.

PAA ₁₅₃ - <i>b</i> -PnBA ₂₅		PAA ₁₅₃ - <i>b</i> -PnBA ₂₀₀	
C_d (μM)	f_s^*	C_d (μM)	f_s^*
2	0.74	1	0.71
7	0.74	3	0.72
35	0.69	14	0.60
69	0.67	27	0.58
207	0.58	81	0.59

The increase in zonal settling rate is dominated by the increase in floc size and thus increasing ABC concentration as indicated in Figs. 5.5C(i) and 5.5C(ii) which show the single element microscopy images of PAA₁₅₃-*b*-PnBA₂₅ ABC-Mg(OH)₂ flocs at 207 μM and 345 μM respectively, and Figs. 5.5D(i) and 5.5D(ii) show the PAA₁₅₃-*b*-PnBA₂₀₀ ABC-Mg(OH)₂ flocs at 41 μM and 81 μM respectively. For both systems there appears to be a change in floc size with concentration. However, the greater MW PAA₁₅₃-*b*-PnBA₂₀₀ ABC system shows even larger flocs compared to the lower MW system, which is indicated in the relative zonal settling rate performances in Fig. 3.6A (Section 3.4.2). An interesting observation is the sudden increase in performance for the greater MW PAA₁₅₃-*b*-PnBA₂₀₀ ABC which occurs beyond the C_d^* . As discussed before, this effective flocculation mechanism has been attributed to the combination of charge-patch, charge neutralisation and hydrophobic attraction mechanisms which manifest as the micellar intermediates adsorbed between particles illustrated in Fig. 5.4D^{94,113}. Conversely, the lower MW PAA₁₅₃-*b*-PnBA₂₅ shows a much more gradual increase in zonal settling rate in Fig. 5.5A, which is in line with its decrease in density in Fig. 5.4C and has an approximated unimer-micellar adsorption transition concentration of 269 μM as shown in Table 5.1. The change in adsorption intensity at C_d^* in Fig. 5.2B is much less drastic for the lower MW ABC. With the lower hydrophobic chain length of PAA₁₅₃-*b*-PnBA₂₅ likely resulting in a lower degree of hydrophobic interaction, indicated by the higher f_s^* value at C_d^* and lower zonal settling rates even above the lower MW C_d^* ^{91,113}.

The mass percentage of recovered Mg(OH)₂ during batch flotation operations with dosed concentration ABC is displayed in Fig. 5.6A. Showing the performance of three ABCs, PAA₁₅₃-*b*-PnBA₂₅, PAA₁₅₃-*b*-PnBA₁₀₀ and PAA₁₅₃-*b*-PnBA₂₀₀ which were benchmarked

against the performance of SDS as a collector in Chapter 4. The SDS system appears to outperform all three ABC systems in terms of mass of $\text{Mg}(\text{OH})_2$ recovery, with an increase in mass recovery with increasing SDS dosed concentration, which plateaus at 93% recovery. Importantly, at dosed concentrations above C_d^* , the SDS began to form a bilayer, reducing particle surface energy thus preventing particle-bubble attachment. Meaning particle recovery was primarily through entrainment in the foam lamella. For the ABC systems at lower concentrations, the larger the hydrophobic chain length, the greater the $\text{Mg}(\text{OH})_2$ recovery, with lowest MW PAA₁₅₃-*b*-PnBA₂₅ recovering the least mass of $\text{Mg}(\text{OH})_2$ and the greatest MW PAA₁₅₃-*b*-PnBA₂₀₀ recovering the greatest mass of $\text{Mg}(\text{OH})_2$ (peaking at 52%) and the intermediate MW PAA₁₅₃-*b*-PnBA₁₀₀ recovering an intermediate amount. This trend does however deviate at the greatest dosed concentrations of ABC, where the greatest and intermediate MW systems recovery performance drops significantly and the lowest MW system begins to increase, albeit only marginally.

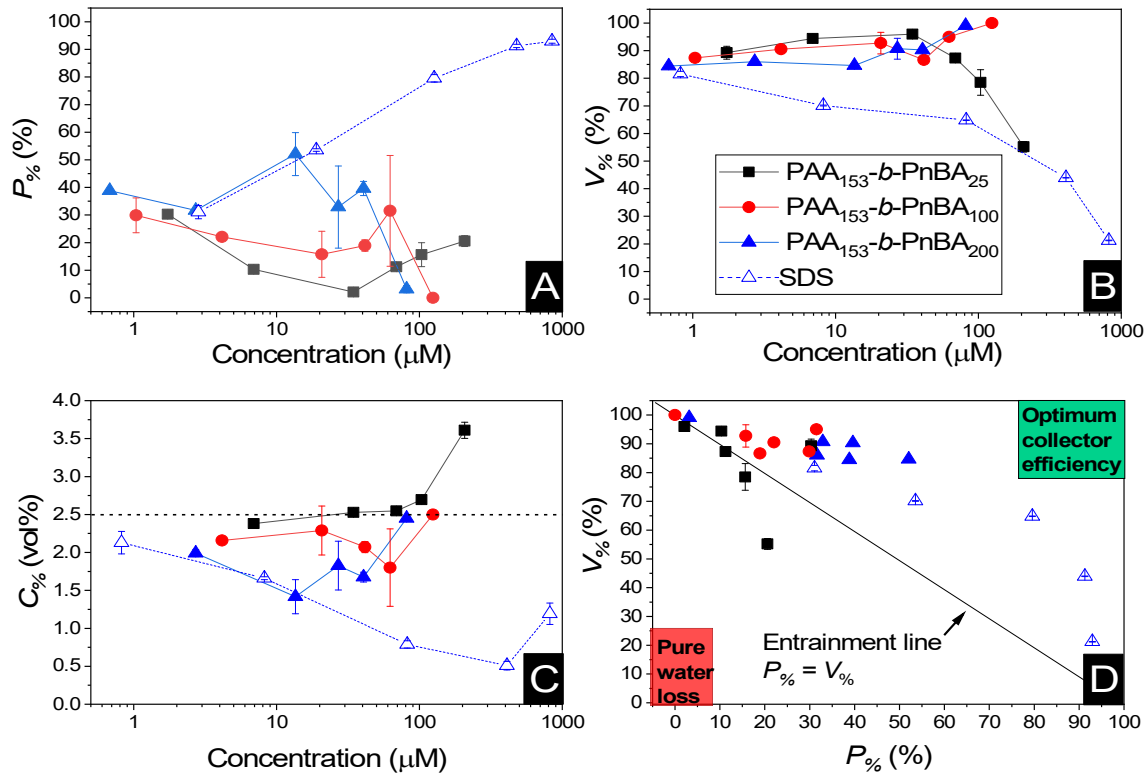


Figure 5.6: A) Percentage of Mg(OH)₂ recovered during amphiphilic block copolymer (ABC) PAA₁₅₃-*b*-PnBA₂₅, PAA₁₅₃-*b*-PnBA₁₀₀ and PAA₁₅₃-*b*-PnBA₂₀₀ and sodium dodecyl sulphate (SDS) surfactant flotation as a function of concentration. B) Remaining suspension volume after flotation operations as a function of concentration. C) The residual bulk concentration of Mg(OH)₂ remaining in the cell post flotation. D) Comparison of PAA₁₅₃-*b*-PnBA₂₀₀ and sodium dodecyl sulphate residual bulk concentration of Mg(OH)₂ as a function of the percentage of Mg(OH)₂ recovered during flotation operations.

Fig. 5.6B shows the remaining mass of water remaining in the flotation cell post-flotation as a function of dose ABC concentration. An interesting observation is the significant water losses associated with the SDS and lowest MW PAA₁₅₃-*b*-PnBA₂₅ ABC. Fig. 5.2A indicated that SDS and PAA₁₅₃-*b*-PnBA₂₅ collectors have the greatest AWI surface activity with the greatest reductions in surface tension, additionally these collectors also displayed the greatest dilational viscoelasticities in Fig. 5.2B, which has been related to increase foam stability in flotation operations¹²⁹. The small rise in Mg(OH)₂ recovery at higher dosed concentrations for the lower MW ABC is likely related to the enhanced water loss at this higher dosed concentration through entrainment much like the SDS system. There are lower rates of water loss when considering the intermediate and greater MW ABCs, which is

likely due to their non/lower surface activity as reported for these higher hydrophobic chain length ABCs^{90,91} which is shown in Fig 5.2A. Interestingly, there is a notable water loss at lower dosed concentrations than at higher doses for the greatest MW PAA₁₅₃-*b*-PnBA₂₀₀ ABC, which is inverse to the change in surface tension associated with this macromolecule shown in Fig. 5.2A. This is likely related to the higher Mg(OH)₂ recovery at lower dosed concentrations. Hydrophobised floc attachment to the AWI in the foam phase can stabilise the particle loaded foam through retarding film drainage in the lamella via film stratification^{129,190,215-217}. This stratification mechanism has found to be more important for dynamic wet foams found in flotation operations, which implies that they have greater water retention at their equilibrium by reducing lamella fluid drainage¹⁴⁴.

The compound effects of the relative Mg(OH)₂ recovery and water retained in the flotation cell are summarised in Fig. 5.6C, which displays the residual cell concentration (vol.%) post flotation as function of dosed collector concentration. Fig. 5.6D shows the relative mass of particles recovered as a function of water remaining in the flotation cell, which is compared to an entrainment line ($P\%=W\%$). What is apparent is that when considering the residual cell concentration, SDS appears to reduce the flotation cell concentration most effectively, which is also reflected in Fig. 5.6D, which indicates that a greater mass of particles were recovered than mass of water lost from the flotation cell. However, these enhanced particle recoveries were associated with greater degrees of water loss from the cell. At lower concentrations, the greatest MW PAA₁₅₃-*b*-PnBA₂₀₀ ABC performed comparatively to the SDS system, then at concentrations above its predicted unimer-micellar transition concentration, solid-liquid separation reduced to almost no detectable particle recovery. This was also observed for the greatest MW ABC when considering the remaining fluid mass percentage against the particle mass percentage of Mg(OH)₂ recovered in Fig. 5.6D.

The lowest MW ABC shows some interesting performance characteristics, as Fig. 5.6C shows that the residual cell concentration increases with increasing dosed ABC concentration to above the initial 2.5 vol.% Mg(OH)₂ suspension concentration. This is likely because there is a greater mass of water lost than mass of Mg(OH)₂ particles recovered. Further indicating that small increase in recovery at higher ABC concentration doses was likely due to entrainment rather than hydrophobic interactions. Likely due to the high surface activity and thus foamability of PAA₁₅₃-*b*-PnBA₂₅ as observed with the SDS

model system. Again, the intermediate MW PAA₁₅₃-*b*-PnBA₁₀₀ ABC had an intermediate performance by all four metrics in comparison to the lowest and greatest MW ABCs.

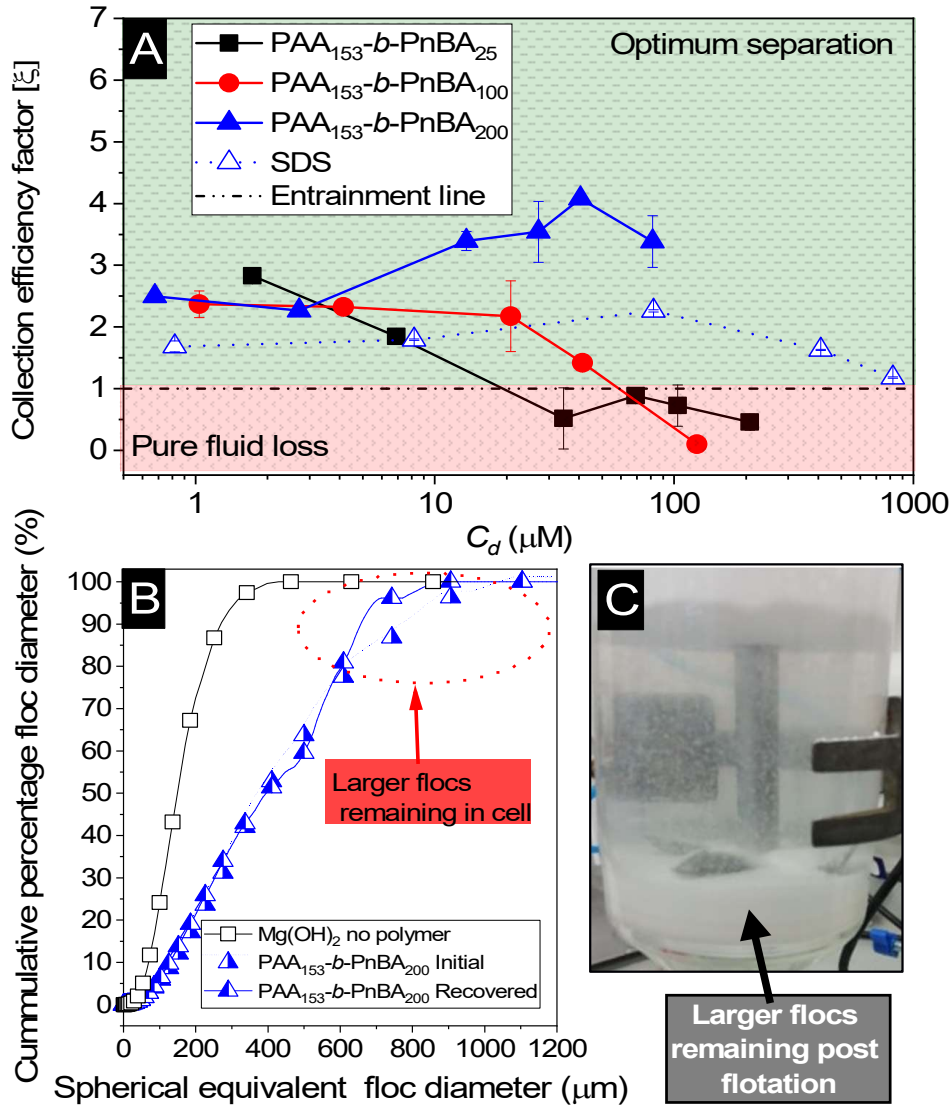


Figure 5.7: A) The collection efficiency factor calculated using Eqn. 4.7 as a function of dosed concentration of ABC and SDS. B) Data showing the cumulative frequency distribution of particle size populations for Mg(OH)₂ in the batch flotation cell agitated at 250 rpm for 5 minutes. Mg(OH)₂ flocculated with 500 ppm of amphiphilic block copolymer (ABC) PAA₁₅₃-*b*-PnBA₂₀₀ agitated 250rpm for 5 minutes. The cumulative frequency floc size distribution of ABC-Mg(OH)₂ flocs extracted during flotation in the foam phase. C) Image of flocculation cell post flotation.

The collection efficiency factor calculated using Eqn. 4.7 allows one to quantify the dewatering ratios of the three ABCs and SDS, which may be related to ABC adsorption and flocculation characteristics. Fig. 5.7A shows the collection efficiency factors for the

three ABCs and SDS as a function of dosed concentration. The same mechanistic observations are made regarding Figs. 5.7C and 5.7D, where the entrainment line is represented by $\zeta=1$. When $\zeta<1$, there is a greater mass of water being recovered than $\text{Mg}(\text{OH})_2$ particles and when $\zeta>1$ there is successful dewatering occurring. Where the greater the magnitude of ζ , the greater the collection efficiency. In Chapter 4, it was found that SDS, which is displayed as a benchmark in Fig. 5.7A, displayed the greatest ζ values when the SDS surface adsorption density reached monolayer coverage. Beyond this point as a bilayer of SDS began to form, the performance decreased and $\text{Mg}(\text{OH})_2$ recovery was mainly through entrainment due to excess fluid loss rather than hydrophobic interactions reflected by the collection performance approaching $\zeta=1$.

As dosed concentration of ABC increases, the lowest MW PAA₁₅₃-*b*-PnBA₂₅ ABC decreases in collection efficiency. As this decrease in collection efficiency to $\zeta<1$ occurs at concentrations below PAA₁₅₃-*b*-PnBA₂₅ unimer-micellar dosed concentration ($C_d^*=269$ μM , see Table 5.1), but the percentage of ABC adsorbed increases gradually with increasing dosed concentration (Fig. 5.3A), indicates that the ABC concentration at the AWI gradually increases resulting in a decrease in surface tension (Fig. 5.2A). This results in increasing foamability^{90,91} with increasing dosed concentration, which is reflected in Fig. 5.6B by increased water loss from the flotation cell. The fact that the lowest MW system also records very little $\text{Mg}(\text{OH})_2$ recovery (Fig. 5.6A) at lower dosed concentrations, which increases as water loss increases, shows that the ratio of water loss to particles recovered increases. When analysed alongside the floc size increases with increasing dosed concentration of ABC (Figs. 5.5A-D(ii)), and considering that entropic considerations imply that below the C_d^* , surface energy should increase with increasing ABC surface coverage^{65,80,240}. There are implications that $\text{Mg}(\text{OH})_2$ recovery is prohibited by increasing hydrodynamic restrictions coupled with inadequate hydrophobisation provided by the lowest MW PAA₁₅₃-*b*-PnBA₂₅ ABC.

For the PAA₁₅₃-*b*-PnBA₂₀₀, there is a slightly different trend observed. An increase in collection efficiency is observed with increasing dosed concentration, but recovery initially peaks then decreases (Fig. 5.6A) to very low levels of $\text{Mg}(\text{OH})_2$ recovery beyond its unimer-micellar transition concentration ($C_d^*=54$ μM , see Table 5.1). As previously discussed regarding PAA₁₅₃-*b*-PnBA₂₀₀, there is an increase in fluid remaining in the cell with increasing dosed concentration for PAA₁₅₃-*b*-PnBA₂₀₀. Which when compared to the

surface tension decrease shown in Fig. 5.2A, suggests there may be particle stabilisation effects occurring in the foam rather than mechanistic resistance to foam breakage provided by viscoelastic modification. Making viscoelasticity a poor indication of flotation performance alone due to competing particle foam stabilisation effects, but a good indicator of unimer-micellar transition concentrations¹⁴⁰.

Interestingly, the ratio of particles to water recovered increases with increasing concentration, but the peak $\text{Mg}(\text{OH})_2$ recovery occurs at $C_d = 14 \mu\text{M}$ (see Fig. 5.6A), followed by a decrease in particle recovery, but increase in fluid remaining in the cell below the inflection point in dilational viscoelasticity shown in Fig. 5.2B. This could be due to a variety of factors. As $\text{PAA}_{153}\text{-}b\text{-PnBA}_{200}$ dosed concentration increases, there is an increase in floc size indicated in Figs 5.5-D(ii) to a greater degree $\text{PAA}_{153}\text{-}b\text{-PnBA}_{25}$, indicating there may be increasing hydrodynamic restrictions with increasing ABC dose preventing mass transfer of flocs to the foam phase⁶⁸. The decreased particle recovery at these higher concentrations provides a lower degree of stratification at the AWIs in the foam, reducing the effect of the steric barrier preventing fluid draining from the foam lamella back into the flotation cell^{129,144}. Additionally, increased floc sizes in flotation operations have also been reported to increase film piercing which may exacerbate drainage¹⁴⁰. Another consideration is that ABC self-assembly produces wettable charged corona of PAA blocks on the micellar surface above the CMC much like the SDS system^{83,84,88,146,186}. The same trends in hydrophobic chain length regarding flotation performance are also observed in Fig. 5.7A, with the intermediate MW $\text{PAA}_{153}\text{-}b\text{-PnBA}_{100}$ ABC showing intermediate performance. As the length of the hydrophobic chain increases, the surface energy increases making the flocs more entropically compatible with flotation operations below their CMC.

The limitation of flotation using ABCs appears to be a balance of the ABCs hydrophobising capacity (which is prohibited beyond micellization concentrations) and the resultant floc size which hydrodynamically limits $\text{Mg}(\text{OH})_2$ recovery. This is ultimately highlighted when comparing the $\text{PAA}_{153}\text{-}b\text{-PnBA}_{200}$ ABC performance directly with SDS. Where the $\text{PAA}_{153}\text{-}b\text{-PnBA}_{200}$ system has much greater collection efficiency compared to SDS. $\text{PAA}_{153}\text{-}b\text{-PnBA}_{200}$ higher efficiency is due to its superior hydrophobising capacity granted by the much larger hydrophobic chain length and near non-surface activity reducing excess water loss.

The hydrodynamic restrictions of the flotation operation were probed in Fig. 5.7B. The best particle recovery system was selected for hydrodynamic performance inspection (PAA₁₅₃-*b*-PnBA₂₀₀ ABC system at 14 μM dosed concentration) as this allowed for the greatest proportion of particles to compare before and after flotation operation. Interestingly, given the unimer-micellar transition dosed concentration is calculated as being $\sim 54 \mu\text{M}$ (see Table 5.1), the selected 14 μM represents only $\sim 80\%$ (When $C_d = 14 \mu\text{M}$, $q_e = 0.38 \mu\text{mol}\cdot\text{m}^{-2}$) of the maximum unimer adsorption density. The closest recorded flotation performance for the greatest MW system to its respective C_d^* is at 41 μM but results in a particle recovery mass percentage of only 39%. This is likely due to the increased flocculation at increasing concentrations of ABCs adsorbed to the surface of $\text{Mg}(\text{OH})_2$ particles, resulting in a loss of foam stability as previously discussed⁶⁸. In Chapter 4 when investigating the adsorption of SDS onto $\text{Mg}(\text{OH})_2$ as a collector agent, there was no significant flocculation observed, even though SDS adsorption increased the surface energy of the particles⁷¹. This meant that adsorption could reach maximum unimer coverage densities with no competing hydrodynamic restrictions unlike the ABCs systems in this work. Additionally, ABCs have been found to form pre-micellar aggregates which may lower the optimum flotation performance by increasing flocculation below its respective $C_d^{*31,133,134}$.

Table 5.3: Data showing the 10th (d_{10}), (d_{50}) and (d_{90}) cumulative percentile spherical equivalent floc diameters for $\text{Mg}(\text{OH})_2$ without amphiphilic block copolymer (ABC) and dosed with 500ppm PAA₁₅₃-*b*-PnBA₂₀₀ and extracted ABC- $\text{Mg}(\text{OH})_2$ flocs from the foam phase.

Sample	d_{10}	d_{50}	d_{90}
$\text{Mg}(\text{OH})_2$ no ABC (μm)	68	151	271
Initial floc size in cell (μm)	136	390	804
Recovered floc size from foam phase (μm)	127	394	660

The d_{10} , d_{50} and d_{90} cumulative percentile spherical equivalent floc diameters for the system before flocculation, pre-flotation from the cell and post-flotation from the collector tray are recorded in Table 5.3, which are extracted from the cumulative frequency distributions of floc size in Fig. 5.7B. The application of ABC collectors flocculate the particles effectively, increasing size significantly across the entire PSD. Comparing the PSDs before and after flotation can help establish the hydrodynamic limitations of using ABCs as collectors. Noticeably, the d_{10} and d_{50} values are very similar pre and post-flotation. However, the d_{90} values are significantly different, with pre-flotation showing a d_{90} spherical equivalent floc diameter of 804 μm , whereas post-flotation samples from the collector tray indicate a d_{90}

spherical equivalent floc diameter of 660 μm . This indicates that flotation using ABCs as collector agents effectively targets fines and intermediate particle sizes but is ineffective at removing larger flocs in the system. This is qualitatively reflected in Fig. 5.7C, which shows the flotation cell post-flotation using the greatest MW system at 14 μM , showing only visibly larger flocs remain in the flotation cell which is significantly less turbid.

Table 5.4: The change in dimensionless permeability number, f_s^* , post-flotation with increasing dosed concentration of amphiphilic block copolymers (PAA₁₅₃-*b*-PnBA₂₅ & PAA₁₅₃-*b*-PnBA₂₀₀) compared to the pre-flotation values shown in Table 5.2.

PAA ₁₅₃ - <i>b</i> -PnBA ₂₅			PAA ₁₅₃ - <i>b</i> -PnBA ₂₀₀		
C_d (μM)	f_s^* post-flotation	Change (%)	C_d (μM)	f_s^* post-flotation	Change (%)
2	0.74	0	1	0.71	0
7	0.75	1.5	3	0.77	7.0
35	0.69	-0.5	14	0.75	25.9
69	0.66	-0.8	27	0.68	16.6
207	0.45	-23.3	81	0.59	1.2

Whilst the ABC collectors produce flocs of sizes above hydrodynamic limits which will remain in the flotation cell, these larger flocs can be targeted using a subsequent sedimentation stage which is often built into flotation cells as waste sludge outlets⁷⁵. As previously discussed, the sedimentation of $\text{Mg}(\text{OH})_2$ suspensions using ABCs can be described using the FMRZ model^{18,22}. Using the SLS data in Figs 5.4A and 5.4B, the dimensionless permeability number f_s^* was calculated from the initial solids volume fraction of 2.5 vol.% as shown in Table 5.2. For the FMRZ model, the zonal settling rate is directly proportional to the dimensionless permeability number assuming a constant terminal velocity of individual flocs^{18,22}. In Chapter 3, it was found that when using statistical copolymers of PAA- *co*-PAM, the largest floc sizes were most influential on zonal settling rate, which was likely due to ‘netting’ effects similar to those observed in sweeping flocculation. Given that through the hydrodynamic observations made in Fig. 5.7B and Table 5.3 that the largest flocs remain in the cell, it can be assumed that the terminal settling velocity remains unaffected, although in a reduced hindered settling regime, due to the large size of the remaining flocs there may be boundary layer separation resulting in drag forces hindering settling to consider²⁴⁷. However, as the f_s^* values in Table 5.2 were order unity pre-flotation indicating inter-aggregate flow, it is likely these effects

are already present and floc terminal velocity can be assumed to be unaffected by flotation operations.

Using the residual cell concentrations in Fig. 5.7C, the post-flotation dimensionless permeability numbers were calculated and shown in Table 5.4, with their corresponding percentage change on pre-flotation f_s^* values in Table 5.2. For the lowest MW ABC, there is a decrease in f_s^* with increasing ABC concentration, which is reflected in the low collection efficiency factors shown in Fig 5.7A, where a greater amount of water is recovered than particles. Resulting in the solids concentration remaining in the flotation cell increasing, thus increasing hindering effects during sedimentation increasing the zonal settling rate. For the greatest MW ABC, the post-flotation increases and peaks at 14 μM , which is the optimum particle recovery concentration, and then decreases back to pre-flotation values. Whilst 14 μM isn't the optimum dewatering dosed concentration, it removes the most particles with little comparable additional water loss, meaning the residual cell concentration is at its lowest at 14 μM and thus reduces the hindering effects by up to ~25%, suggesting improved sedimentation dynamics post-flotation to target coarse aggregates during dewatering.

5.4) Conclusions

Amphiphilic block copolymers (ABCs) of poly(acrylic acid)-*b*-poly(n-butyl acrylate), with consistent hydrophilic poly(acrylic acid) chain length, were investigated as dual flocculant-collector agents in combined flotation-sedimentation dewatering operations to remove $\text{Mg}(\text{OH})_2$ suspended particulates. The surface activity of the ABCs was found to be a function of their hydrophobic poly(n-butyl acrylate) block length. Where increasing hydrophobic block length reduced both the magnitude of surface tension reduction and dilational viscoelasticity with increasing ABC concentration. The longest hydrophobic chain length ABC had a greater proportion of ABC adsorbed to $\text{Mg}(\text{OH})_2$ particle surfaces than in solution, which remained constant with increasing ABC concentration. For the shortest chain length ABC, this proportion increased with increasing concentration of ABC. ABC adsorption onto $\text{Mg}(\text{OH})_2$ was found to take place in unimer and micellar regimes. The transition point between these adsorption mechanisms occurred at a lower concentration for the longest hydrophobic chain length ABC, occurring in the concentration regions of both the investigated ABCs respective peaks of dilational viscoelasticity,

suggesting that this may be related to their critical micelle concentrations (CMCs). The structure of these resultant flocs was probed using static light scattering, and the floc size was found to increase in increasing ABC concentration, with the longest hydrophobic chain length ABC increasing size to a greater degree at lower ABC concentrations. The fractal dimension of the two ABCs was determined to be between ~ 2.2 - 2.4 and appeared to be relatively constant with increasing ABC concentration. The resulting floc structure densities decreased with increasing ABC concentration, with the shortest hydrophobic chain length ABC gradually decreasing to a density of $\sim 1230 \text{ kg.m}^{-3}$, whereas the longest hydrophobic chain length ABC quickly decreased then plateaued at this density.

As floc sized increased with increasing ABC concentration, the zonal settling rate of the flocculated suspensions increased, with the largest hydrophobic chain length polymer displaying superior sedimentation rates, particularly above its suspected CMC in its micellar adsorption regime. It is likely that during the increased adsorption in the micellar regime, hydrophobic interactions between the densely adsorbed hydrophobic chains promoted increased aggregation to reduce surface energy, which is reflected by the sudden increase in sedimentation performance in the micellar regime. This relationship was also observed during batch flotation tests, where the flotation performance for the longest chain length ABC was far superior to the shortest, removing a greater percentage of Mg(OH)_2 , which reduced to near zero above the micellar transition concentration. The shortest chain length ABC flotation performance was holistically poor, recovering a far greater proportion of water than Mg(OH)_2 , resulting in a more concentrated residual flotation cell concentration than pre-flotation operations. This was linked to its comparatively high surface activity, which promoted a greater degree of foaming entraining excess water. Hydrodynamically, the longest chain length ABC was found to be able to recover a large range of the particle size distribution in the cell, with only differences in the 90th percentile cumulative floc size values pre and post-flotation. Meaning the ABCs successfully flocculate fine material to be compatible with flotation and only fail in recovering the largest flocs in the flotation cell. Finally, the effect of decreasing the residual flotation cell concentration on zonal settling rate was compared using a dimensionless permeability number, which has been extensively used in fractal modified Richardson-Zaki settling models. It was found that the lower residual cell solid concentrations resulted in the greatest dimensionless permeability number increase which is directly proportional to zonal sedimentation rates.

5.5) Nomenclature for Chapter 5

A_s	Specific surface area	$\text{m}^2.\text{g}^{-1}$
C^*	Concs. at unimer-micellar transition point	μM
$C\%$	$\text{Mg}(\text{OH})_2$ concentration remaining in the flotation cell	vol.%
C_d	Initial supernatant collector concentration	μM
C_e	Equilibrium supernatant collector concentration	μM
D_f	Diameter of minimum repeating flocs	m
D_p	Primary particle Diameter	m
d_f	Fractal dimension	-
d_{10}	Cumulative 10% point of diameter in a PSD	m
d_{50}	Cumulative 50% point of diameter in a PSD	m
d_{90}	Cumulative 90% point of diameter in a PSD	m
f_s	Functional permeability of a suspension	-
g	Gravitational acceleration	$\text{m}.\text{s}^{-2}$
$I(Q)$	Scattering intensity	-
k_f	Freundlich constant related to the adsorption capacity	$\text{mg}.\text{g}^{-1}$
M_r	Relative molecular mass	$\text{g}.\mu\text{mol}^{-1}$
M_{rp}	Mass of recovered particles in the collector tray	g
M_{rw}	Mass of recovered water in the collector tray	g
M_{Tp}	Mass of total particles initially in the flotation cell	g
M_{Tw}	Mass of total water initially in the flotation cell	g
N	Number of particles in an aggregate/floc	-
n	Freundlich adsorption intensity-based coefficient	-
$P\%$	Mass.% of $\text{Mg}(\text{OH})_2$ recovered from the flotation cell	%
q_e	Collector adsorption density on $\text{Mg}(\text{OH})_2$ surfaces	$\mu\text{mol}.\text{m}^{-2}$
Q	Scattering wave vector	nm^{-1}
V_f	Volume of floc	m^3
V_p	Volume of primary particle	m^3
$W\%$	Mass% of water remaining the flotation cell	%
ε	Dilational viscoelasticity	$\text{mN}.\text{m}^{-1}$
γ	Interfacial surface tension	$\text{mN}.\text{m}^{-1}$

ξ Collector efficiency factor -

Chapter 6:

A comparison of the sedimentation dynamics of statistical and block copolymer flocculation aids in radwaste dewatering

6.1) Introduction

As discussed in Chapter 3, modifications have been made to Stokes law including a dimensionless permeability number, which mathematically represents sedimentation hindrance in multiple particle settling²¹. And a fractal dimension function, which allows for a modification based on porosity, affecting particle density and the effective occupied volume of the flocs from their initial flocculated state^{18,22,49}. This has been referred to in Chapter 3 as the fractal modified Richardson-Zaki (FMRZ) model described in Eqn. 3.10 (Section 3.2.2). For polydisperse particle size distributions (PSDs), the value of the representative floc population size, \overline{D}_f , is problematic, as it requires one particle size to be selected to represent an entire PSD. In Chapter 3, it was found that the larger floc sizes, particularly those around the 90th cumulative percentile values, provided the most accurate predictions of zonal settling rate for bridging flocculation of Mg(OH)₂. Likely due to particle netting interactions as larger flocs sedimented at a greater velocity¹⁵⁵⁻¹⁵⁷.

In Chapter 5, it was found that the longest hydrophobic chain length amphiphilic block copolymer effectively flocculated Mg(OH)₂ and could remove 52 mass% of the Mg(OH)₂ suspension via flotation, whilst retaining >80% of the water. A performance which exceeded dewatering ratios by traditional collector agents used in flotation such as sodium dodecyl sulphate in Chapter 4. However, the optimum dewatering dosed concentration of amphiphilic block copolymer for flotation performance was not the same as the optimum concentration for sedimentation, due to hydrodynamic differences between flotation and sedimentation operations. The combination of flotation and flocculation resulted in a lower volume fraction of particles post-flotation, with greater floc diameters, which by reasoning using Eqn. 3.10, should improve the zonal settling rate of the resultant suspension. Though due to increased inter-aggregate spacing compared to the suspension permeabilities analysed in Chapter 3, settling will likely be affected by drag effects through boundary layer separation around the flocs and should be incorporated into the FMRZ model.

In this Chapter, the aim is to compare the performance of two different flocculants to improve SPP1 residence times. Firstly, poly(acrylic acid)-*co*-poly(acrylamide) (PAA-*co*-PAM) with an AA molar ratio of 30%, which was used in Chapter 3 to improve the sedimentation dynamics of Mg(OH)₂ suspension. Secondly, the novel amphiphilic block copolymer, consisting of two segregated homopolymer blocks of poly(acrylic acid)₁₅₃ and poly(*n*-butyl acrylate)₂₀₀, referred to hereon as PAA-*b*-PnBA. As PAA-*b*-PnBA both flocculates Mg(OH)₂ and makes the resultant flocs compatible with flotation operations by providing hydrophobization, the aim was to use a flotation cell, which could be retrofit between FGMSF and SPP1, to target and recover fines associated with actinide incorporation⁷.

To compare performance, five scenarios (including a no settling aid baseline scenario) were selected and compared to see which would result in the greatest decrease in SPP1 residence time based on previously collected size and sedimentation data from Chapters 3 and 5. The first four scenarios are sedimentation operations alone using different polymers and concentrations, the fifth is a combined flotation-flocculation process. As the settling rates post-flotation for PAA-*b*-PnBA could not be determined due to the lack of a clear interface, the settling rates were modelled using a drag modified FMRZ sedimentation model, computing different size/ exponent inputs and validated against experimental data collected in Chapter 5. Additionally, metrics such as final bed volume fractions were also considered, which unlike the sedimentation data which was collected in previous chapters, was experimentally determined for this work. Finally, strategic caveats and future considerations, which require additional research, were discussed to help inform strategic decision making in FGMSF decommissioning when using polymeric flocculants.

6.2) Deployment scenarios

- **Scenario 1:** No polymeric flocculants are used. Dewatering is completed using only sedimentation. Shown in Fig. 6.1 and detailed in Table 6.1.
- **Scenario 2:** Sedimentation is enhanced using 20 ppm PAA-*co*-PAM. Dewatering is completed using polymer aided sedimentation only. Shown in Fig. 6.1 and detailed in Table 6.1. This is the optimum concentration for sedimentation performance established in Chapter 3.

- **Scenario 3:** Sedimentation is enhanced using 81 μM PAA-*b*-PnBA. Dewatering is completed using polymeric aided sedimentation only. Shown in Fig. 6.1 and detailed in Table 6.1. This is the optimum sedimentation performance established in Chapter 5.
- **Scenario 4:** $\text{Mg}(\text{OH})_2$ is flocculated using 14 μM PAA-*b*-PnBA. Dewatering is completed using polymeric aided sedimentation only. Shown in Fig. 6.1 and detailed in Table 6.1. This was the concentration which delivered the greatest removal of particulates and reduced functional permeability of the suspension by the greatest amount (see Table 5.4 in Chapter 5).
- **Scenario 5:** $\text{Mg}(\text{OH})_2$ is flocculated using 14 μM PAA-*b*-PnBA and fines removed using dispersed air flotation. The remaining cell suspension is then dewatered using polymer aided sedimentation. Shown in Fig. 6.1 and detailed in Table 6.1.

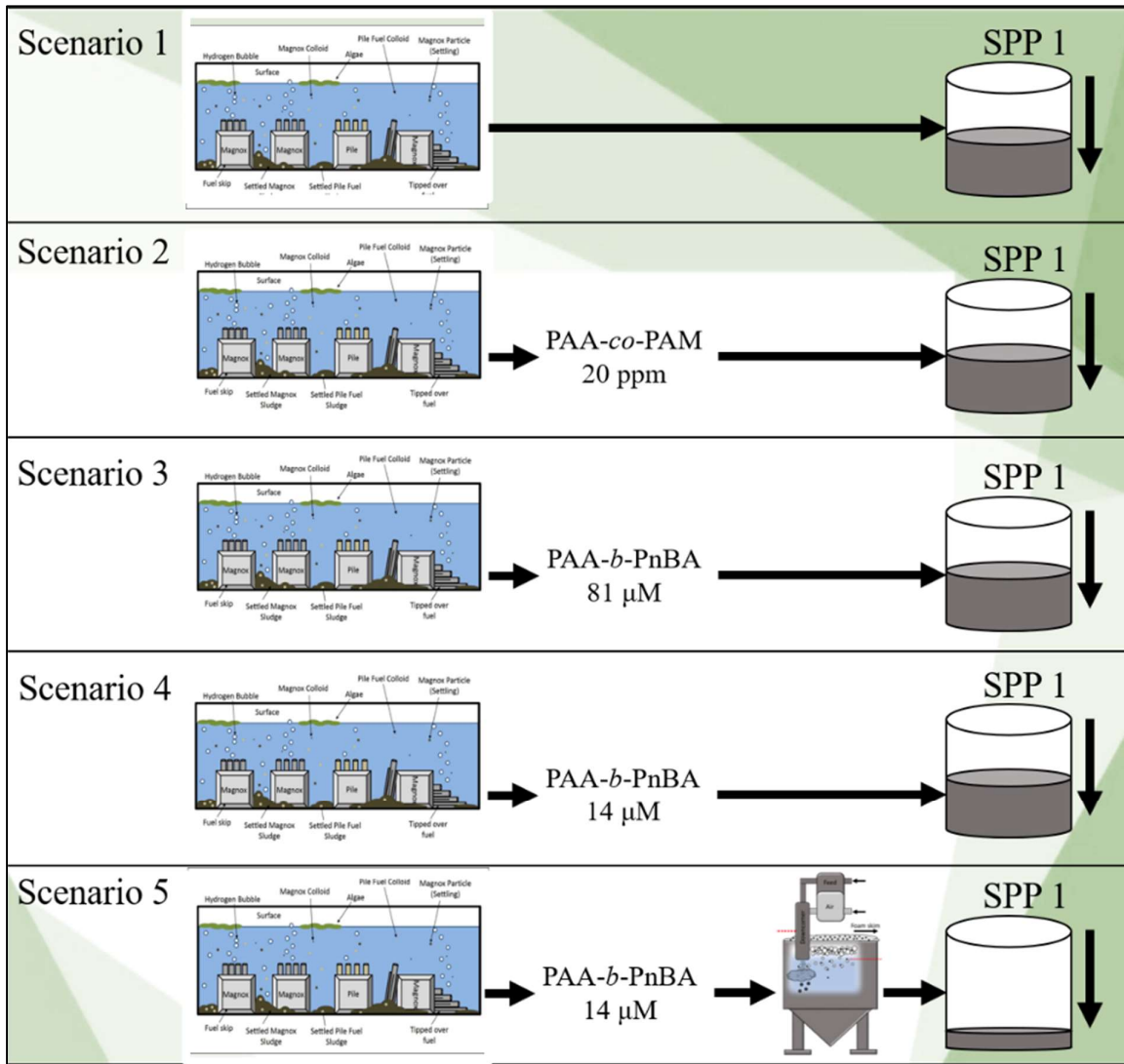


Figure 6.1: Diagram of Strategies 1-5.

6.3) Materials and methodology

6.3.1) Materials

Materials used for bed consolidation solids concentration in this work (and data collected in previous chapters) include: $Mg(OH)_2$ (Versamag, Martin Marietta, US) was used for flocculation and flotation experiments at 2.5 vol.% (see Chapter 3, Section 3.3.1). The polymers used in the study were firstly a water soluble anionic PAA-co-PAM (30 mol.% PAA and 70 mol.% PAM) copolymer used in Chapter 3. Secondly, a novel amphiphilic block copolymer $PAA_{153}-b-PnBA_{200}$ was synthesised using reversible addition fragmentation chain-transfer polymerisation (see Chapter 5, Section 5.2.1). The scenarios

with their respective polymer flocculants, flocculant dose and initial solids concentration are listed below in Table 6.1.

Table 6.1: Modelled scenarios with respective polymer flocculant, flocculant dosages and initial solids concentration.

Scenario	Flocculant	Polymer dose	Initial suspension conc.	Process
1	N/A	N/A	2.5 vol.%	Settling
2	PAA-co-PAM	20 ppm	2.5 vol.%	Settling
3	PAA-b-PnBA	81 μM	2.5 vol.%	Settling
4	PAA-b-PnBA	14 μM	2.5 vol.%	Settling
5	PAA-b-PnBA	14 μM	1.4 vol.%	Flotation & settling

6.3.2) Floc structure characterisation

The size and structure of the resultant flocs in Scenarios 2-5 were computed in Chapters 3 and 5. The PAA-co-PAM polymer in Scenario 2 had a more open floc structure, displaying a fractal dimension of 2.07 and minimum repeating floc size and primary particle size of 6.74 and 0.28 μm respectively, resulting in a solid volume fraction of 3.4%. For Scenarios 3, 4 and 5, floc structure was found in Chapter 5 to vary with different PAA-b-PnBA concentrations. For Scenario 3, with a PAA-b-PnBA concentration of 81 μM , the resultant flocs displayed a fractal dimension of 2.38, density of 1238 $\text{kg}\cdot\text{m}^{-3}$ and minimum repeating floc size and primary particle size of 1.68 and 0.16 μm respectively. For Scenarios 4 and 5, with a PAA-b-PnBA concentration of 14 μM , the resultant flocs displayed a fractal dimension of 2.29, density of 1236 $\text{kg}\cdot\text{m}^{-3}$ and minimum repeating floc size and primary particle size of 1.26 and 0.17 μm respectively. The dimensionless permeability numbers of Scenarios 2-4 were calculated using Eqn. 5.1. For scenarios 2, 3 and 4/5, the dimensionless permeability numbers are calculated from data in Tables 6.1 and 6.2 and are 0.05, 0.58, 0.6 and 0.75 respectively.

Table 6.2: Floc structure variables for Scenarios 2-4 showing the fractal dimension, d_f , minimum repeating floc diameter, D_f , primary particle size, D_p , the floc density, ρ_f and the dimensionless permeability number f_s^* .

Variable	Scenario 2	Scenario 3	Scenario 4	Scenario 5
d_f	2.07	2.38	2.29	2.29
D_f [μm]	6.74	1.68	1.26	1.26
D_p [μm]	0.28	0.16	0.17	0.17
ρ_f [$\text{kg}\cdot\text{m}^{-3}$]	1045	1238	1236	1236
f_s^*	0.05	0.58	0.60	0.75

6.3.3) Sedimentation analysis and settled bed concentration

Sedimentation was previously analysed in Chapters 3 and 5 for the statistical and block copolymers respectively in two differing ways as a function of available copolymer. As per Chapter 3, the PAA-co-PAM system analysed in Scenario 2 were prepared in a 1 litre reactor vessel. The reactor vessel was 25 cm in diameter with four baffles and mixed using a four-blade axial flow impeller of 50 mm diameter, and 60° pitch, which was located 2 cm from the base of the reactor vessel. Impeller rotation rate was at 300 rpm, as this was determined to be a sufficient agitation rate to keep flocs suspended and prevent sedimentation, while reducing shear degradation experienced with higher mixing rates (see Chapter 3). The required polymer was then added in 5 ml aliquots via a calibrated micropipette over a period of no more than 10 seconds at the centre of the suspension, to ensure an even distribution throughout the system. Visual observation of suspension-supernatant boundary level change with time was used to measure the influence of polymer concentration on hindered settling rates. Flocculated suspensions were then transferred to 1 litre measuring cylinders of 61 mm diameter. The cylinders were inverted 5 times to evenly re-suspend flocs and the interfacial height was measured over time. The settled bed concentration was determined by allowing the flocculated and raw suspensions to settle for 48 hours. Then the final solids concentration, Φ_f , was computed from the product of the ratio of the initial and final suspension height (H_i and H_f respectively) and initial solids concentration Φ_i (2.5 vol.%) shown in Eqn. 6.1.

$$\Phi_f = \frac{H_i}{H_f} \Phi_i \quad (\text{Eqn. 6.1})$$

The sedimentation analysis for the PAA-*b*-PnBA system, by contrast, was completed by stirred using a magnetic stirring a 250 ml 2.5 vol.% Mg(OH)₂ suspension at 400 rpm for 10 minutes to ensure an even suspension of Mg(OH)₂. Given volumes of the chosen polymer stock solution were then added to the beaker which continued to be stirred at 400 rpm for a further 20 minutes. Turning the stirrer off and removing the magnetic stirrer bar, the solution was then poured into a volumetric cylinder (100 ml). Waiting for the mudline to appear and fall, a stopwatch was used to measure the time taken for the mudline to fall from the 80 ml to 60 ml mark on the measuring cylinder, as shown by the photograph of the experiment set up in Fig. 6.2. The settled bed concentration was determined by allowing

the flocculated and raw suspensions to settle for 48 hours then the final solids concentration was recorded using Eqn. 6.1.

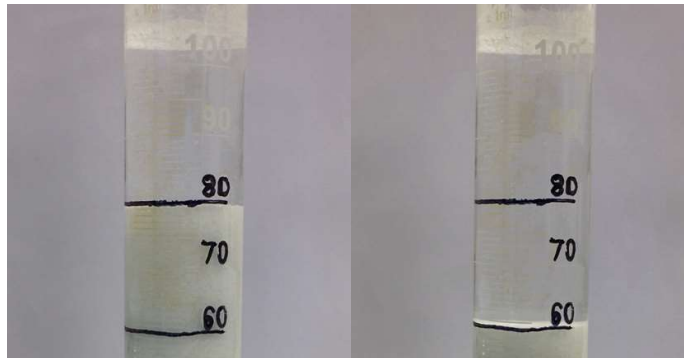


Figure 6.2: Photograph taken of the set up for batch settling rate experiments in a 100 ml volumetric cylinder, showing the fall of the mudline over time.

6.4) Results, discussion and implementation considerations

6.4.1) Scenario 4 and 5 floc size characterisation

The structural differences between Scenarios 2-5 are a function of the both the polymer and polymer dosages used. Firstly, for the PAA-*co*-PAM used in Scenario 2, both floc density and the fractal dimension were lower than the other polymer driven dewatering strategies in Scenarios 3-5. This is commonly observed when using lower charge density higher molecular weight polymers to flocculate counter-ionically charged particles^{19,103}. The slower conformation of the polymer chains onto the surface of the Mg(OH)₂ results in greater loops and tails which extend beyond the Debye layer³³. Additionally, the process of adsorption of anionic functional groups onto the cationic particle surface reduces the ionic strength of the particle and thus the extent of the Debye layer¹⁷. These loops and tails result in more open structures and thus lower densities commonly observed in bridging flocculation. This was also observed using cryogenic scanning electron microscopy in Chapter 3.

In Chapter 5, Scenario 3 utilised a concentration of 81 μ M, this concentration was associated with a multi-layer adsorption mechanism. Scenarios 4 and 5 which utilised PAA-*b*-PnBA concentrations of 14 μ M are assumed structurally identical. Our previous work indicated that the adsorption regime utilised at this concentration was unimer adsorption. Interestingly there was not a notable difference in floc density between Scenarios 3-5,

although their fractal dimensions were different. With Scenario 3 displaying a fractal dimension of 2.38 whereas Scenarios 4 & 5 had fractal dimensions of 2.29. It was suggested that because amphiphilic block copolymers such as PAA-*b*-PnBA form pre-micellar aggregates, which have an affinity for the Mg(OH)₂ surface likely resulting in a structural transition to a more open structure, utilising a combination of charge patch, charge neutralisation and hydrophobic interactions to facilitate flocculation. However, due to the highly hydrophobic nature of the non-ionic PnBA chain segment, some floc contraction and densification may be occurring with increasing surface coverage due to entropically driven water liberation from the floc⁹⁴. In our previous work, Scenario 4 was analysed using single-element optical microscopy, the particle size distribution pre-flotation is shown in Fig. 5.7, the d_{10} , d_{50} and d_{90} values were found to be 136 μm , 390 μm and 804 μm respectively. Post-flotation there was a lower d_{90} reported (660 μm) indicating that the flotation process was hydrodynamically hindered. At the optimum flotation concentration of 14 μM , the resultant recovered foam phase consisted of a liquor with solids volume concentration of 8.5 ± 0.74 vol.%, which can be processed separately to the settled liquor or even blended into a grouted encapsulant for final disposal in a geological disposal facility.

6.4.2) Scenario 5 sedimentation model selection and validation

The selection of sedimentation models for predicting zonal rates is vital in being able to decide residence times for sludge batches sent from FGMSP to SPP1. Whilst work has been completed in acoustic backscatter to help monitor sedimentation²², more work is required in understanding the sedimentation dynamics of these suspensions, especially when considering Mg(OH)₂ flocculated with polymers which aggregate particles by different flocculation mechanisms. For example, because of the greater effective suspension volume due to the lower fractal dimension flocs facilitated using the statistical copolymer PAA-*co*-PAM, there is a lower dimensionless permeability number (see Table 6.2) for Scenario 2 than in Scenarios 3-5. It was established in Chapter 3 that this increasing in effective floc volume meant that inter-aggregate packing density approached intra-aggregate packing and there was significant particle interactions. Larger flocs mostly influenced the sedimentation rate and the reduction in inter-aggregate spacing allowed an assumption that drag effects and shape effects would be negligible and that there was likely significant flow through the flocs porous structure¹⁸.

Using the experimentally determined zonal settling rates in Scenario 4, recorded size data in Fig. 5.7 was used to firstly determine appropriate sedimentation models. Sedimentation models which could be used to estimate SPP1 residence times and secondly determine which size data was appropriate to represent a polydisperse suspension. Previously, Vahedi and Gorczyca¹¹⁸ suggested a terminal settling velocity relationship shown in Eqn. 6.2 which incorporates a drag coefficient, which is a function of the particle Reynolds number, Re , shown in Eqn. 6.3. Hereon Eqn. 6.2 will be referred to as the DRAG model and Eqn. 3,10 as the FMRZ model. Additionally, Vahedi and Gorczyca¹¹⁸ include a non-sphericity factor, η , which is a function of the floc aspect ratio, however due to high aspect ratios of ~ 0.7 indicating near sphericity for more open floc structures found in Chapter 3, η is assumed to be 1. Previous work by Paul et al.¹⁷³ found when investigating the sedimentation of Caesium phosphomolybdate, zirconium molybdate and zirconium citromolybdate displaying spheroidal, cubic and rectangular cuboidal morphologies respectively, the Richardson-Zaki (RZ) exponent, n in Eqn. 6.2, was greater than 4.65 due to shape induced drag.

$$U_i = \frac{\eta(\rho_p - \rho_w)g}{18\mu_w} D_p^{3-d_f} \frac{\overline{D}_f^{d_f-1}}{1 + 0.15Re^{0.687}} \left(1 - \Phi_p \left(\frac{D_f}{D_p} \right)^{3-d_f} \right)^n \quad (\text{Eqn. 6.2})$$

$$Re = \frac{U_T \overline{D}_f \rho_w}{\mu_w} \quad (\text{Eqn. 6.3})$$

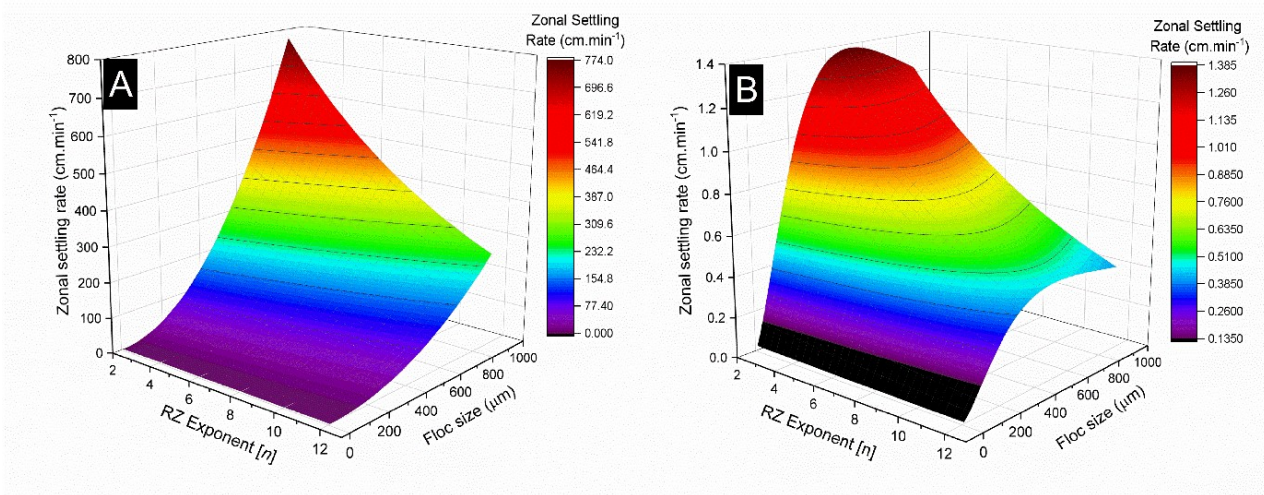


Figure 6.3: Multivariate analysis of A) Fractal modified Richardson-Zaki (FMRZ) settling model shown in Eqn. 3.10 and B) drag-modified FMRZ (DRAG) settling model shown in Eqn. 6.2, which are used to predict sedimentation rates of 2.5 vol.% Mg(OH)₂ flocculated using 14 μM Poly(acrylic acid)-*block*-poly(n-butyl acrylate)[see Scenario 4]. Here the sensitivity of zonal settling rate was investigated by varying the polydisperse floc size, \overline{D}_f , and the Richardson-Zaki (RZ) exponent, n . Where $\rho_p = 2340.6 \text{ kg.m}^{-3}$, $\rho_w = 1000 \text{ kg.m}^{-3}$, $\mu_w = 8.9 \times 10^{-4} \text{ kg.m}^{-1}.\text{s}^{-1}$, $D_f = 1.26 \text{ }\mu\text{m}$ and $D_p = 0.17 \text{ }\mu\text{m}$.

A multivariate analysis was performed probing the FMRZ and DRAG model's sensitivity to polydisperse floc size (0-1000 μm) and the RZ-Exponent (2-12) shown in Fig. 6.3A and 6.3B respectively. There are marked differences between the two models, where the FMRZ model in Fig. 6.3A shows a drastic increase in zonal settling rate over the same polydisperse floc size and RZ-exponent range. The distinct difference between the two models is that the DRAG model, by definition, incorporates a drag coefficient which is a function of the non-linear reciprocal of floc diameter. This drag coefficient, d_c , is proportional to the particle Reynolds number where $U_i \propto d_c \propto \frac{1}{1+0.15Re^{0.687}}$ and $Re \propto \overline{D}_f$. This non-linear reciprocal relationship between zonal settling rate and polydisperse floc size means that zonal settling rate increases initially with increasing floc diameter. Then as boundary layer separation occurs when the viscous forces in the fluid begins to dominate settling dynamics, the floc size increase begins to inhibit zonal settling rate^{21,247}. This limits the zonal settling rate to $>1.5 \text{ cm.min}^{-1}$ rather than increasing indefinitely in the FMRZ model. Additionally, the effect of increasing RZ-exponent further inhibits the zonal settling rate as it is order unity to the power of increasing exponent values, models the increasing hindered drag and shape effects in hindered settling regimes observed by Paul et al.¹⁷³.

6.4.3) Scenario 5 post-flotation sedimentation modelling

To validate which model is more representative of Scenario 4, the FMRZ and DRAG models were compared in Table 6.4 which uses the experimentally measured sedimentation rate of Scenario 4, $U_i = 1.33 \pm 0.06 \text{ cm}\cdot\text{min}^{-1}$, to calculate the polydisperse floc diameters using the FMRZ and DRAG models. These were then compared to the measured d_{50} and d_{90} polydisperse floc diameters for Scenario 4 in Fig. 5.7. Notably when using the FMRZ model assuming the linear spherical RZ-exponent, $n = 4.65$, the computed polydisperse floc diameter was significantly lower than the experimentally determined d_{50} and d_{90} Scenario 4 values at $\sim 43 \mu\text{m}$. The diameter was computed iteratively using the DRAG model approximating a polydisperse floc diameter of $\sim 328 \mu\text{m}$ which more closely reflected experimentally determined floc diameters in Fig. 5.7, specifically Scenario 4's d_{50} . As the DRAG model appeared to be more likely to give a good first approximation of sedimentation rates in Scenario 4 and thus more accurate modelled Scenario 5 zonal settling rates, the experimentally determined d_{50} and d_{90} values in Fig. 5.7 were used to compute the RZ-exponent iteratively using the experimentally determined zonal settling rates. This computed RZ-exponents of 6.52 and 13.77 for the d_{50} and d_{90} values respectively shown in Table 6.4. Whilst greater than the linear sphericity RZ-exponent, similar RZ-exponents were reported by Johnson et al.¹⁶ and Paul et al.¹⁷³ in hindered sedimentation work.

Table 6.4: Experimentally and modelled polydisperse floc diameters using the fractal modified Richardson-Zaki (FMRZ) settling model and the drag-modified FMRZ (DRAG) settling model, using experimentally determined zonal settling rates and various RZ-exponent (n) inputs.

System	Zonal settling rate [U_i]	Polydisperse floc diameter [\bar{D}_f]
Experimentally determined d_{50}	1.33	390 μm
FMRZ model (Eqn. 3.10, d_{90}), $n=4.65$	1.33	43 μm
DRAG model (Eqn. 6.2, d_{50}), $n=4.65$	1.33	328 μm
DRAG model (Eqn. 6.2, d_{50}), $n=6.52$	1.33	390 μm
DRAG model (Eqn. 6.2, d_{90}), $n=13.77$	1.33	804 μm

The selection of model inputs are complex, when investigating Scenario 2 in Chapter 3, the FMRZ model required an input of the d_{90} floc size to produce first approximation of sedimentation rate. It was argued that because of the lack of inter-aggregate spacing computed from the low dimensionless permeability number, that particle interactions were not negligible and that larger flocs dominate the sedimentation rate. Larger flocs may encompass smaller flocs as they settle at a greater rate similar to what is observed in sweeping flocculation systems as discussed in Chapter 3. However, in this system, because

inter-aggregate spacing is greater, these particle interactions may be less prominent. It should be noted that the block copolymer flotation process in Chapter 5 (shown in Fig. 5.7) was found to target fine material and was hydrodynamically limited prohibiting the flotation of larger floc sizes >660 μm . This implies that larger floc sizes may be more appropriate for modelling post-flotation sedimentation rates.

The predicted zonal settling rate for Scenario 5 was modelled by taking the experimentally determined zonal settling rate, $U_{i.S4} = 1.33 \pm 0.06 \text{ cm.min}^{-1}$, and applying the functional permeability number proportionalities shown in Eqn. 6.4, where $\Phi_{p.S4}$ & $\Phi_{p.S5}$ are the solid volume fractions for scenario 4 (0.025) and 5 (0.014) respectively. The RZ-exponent, n , was varied between 4.65, 6.52 and 13.77 to reflect the use of the linear spherical assumption and the experimentally determined d_{50} and d_{90} values used as inputs respectively. Interestingly, the increase in RZ-exponent value increases the predicted zonal settling rate, where the use of the d_{90} floc size (804 μm) and $n=13.77$ predicts the greatest zonal settling rate of 2.6 cm.min^{-1} .

$$U_{i.S5} = U_{i.S4} \times \frac{\left(1 - \Phi_{p.S5} \left(\frac{D_f}{D_p}\right)^{3-d_f}\right)^n}{\left(1 - \Phi_{p.S4} \left(\frac{D_f}{D_p}\right)^{3-d_f}\right)^n} \quad (\text{Eqn. 6.4})$$

Comparing zonal settling rates, Scenarios 1-4 are experimentally determined whereas Scenario 5 is modelled based on FMRZ and DRAG models. Fig. 6.4 shows that all Scenarios 2-5 display a greater zonal settling rate than Scenario 1. Where Scenario 1 represents the $\text{Mg}(\text{OH})_2$ sedimentation rate without the aid of polymeric flocculants and displays a sedimentation rate of 0.42 cm.min^{-1} . Scenario 2, which utilises the statistical copolymer PAA-co-PAM, produces the greatest zonal settling rate of the five scenarios with a sedimentation rate of 3.04 cm.min^{-1} . Comparing Scenarios 3 and 4, the greater concentration of the amphiphilic block copolymer, PAA-*b*-PnBA, produced larger flocs which were more compact with a fractal dimension of 2.38 for Scenario 3 (81 μM), whereas the lower concentration used in Scenario 4 (14 μM) has a lower fractal dimension of 2.29, indicating more open structured flocs. The average densities of flocs in scenarios 3 and 4 are effectively identical as shown in Table 6.2. The greater the concentration of PAA-*b*-PnBA, the greater the zonal settling rate of the suspension (Scenario 3 = 2.09 cm.min^{-1} and

Scenario 4 = 1.33 cm.min⁻¹), which is linked to the greater floc sizes associated with an increase in polymer concentration given the consistent floc densities with polymer dose.

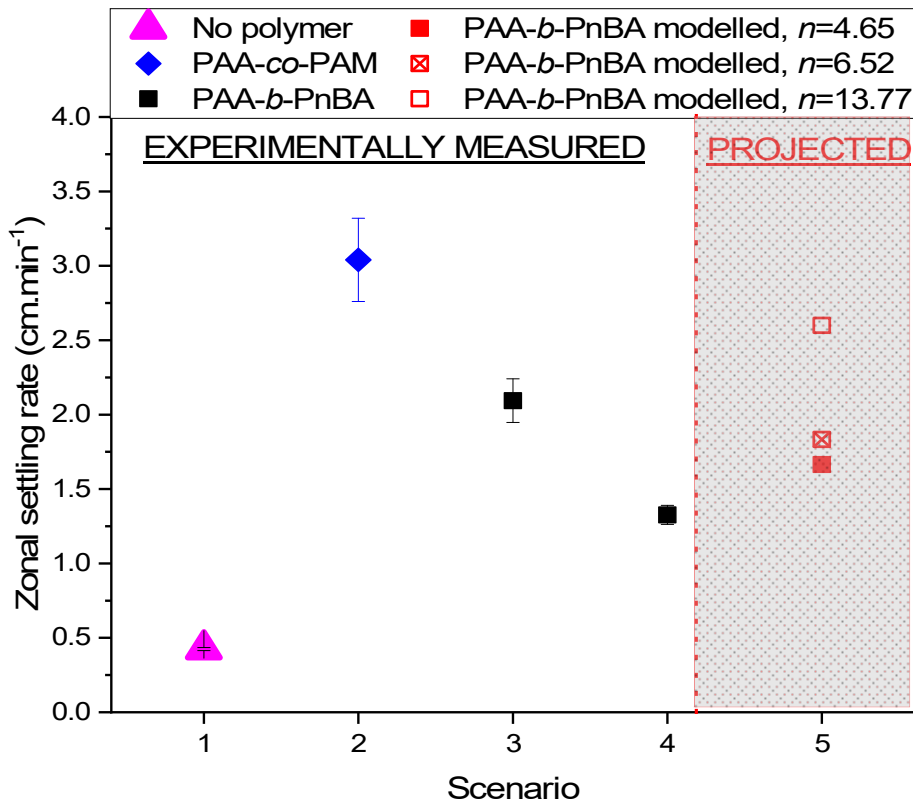


Figure 6.4: Scenarios 1-5 with their corresponding zonal settling rates.

Scenario 5 shows an increased sedimentation rate, which is attributed to the modelled increase in the functional permeability number, due to a decrease in the solid suspension concentration thus reducing hindering effects post-flotation. Given the issues associated with selecting a single floc size to represent an entire polydisperse floc population, it is likely that the appropriate polydisperse floc size lays between the d_{50} and d_{90} flocs size. Volume weight mean diameters, or De Brouckere mean diameter ($d_{[4,3]}$), are often quoted as being an appropriate floc size to represent the floc population²⁴⁷, which is calculated using Eqn. 6.5 computing a $d_{[4,3]}$ size of 573 μm . Using the DRAG model, the RZ-exponent was calculated as $n=10.51$. Using Eqn. 6.4, the $d_{[4,3]}$ zonal settling rate post-flotation was predicted as 2.23 cm.min⁻¹. Ultimately, whilst there is some uncertainty as to the degree of increase in zonal settling rate post-flotation, there is high confidence that the zonal settling rate is likely between 1.66 - 2.6 cm.min⁻¹.

$$d_{[4,3]} = \frac{\int_0^1 \overline{D_f}^4 dF_n}{\int_0^1 \overline{D_f}^3 dF_n} = \frac{\sum f_{n,i} \overline{D_{f,i}}^4}{\sum f_{n,i} \overline{D_{f,i}}^3} \quad (\text{Eqn. 6.5})$$

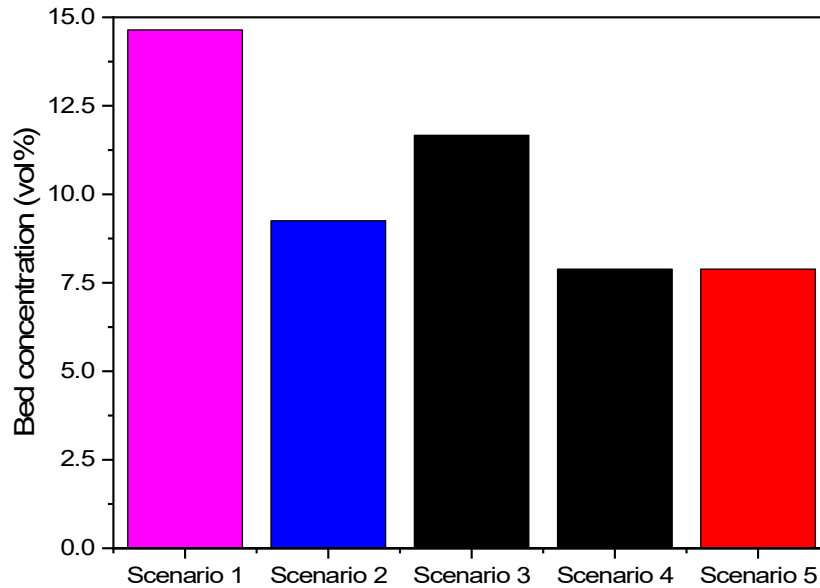


Figure 6.5: Settled bed concentrations for each of the 5 experimentally determined and modelled dewatering scenarios for sludge packaging plant 1.

Comparing settled bed concentrations of the five scenarios, it is clear from Fig. 6.5, that the application of polymeric flocculants decreases the consolidated bed concentrations. Interestingly, there is a marked difference between Scenarios 3 & 4/5, where Scenario 5 is assumed to be of equal concentration to Scenario 4 but only 48% of the final volume post-flotation. Scenario 3 has a greater bed concentration than Scenario 4, which is likely a reflection of the structural and flocculation mechanistic differences which is a function of concentration. However, an investigation by O'Shea et al.⁸⁵ found when investigating statistical copolymers of PAA and PNIPAM, where PNIPAM is temperature sensitive, at 50°C the polymer was hydrophobic and facilitated flocculation. At 25°C (below the LCST), the polymer had a much more consolidated bed than when heated to 50°C, which was due to the increased mechanistic strength provided by the particle-particle attraction resisting the downward weight of the sediment bed. This relationship was also observed by Franks⁸⁹ when investigating pH sensitive polymers such as chitosan which became hydrophobic at

greater pH's promoting flocculation, then by reducing the pH became repulsive allowing beds to consolidate further.

In the block copolymers system (Chapter 5) where the opposite is observed, it is likely that due to the micellar adsorption, there is a high degree of hydrophobic water liberation from the settled floc structures. A previous investigation by Volpert et al.⁹⁴ of adsorption of amphiphilic block copolymers onto clay surfaces found that highly hydrophobic adsorbed layers would liberate water almost completely from particle surfaces depending on the comonomer functional group hydrophobicity. This implies that there could be floc contraction with increasing PAA-*b*-PnBA adsorption in the micellar regime as water may be liberated from the structure, increasing floc density and reducing bed volumes. Additionally, the molecular weight of the PAA-*b*-PnBA is substantially lower ($\sim 10^4$ g.mol⁻¹) than those investigated by O'Shea et al.⁸⁵ and Franks.⁸⁹ ($\sim 10^6$ g.mol⁻¹). Where the latter work used polymers associated with bridging flocculation and reported substantially lower surface adsorption when compared with PAA-*b*-PnBA in this work. It has been observed by Avadiar et al.⁴³ that there is a relationship between polymeric flocculant molecular weight (but more specifically the flocculation mechanism) and the resultant yield stress of sedimented beds which display non-Newtonian behaviour. The larger molecular weight polymers utilised a bridging flocculation mechanism produced a complex network, where this interlinking network produced the increased yield stress, this observation has also been linked to the bed resistance to consolidation by O'Shea et al.⁸⁵.

There are many factors to consider when selecting which scenario is optimum for site operation and additional considerations must be made outside the scope of this investigation. Whilst improving the sedimentation rate of the flocculated suspensions is important to reduce residence times and total operation time, the resultant bed solid volume fraction is an important consideration. Whilst reducing bed volumes directly influences the amount of waste required to be dedicated to a geological waste disposal facility, the sedimented sludge must be further processed, which includes transport from SPP1⁶. Given multiphase transport is further complicated by nuclear industrial environments, where blockages and pump failures can be orders of magnitude more difficult to address, the settled flocculated sludge rheology in this intermediate stage is an important consideration and the resultant bed yield stresses of these systems should be addressed in future work. However, retrofitting a flotation cell such as the Jameson cell would allow the opportunity

to deploy additional mixing capability, notably the downcomer illustrated in Fig. 1.7, which would allow homogenous deployment of polymer to flocculated Magnox particulates.

Additionally, there are other caveats which should be considered when proposing the discussed technologies in this work. Whilst flotation has several deployability advantages including low geographical footprint requirements (Jameson flotation cell tank diameters can be as small as 0.19 m² and other designs are even mobile⁷⁵), no moving parts inside the tank as well as a notable chemical robustness to variable feed compositions^{66,74}, aerosolization of radionuclides is a possibility. And may require more robust engineering solutions such as implementation of HEPA filters. The foam phase of flotation will not only have a lower water content due to air bubbles meaning gamma ray shielding would need to be considered, but this scenario requires the design of an additional radwaste stream. The resilience of polymeric flocculants to alpha and beta radiation from the embedded radionuclides on the Mg(OH)₂ surface in real sludge should also be considered⁷. Particularly the potential environmental chemistry of the radiolytic and high alkalinity degradation products, to ensure they do not facilitate radioisotope mobility in geological disposal facilities. Whilst there are many uncertainties that require investigation, polymeric flocculants have shown to be very effective and economical tools to improve and aid in dewatering of these self-confessed intolerable risk facilities at Sellafield site and should be further investigated.

6.5) Conclusions

Five hypothetical scenarios were analysed and modelled to compare the deployment of two different polymers to improve the dewatering of a nuclear fuel storage pond, where one scenario incorporated flotation to first remove some material prior to sedimentation, specifically the fines. Polymeric flocculants were shown to be effective at increasing zonal settling rates of a radwaste simulant based on corroded Magnox fuel cladding. The large molecular weight, bridging mechanism flocculant, PAA-*co*-PAM, was more effective at improving zonal settling rates. This was due to their large open structure flocs compared to lower molecular weight, PAA-*b*-PnBA, diblock polymer alternative. PAA-*b*-PnBA was found to produce denser flocs than the PAA-*co*-PAM system, which remained constant with increasing floc size. As the PAA-*b*-PnBA flocs were much more compact, the greater

inter-aggregate spacing compared to the PAA-*co*-PAM system meant that drag effects had to be incorporated into an established fractal-modified Richardson-Zaki sedimentation model to accurately predict zonal settling rates and floc diameters. The modelled post-flotation scenario had imbedded uncertainty due to the polydispersity of the particle size distribution, however, the performance post-flotation was greater than pre-flotation. The resultant bed concentrations showed that the PAA-*co*-PAM system displayed documented resistance to compression due to the complex interlinking particle network providing additional mechanical strength. The PAA-*b*-PnBA system with more compact flocs also produced the most compact bed at its optimum sedimentation concentration. Further work is required to underpin the optimum scenario to implement to most effective settling aid to sediment Magnox radwaste, especially regarding settled bed rheology, which may affect downstream operations and result in particulate resuspension.

From the data collected in this thesis and a balance of the benefits of a novel flotation technology against the caveats. And given the high technology readiness level of flotation cells, the recommendation is to consider deployment of a retrofit, small footprint flotation cell to target radionuclide bearing fine material which threatens SIXEP ion exchange beds. Fundamental research strongly suggests that these flotation cell technologies, coupled with amphiphilic block copolymers could rapidly reduce colloidal and fine particulate challenges to SIXEP, whilst improving sedimentation rates of coarse aggregates to decrease sedimentation residence times thus shorting the length of cumbersome and costly decommissioning of legacy ponds and silos at Sellafield site.

Chapter 7:

Conclusions and future work

7.1) Conclusions

This work investigated the use of polymeric flocculants to aid in dewatering sludges generated from the long term corrosion of Magnox alloy clad spent nuclear fuel. Currently, Sellafield Ltd. are utilising gravitation sedimentation to dewater these sludges. However, the presence of slow settling and colloidal $\text{Mg}(\text{OH})_2$ species makes the required residence time in Sludge Packaging Plant 1 (SPP1) inefficient at removing fine particulates. Therefore the application of polymeric flocculants has been suggested to decrease both supernatant turbidity and SPP1 residence times. Additionally, there was scope to investigate more rapid dewatering techniques, as even with settling aids, sedimentation is a sluggish process. Regulatory requirements placed constraints on the range of dewatering engineering solutions which could be deployed. This drove the decision to investigate gravity driven sedimentation and dispersed air flotation which met the strict regulatory criteria (i.e. no moving parts, low geographical footprint etc.).

Current literature was scrutinised to investigate the types of polymer which could be deployed to flocculate cationic charged $\text{Mg}(\text{OH})_2$ particulate suspensions selected as a radwaste analogue for all the investigations in this thesis. Due to *in situ* monitoring restrictions, the mudline and turbidity of the settling tank in SPP1 is difficult to discern. Sedimentation models for polymerically flocculated material have been developed in literature, but applying the models for polydisperse fractal systems required more understanding to apply to flocculated suspensions at Sellafield. Firstly, two high molecular weight statistical copolymers of poly(acrylic acid) (one copolymer consisting of 30 mol.% and the second 40 mol.%) and polyacrylamide were used to flocculate 2.5 vol.% $\text{Mg}(\text{OH})_2$ suspensions and the two systems' sedimentation dynamics were compared. The structures of the two systems were investigated using static light scattering (SLS) to determine the floc fractal properties. It was found that the two systems displayed very similar densities, but the 30 mol.% anionic charged polymer produced larger flocs which had superior sedimentation dynamics. A fractal modified Richardson-Zaki (FMRZ) sedimentation model was used to predict zonal settling rates for validation as a SPP1 residence time estimation tool. It was found through multivariate analysis that the model provides first

order approximations of zonal settling rates, but is very sensitive to changes in fractal dimension due to non-linearity. Additionally, the size of flocs selected to predict accurate zonal settling rates was found to be around the 90th cumulative percentile floc size, suggesting that larger flocs have greater influence in hindered settling systems, encompassing smaller flocs as they settle.

Dispersed air flotation was investigated as an alternative dewatering technology. In current literature flotation has been deployed to address nuclear waste management for other nuclear waste types, such as wastes found at the Fukushima Daichi disaster site. Due to $Mg(OH)_2$ slight cationic nature, flotation was studied using anionic surfactants, one industry standard collector reagent (Sodium dodecyl sulphate) and one novel surfactant previously unused in literature as a collector to the author's knowledge (sodium lauroyl isethionate). Methyl isobutyl carbinol was selected as a frother for all flotation experiments. Firstly, the aggregation of $Mg(OH)_2$ in deionised water, potassium nitrate and surfactant dosed systems were compared and it was found that both surfactants had negligible effect on $Mg(OH)_2$ aggregation (especially when compared to electrical double layer reducing salt species) which is important for hydrodynamic considerations in flotation. The adsorption mechanisms of the two surfactants were investigated using a Total Organic Carbon (TOC) analyser and fitted to a linearised Freundlich adsorption isotherm. Two adsorption regions on $Mg(OH)_2$ were identified, monolayer adsorption and bilayer adsorption, by fitting two linearised Freundlich isotherms in these regions. Where the intercept of the two isotherms indicates the maximum monolayer adsorption density dosed concentration of surfactant and by extension, maximum hydrophobic modification. Flotation performance was assessed using four metrics: mass of particles recovered, fluid lost from the flotation cell, residual solids concentration in the flotation cell and an efficiency factor to compare dewatering ratios against dosed concentrations. There was a strong correlation between optimum flotation performance and the maximum monolayer surfactant adsorption density onto $Mg(OH)_2$. Sodium dodecyl sulphate was the best performing collector, with the greatest monolayer adsorption density (function of polar head group charge density) best dewatering ratios and greatest mass of particles extracted. Though, even at sodium dodecyl sulphate's optimum collection efficiency concentration, considerable water was still lost from the cell, entrained in the foam lamella.

Traditional surfactant driven flotation has two major technological deficits which are integral to meeting operational and regulatory requirements for an effective Sellafield Ltd. dewatering system. Firstly, surfactants are surface active, where their adsorption to air-water interfaces reduces surface tension resulting in wet foams which entrain additional water in the foam lamella. Secondly, even at maximum monolayer adsorption density (thus hydrophobic conditions), previous literature has indicated that fine and coarse particles have hydrodynamic limitations to bubble attachment and thus mass transfer to the foam phase for particulate recovery. Fine particulates lack the inertia to overcome slipstreams created by rising bubbles in flotation cells, therefore the application of dual flocculation-collector agents such as copolymers can be deployed so fines are compatible with the operational envelope of the flotation cell. In previous literature, polymeric aids required stimuli switches (such as temperature or pH alterations) to become hydrophobic, which are prohibited by economic and regulatory restrictions in the nuclear waste management industry. Therefore, it was proposed that amphiphilic block copolymers could be utilised. Here, block copolymer self-assembly characteristics were exploited to give a concentration controlled switch between optimum sedimentation and flotation behaviour. However, coarse particulates have high particle detachment energies, and polymeric flocculation will only increase the size and thus mass of these aggregates. Therefore a sequential flocculation-sedimentation process was proposed to maximise SPP1 supernatant turbidity reduction whilst retaining as much supernatant liquor as possible to satisfy the environmental waste management hierarchy.

Three amphiphilic block copolymers (ABCs) of poly(acrylic acid) and poly(*n*-butyl acrylate) [PAA₁₅₂-*b*-PnBA₂₅, PAA₁₅₂-*b*-PnBA₁₀₀ and PAA₁₅₂-*b*-PnBA₂₀₀] were synthesised using reversible addition fragmentation chain-transfer (RAFT) polymerisation. Where the PAA anionic homopolymer block was designed to have an affinity for cationic Mg(OH)₂ surfaces, with a high charge density to promote charge neutralisation/reversal on patches of the Mg(OH)₂ to promote flocculation. The varying chain length hydrophobic PnBA blocks promoted amphiphilic behaviour and contributed to flocculation through hydrophobic association with other PnBA tails on the Mg(OH)₂ surface. Whilst the amphiphilic nature of the ABCs was analogous to lower MW surfactants, the increase in hydrophobic chain length had significant effect on the surface tension and dilational viscoelasticity of the ABCs. The PAA₁₅₂-*b*-PnBA₂₀₀ example displayed very little surface tension reduction and thus low foamability, whereas PAA₁₅₂-*b*-PnBA₂₅ displayed similar

surface active properties to sodium dodecyl sulphate. Additionally, PAA₁₅₂-*b*-PnBA₂₀₀ displayed the greatest affinity to Mg(OH)₂ surfaces, displaying unimer and micellar adsorption regimes, when investigated using TOC and linearised Freundlich adsorption isotherm fitting, similar to the surfactant systems. The maximum unimer adsorption density was associated with the points of inflection of the change in dilational viscoelasticity as a function of dosed concentration, which due to the change in rate of molecular transfer to perturbed air-water interfaces is associated with the critical micelle concentration of amphiphilic molecules. PAA₁₅₂-*b*-PnBA₂₀₀ was also the better flocculation agent, with a significant increase in zonal settling rate beyond the suspected CMC, which was likely due to a change from a charge-patch to micellar-intermediate pseudo-bridging mechanism previously seen in block copolymer flocculant systems.

Similarly to the surfactant collector investigation, the flotation performance was investigated using the same four metrics. There was a trend of increased performance with increasing hydrophobic chain length where PAA₁₅₂-*b*-PnBA₂₀₀ was the best performing ABC. The optimum dosed concentration for flotation performance was strongly linked to the maximum unimer adsorption density. However, whilst the mass recovery of the PAA₁₅₂-*b*-PnBA₂₀₀ system was only 52%, the system retained significantly more water (~80% retention) than the sodium dodecyl sulphate system. Where beyond the suspected CMC, it is suspected that particulate recovery was limited by both hydrophobic (ABC self-assembly resulting in an anionic PAA micellar corona thus increasing aggregate wettability) and hydrodynamic (increasing floc size with increasing ABC concentration and micellar-intermediate pseudo-bridging flocculation) effects.

A consequence of applying polymeric flocculants on particulate suspensions is that the resulting aggregates are fractal in nature and have an invariable scaling dilatational symmetry and as a result have a decreased density thus increased volume for the same unit of mass. This impacts the inter-particulate spacing in suspensions due to the expansion of unit particle perimeters. As previously discussed in Chapter 3, the effect of high MW statistical copolymers on floc structure was investigated using SLS. Due to the quantified fractal dimension, this resulted in a very high effective volume fraction of the suspension, resulting in increased hindered settling effects reducing the zonal settling rate of the suspension. SLS investigation of the amphiphilic block copolymer floc structures actually computed higher floc densities, thus greater inter-particulate spacing and reduced hindered

settling effects. Post-flotation, this interparticle spacing was increased further as 52% of the $\text{Mg}(\text{OH})_2$ by mass had been separated from the suspension further reducing hindered settling effects thus increasing zonal settling rates.

Five deployment scenarios were hypothesised and compared. Firstly, sedimentation of $\text{Mg}(\text{OH})_2$ without settling aids. Secondly, $\text{Mg}(\text{OH})_2$ sedimented using the optimum polymer and concentration for high MW statistical copolymers. Thirdly, the highest MW ABC at its optimum zonal settling rate concentration. Fourthly, the same ABC at its optimum flotation concentration, but using sedimentation only. Lastly, the ABC at its optimum flotation concentration was used to first float the aggregated fines removing 52% of material, and the remaining suspension was sedimented. As the remaining suspension was of a solids concentration that meant no discernible mudline could be observed, the settling rate was modelled. As the inter-particulate spacing was sufficient, drag force modifications were made to the FMRZ model in Chapter 3 and validated against the fourth scenario's experimental data. When the five scenarios were compared, the high MW statistical copolymer gave the best sedimentation dynamics. However, the final settled bed volume was not as consolidated as the ABC systems, likely due to the mechanical strength implied on the bed by the inter-particulate polymer network.

7.2) Future work

A key omission from the FMRZ models in this work is the incorporation of internal permeability of the flocs as inter-particulate spacing approaches intra-aggregate spacing, which would increase the modelled flux of water through the settling bed alleviating hindered settling affects to a degree. If these internal flow drag reduction term is added to fractal-modified Stokes settling model the influence of floc size on boundary layer separation could be better quantified and omitted/ included with greater confidence in residence time calculations. The compressibility and shear stresses of the settled flocculated beds for all polymers deployed in this thesis should be investigated. Understanding the rheology of these consolidated beds would be informative for future waste treatment processes, when the beds require moving from SPP1. The application of non-ionic polymers (such as polyacrylamide homopolymers) which may have an affinity for the $\text{Mg}(\text{OH})_2$ surface, especially in high ionic strength suspensions which have been indicated to promote aggregation in this work, would be of value, especially when comparing the

settled bed rheology and consolidation volume. It would be very useful to Sellafield to understand the effects of re-suspension on settling rates between the statistical and block copolymer flocs, where the former was shown to be sensitive to shear. Furthermore, the application of additional polymer to re-sediment statistical copolymer suspensions after being disturbed should be investigated. Specifically the risk of steric stabilization should be further understood should the need arise to disturb beds in SPP1 at Sellafield.

Previous literature indicated that for ABCs, there are varying degrees of hydrophobicity and hydrophilicity in their block components which affects their surface activity. Therefore, changing the block polymer species and investigating the effects these different species have on surface activity, $Mg(OH)_2$ adsorption, and flotation performance would be valuable. As the flotation of $Mg(OH)_2$ using ABCs was found to likely be limited by hydrodynamic restrictions, the cell shear could be altered to break some of the larger flocs so they are within the recoverable operational envelope of the flotation cell. Finally, the nuclear specific challenges should also be considered. Copolymer radiolytic and chemical stability should be investigated in detail. Not only do these macromolecules adsorb to alpha and beta emitting particulates which may cause copolymer degradation, but current final disposal strategies involve encapsulation in concrete, which is a highly alkali environment. The resultant degradation products should be studied to inform environmental stakeholders that the resultant organics do not mobilise radionuclide species in geological disposal facilities.

Bibliography

- (1) Arnold, L. *Windscale 1957 : Anatomy of a Nuclear Accident*; Palgrave Macmillan, 2007.
- (2) Barnham, K. Hart, D. Nelson, J. Stevens, R. Production and Destination of British Civil Plutonium. *Nature* **1985**, 317, 213–217.
- (3) RWMD. Packaging of Encapsulation of Legacy Fuel and Fuel Bearing Materials from Sellafield Ponds (Conceptual stage) Summary of Assessment Report <https://rwm.nda.gov.uk/publication/encapsulation-of-legacy-fuel-and-fuel-bearing-materials-from-sellafield-ponds/>.
- (4) Jackson, S. F.; Monk, S. D.; Riaz, Z. An Investigation towards Real Time Dose Rate Monitoring, and Fuel Rod Detection in a First Generation Magnox Storage Pond (FGMSP). *Appl. Radiat. Isot.* **2014**, 94, 254–259.
- (5) Hastings, J. J.; Rhodes, D.; Fellerman, A. S.; Mckendrick, D.; Dixon, C. New Approaches for Sludge Management in the Nuclear Industry. *Powder Technol.* **2007**, 174 (1–2), 18–24.
- (6) Grant, I.; Weintrager, U.; Richardson, I. E.; Wilson, D. Sellafield FGMSP Additional Sludge Retrievals A Significant Step in Decommissioning Part of the U.K.'s Nuclear Legacy -16180. In *Waste Management Symposium*; Phoenix, Arizona, USA, 2016.
- (7) Maher, Z.; Ivanov, P.; O'Brien, L.; Sims, H.; Taylor, R. J.; Heath, S. L.; Livens, F. R.; Goddard, D.; Kellet, S.; Rand, P.; Bryan, N. D. Americium and Plutonium Association with Magnesium Hydroxide Colloids in Alkaline Nuclear Industry Process Environments. *J. Nucl. Mater.* **2016**, 468, 84–96.
- (8) Hallam, K. R.; Minshall, P. C.; Heard, P. J.; Flewitt, P. E. J. Corrosion of the Alloys Magnox AL80, Magnox ZR55 and Pure Magnesium in Air Containing Water Vapour. *Corros. Sci.* **2016**, 112, 347–363.
- (9) Foster, L.; Boothman, C.; Ruiz-Lopez, S.; Boshoff, G.; Jenkinson, P.; Sigee, D.; Pittman, J. K.; Morris, K.; Lloyd, J. R. Microbial Bloom Formation in a High PH Spent Nuclear Fuel Pond. *Sci. Total Environ.* **2020**, 720, 137515.
- (10) Department for Business Energy and Industrial Strategy. *2019 UK Radioactive Waste Detailed Data*; 2019.
- (11) Richardson, A.; Maher, P. Sellafield Fuel Handling Plant Pondwater update NuSAC(04)P17. (Update of NuSAC(03)P10)

- <http://www.hse.gov.uk/aboutus/meetings/iacs/nusac/051104/p10.pdf> (accessed Jun 16, 2018).
- (12) Dyer, A.; Chimedtsogzol, A.; Campbell, L.; Williams, C. Uptake of Caesium and Strontium Radioisotopes by Natural Zeolites from Mongolia. *Microporous Mesoporous Mater.* **2006**, *95* (1–3), 172–175.
 - (13) Auns, L. L. The Cationic Sieve Properties of Clinoptilolite. *Am. Mineral.* **1960**, **1960**. *45* (5-6): 689–700.
 - (14) Maher, Z.; Bryan, N. D.; O'brien, L.; Sims, H.; Taylor, R. J.; Goddard, D.; Ivanov, P.; Heath, S. L.; Livens, F. R.; Kellet, S.; Rand, P. Colloidal Processes in SIXEP Streams Introduction (1). In *NNL Technical Conference*; 2015.
 - (15) Maher, Z. Actinide Abatement in SIXEP. <http://www.nnl.co.uk/media/1590/nnl-tech-conference-presentation-zoe-maher-sixep-may-14.pdf> (accessed Sep 5, 2017).
 - (16) Johnson, M.; Peakall, J.; Fairweather, M.; Biggs, S.; Harbottle, D.; Hunter, T. N. Characterization of Multiple Hindered Settling Regimes in Aggregated Mineral Suspensions. *I&EC Res.* **2016**, *55*, 9983–9993.
 - (17) Nasser, M. S.; James, A. E. The Effect of Polyacrylamide Charge Density and Molecular Weight on the Flocculation and Sedimentation Behaviour of Kaolinite Suspensions. *Sep. Purif. Technol.* **2006**, *52* (2), 241–252.
 - (18) Heath, A. R.; Bahri, P. A.; Fawell, P. D.; Farrow, J. B. Polymer Flocculation of Calcite: Relating the Aggregate Size to the Settling Rate. *AIChE J.* **2006**, *52* (6), 1987–1994.
 - (19) Zhou, Y.; Franks, G. V. Flocculation Mechanism Induced by Cationic Polymers Investigated by Light Scattering. *Langmuir* **2006**, *22* (16), 6775–6786.
 - (20) Franks, G. V.; Yates, P. D.; Lambert, N. W. A.; Jameson, G. J. Aggregate Size and Density after Shearing, Implications for Dewatering Fine Tailings with Hydrocyclones. *Int. J. Miner. Process.* **2005**, *77* (1), 46–52.
 - (21) Rhodes, M. *Introduction to Particle Technology*: Martin J. Rhodes; Wiley, 2008.
 - (22) Hunter, T. N.; Peakall, J.; Egarr, D.; Cowell, D. M. J.; Freear, S.; Tonge, A. S.; Horton, L.; Rice, H. P.; Smith, I.; Malone, K.; Burt, D.; Barnes, M.; Randall, G.; Biggs, S.; Fairweather, M. Concentration Profiling of a Horizontal Sedimentation Tank Utilising a Bespoke Acoustic Backscatter Array and CFD Simulations. *Chem. Eng. Sci.* **2020**, *218*, 115560.
 - (23) Li, H.; O'Shea, J.-P.; Franks, G. V. Effect of Molecular Weight of Poly(*N*-Isopropyl Acrylamide) Temperature-Sensitive Flocculants on Dewatering. *AIChE J.* **2009**, *55*

- (8), 2070–2080.
- (24) Biggs, S.; Nabi, R.; Poole, C.; Patel, A. The Influence of Zeta Potential and Yield Stress on the Filtration Characteristics of a Magnesium Hydroxide Simulant. In *11th International Conference on Environmental Remediation and Radioactive Waste Management, Parts A and B*; ASME, 2007; pp 1133–1139.
- (25) Barlow, S. T.; Stennett, M. C.; Hand, R. J.; Morgan, S. P.; Hyatt, N. C. Thermal Treatment of UK Magnox Sludge. In *2nd Petrus-OPERA PhD and early stage researcher conference 2016* ; 2016.
- (26) Harvey, E, J. White, M, J. Mackenzie, J. McKinley, I. Watson, S. P. *Geological Disposal Concept Options for Vitrified HLW*; 2012.
- (27) Harrison, M. T.; Brown, G. C. Chemical Durability of UK Vitrified High Level Waste in Si-Saturated Solutions. *Mater. Lett.* **2018**, *221*, 154–156.
- (28) Costine, A.; Cox, J.; Travaglini, S.; Lubansky, A.; Fawell, P.; Misslitz, H. Variations in the Molecular Weight Response of Anionic Polyacrylamides under Different Flocculation Conditions. *Chem. Eng. Sci.* **2018**, *176*, 127–138.
- (29) Nasser, M. S.; James, A. E. The Effect of Electrolyte Concentration and PH on the Flocculation and Rheological Behaviour of Kaolinite Suspensions. *J. Eng. Sci. Technol.* **2009**, *4* (4), 430–446.
- (30) Scheutjens, J. M. H. M.; Fleer, G. J. Statistical Theory of the Adsorption of Interacting Chain Molecules. 1. Partition Function, Segment Density Distribution, and Adsorption Isotherms. *J. Phys. Chem.* **1979**, *83* (12), 1619–1635.
- (31) Yazhgur, P. A.; Akent'Ev, A. V.; Bilibin, A. Y.; Zorin, I. M.; Noskov, B. A. Dynamic Surface Properties of Sodium N-Acryloyl-11-Aminoundecanoate and Poly(Sodium N-Acryloyl-11-Aminoundecanoate). *Colloid J.* **2012**, *74* (6), 743–750.
- (32) Yan, Y. D.; Glover, S. M.; Jameson, G. J.; Biggs, S. The Flocculation Efficiency of Polydisperse Polymer Flocculants. *Int. J. Miner. Process.* **2004**, *73* (2–4), 161–175.
- (33) Gregory, J.; Barany, S. Adsorption and Flocculation by Polymers and Polymer Mixtures. *Adv. Colloid Interface Sci.* **2011**, *169* (1), 1–12.
- (34) Hogg, R. Bridging Flocculation by Polymers. *KONA Powder Part. J.* **2013**, *30*, 3–14.
- (35) Krysiak-Baltyn, K.; Cavalida, R.; Thwaites, B.; Reeve, P. J.; Scales, P. J.; Van den Akker, B.; Ong, L.; Martin, G. J. O.; Stickland, A. D.; Gras, S. L. Comparison of Physical Characteristics and Dewatering Behaviour between Granular and Floccular Sludges Generated from the Same Sewage Source. *J. Water Process Eng.* **2019**, *29*,

- 100785.
- (36) Grabsch, A. F.; Fawell, P. D.; Adkins, S. J.; Beveridge, A. The Impact of Achieving a Higher Aggregate Density on Polymer-Bridging Flocculation. *Int. J. Miner. Process.* **2013**, *124*, 83–94.
- (37) Lin, J. L.; Huang, C.; Chin, C. J. M.; Pan, J. R. Coagulation Dynamics of Fractal Floccs Induced by Enmeshment and Electrostatic Patch Mechanisms. *Water Res.* **2008**, *42* (17), 4457–4466.
- (38) Guérin, L.; Frances, C.; Liné, A.; Coufort-Saudejaud, C. Fractal Dimensions and Morphological Characteristics of Aggregates Formed in Different Physico-Chemical and Mechanical Flocculation Environments. *Colloids Surfaces A Physicochem. Eng. Asp.* **2019**, *560*, 213–222.
- (39) Stokes, G. G. On the Effect of the Internal Friction of Fluids on the Motion of Pendulums. *Trans. Cam. Phil.* **1851**, *9* (8).
- (40) Richardson, J. F.; Zaki, W. N. Sedimentation and Fluidisation: Part1. *Trans. Instn. Chem. Engrs.* **1954**, *32*, 35–53.
- (41) Sharma, S. Lin, C, Miller, J, D. Multi-Scale Features Including Water Content of Polymer Induced Kaolinite Flocc Structures. *Miner. Eng.* **2017**, *101*, 20–29.
- (42) Zbik, M. S.; Smart, R. S. C.; Morris, G. E. Kaolinite Flocculation Structure. *J. Colloid Interface Sci.* **2008**, *328* (1), 73–80.
- (43) Avadiar, L.; Leong, Y. K.; Fourie, A. Effects of Polyethylenimine Dosages and Molecular Weights on Flocculation, Rheology and Consolidation Behaviors of Kaolin Slurries. *Powder Technol.* **2014**, *254*, 364–372.
- (44) Bushell, G. C.; Yan, Y. D.; Woodfield, D.; Raper, J.; Amal, R. On Techniques for the Measurement of the Mass Fractal Dimension of Aggregates. *Adv. Colloid Interface Sci.* **2002**, *95* (1), 1–50.
- (45) Xiao, F.; Lam, K. M.; Li, X. Investigation and Visualization of Internal Flow through Particle Aggregates and Microbial Floccs Using Particle Image Velocimetry. *J. Colloid Interface Sci.* **2013**, *397*, 163–168.
- (46) Mandelbrot, B. B. *Fractals : Form, Chance, and Dimension*; W.H. Freeman, 1977.
- (47) Wijnen, P. W. J. G.; Beelen, T. P. M.; Rummens, C. P. J.; Van Santen, R. A. Diffusion-and Reaction-Limited Aggregation of Aqueous Silicate Solutions. *J. Non-Crystalline Solids* **1991**, *136* (1–2), 119–125.
- (48) Glover, S. M.; Yan, Y.; Jameson, G. J.; Biggs, S. Bridging Flocculation Studied by Light Scattering and Settling. *Chem. Eng. J.* **2000**, *80* (1–3), 3–12.

- (49) Khelifa, A.; Hill, P. S. Models for Effective Density and Settling Velocity of Floccs. *J. Hydraul. Res.* **2006**, *44* (3), 390–401.
- (50) Vahedi, A.; Gorczyca, B. Application of Fractal Dimensions to Study the Structure of Floccs Formed in Lime Softening Process. *Water Res.* **2011**, *45* (2), 545–556.
- (51) Maggi, F. Variable Fractal Dimension: A Major Control for Floc Structure and Flocculation Kinematics of Suspended Cohesive Sediment. *J. Geophys. Res. Ocean.* **2007**, *112* (7), 1–12.
- (52) Chakrabarty, R. K.; Garro, M. A.; Garro, B. A.; Chancellor, S.; Moosmüller, H.; Herald, C. M. Simulation of Aggregates with Point-Contacting Monomers in the Cluster–Dilute Regime. Part 2: Comparison of Two- and Three-Dimensional Structural Properties as a Function of Fractal Dimension. *Aerosol Sci. Technol.* **2011**, *45* (8), 903–908.
- (53) Burns, J. L.; Yan, Y.-D.; Jameson, G. J.; Biggs, S. A Light Scattering Study of the Fractal Aggregation Behavior of a Model Colloidal System. *Langmuir* **1997**, *13* (24), 6413–6420.
- (54) Guan, L.; Yuan, Z.; Moghtaderi, B.; Peng, Z.; Evans, G. M.; Gu, C.; Doroodchi, E. Prediction of Terminal Velocity of Fractal Aggregates with IBM-LBM Method. *Powder Technol.* **2020**, *361*, 1060–1069.
- (55) Vajihinejad, V.; Soares, J. B. P. Monitoring Polymer Flocculation in Oil Sands Tailings: A Population Balance Model Approach. *Chem. Eng. J.* **2018**, *346*, 447–457.
- (56) Cobbleddick, J.; Nguyen, A.; Latulippe, D. R. Demonstration of FBRM as Process Analytical Technology Tool for Dewatering Processes via CST Correlation. *Water Res.* **2014**, *58*, 132–140.
- (57) Raj, P.; Blanco, A.; de la Fuente, E.; Batchelor, W.; Negro, C.; Garnier, G. Microfibrillated Cellulose as a Model for Soft Colloid Flocculation with Polyelectrolytes. *Colloids Surfaces A Physicochem. Eng. Asp.* **2017**, *516*, 325–335.
- (58) Li, H.; Liu, M.; Liu, Q. The Effect of Non-Polar Oil on Fine Hematite Flocculation and Flotation Using Sodium Oleate or Hydroxamic Acids as a Collector. *Miner. Eng.* **2018**, *119*, 105–115.
- (59) Raj, P.; Batchelor, W.; Blanco, A.; de la Fuente, E.; Negro, C.; Garnier, G. Effect of Polyelectrolyte Morphology and Adsorption on the Mechanism of Nanocellulose Flocculation. *J. Colloid Interface Sci.* **2016**, *481*, 158–167.
- (60) Benn, F. A.; Fawell, P. D.; Halewood, J.; Austin, P. J.; Costine, A. D.; Jones, W. G.;

- Francis, N. S.; Druett, D. C.; Lester, D. Sedimentation and Consolidation of Different Density Aggregates Formed by Polymer-Bridging Flocculation. *Chem. Eng. Sci.* **2018**, *184*, 111–125.
- (61) Fleischmann, M.; Tildesley, D. J.; Ball, R. C.; Royal Society (Great Britain). Series A. *Fractals in the Natural Sciences: A Discussion*; Princeton University Press, 1990.
- (62) Liao, J. Y. H.; Selomulya, C.; Bushell, G.; Bickert, G.; Amal, R. On Different Approaches to Estimate the Mass Fractal Dimension of Coal Aggregates. *Part. Part. Syst. Charact.* **2005**, *22* (5), 299–309.
- (63) Sorensen, C. M. Light Scattering by Fractal Aggregates: A Review. *Aerosol Sci. Technol. Am. Assoc. Aerosol Res.* **2001**, *35*, 648–687.
- (64) Yang, Z.; Yang, H.; Jiang, Z.; Huang, X.; Li, H.; Li, A.; Cheng, R. A New Method for Calculation of Flocculation Kinetics Combining Smoluchowski Model with Fractal Theory. *Colloids Surfaces A Physicochem. Eng. Asp.* **2013**, *423*, 11–19.
- (65) Sun, K.; Liu, T.; Zhang, Y.; Liu, X.; Wang, B.; Xu, C. Application and Mechanism of Anionic Collector Sodium Dodecyl Sulfate (SDS) in Phosphate Beneficiation. *Minerals* **2017**, *7* (2), 29.
- (66) Harbort, G.; De Bono, S.; Carr, D.; Lawson, V. Jameson Cell Fundamentals—a Revised Perspective. *Miner. Eng.* **2003**, *16* (11), 1091–1101.
- (67) Zeng, X.; Xu, L.; Tian, J.; Yin, W.; Yang, Y.; Deng, W. Effect of a CA Depressant on Flotation Separation of Celestite from Fluorite and Calcite Using SDS as a Collector. *Miner. Eng.* **2017**, *111*, 201–208.
- (68) Norori-McCormac, A.; Brito-Parada, P. R.; Hadler, K.; Cole, K.; Cilliers, J. J. The Effect of Particle Size Distribution on Froth Stability in Flotation. *Sep. Purif. Technol.* **2017**, *184*, 240–247.
- (69) Melo, F.; Laskowski, J. S. Fundamental Properties of Flotation Frothers and Their Effect on Flotation. *Miner. Eng.* **2006**, *19* (6–8), 766–773.
- (70) Hyde, R. A.; Miller, D. G.; Packham, R. F.; Richards, W. N. Water Clarification by Flotation. *Journal (American Water Works Association)*. Wiley pp 369–374.
- (71) Prajitno, M. Y.; Tangparitkul, S.; Zhang, H.; Harbottle, D.; Hunter, T. N. The Effect of Cationic Surfactants on Improving Natural Clinoptilolite for the Flotation of Cesium. *J. Hazard. Mater.* **2021**, *402*, 123567.
- (72) Bunker, D. Q.; Edzwald, J. K.; Dahlquist, J.; Gillberg, L. Pretreatment Considerations for Dissolved Air Flotation: Water Type, Coagulants and

- Flocculation. *Water Sci. Technol.* **1995**, *31* (3–4), 63–71.
- (73) Teixeira, M. R.; Rosa, M. J. Comparing Dissolved Air Flotation and Conventional Sedimentation to Remove Cyanobacterial Cells of *Microcystis Aeruginosa*: Part I: The Key Operating Conditions. *Sep. Purif. Technol.* **2006**, *52* (1), 84–94.
- (74) Osborne, D.; Euston, J. *Independent Report Value of the Jameson Cell to the Australian Economy Contents*; Wellington point, Australia, 2015.
- (75) Ortiz-Oliveros, H. B.; Flores-Espinosa, R. M. Design of a Mobile Dissolved Air Flotation System with High Rate for the Treatment of Liquid Radioactive Waste. *Process Saf. Environ. Prot.* **2020**, *144*, 23–31.
- (76) Cagnetta, C.; Saerens, B.; Meerburg, F. A.; Decru, S. O.; Broeders, E.; Menkveld, W.; Vandekerckhove, T. G. L.; De Vrieze, J.; Vlaeminck, S. E.; Verliefde, A. R. D.; De Gussemé, B.; Weemaes, M.; Rabaey, K. High-Rate Activated Sludge Systems Combined with Dissolved Air Flotation Enable Effective Organics Removal and Recovery. *Bioresour. Technol.* **2019**, *291*, 121833.
- (77) Huang, Y.; Takaoka, M.; Takeda, N.; Oshita, K. Polychlorinated Biphenyls Removal from Weathered Municipal Solid Waste Incineration Fly Ash by Collector-Assisted Column Flotation. *J. Hazard. Mater.* **2003**, *100* (1–3), 259–270.
- (78) Wang, G.; Nguyen, A. V.; Mitra, S.; Joshi, J. B.; Jameson, G. J.; Evans, G. M. A Review of the Mechanisms and Models of Bubble-Particle Detachment in Froth Flotation. *Separation and Purification Technology.* **2016**, *170*, 155–172.
- (79) Epple, M.; Schmidt, D. C.; Berg, J. C. The Effect of Froth Stability and Wettability on the Flotation of a Xerographic Toner. *Colloid Polym. Sci.* **1994**, *272* (10), 1264–1272.
- (80) Bai, B.; Hankins, N. P.; Hey, M. J.; Kingman, S. W. In Situ Mechanistic Study of SDS Adsorption on Hematite for Optimized Froth Flotation. *Ind. Eng. Chem. Res.* **2004**, *43* (17), 5326–5338.
- (81) Mohammed, A. A.; Ebrahim, S. E.; Alwared, A. I. Flotation and Sorptive-Flotation Methods for Removal of Lead Ions from Wastewater Using SDS as Surfactant and Barley Husk as Biosorbent. *J. Chem.* **2013**, *2013*, 413948.
- (82) Rao, S. R.; Leja, J. *Surface Chemistry of Froth Flotation. Volume 1, Fundamentals.*; Springer US, 2004.
- (83) De F. Gontijo, C.; Fornasiero, D.; Ralston, J. The Limits of Fine and Coarse Particle Flotation. *Can. J. Chem. Eng.* **2008**, *85* (5), 739–747.
- (84) Ng, W. S.; Connal, L. A.; Forbes, E.; Franks, G. V. A Review of Temperature-

- Responsive Polymers as Novel Reagents for Solid-Liquid Separation and Froth Flotation of Minerals. *Miner. Eng.* **2018**, *123*, 144–159.
- (85) O’Shea, J. P.; Qiao, G. G.; Franks, G. V. Solid-Liquid Separations with a Temperature-Responsive Polymeric Flocculant: Effect of Temperature and Molecular Weight on Polymer Adsorption and Deposition. *J. Colloid Interface Sci.* **2010**, *348* (1), 9–23.
- (86) Ng, W. S.; Connal, L. A.; Forbes, E.; Mohanarangam, K.; Franks, G. V. In Situ Investigation of Aggregate Sizes Formed Using Thermo-Responsive Polymers: Effect of Temperature and Shear. *J. Colloid Interface Sci.* **2017**, *494*, 139–152.
- (87) Ng, W. S.; Cooper, L.; Connal, L. A.; Forbes, E.; Jameson, G. J.; Franks, G. V. Tuneable Collector/Depressant Behaviour of Xanthate-Functional Temperature-Responsive Polymers in the Flotation of Copper Sulfide: Effect of Shear and Temperature. *Miner. Eng.* **2018**, *117*, 91–99.
- (88) Forbes, E.; Bradshaw, D.; Franks, G. Temperature Sensitive Polymers as Efficient and Selective Flotation Collectors. *Miner. Engineeirng* **2011**, *24* (8), 772–777.
- (89) Franks, G. V. Stimulant Sensitive Flocculation and Consolidation for Improved Solid/Liquid Separation. *J. Colloid Interface Sci.* **2005**, *292* (2), 598–603.
- (90) Ghosh, A.; Yusa, S. I.; Matsuoka, H.; Saruwatari, Y. Non-Surface Activity and Micellization Behavior of Cationic Amphiphilic Block Copolymer Synthesized by Reversible Addition-Fragmentation Chain Transfer Process. *Langmuir* **2011**, *27* (15), 9237–9244.
- (91) Ghosh, A.; Yusa, S. I.; Matsuoka, H.; Saruwatari, Y. Chain Length Dependence of Non-Surface Activity and Micellization Behavior of Cationic Amphiphilic Diblock Copolymers. *Langmuir* **2014**, *30* (12), 3319–3328.
- (92) Garnier, S.; Laschewsky, A. New Amphiphilic Diblock Copolymers: Surfactant Properties and Solubilization in Their Micelles. *Langmuir* **2006**, *22* (9), 4044–4053.
- (93) Kaewsaiha, P.; Matsumoto, K.; Matsuoka, H. Non-Surface Activity and Micellization of Ionic Amphiphilic Diblock Copolymers in Water. Hydrophobic Chain Length Dependence and Salt Effect on Surface Activity and the Critical Micelle Concentration. *Langmuir* **2005**, *21* (22), 9938–9945.
- (94) Volpert, E.; Selb, J.; Candau, F.; Green, N.; Argillier, J. F.; Audibert, A. Adsorption of Hydrophobically Associating Polyacrylamides on Clay. *Langmuir* **1998**, *14* (7), 1870–1879.
- (95) Matsuoka, H.; Matsutani, M.; Mouri, E.; Matsumoto, K. Polymer Micelle Formation

- without Gibbs Monolayer Formation: Synthesis and Characteristic Behavior of an Amphiphilic Diblock Copolymer Having Strong Acid Groups. *Macromolecules* **2003**, *36* (14), 5321–5330.
- (96) Matsuoka, H.; Maeda, S.; Kaewsaiha, P.; Matsumoto, K. Micellization of Non-Surface-Active Diblock Copolymers in Water. Special Characteristics of Poly(Styrene)-Block-Poly(Styrenesulfonate). *Langmuir* **2004**, *20* (18), 7412–7421.
- (97) Guenoun, P.; Davis, H. T.; Tirrell, M.; Mays, J. W. Aqueous Micellar Solutions of Hydrophobically Modified Polyelectrolytes. *Macromolecules* **1996**, *29* (11), 3965–3969.
- (98) Jacquin, M.; Muller, P.; Talingting-Pabalan, R.; Cottet, H.; Berret, J. F.; Futterer, T.; Théodoly, O. Chemical Analysis and Aqueous Solution Properties of Charged Amphiphilic Block Copolymers PBA-b-PAA Synthesized by MADIX®. *J. Colloid Interface Sci.* **2007**, *316* (2), 897–911.
- (99) Carissimi, E.; Rubio, J. Polymer-Bridging Flocculation Performance Using Turbulent Pipe Flow. *Miner. Eng.* **2015**, *70*, 20–25.
- (100) Gregson, C. R.; Goddard, D. T.; Sarsfield, M. J.; Taylor, R. J. Combined Electron Microscopy and Vibrational Spectroscopy Study of Corroded Magnox Sludge from a Legacy Spent Nuclear Fuel Storage Pond. *J. Nucl. Mater.* **2011**, *412* (1), 145–156.
- (101) Parry, S. A.; O'brien, L.; Fellerman, A. S.; Eaves, C. J.; Milestone, N. B.; Bryan, N. D.; Livens, F. R. Plutonium Behaviour in Nuclear Fuel Storage Pond Effluents. *Energy Environ. Sci* **2011**, *4*, 1457–1464.
- (102) Shaw, D. J. *Introduction to Colloid and Surface Chemistry*; Butterworth-Heinemann, 1992.
- (103) Israelachvili, J. N. *Intermolecular and Surface Forces: Third Edition*; Elsevier Inc., 2011.
- (104) Fleer, G. J. (Gerard J. .; Stuart, M. A. C.; Scheutjens, J. M. H. M.; Cosgrove, T.; Vincent, B. *Polymers at Interfaces*; Springer Netherlands: Dordrecht, 1998.
- (105) Fleer, G. J.; Lyklema, J. Polymer Adsorption and Its Effect on the Stability of Hydrophobic Colloids. II. The Flocculation Process as Studied with the Silver Iodide-Polyvinyl Alcohol System. *J. Colloid Interface Sci.* **1974**, *46* (1), 1–12.
- (106) Bischofberger, I.; Calzolari, D. C. E.; De Los Rios, P.; Jelezarov, I.; Trappe, V. Hydrophobic Hydration of Poly-N-Isopropyl Acrylamide: A Matter of the Mean Energetic State of Water. *Sci. Rep.* **2014**, *4* (1), 1–7.
- (107) Sung Ng, W.; Connal, L. A.; Forbes, E.; Mohanarangam, K.; Franks, G. V. In Situ

- Study of Aggregate Sizes Formed in Chalcopyrite-Quartz Mixture Using Temperature-Responsive Polymers. *Adv. Powder Technol.* **2018**, 29 (8), 1940–1949.
- (108) Hunter, R. J. *Foundations of Colloid Science*; Oxford University Press, 2001.
- (109) Barany, S.; Kozakova, I.; Marcinova, L.; Skvarla, J. Electrokinetic Potential of Bentonite and Kaolin Particles in the Presence of Polymer Mixtures. *Colloid J.* **2010**, 72 (5), 595–601.
- (110) Hubbe, M. A. Flocculation And Redispersion Of Cellulosic Fiber Suspensions: A Review Of Effects Of Hydrodynamic Shear And Polyelectrolytes. *Bioresources* **2007**, 2 (2), 208–331.
- (111) Vajihinejad, V.; Gumfekar, S. P.; Bazoubandi, B.; Rostami Najafabadi, Z.; Soares, J. B. P. Water Soluble Polymer Flocculants: Synthesis, Characterization, and Performance Assessment. *Macromol. Mater. Eng.* **2019**, 304 (2), 1800526.
- (112) Suslu, A.; Wu, K.; Sahin, H.; Chen, B.; Yang, S.; Cai, H.; Aoki, T.; Horzum, S.; Kang, J.; Peeters, F. M.; Tongay, S. Unusual Dimensionality Effects and Surface Charge Density in 2D Mg(OH)₂. *Sci. Rep.* **2016**, 6 (1), 1–7.
- (113) O'Shea, J. P.; Qiao, G. G.; Franks, G. V. Temperature-Responsive Solid-Liquid Separations with Charged Block-Copolymers of Poly(N-Isopropyl Acryamide). *Langmuir* **2012**, 28 (1), 905–913.
- (114) Lu, C. F.; Spielmant, L. A. Kinetics of Floc Breakage and Aggregation in Agitated Liquid Suspensions. *Colloid Interface Sci.* **1985**, 103 (1), 95–105.
- (115) Kyoda, Y.; Costine, A. D.; Fawell, P. D.; Bellwood, J.; Das, G. K. Using Focused Beam Reflectance Measurement (FBRM) to Monitor Aggregate Structures Formed in Flocculated Clay Suspensions. *Miner. Eng.* **2019**, 138, 148–160.
- (116) Friedlander, S. K. *Smoke, Dust, and Haze : Fundamentals of Aerosol Dynamics*; Oxford University Press, 2000.
- (117) de Martín, L.; Fabre, A.; Ruud van Ommen, J. The Fractal Scaling of Fluidized Nanoparticle Agglomerates. *Chem. Eng. Sci.* **2014**, 112, 79–86.
- (118) Vahedi, A.; Gorczyca, B. Settling Velocities of Multifractal Flocs Formed in Chemical Coagulation Process. *Water Res.* **2014**, 53, 322–328.
- (119) Maggi, F.; Winterwerp, J. C. Method for Computing the Three-Dimensional Capacity Dimension from Two-Dimensional Projections of Fractal Aggregates. *Phys. Rev. E - Stat. Physics, Plasmas, Fluids, Relat. Interdiscip. Top.* **2004**, 69 (1), 8.
- (120) Tang, P. Greenwood, J. and Raper, J. A. A Model to Describe the Settling Behaviour

- of Fractal Aggregates. *J. Colloid Interface Sci.* **2002**, *247*, 210–219.
- (121) Gmachowski, L. Mechanism of Shear Aggregation. *Water Res.* **1995**, *29* (8), 1815–1820.
- (122) Lasue, J.; Maroger, I.; Botet, R.; Garnier, P.; Merouane, S.; Mannel, T.; Levasseur-Regourd, A. C.; Bentley, M. S. Flattened Loose Particles from Numerical Simulations Compared to Particles Collected by Rosetta. *Astronomy & Astrophysics.* **1998**. *630*, 9.
- (123) Adachi, Y. Tanaka, Y. Settling Velocity of an Aluminium-Kaolinite Floc. *Wat. Res.* **1997**, *31* (3), 449–454.
- (124) Adelman, M. J.; Hurst, M. W.; Weber-Shirk, M. L.; Cabrito, T. S.; Somogyi, C.; Lion, L. W. Floc Roll-Up and Its Implications for the Spacing of Inclined Settling Devices. *Environ. Eng. Sci.* **2013**, *30* (6), 302–310.
- (125) Camenen, B.; Pham Van Bang, D. Modelling the Settling of Suspended Sediments for Concentrations Close to the Gelling Concentration. *Cont. Shelf Res.* **2011**, *31*, 106–111.
- (126) Michaels, A. Bolger, J. Settling Rates and Sediment Volumes of Flocculated Kaolin Suspensions. *I&EC Fundam.* **1962**, *1* (1), 24–33.
- (127) Winterwerp, J. C. A Simple Model for Turbulence Induced Flocculation of Cohesive Sediment. *J. Hydraul. Res.* **1998**, *36* (3), 309–326.
- (128) Vahedi, A.; Gorczyca, B. Predicting the Settling Velocity of Flocs Formed in Water Treatment Using Multiple Fractal Dimensions. *Water Res.* **2012**, *46* (13), 4188–4194.
- (129) Pugh, R. J. *Bubble and Foam Chemistry*; Cambridge, 2016.
- (130) Fluksman, A.; Benny, O. A Robust Method for Critical Micelle Concentration Determination Using Coumarin-6 as a Fluorescent Probe. *Anal. Methods* **2019**, *11* (30), 3810–3818.
- (131) Jeraal, M. I.; Roberts, K. J.; McRobbie, I.; Harbottle, D. Process-Focused Synthesis, Crystallization, and Physicochemical Characterization of Sodium Lauroyl Isethionate. *ACS Sustain. Chem. Eng.* **2018**, *6* (2), 2667–2675.
- (132) Eghbali, E.; Colombani, O.; Drechsler, M.; Müller, A. H. E.; Hoffmann, H. Rheology and Phase Behavior of Poly(n-Butyl Acrylate)-Block-Poly(Acrylic Acid) in Aqueous Solution. *Langmuir* **2006**, *22* (10), 4766–4776.
- (133) Degen, P.; Paulus, M.; Zwar, E.; Jakobi, V.; Dogan, S.; Tolan, M.; Rehage, H. Surfactant-mediated Formation of Alginate Layers at the Water-air Interface. *Surf.*

- Interface Anal.* **2019**, *51* (11), 1051–1058.
- (134) Zhang, Q.; Li, Y.; Cao, L.; Li, L.; Huang, K.; Li, W.; Yang, C. Dilational Viscoelastic Properties of Water-Fuel Interfaces in Single and Binary Surfactant Systems. *Energy and Fuels* **2019**, *33* (9), 9055–9066.
- (135) Rasera, J. N.; Cilliers, J. J.; Lamamy, J. A.; Hadler, K. The Beneficiation of Lunar Regolith for Space Resource Utilisation: A Review. *Planetary and Space Science*. **2020**, *186* 104879.
- (136) Atkins, P. W. (Peter W.; De Paula, J. *Atkins' Physical Chemistry*; Oxford University Press, 2010.
- (137) Bera, A.; Kumar, T.; Ojha, K.; Mandal, A. Adsorption of Surfactants on Sand Surface in Enhanced Oil Recovery: Isotherms, Kinetics and Thermodynamic Studies. *Appl. Surf. Sci.* **2013**, *284*, 87–99.
- (138) Saikia, N.; Sarma, J.; Borah, J. M.; Mahiuddin, S. Adsorption of 3,4-Dihydroxybenzoic Acid onto Hematite Surface in Aqueous Medium: Importance of Position of Phenolic -OH Groups and Understanding of the Same Using Catechol as an Auxiliary Model. *J. Colloid Interface Sci.* **2013**, *398*, 227–233.
- (139) Rupprecht, H.; Gu, T. Structure of Adsorption Layers of Ionic Surfactants at the Solid/Liquid Interface. *Colloid Polym. Sci.* **1991**, *269* (5), 506–522.
- (140) Hunter, T. N.; Pugh, R. J.; Franks, G. V.; Jameson, G. J. The Role of Particles in Stabilising Foams and Emulsions. *Advances in Colloid and Interface Science*. **2008**, *137* (2), 57–81.
- (141) Hadler, K.; Greyling, M.; Plint, N.; Cilliers, J. J. The Effect of Froth Depth on Air Recovery and Flotation Performance. *Miner. Eng.* **2012**, *36–38*, 248–253.
- (142) Gupta, A. K.; Banerjee, P. K.; Mishra, A.; Satish, P.; Pradip. Effect of Alcohol and Polyglycol Ether Frothers on Foam Stability, Bubble Size and Coal Flotation. *Int. J. Miner. Process.* **2007**, *82* (3), 126–137.
- (143) Laskowski, J. S.; Cho, Y. S.; Ding, K. Effect of Frothers on Bubble Size and Foam Stability in Potash Ore Flotation Systems. *Can. J. Chem. Eng.* **2008**, *81* (1), 63–69.
- (144) Hunter, T. N.; Wanless, E. J.; Jameson, G. J. Effect of Esterically Bonded Agents on the Monolayer Structure and Foamability of Nano-Silica. *Colloids Surfaces A Physicochem. Eng. Asp.* **2009**, *334* (1–3), 181–190.
- (145) Hadler, K.; Cilliers, J. J. The Effect of Particles on Surface Tension and Flotation Froth Stability. *Mining, Metall. Explor.* **2019**, *36* (1), 63–69.
- (146) Ng, W. S.; Sonsie, R.; Forbes, E.; Franks, G. V. Flocculation/Flotation of Hematite

- Fines with Anionic Temperature-Responsive Polymer Acting as a Selective Flocculant and Collector. *Miner. Eng.* **2015**, *77*, 64–71.
- (147) Sakohara, S.; Kawachi, T.; Gotoh, T.; Iizawa, T. Consolidation of Suspended Particles by Using Dual Ionic Thermosensitive Polymers with Incorporated a Hydrophobic Component. *Sep. Purif. Technol.* **2013**, *106*, 90–96.
- (148) Ofori, P.; O'Brien, G.; Firth, B.; McNally, C. The Use of Tri-Block Copolymer Surfactants as Promoters to Improve Flotation Recovery of Poorly Floating Coal Components. *Int. J. Coal Prep. Util.* **2012**, *32* (3), 103–119.
- (149) Moon, T.; Nagarajan, R. Deinking Xerographic and Laser-Printed Paper Using Block Copolymers. *Colloids Surfaces A Physicochem. Eng. Asp.* **1998**, *132* (2–3), 275–288.
- (150) Pelssers, E. G. M.; Cohen Stuart, M. A.; Fleer, G. J. Kinetics of Bridging Flocculation Role of Relaxations in the Polymer Layer. *J. Chem. Soc. Faraday Trans* **1990**, *86* (9), 1355–1361.
- (151) Sher, F.; Malik, A.; Liu, H. Industrial Polymer Effluent Treatment by Chemical Coagulation and Flocculation. *J. Environ. Chem. Eng.* **2013**, *1* (4), 684–689.
- (152) Brostow, W.; Hagg Lobland, H. E.; Pal, S.; Singh, R. P. Polymeric Flocculants for Wastewater and Industrial Effluent Treatment. *J. Mater. Educ.* **2009**, *31* (4), 157–166.
- (153) Gregory, J. Monitoring Particle Aggregation Processes. *Adv. Colloid Interface Sci.* **2009**, *147*, 109–123.
- (154) Joseph-Soly, S.; Saldanha, T.; Nosrati, A.; Skinner, W.; Addai-Mensah, J. Improved Dewatering of Clay Rich Mineral Dispersions Using Recyclable Superabsorbent Polymers. *Chem. Eng. Res. Des.* **2019**, *142*, 78–86.
- (155) Shi, B.; Wei, Q.; Wang, D.; Zhu, Z.; Tang, H. Coagulation of Humic Acid: The Performance of Preformed and Non-Preformed Al Species. *Colloids Surfaces A Physicochem. Eng. Asp.* **2007**, *296* (1–3), 141–148.
- (156) Jarvis, P.; Jefferson, B.; Parsons, S. A. Floc Structural Characteristics Using Conventional Coagulation for a High Doc, Low Alkalinity Surface Water Source. *Water Res.* **2006**, *40* (14), 2727–2737.
- (157) Ghernaout, D.; Ghernaout, B. Sweep Flocculation as a Second Form of Charge Neutralisation—a Review. *Desalin. Water Treat.* **2012**, *44* (1–3), 15–28.
- (158) Gregory, J. Polymer Adsorption and Flocculation in Sheared Suspensions. *Colloids and Surfaces* **1988**, *31*, 231–253.

- (159) Heath, P. G.; Stewart, M. W. A.; Moricca, S.; Hyatt, N. C. Hot-Isostatically Pressed Wasteforms for Magnox Sludge Immobilisation. *J. Nucl. Mater.* **2018**, *499*, 233–241.
- (160) Cao, F.; Miao, M.; Yan, P. Effects of Reactivity of MgO Expansive Agent on Its Performance in Cement-Based Materials and an Improvement of the Evaluating Method of MEA Reactivity. *Constr. Build. Mater.* **2018**, *187*, 257–266.
- (161) Ulusoy, U.; Kursun, I. Comparison of Different 2D Image Analysis Measurement Techniques for the Shape of Talc Particles Produced by Different Media Milling. *Miner. Eng.* **2011**, *24*, 91–97.
- (162) Zhang, Y.; Kong, X.; Gao, L.; Bai, Y. Characterization of the Mesostructural Organization of Cement Particles in Fresh Cement Paste. *Constr. Build. Mater.* **2016**, *124*, 1038–1050.
- (163) Zhang, D.-W.; Wang, D.; Liu, Z.; Xie, F. Rheology, Agglomerate Structure, and Particle Shape of Fresh Geopolymer Pastes with Different NaOH Activators Content. *Constr. Build. Mater.* **2018**, *187*, 674–680.
- (164) Kim, S.; Palomino, A. M. Polyacrylamide-Treated Kaolin: A Fabric Study. *Appl. Clay Sci.* **2009**, *45* (4), 270–279.
- (165) Wu, M.-Y.; Adachi, Y. Effects of Electrolyte Concentration and PH on the Sedimentation Rate of Coagulated Suspension of Sodium Montmorillonite. *Asp. Colloids Surfaces A Physicochem. Eng. Asp.* **2016**, *506* (506), 686–693.
- (166) Font, R.; Pérez, M. Hydrodynamic Parameters from the Michaels and Bolger Method. *Chem. Eng. J.* **2000**, *80*, 167–175.
- (167) Kinoshita, T.; Nakaishi, K.; Kuroda, Y. Determination of Kaolinite Floc Size and Structure Using Interface Settling Velocity. *Appl. Clay Sci.* **2017**, *148*, 11–16.
- (168) Meakin, P.; Family, F. Structure and Kinetics of Reaction-Limited Aggregation. *Phys. Rev. A* **1988**, *38* (4), 2110–2123.
- (169) Martin Marietta Magnesia Specialties. Versamag Mg(OH)₂ MSDS. *Fed. Regist.* **2016**, *77* (58), 1–7.
- (170) Elliott, L. N.; Bourne, R. A.; Hassanpour, A.; Edwards, J. L.; Sutcliffe, S.; Hunter, T. N. Salt Enhanced Solvent Relaxation and Particle Surface Area Determination via Rapid Spin-Lattice NMR. *Powder Technol.* **2018**, *333*, 458–467.
- (171) Barrett, P.; Glennon, B. Characterizing the Metastable Zone Width and Solubility Curve Using Lasentec FBRM and PVM. *Chem. Eng. Res. Des.* **2002**, *80* (7), 799–805.

- (172) Wilkinson, D.; Li, M.; Patchigolla, K. Determining Particle Size Distribution of Non-Spheres from Chord Length Measurements. In *AIChE Spring National Meeting-5th World Congress on Particle Technology*; Orlando, FL, USA, 2006.
- (173) Paul, N.; Biggs, S.; Shiels, J.; Hammond, R. B.; Edmondson, M.; Maxwell, L.; Harbottle, D.; Hunter, T. N. Influence of Shape and Surface Charge on the Sedimentation of Spheroidal, Cubic and Rectangular Cuboid Particles. *Powder Technol.* **2017**, *322*, 75–83.
- (174) Tomkins, M. R.; Baldock, T. E.; Nielsen, P. Hindered Settling of Sand Grains. *Sedimentology* **2005**, *52* (6), 1425–1432.
- (175) Jungblut, S.; Joswig, J.-O.; Eychmüller, A. Diffusion- and Reaction-Limited Cluster Aggregation Revisited. *Phys. Chem. Chem. Phys.* **2019**, *21* (10), 5723–5729.
- (176) Usher, S. P.; Spehar, R.; Scales, P. J. Theoretical Analysis of Aggregate Densification: Impact on Thickener Performance. *Chem. Eng. J.* **2009**, *151* (1–3), 202–208.
- (177) Grassia, P.; Zhang, Y.; Martin, A. D.; Usher, S. P.; Scales, P. J.; Crust, A. H.; Spehar, R. Effects of Aggregate Densification upon Thickening of Kynchian Suspensions. *Chem. Eng. Sci.* **2014**, *111*, 56–72.
- (178) van Deventer, B. B. G.; Usher, S. P.; Kumar, A.; Rudman, M.; Scales, P. J. Aggregate Densification and Batch Settling. *Chem. Eng. J.* **2011**, *171* (1), 141–151.
- (179) Zhang, Y.; Martin, A.; Grassia, P. Prediction of Thickener Performance with Aggregate Densification. *Chem. Eng. Sci.* **2013**, *101*, 346–358.
- (180) Bux, J.; Peakall, J.; Rice, H. P.; Manga, M. S.; Biggs, S.; Hunter, T. N. Measurement and Density Normalisation of Acoustic Attenuation and Backscattering Constants of Arbitrary Suspensions within the Rayleigh Scattering Regime. *Appl. Acoust.* **2019**, *146*, 9–22.
- (181) Calvin, T. Decommissioning Sellafield's First Fuel Storage Pond -11125. In *Waste Management Symposium*; Phoenix, Arizona USA, 2011.
- (182) Burrows, C.; Phillips, C.; Milliken, A. The Thermal Oxide Reprocessing Plant at Sellafield – Lessons Learned from 10 Years of Hot Operations and Their Applicability to the DOE Environmental Management Program; Waste Management Symposium: Phoenix, Arizona USA, 2006.
- (183) Sinkov, S.; Delegard, C.; Schmidt, A. *Mitigation of Hydrogen Gas Generation from the Reaction of Uranium Metal with Water in K Basin Sludge and Sludge Waste Forms*; 2011.

- (184) Fuerstenau, M.C.; Jameson, G.; Yoon, R. *Froth Flotation: A Century of Innovation*; 2007.
- (185) Chang, L.; Cao, Y.; Fan, G.; Li, C.; Peng, W. A Review of the Applications of Ion Flotation: Wastewater Treatment, Mineral Beneficiation and Hydrometallurgy. *RSC Adv.* **2019**, *9* (35), 20226–20239.
- (186) Kowalczyk, P. B.; Sahbaz, O.; Drzymala, J. Maximum Size of Floating Particles in Different Flotation Cells. *Miner. Eng.* **2011**, *24* (8), 766–771.
- (187) Ramos, O.; Castro, S.; Laskowski, J. S. Copper-Molybdenum Ores Flotation in Sea Water: Floatability and Frothability. *Miner. Eng.* **2013**, *53*, 108–112.
- (188) Farhadi, H.; Riahi, S.; Ayatollahi, S.; Ahmadi, H. Experimental Study of Nanoparticle-Surfactant-Stabilized CO₂ Foam: Stability and Mobility Control. *Chem. Eng. Res. Des.* **2016**, *111*, 449–460.
- (189) Evans, L.; Paul Thalody, B.; Morgan, J. D.; Nicol, S. K.; Napper, D. H.; Warr, G. G. Ion Flotation Using Carboxylate Soaps: Role of Surfactant Structure and Adsorption Behaviour. *Colloids Surfaces A Physicochem. Eng. Asp.* **1995**, *102* (C), 81–89.
- (190) Stiller, S.; Gers-Barlag, H.; Lergenmueller, M.; Pflücker, F.; Schulz, J.; Wittern, K. P.; Daniels, R. Investigation of the Stability in Emulsions Stabilized with Different Surface Modified Titanium Dioxides. *Colloids Surfaces A Physicochem. Eng. Asp.* **2004**, *232* (2–3), 261–267.
- (191) Pugh, R. J. Foaming in Chemical Surfactant Free Aqueous Dispersions of Anatase (Titanium Dioxide) Particles. *Langmuir* **2007**, *23* (15), 7972–7980.
- (192) Gao, X.; Chorover, J. Adsorption of Sodium Dodecyl Sulfate (SDS) at ZnSe and α -Fe₂O₃ Surfaces: Combining Infrared Spectroscopy and Batch Uptake Studies. *J. Colloid Interface Sci.* **2010**, *348* (1), 167–176.
- (193) Barbian, N.; Ventura-Medina, E.; Cilliers, J. J. Dynamic Froth Stability in Froth Flotation. *Miner. Eng.* **2003**, *16* (11), 1111–1116.
- (194) Hashemi, S.; Rezaee, A.; Nikodel, M.; Ganjidost, H.; Mousavi, S. M. Equilibrium and Kinetic Studies of the Adsorption of Sodium Dodecyl Sulfate from Aqueous Solution Using Bone Char. *React. Kinet. Mech. Catal.* **2013**, *109* (2), 433–446.
- (195) Yekeen, N.; Manan, M. A.; Idris, A. K.; Samin, A. M.; Risal, A. R. Experimental Investigation of Minimization in Surfactant Adsorption and Improvement in Surfactant-Foam Stability in Presence of Silicon Dioxide and Aluminum Oxide Nanoparticles. *J. Pet. Sci. Eng.* **2017**, *159*, 115–134.

- (196) Gong, W.; Zang, Y.; Xie, H.; Liu, B.; Chen, H.; Li, C.; Ge, L. Properties of Surfactants on High Salt-Affected Sandy Land in Enhanced Sand Fixation: Salt Tolerance, Adsorption Isotherms and Ecological Effect. *RSC Adv.* **2015**, *5* (100), 81847–81856.
- (197) Khoshdast, H.; Mirshekari, S.; Zahab-Nazouri, A. A Model for Predicting Dynamic Frothability Index Value for Dual-Frother Blends. *J. Min. Environ.* **2015**, *6* (1), 119–124.
- (198) Li, P.; Ishiguro, M. Adsorption of Anionic Surfactant (Sodium Dodecyl Sulfate) on Silica. *Soil Sci. Plant Nutr.* **2016**, *62* (3), 223–229.
- (199) Zhang, H.; Kim, Y. K.; Hunter, T. N.; Brown, A. P.; Lee, J. W.; Harbottle, D. Organically Modified Clay with Potassium Copper Hexacyanoferrate for Enhanced Cs^+ Adsorption Capacity and Selective Recovery by Flotation. *J. Mater. Chem. A* **2017**, *5* (29), 15130–15143.
- (200) Czarnecki, J.; Małysa, K.; Pomianowski, A. Dynamic Frothability Index. *J. Colloid Interface Sci.* **1982**, *86* (2), 570–572.
- (201) López-Barajas, M.; López-Tamames, E.; Buxaderas, S.; Tomás, X.; De La Torre, M. C. Prediction of Wine Foaming. *J. Agric. Food Chem.* **1999**, *47* (9), 3743–3748.
- (202) Adekola, F.; Fédoroff, M.; Geckeis, H.; Kupcik, T.; Lefèvre, G.; Lützenkirchen, J.; Plaschke, M.; Preocanin, T.; Rabung, T.; Schild, D. Characterization of Acid-Base Properties of Two Gibbsite Samples in the Context of Literature Results. *J. Colloid Interface Sci.* **2011**, *354* (1), 306–317.
- (203) Rosenqvist, J. Surface Chemistry of Al and Si (Hydr)Oxides, with Emphasis on Nano-Sized Gibbsite ($\alpha\text{-Al}(\text{OH})_3$), Department of Chemistry, Inorganic chemistry Umea University, Sweeden, 2002.
- (204) Buratto, B.; Usher, S. P.; Parris, D.; Scales, P. J. Wall Effects during Settling in Cylinders. *Colloids Surfaces A Physicochem. Eng. Asp.* **2014**, *449*, 157–169.
- (205) Tavacoli, J. W.; Dowding, P. J.; Routh, A. F. The Polymer and Salt Induced Aggregation of Silica Particles. *Colloids Surfaces A Physicochem. Eng. Asp.* **2007**, *293* (1–3), 167–174.
- (206) Pierce, F.; Sorensen, C. M.; Chakrabarti, A. Computer Simulation of Diffusion-Limited Cluster-Cluster Aggregation with an Epstein Drag Force. *Phys. Rev. E* **2006**, *74* (2), 021411.
- (207) Gangula, S.; Suen, S. Y.; Conte, E. D. Analytical Applications of Admicelle and Hemimicelle Solid Phase Extraction of Organic Analytes. *Microchem. J.* **2010**, *95*

- (1), 2–4.
- (208) Bera, A.; Mandal, A. Microemulsions: A Novel Approach to Enhanced Oil Recovery: A Review. *J. Pet. Explor. Prod. Technol.* **2015**, *5*, 255–268.
- (209) Pashley, R. M.; Karaman, M. E.; John Wiley & Sons. *Applied Colloid and Surface Chemistry*; J. Wiley, 2004.
- (210) Kontogeorgis, G. M.; Kiil, S. *Introduction to Applied Colloid and Surface Chemistry*; John Wiley & Sons, Ltd: Chichester, UK, 2016.
- (211) AL-Thabaiti, S. A.; Al-Nowaiser, F. M.; Obaid, A. Y.; Al-Youbi, A. O.; Khan, Z. Formation and Characterization of Surfactant Stabilized Silver Nanoparticles: A Kinetic Study. *Colloids Surfaces B Biointerfaces* **2008**, *67* (2), 230–237..
- (212) Pisárčik, M.; Jampílek, J.; Lukáč, M.; Horáková, R.; Devínský, F.; Bukovský, M.; Kalina, M.; Tkacz, J.; Opravil, T. Silver Nanoparticles Stabilised by Cationic Gemini Surfactants with Variable Spacer Length. *Molecules* **2017**, *22* (10), 1794–1813.
- (213) Mahmoud, M. R.; Soliman, M. A.; Rashad, G. M. Performance Appraisal of Foam Separation Technology for Removal of Co(II)-EDTA Complexes Intercalated into in-Situ Formed Mg-Al Layered Double Hydroxide from Radioactive Liquid Waste. *Chem. Eng. J.* **2017**, *326*, 781–793.
- (214) Bournival, G.; Ata, S.; Jameson, G. J. Bubble and Froth Stabilizing Agents in Froth Flotation. *Miner. Process. Extr. Metall. Rev.* **2017**, *38* (6), 366–387.
- (215) Binks, B. P. Particles as Surfactants - Similarities and Differences. *Curr. Opin. Colloid Interface Sci.* **2002**, *7* (1–2), 21–41.
- (216) Simovic, S.; Prestidge, C. A. Hydrophilic Silica Nanoparticles at the PDMS Droplet-Water Interface. *Langmuir* **2003**, *19* (9), 3785–3792.
- (217) Abend, S.; Bonnke, N.; Gutschner, U.; Lagaly, G. Stabilization of Emulsions by Heterocoagulation of Clay Minerals and Layered Double Hydroxides. *Colloid Polym. Sci.* **1998**, *276* (8), 730–737.
- (218) Tao, D. L. G. Y. R. A Parametric Study of Froth Stability and Its Effect on Column Flotation of Fine Particles. *Int. J. Miner. Process.* **2000**, *59*, 25–43.
- (219) Sun, S.; Weber-Shirk, M.; Lion, L. W. Characterization of Flocs and Floc Size Distributions Using Image Analysis. *Environ. Eng. Sci.* **2016**, *33* (1), 25–34.
- (220) Yang, Z.; Yang, H.; Jiang, Z.; Huang, X.; Li, H.; Li, A.; Cheng, R. A New Method for Calculation of Flocculation Kinetics Combining Smoluchowski Model with Fractal Theory. *Colloids Surfaces A Physicochem. Eng. Asp.* **2013**, *423*, 11–19.

- (221) Hasan, A.; Fatehi, P. Flocculation of Kaolin Particles with Cationic Lignin Polymers. *Nat. Sci. Reports* **2019**, *9* (1), 1–12.
- (222) Kozlova, N.; Santore, M. M. Manipulation of Micrometer-Scale Adhesion by Tuning Nanometer-Scale Surface Features. *Langmuir* **2006**, *22* (3), 1135–1142.
- (223) Sakohara, S.; Hinago, R.; Ueda, H. Compaction of TiO₂ Suspension by Using Dual Ionic Thermosensitive Polymers. *Sep. Purif. Technol.* **2008**, *63* (2), 319–323.
- (224) Sakohara, S.; Nishikawa, K. Compaction of TiO₂ Suspension Utilizing Hydrophilic/Hydrophobic Transition of Cationic Thermosensitive Polymers. *J. Colloid Interface Sci.* **2004**, *278* (2), 304–309.
- (225) Sakohara, S.; Kimura, T.; Nishikawa, K. Flocculation Mechanism of Suspended Particles Using the Hydrophilic/Hydrophobic Transition of a Thermosensitive Polymer [Translated]†. *KONA Powder Part. J.* **2002**, *20* (0), 246–250.
- (226) Théodoly, O.; Jacquin, M.; Muller, P.; Chhun, S. Adsorption Kinetics of Amphiphilic Diblock Copolymers: From Kinetically Frozen Colloids to Macrosurfactants. *Langmuir* **2009**, *25* (2), 781–793.
- (227) Mai, Y.; Eisenberg, A. Self-Assembly of Block Copolymers. *Chem. Soc. Rev.* **2012**, *41* (18), 5969–5985.
- (228) Kataoka, K.; Nagasaki, Y.; Otsuka, H. Self-Assembly of Block Copolymers. *Mater. today* **2001**, *4*, 30–36.
- (229) Liu, L. Y.; Xia, G.; Feng, Z. J.; Hao, Q. H.; Tan, H. G. Self-Assembly of Polyelectrolyte Diblock Copolymers at Monovalent and Multivalent Counterions. *Soft Matter* **2019**, *15* (18), 3689–3699.
- (230) Lovett, J. R.; Warren, N. J.; Armes, S. P.; Smallridge, M. J.; Cracknell, R. B. Order–Order Morphological Transitions for Dual Stimulus Responsive Diblock Copolymer Vesicles. *Macromolecules* **2016**, *49* (3), 1016–1025.
- (231) Sakai, K.; Smith, E. G.; Webber, G. B.; Baker, M.; Wanless, E. J.; Bütün, V.; Armes, S. P.; Biggs, S. PH-Responsive Behavior of Selectively Quaternized Diblock Copolymers Adsorbed at the Silica/Aqueous Solution Interface. *J. Colloid Interface Sci.* **2007**, *314* (2), 381–388.
- (232) Sakai, K.; Smith, E. G.; Webber, G. B.; Wanless, E. J.; Bütün, V.; Armes, S. P.; Biggs, S. Effects of Copolymer Concentration and Chain Length on the PH-Responsive Behavior of Diblock Copolymer Micellar Films. *J. Colloid Interface Sci.* **2006**, *303* (2), 372–379.
- (233) Kim, C.; Lee, S. C.; Shin, J. H.; Yoon, J. S.; Kwon, I. C.; Jeong, S. Y. Amphiphilic

- Diblock Copolymers Based on Poly(2-Ethyl-2-Oxazoline) and Poly(1,3-Trimethylene Carbonate): Synthesis and Micellar Characteristics. *Macromolecules* **2000**, *33* (20), 7448–7452.
- (234) Perrier, S. 50th Anniversary Perspective: RAFT Polymerization - A User Guide. *Macromolecules*. **2017**, *50* (19), 7433–7447.
- (235) Colombani, O.; Ruppel, M.; Schubert, F.; Zettl, H.; Pergushov, D. V.; Müller, A. H. E. Synthesis of Poly(*n*-Butyl Acrylate)-*Block*-Poly(Acrylic Acid) Diblock Copolymers by ATRP and Their Micellization in Water. *Macromolecules* **2007**, *40* (12), 4338–4350.
- (236) Berry, J. D.; Neeson, M. J.; Dagastine, R. R.; Chan, D. Y. C.; Tabor, R. F. Measurement of Surface and Interfacial Tension Using Pendant Drop Tensiometry. *J. Colloid Interface Sci.* **2015**, *454*, 226–237.
- (237) Morse, A. J.; Giakoumatos, E. C.; Tan, S. Y.; Webber, G. B.; Armes, S. P.; Ata, S.; Wanless, E. J. Giant PH-Responsive Microgel Colloidosomes: Preparation, Interaction Dynamics and Stability. *Soft Matter* **2016**, *12* (5), 1477–1486.
- (238) Morse, A. J.; Tan, S. Y.; Giakoumatos, E. C.; Webber, G. B.; Armes, S. P.; Ata, S.; Wanless, E. J. Arrested Coalescence Behaviour of Giant Pickering Droplets and Colloidosomes Stabilised by Poly(Tert-Butylaminoethyl Methacrylate) Latexes. *Soft Matter* **2014**, *10* (31), 5669–5681.
- (239) Thompson, K. L.; Giakoumatos, E. C.; Ata, S.; Webber, G. B.; Armes, S. P.; Wanless, E. J. Direct Observation of Giant Pickering Emulsion and Colloidosome Droplet Interaction and Stability. *Langmuir* **2012**, *28* (48), 16501–16511.
- (240) Hernáinz, F.; Caro, A. Variation of Surface Tension in Aqueous Solutions of Sodium Dodecyl Sulfate in the Flotation Bath. *Colloids Surfaces A Physicochem. Eng. Asp.* **2002**, *196* (1), 19–24.
- (241) Wittmer, J.; Joanny, J. F. Charged Diblock Copolymers at Interfaces. *Macromolecules* **1993**, *26* (11), 2691–2697.
- (242) Trujillo-Cayado, L. A.; Ramírez, P.; Pérez-Mosqueda, L. M.; Alfaro, M. C.; Muñoz, J. Surface and Foaming Properties of Polyoxyethylene Glycerol Ester Surfactants. *Colloids Surfaces A Physicochem. Eng. Asp.* **2014**, *458* (1), 195–202.
- (243) Monroy, F.; Giermanska Kahn, J.; Langevin, D. Dilational Viscoelasticity of Surfactant Monolayers. *Colloids Surfaces A Physicochem. Eng. Asp.* **1998**, *143* (2–3), 251–260.
- (244) Noskov, B. A.; Lin, S. Y.; Loglio, G.; Rubio, R. G.; Miller, R. Dilational

- Viscoelasticity of PEO-PPO-PEO Triblock Copolymer Films at the Air-Water Interface in the Range of High Surface Pressures. *Langmuir* **2006**, 22 (6), 2647–2652.
- (245) Manga, M. S.; Hunter, T. N.; Cayre, O. J.; York, D. W.; Reichert, M. D.; Anna, S. L.; Walker, L. M.; Williams, R. A.; Biggs, S. R. Measurements of Submicron Particle Adsorption and Particle Film Elasticity at Oil-Water Interfaces. *Langmuir* **2016**, 32 (17), 4125–4133.
- (246) Ploehn, H. J. Self-Consistent Field Theory for Polymer Adsorption: Molecular Volume Effects. *Colloids Surfaces A Physicochem. Eng. Asp.* **1994**, 86, 25–40.
- (247) Peakall, J. Ashworth, P. Best, J. Physical Modelling in Fluvial Geomorphology: Principles, Applications and Unresolved Issues. In *The scientific nature of geomorphology: proceedings of the 27th Binghamton Symposium in Geomorphology*; Thorn, C, E. Rhoads, B, L., Ed.; Wiley: New York, 1996; pp 221–253.

Appendix A: Supplementary data for Chapter 3

A.1) Detailed description of Mg(OH)₂ characterisation

Dry scanning electron microscopy (SEM) analysis was conducted on Mg(OH)₂ powder that was sputtered with a 10 nm layer of iridium, before being analysed in a Hitachi SU8230 (Hitachi Hightech) scanning electron microscope. Fig. A1 shows a scanning electron micrograph of Mg(OH)₂ particle agglomerates, formed from pseudo-hexagonal platelets, which agrees with previous literature on brucite particles⁷ and Versamag explicitly¹⁶. Energy dispersive X-ray (EDX) analysis (Fig. A2) of the sample was also conducted during SEM investigation, which highlighted trace amounts of calcium. The particle size distribution (PSD) of the Mg(OH)₂ was found using a Malvern Mastersizer 2000E (Malvern Panalytical Ltd) instrument which utilizes static light scattering to determine particle size. A 2.5 vol.% suspension was suspended in Milli-Q water and sonicated for 20 minutes to break up aggregates. The suspension displayed an average spherical equivalent diameter of ~2.45 μm, which agrees qualitatively with the SEM data displayed in Fig. A1. The fractal dimension of the 2.5 %vol Mg(OH)₂ was determined by the SLS data obtained as the sonicated Mg(OH)₂ aggregated with measurements taken every 15 minutes for 136 minutes. The logarithm for the scattering intensity $I(Q)$ and scattering wave vector collected Q (Fig. A3) were then used to determine the fractal dimension using the theory and techniques outlined in the main manuscript.

The semi-solubility of the material at this concentration produced a self-buffering electrolyte background with a pH of ~10.1, as measured using a pH probe. The ζ-potential of the suspension was measured using a Zetasizer (Malvern Panalytical Ltd). A 0.1 vol.% suspension of Mg(OH)₂ was prepared and sonicated for 20 minutes prior to surface charge investigation, the suspension was then syringed into a zeta cell compatible with electrophoretic light scattering and analysed. This technique produced an average surface potential reading of ~12 mV which is slightly higher than generally reported literature^{7,16,24}. The Brunauer–Emmett–Teller (BET) surface area was obtained by a standard nitrogen adsorption-desorption method¹⁷⁰ at 77.3 K using a TriStar 3000 (Micromeritics) surface analyser. The Mg(OH)₂ was degassed to remove any moisture and surface absorbed gases by using a vacuum oven at 120 °C for 24 h under a vacuum of 10 mmHg. The Mg(OH)₂ sample was then degassed under N₂ for 4 h at 300 °C, and atmospheric pressure. The N₂

adsorption isotherm was used to calculate the BET surface area of $\text{Mg}(\text{OH})_2$ which was found to be $\sim 8 \text{ m}^2\text{g}^{-1}$, similar to values acquired by Biggs et al.²⁴. The semi-solubility and self-buffering characteristics of the suspension gave a relatively constant electrolyte background, thus negating large changes in ζ -potential by controlling electric double layer contraction for increased control of electrostatic charge differentials between the particle surface and polymer charge groups. This cationic surface potential indicated that the anionic polyacrylamide-acrylate copolymers used in this work would be compatible and viable candidates for effective flocculation of the suspended $\text{Mg}(\text{OH})_2$ particulates, based on previous work with these systems.

A.2) Supplementary figures

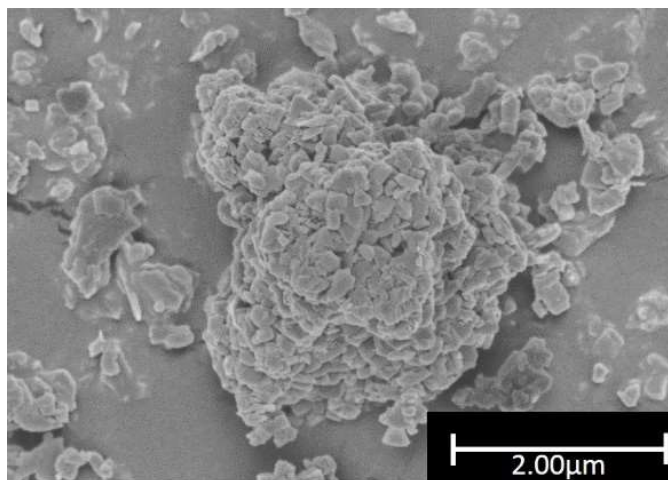


Figure A1: Scanning Electron Micrograph of dry $\text{Mg}(\text{OH})_2$ imaged using a Hitachi SU8230 scanning electron microscope at 20000 times magnification and 1 kV electron voltage.

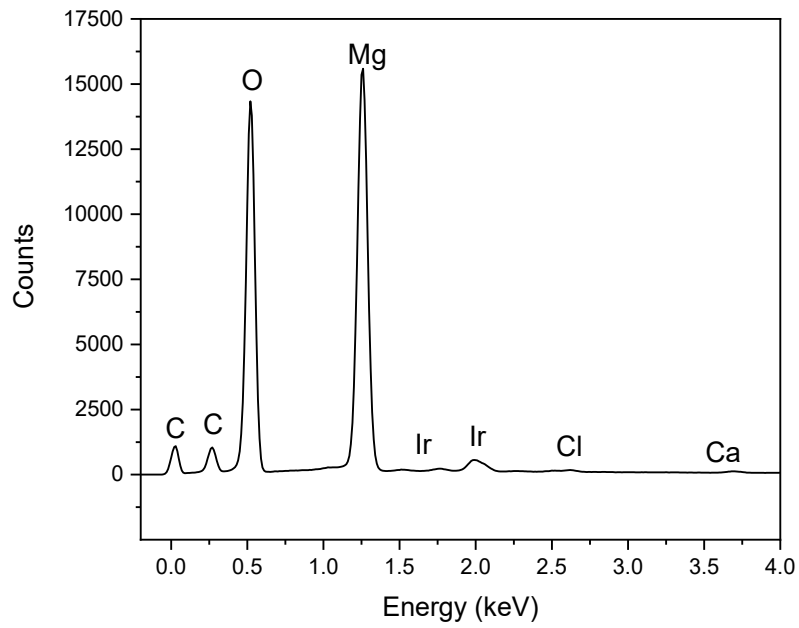


Figure A2: Energy dispersive X-ray spectra for Mg(OH)₂

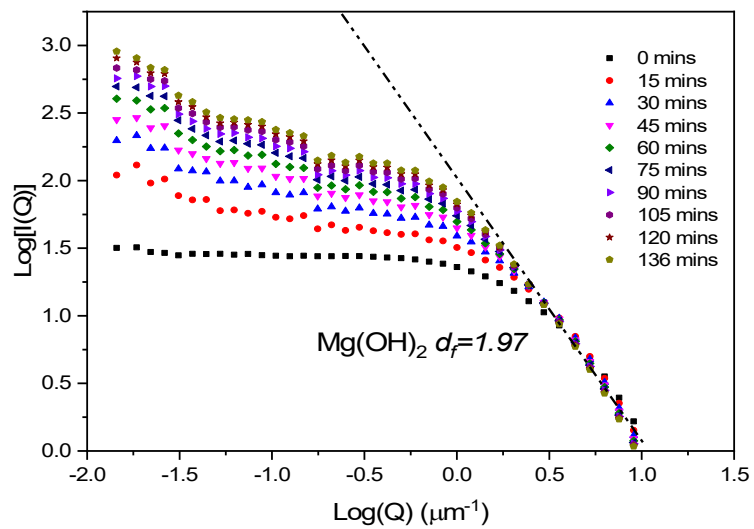


Figure A3: Static light scattering fractal dimension analysis of 2.5 vol.% Mg(OH)₂ suspensions without polymer.

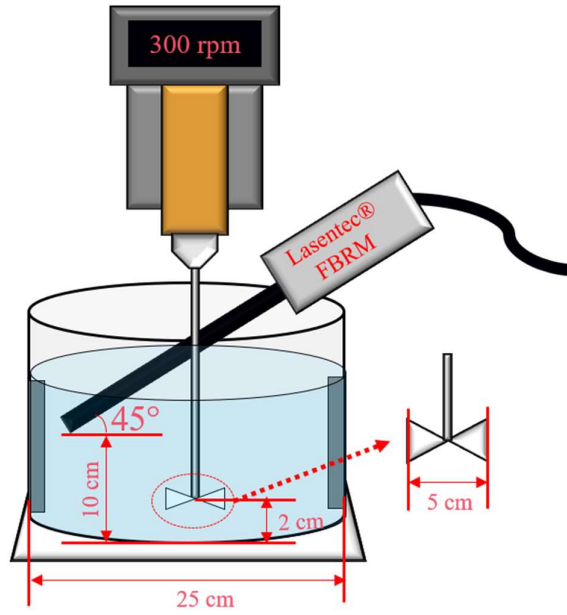


Figure A4: Diagram of experimental setup for the FBRM measurements of flocculation kinetics.

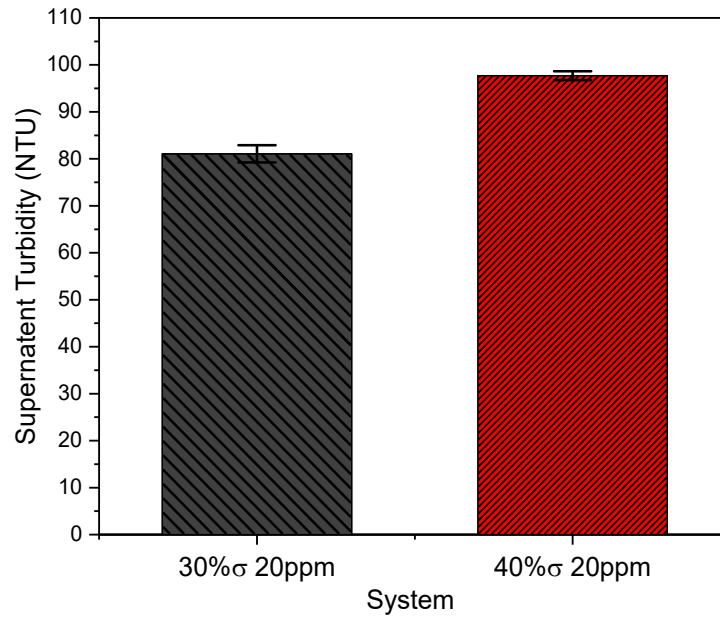
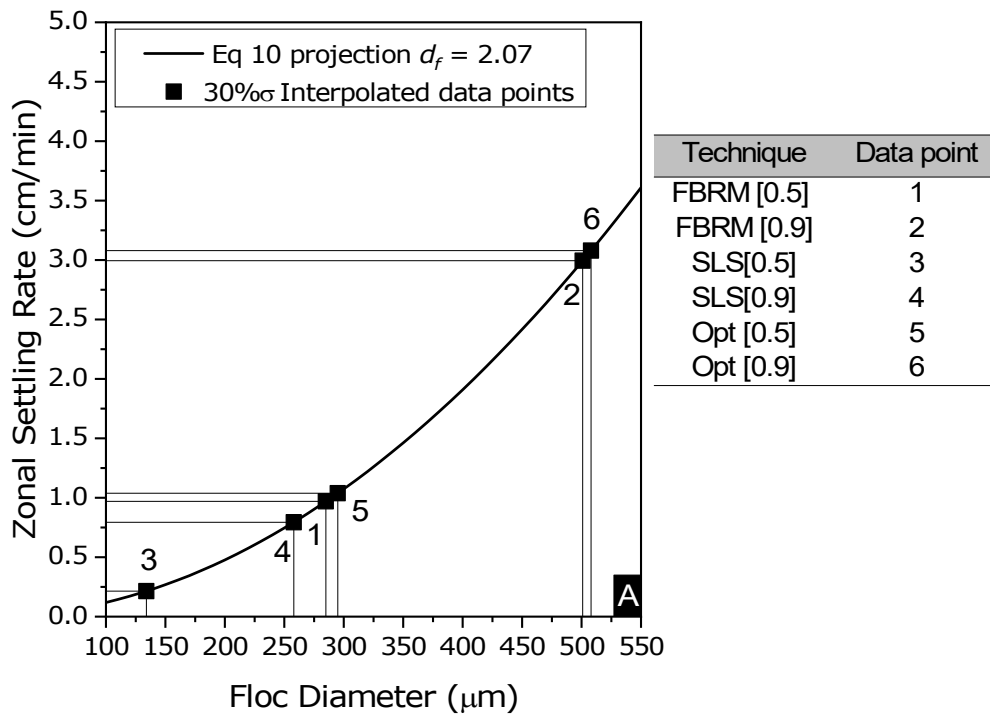


Figure A5: Comparison of supernatant turbidity after 30 minutes of sedimentation, of 2.5 vol.% Mg(OH)₂ suspensions flocculated with 30%σ and 40%σ polymers in a reactor agitated at 300 rpm for 1000 s.

Table A6: Comparison of the 50th (d_{50}) and 90th (d_{90}) percentile equivalent floc diameters, using focused beam reflectance measurement (FBRM) and static light scattering (SLS), for 30% σ and 40% σ polymer- Mg(OH)₂ systems at 2.5 vol.%, dosed at 10 ppm polymer concentration.

Measurement	30% σ 10 ppm	40% σ 10 ppm
d_{50} (FBRM) (μm)	180	151
d_{90} (FBRM) (μm)	317	271
d_{50} (SLS) (μm)	74	46
d_{90} (SLS) (μm)	159	112
Fractal Dimension	2.023	2.005



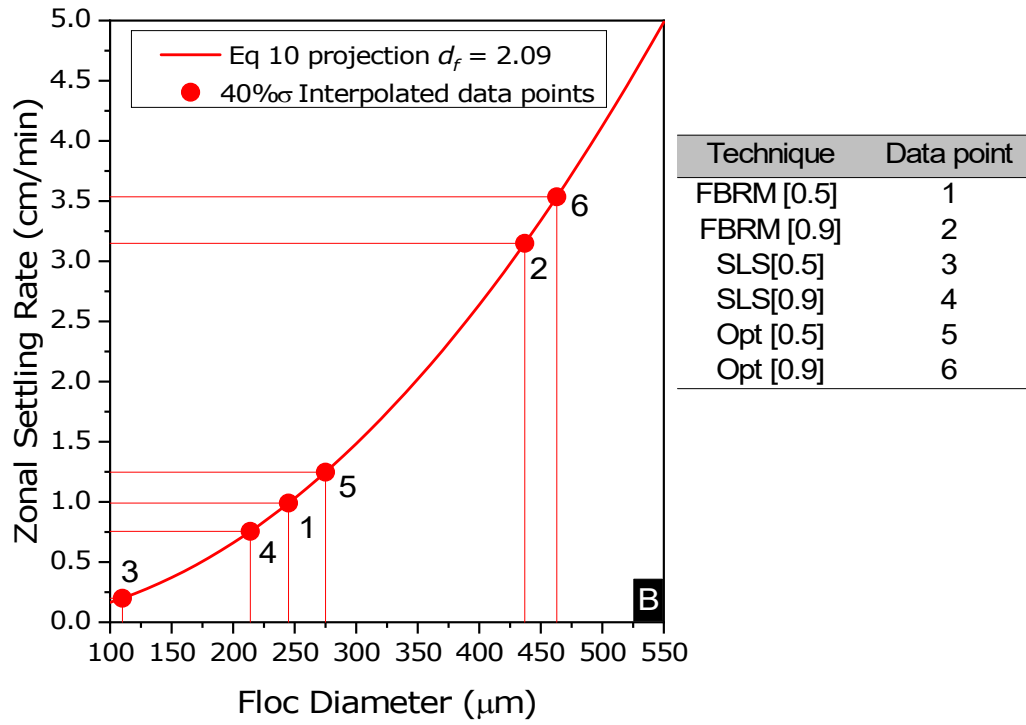


Figure A6: Zonal settling rate projections interpolated from the fractal modified Richardson-Zaki model (Eqn. 3.10) as a function of measured floc diameter for A) $d_f = 2.07$, $D_f = 6.74 \mu\text{m}$, $D_p = 0.28 \mu\text{m}$ and B) $d_f = 2.09$, $D_f = 8.01 \mu\text{m}$, $D_p = 0.34 \mu\text{m}$. Here, $\rho_p = 2340.6 \text{ kg}\cdot\text{m}^{-3}$, $\rho_w = 1000 \text{ kg}\cdot\text{m}^{-3}$, $g = 9.81 \text{ m}\cdot\text{s}^{-2}$, $\mu_w = 8.9 \times 10^{-4} \text{ kg}\cdot\text{m}^{-1}\cdot\text{s}^{-1}$, and $\Phi_p = 0.025$ in all cases.

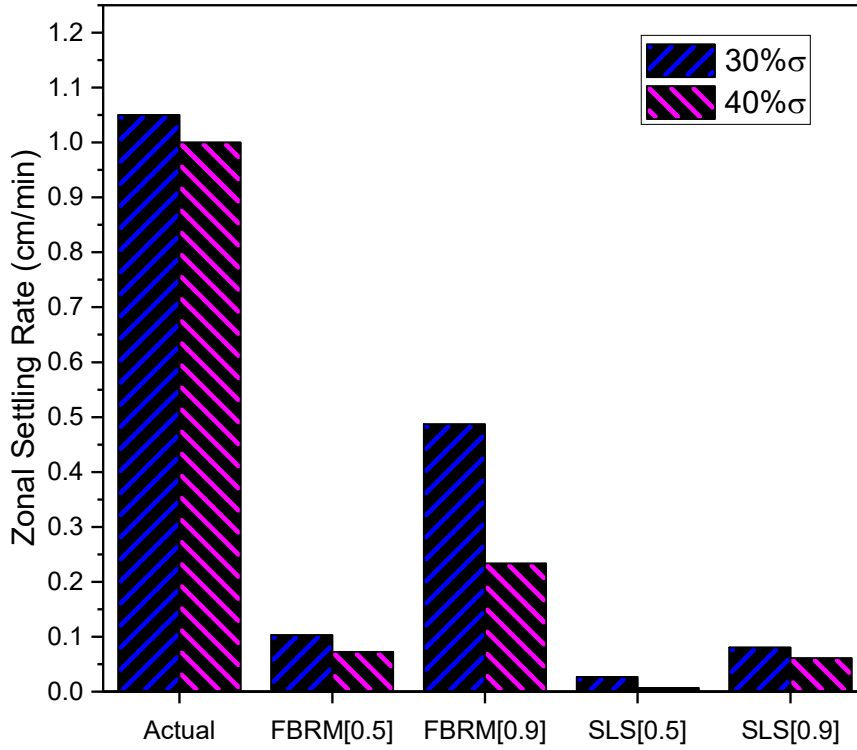


Figure A7: Comparison of measured (actual) zonal settling rates for flocculated 2.5 vol.% Mg(OH)₂ suspensions mixed with 10 ppm 30%σ and 40%σ polymer, to those predicted by the fractal modified Richardson-Zaki equation (Eqn. 3.10). Comparison using median [0.5] and 90th percentile [0.9] sizes measured by *in situ* focused beam reflectance meter (FBRM) and *ex situ* static light scattering (SLS) that incorporated a 900 rpm agitated feed-cell.

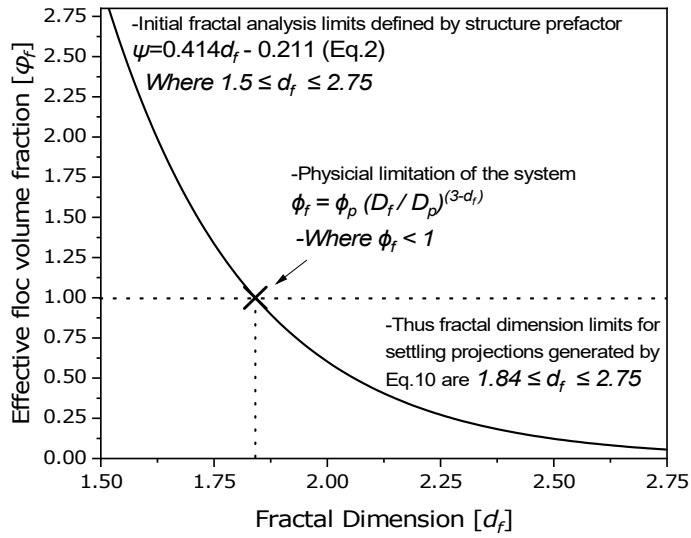


Figure A8: Changes in the effective floc volume fraction (using Eqn. 3.9) with changes in fractal dimension, used to interpolate the fractal dimension limits of Eqn. 3.10 where $\phi_f \leq 1$.

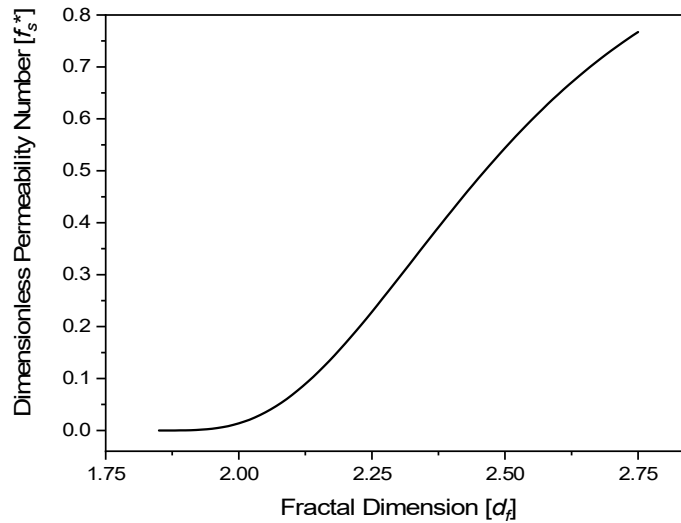


Figure A9: Change in dimensionless permeability number, $f_s^* = \left(1 - \phi_p \left(\frac{D_f}{D_p}\right)^{3-d_f}\right)^{4.65}$, as a function of changes in fractal dimension for fixed values of D_f and D_p for the 30%σ 20 ppm system in Table 3.2 and at an initial particle concentration of 2.5 vol.%.

Appendix B: Supplementary data for Chapter 4.

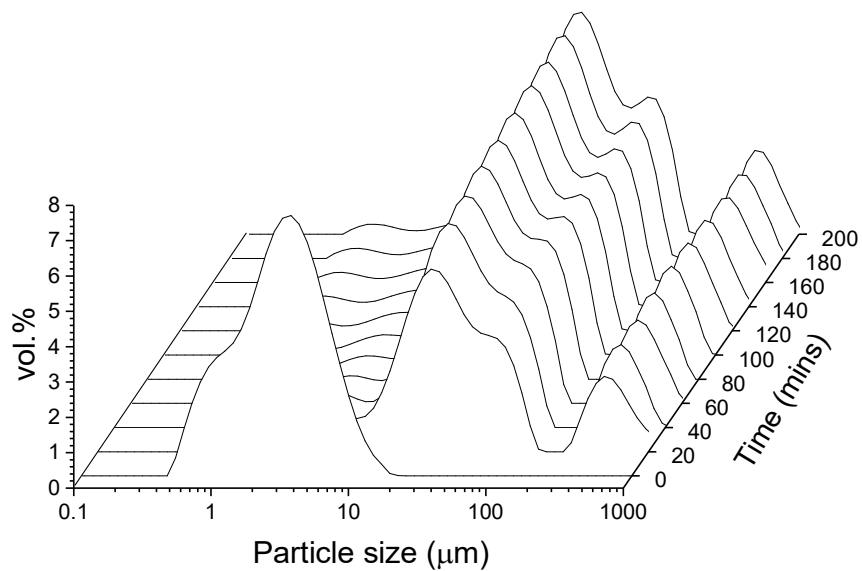


Figure B2: The change in the volume based (vol.%) particle size distribution of Mg(OH)₂ agitated at 900 rpm and dosed with 10⁻² M KNO₃ with time.

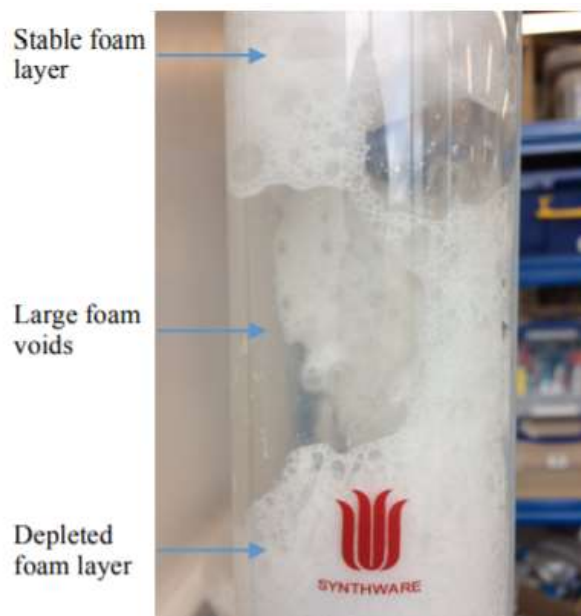


Figure B3: Photograph of Bikerman column during foamability tests, showing stabilised collapsed foam layers preventing further foamability readings.

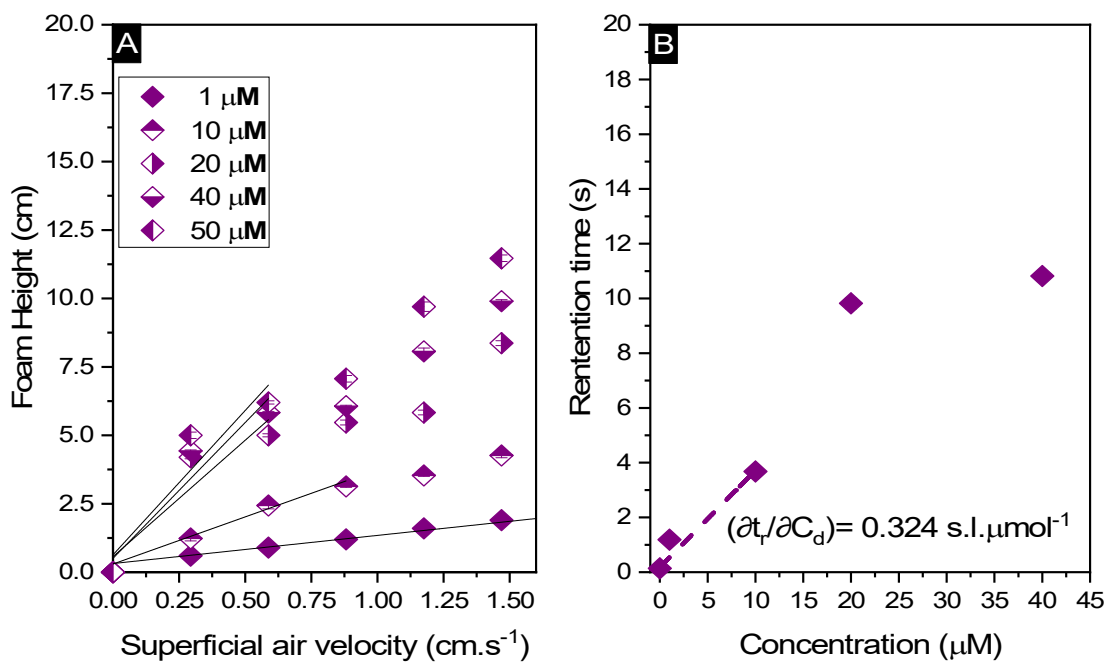


Figure B4: A) The change in foam height with superficial air velocity for sodium lauryl isethionate without Mg(OH)₂ particles. B) The retention time variation (calculated using Eqn. 4.2) with collector/frother concentration.

Appendix C: Supplementary data for Chapter 5

C.1) Detailed description of amphiphilic block copolymer synthesis

The poly(acrylic acid) (PAA) degree of polymerisation (P_d) was selected arbitrarily as 160. The PAA was then used as macro-chain-transfer agent (macro-CTA) for RAFT emulsion polymerisation of n-butyl acrylate to form the amphiphilic block copolymer (ABC). The relative ratios of the initiator 4,4'-Azobis(4-cyanovaleric acid) (ACVA), chain-transfer agent 3-(((1-carboxylethyl)thio)carbonothioyl)thio)propanoic acid (CCTP) and acrylic acid monomer were 0.4:1:160 respectively. A solids concentration of 30 wt.% was selected to ensure lower aqueous ABC solution viscosity for ease of manipulation. The experimental method was as follows: polymer reagents were formulated and gently agitated with a magnetic stirrer for 2 hours to ensure full reagent dissolution. The resultant aqueous polymer mixture was then transferred to a 250 ml round bottom flask containing a magnetic stirrer bar and sealed with a rubber septum, with a needle exhaust as an outlet for excess nitrogen during purging. A second needle connected to a nitrogen supply was inserted into the septum and the tip submerged in the aqueous polymer mixture reaction solution. The reaction solution was then placed on a magnetic stirrer operating at 500 rpm and sparged with nitrogen for 1 hour. The reaction was initiated by placing the flask into a paraffin oil bath heated at 70°C and stirred at 500 rpm under a continuous nitrogen atmosphere, with the nitrogen inlet raised above that of the liquid into the headroom of the flask.

To enable determination of the extent of polymerisation, 0.4 ml aliquots were extracted from the reaction vessel using a degassed syringe fitted with a needle and placed into NMR tubes before the polymerisation reaction and after 45 minutes. At this point the flask was removed from the paraffin oil bath and exposed to the atmosphere. Aliquots taken pre and post-reaction were analysed using NMR to calculate the macro-CTA conversion X_{AA} which is shown in Fig. C1. The aliquots were analysed using a Magritek® ^1H Spinsolve 60 MHz Ultra benchtop NMR spectrometer. The series of NMR spectra in Figure C1 show the appearance of broad peaks corresponding to the polymer backbone protons confirming formation of polymer. at $\delta=0.1$ ppm to 2.9 ppm. From the spectra the monomer conversion was calculated as a function of reaction time. Where the conversion of monomer, X_{AA} , at time t is $X_{AA}=1 - A_t/A_0$, where A_t and A_0 are the ratios of the integrated peaks of monomer

acrylic acid to PAA in the NMR spectra at t_i and t_0 respectively [236]. The final conversion was calculated as 96 %, yielding a macro-CTA of PAA₁₅₃.

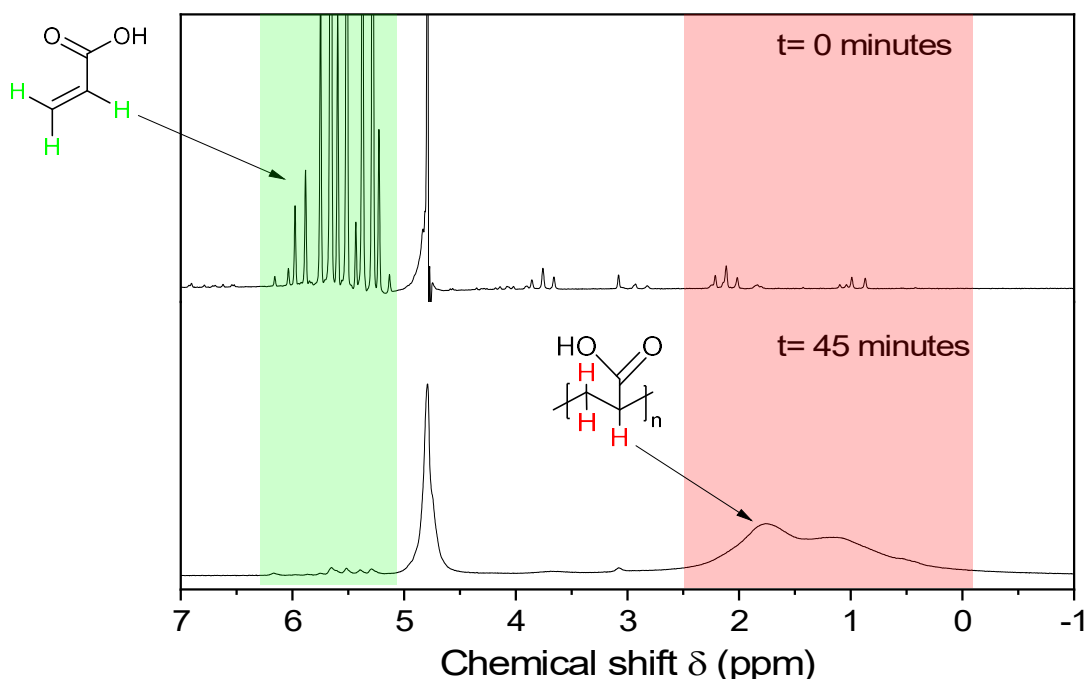


Figure C1: Nuclear magnetic spectroscopic spectra of the initial monomer (acrylic acid), initiator (ACVA) and chain transfer agent (CCTP) and the final polymer conversion at 45 minutes using the area reduction in vinyl proton environment peaks labelled in green ($\delta = 6.5-5.1$ ppm) and production of polymer backbone peaks labelled in red ($\delta = 2.5-0$ ppm).

The macro-CTA was then directly used in the synthesis of the ABCs without further purification (as a 30 wt.% solution). The ABCs were synthesised by polymerizing n-butyl acrylate (nBA) using ACVA as the initiator and the previously synthesised macro-CTA. Three ABCs were selected for synthesis: PAA₁₅₃-*b*-PnBA₂₅, PAA₁₅₃-*b*-PnBA₁₀₀ and PAA₁₅₃-*b*-PnBA₂₀₀ (P_d and initiator: macro-CTA: monomer ratios detailed in Table C1). The reaction procedure was the same as for the macro-CTA (PAA) synthesis, but differed regarding characterisation and reaction time. Unlike the synthesis of the macro-CTA, maximum conversion was preferably required. To achieve this high conversion, the reaction residence time was extended to 3 hours to ensure complete depletion of vinyl groups characterised by the NMR spectra in Fig. C2. During this reaction, there was an increase in viscosity due to interactions between the amphiphilic chains. This resulted in difficulty extracting aliquots from the reaction vessel without using a needle gauge that compromised the integrity of the suba-seal. Therefore, the polymer was characterised *ex*

situ. Due to the immiscibility of nBA and water, the mixture was dissolved in 90% methanol. Integration of the relevant peaks in the spectrum was difficult in this case due to overlap between polymer and methanol ($\delta=0.1$ ppm to 2.9 ppm). Therefore, an NMR standard, TMS salt with peaks around $\delta = -0.6$ ppm, was added into the reaction (0.4 g.g⁻¹ solid polymer). The peaks from the TMS salt could then be compared with the depletion of those from the vinyl protons in the monomer. A presaturation solvent suppression technique was also used to reduce the magnitude of methanol peaks in the spectra for ease of analysis.

The 3 resultant polymers were then dissolved and diluted in Milli-Q water to make up 1000 ppm stock solutions for experimental use. Fig. C2 shows the NMR spectra of the target polymer PAA₁₅₃-*b*-PnBA₂₀₀ initially and after 3 hours of polymerisation. After 3 hours the vinyl proton environment peak ($\delta = 6.5$ -5.1 ppm, in which the area beneath the peaks is proportional to concentration) was found to reduce to be within the noise of the spectra indicating over 99% conversion of monomer to polymer. It should be noted that within these spectra, the formation of the PnBA polymer backbone is not observed since this component is not soluble in the methanol NMR solvent and therefore remains as the cores of the polymer. According to NMR all three ABCs achieved over 99% conversion from nBA to PnBA.

Table C1: Poly(acrylic acid)-*block*-poly(n-butyl acrylate) synthesis target degrees of polymerisation and required relative molecular ratios of 4,4'-Azobis(4-cyanovalric acid) (ACVA) initiator to poly(acrylic acid) (PAA) macro chain-transfer agent to n-butyl acrylate (nBA) monomer per target polymer.

Target polymer	Target PnBA P_d	Initiator: macro-CTA: monomer- molecular ratios
PAA ₁₅₃ - <i>b</i> -PnBA ₂₅	25	0.4:1:25
PAA ₁₅₃ - <i>b</i> - PnBA ₁₀₀	100	0.4:1:100
PAA ₁₅₃ - <i>b</i> - PnBA ₂₀₀	200	0.4:1:200

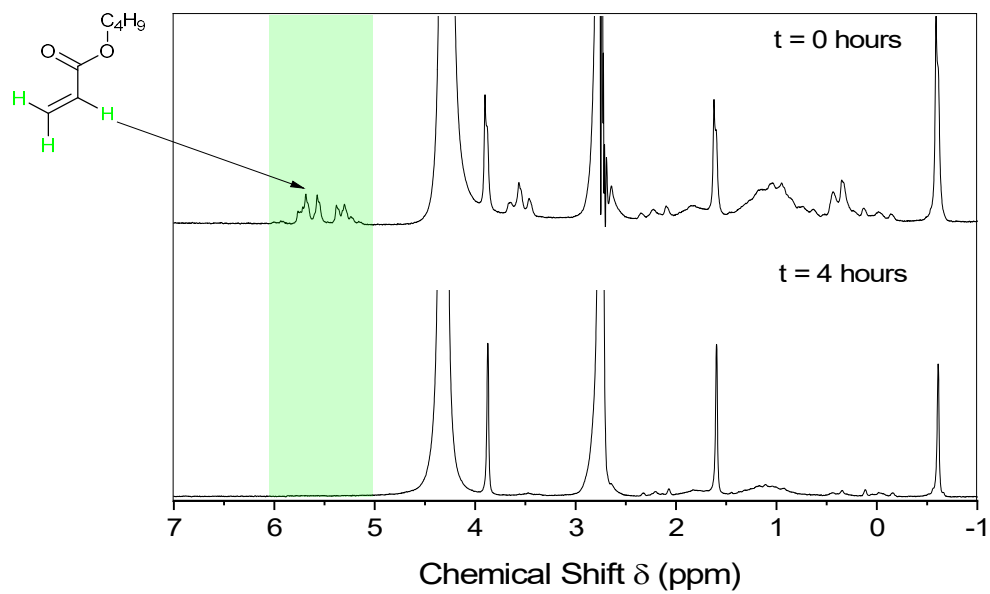
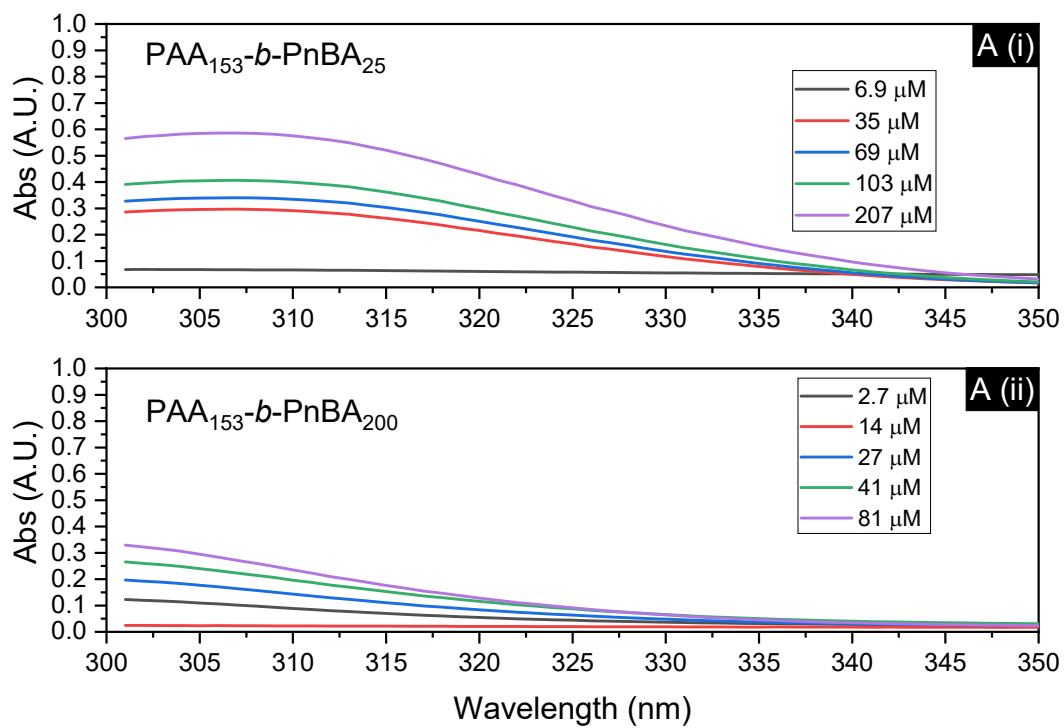


Figure C2: Nuclear magnetic spectroscopic spectra of the initial monomer (n-butyl acrylate), initiator (ACVA) and macro-chain transfer agent (PAA) and the final polymer conversion after 3 hours indicating the detectable total depletion of vinyl groups in the n-butyl acrylate species ($\delta = 6.5 - 5.1$ ppm).

C.2) Supplementary Figures



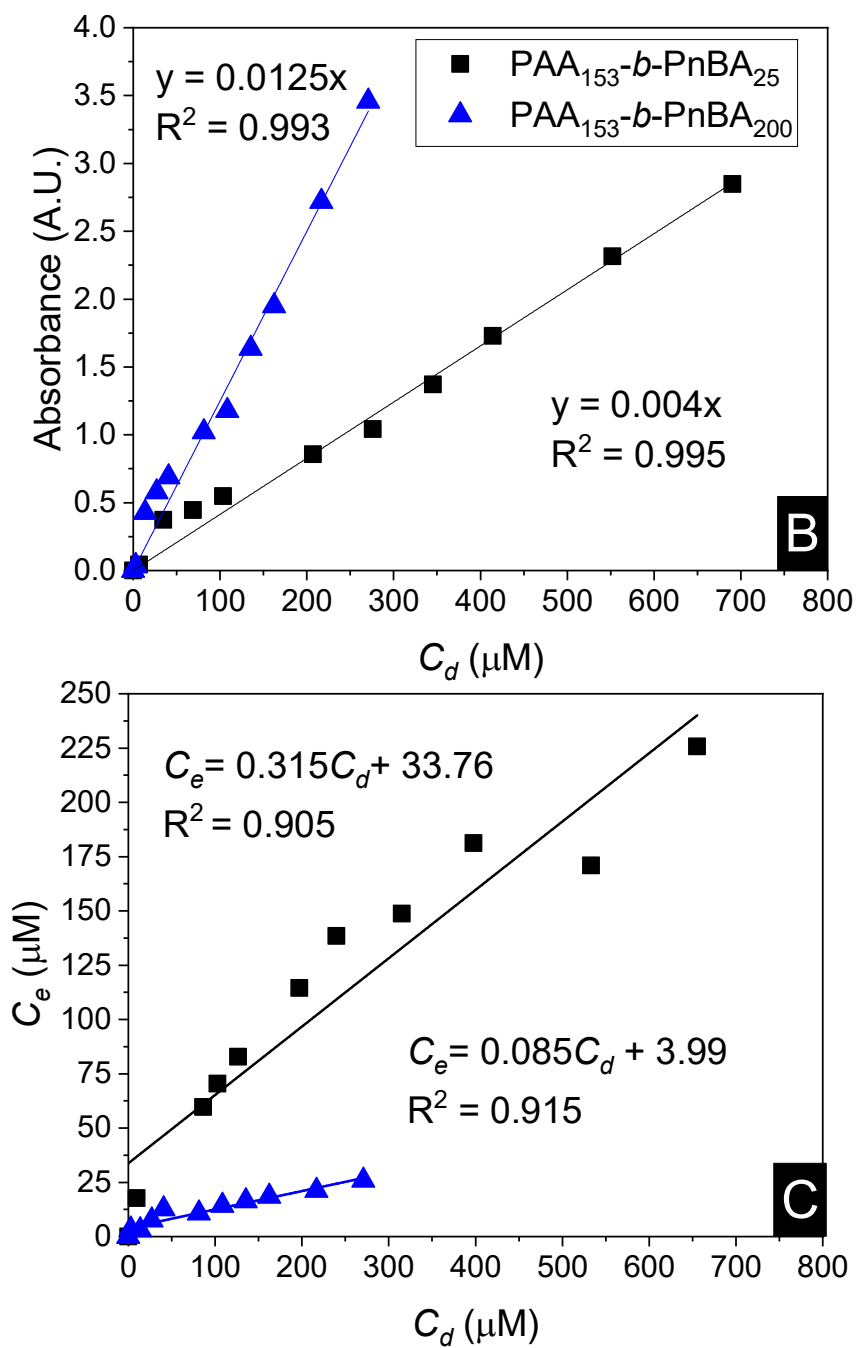


Figure C3: A) UV-Vis spectra between 300 and 350 nm of (i) $\text{PAA}_{153}\text{-}b\text{-PnBA}_{25}$ and (ii) $\text{PAA}_{153}\text{-}b\text{-PnBA}_{200}$ respectively as a function of ABC concentration. B) Correlation of the UV visible light absorbance as a function of amphiphilic block copolymer concentration. C) The correlation between initial dosed and supernatant equilibrium concentration of amphiphilic block copolymers.

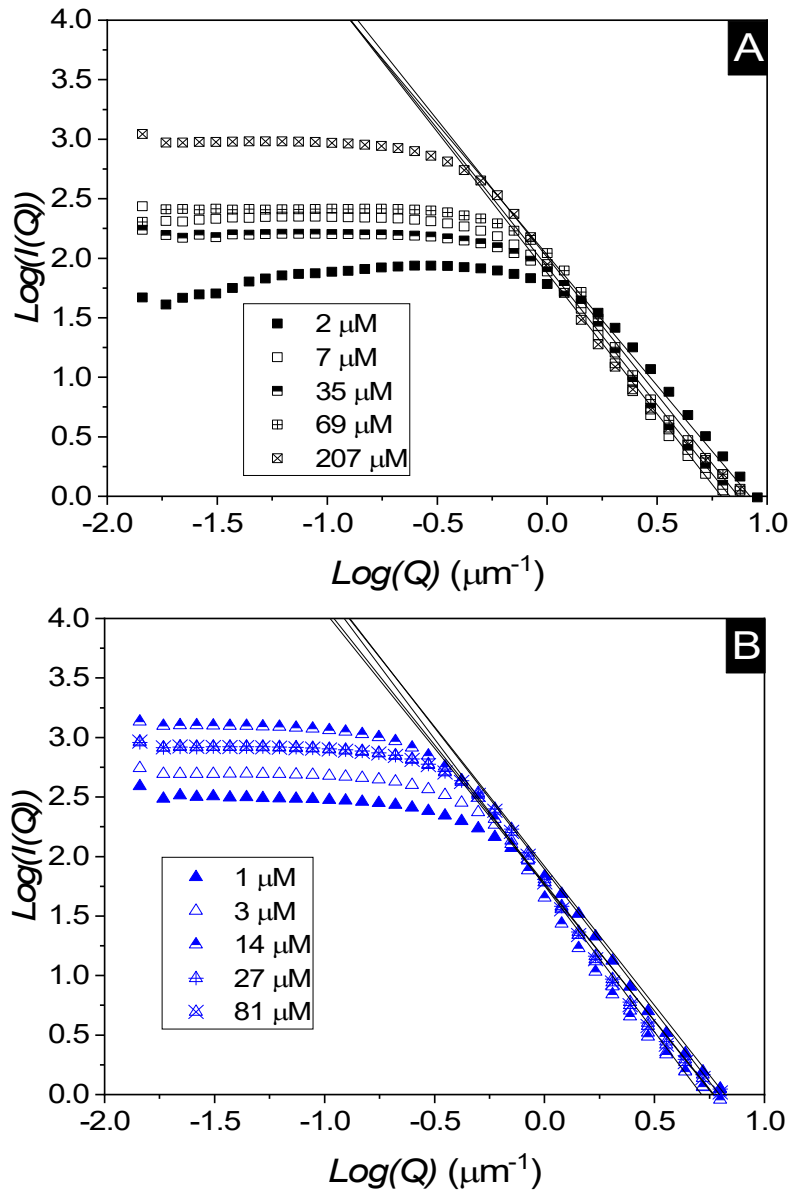


Figure C4: Logarithmic Scattering intensity, $I(Q)$, against the logarithmic wave scatter vector, Q , for A) PAA₁₅₃-*b*-PnBA₂₅ and B) PAA₁₅₃-*b*-PnBA₂₀₀